Comparison of Space Radiation Models and Evaluation of Shielding Efficiency by using the Monte Carlo Code PHITS

Joris Gackowski

Academic year 2019 - 2020

Promotor:
Prof. Dr. Ir. Klaus Bacher, UGent
Mentors:
Dr. Alessio Parisi, SCK•CEN
Dr. Olivier Van Hoey, SCK•CEN
Gerald Degreef, Tractebel ENGIE

Thesis submitted in partial fulfilment of the requirements for the degree of Master of Science in Nuclear Engineering

Belgian Nuclear Higher Education Network, c/o SCK•CEN, Boeretang 200, BE-2400 Mol, Belgium

[1] BNEN is a consortium of the Belgian universities Katholieke Universiteit Leuven (KU Leuven), Université catholique de Louvain (UCL), Université de Liège (ULg), Universiteit Gent (UGent), Vrije Universiteit Brussel (VUB) and Université Libre de Bruxelles (ULB) in collaboration with the Belgian Nuclear Research Centre SCK•CEN.

Master of Science in Nuclear Engineering

BNEN

Thesis Summary Page

Name of the student:

Joris Gackowski

Title:

Comparison of Space Radiation Models and Evaluation of Shielding Efficiency by using the Monte Carlo Code PHITS

Abstract:

This work focused on performing radiation transport calculations for optimizing the shielding efficiency against GCR and SPE in deep space (1 AU). The effect of shielding has been investigated for Al (non-light reference material), liquid H, liquid H_2O, PE, borated PE and a compound of Al and borated PE (light materials). OLTARIS was used to generate spectral data (source terms), while PHITS was used to perform Monte Carlo calculations. Enveloping and/or worst-case spectral data served as input for the transport calculations. A realistic 3D setup was considered for the geometries and for the source term distributions. Benchmarking validated the reliability of the dose calculations. The results confirmed the superior passive shielding characteristics of light materials for GCR and SPE, in which the latter component is easier to shield against, and their dependency on the solar activity. Additionally, the thickness of Al and PE required to reach Earthly dose rates in deep space has been estimated.

Promotor: Prof. Dr. Klaus Bacher

Mentors: Dr. Alessio Parisi
Dr. Olivier Van Hoey
Gerald Degreef

Assessors: Prof. Dr. Nicolas Pauly
Prof. Dr. Peter Baeten

Approval for submission by promotor:

Academic Year 2019-2020

Belgian Nuclear higher Education Network, c/o SCK•CEN, Boeretang 200, BE-2400 Mol, Belgium

ACKNOWLEDGEMENTS

Firstly, I would like to thank my mentors Dr. Alessio Parisi (SCK•CEN, Belgium) and Dr. Olivier Van Hoey (SCK•CEN, Belgium) for gradually introducing me to the field of space radiation physics and to the Monte Carlo transport code PHITS. I greatly appreciate their tremendous support, patience and continual guidance.

Also, I would like to thank my mentor Gerald Degreef (Tractebel ENGIE, Belgium) for providing me a more high-level view on the topic, but mostly for his support, encouragements and motivational talks throughout the completion of this work.

Furthermore, I would like to thank Prof. Dr. Ir. Klaus Bacher (UGent, Belgium) for his willingness to be my promotor, for delineating the scope, and for reviewing the work performed in the framework of this Master thesis.

Moreover, I am very grateful for the support provided by (1) Dr. Takuya Furuta (PHITS office, Japan), (2) Dr. Chris Sandridge (NASA LaRC, U.S.) and Dr. Tony Slaba (NASA LaRC, U.S.), and (3) Dr. Neophytos Messios (BIRA-IASB, Belgium). Their clarifications on (1) the Monte Carlo transport code PHITS, (2) the On-Line Tool for the Assessment of Radiation In Space, and (3) the SPace ENVironment Information System, respectively, were of great help.

Lastly, I would like to thank the Nuclear Department of Tractebel ENGIE (Belgium) and the Corporate Nuclear Safety Department of Electrabel ENGIE (Belgium) for giving me the opportunity, the time, and the resources for pursuing this Advanced Master-after-Master in Nuclear Engineering

Without the continuous support of my family and friends, this work could not have been accomplished. Special thanks to my beloved friend Raiko (†) for his endless support throughout the entire BNEN program.

Joris Gackowski

EXECUTIVE SUMMARY

For human deep space missions, ionizing radiation is recognized to be the primary concern in terms of negative health effects on the human body. The most important sources of radiation in space at a distance of 1 astronomical unit (AU) from the Sun (outside the Earth's magnetosphere) are **Galactic Cosmic Radiation** (GCR) and **Solar Particles Events** (SPEs). While SPEs are stochastic from nature and therefore not necessarily affect a concerned mission, literature has demonstrated that the continuous exposure to intensive GCR can lead to life-threateningly high doses for humans traveling on long-duration missions. Following the fact that the interest of space agencies and private commercial industries in deep space travel is accelerating rapidly, methods to mitigate the exposure levels, such as shielding optimization, are important to be studied.

This work focused on performing radiation transport calculations for optimizing the shielding efficiency against GCR and SPE with the objective of reducing the astronauts' dose uptake during long-duration deep space explorations missions. By evaluating the **passive shielding efficiency** of different materials, one is able to define which materials could be considered for constructing so-called "storm shelters" in the spacecraft. The need of such storm shelters has been confirmed by the International Commission on Radiological Protection (ICRP) by expressing the need of areas where the dose rates are lower than elsewhere in the spacecraft.

Based on the interactions most likely to occur according to space radiation physics, literature suggests using **light materials** for space radiation shielding. Hence, in this work, the effect of shielding on the dose (rate) has been evaluated for liquid H, liquid H_2O, non-borated polyethylene, borated polyethylene and a compound of aluminium and borated polyethylene (light materials). Plain aluminium has also been considered as a non-light reference material for benchmarking purposes as the latter is currently most widely used for space shielding applications, although it is known to have non-optimal shielding characteristics (especially for GCR).

The On-Line Tool for the Assessment of Radiation In Space (OLTARIS) has been used to generate source terms (i.e. GCR and SPE spectral data) in deep space, while the Particle and Heavy Ion Transport code System (PHITS) has been used for performing **Monte Carlo calculations**. Enveloping and/or worst-case spectral data have been considered in the transport calculations. These calculations have been performed for each source term (GCR and SPE) individually. This approach has been adopted as the occurrence of both radiation components is different in time. GCR is continuously present in space (i.e. continuous exposure), while SPE radiation lasts for a few hours or days, giving rise to an exposure limited in time. Consequently, the spectral data was integrated over different time intervals.

A realistic three-dimensional setup was considered for the geometries as well as for the source term distributions and this for all shielding configurations studied. Extensive GCR and SPE **benchmarking** confirmed the reliability of the Monte Carlo transport calculations (modelling parameters, etc.) and the application of the dose (rate) calculation methodology.

Based on the results obtained by evaluating the dose reduction and the shielding efficiency of **light materials** against GCR and SPE[2] at a distance of 1 AU from the Sun, it has been observed that light materials indeed have **superior** shielding characteristics. In fact, in terms of shielding efficiency, it has been observed that for GCR and SPE, **Liquid H** overall yields the **best** shielding efficiency while the compound **Al PE-B** generally yields the **worst** shielding efficiency with increasing shielding thickness (among the materials evaluated), and this for both the absorbed dose (rates) and the dose equivalent (rates).

By analysing the effect of shielding to GCR and SPE, it has clearly been observed that **SPEs** are much **easier to shield** against than **GCR**, and that besides passive shielding, the dose (rate) reduction also depends on the **solar activity**. Based on the outcome of this work, it was concluded that the overall shielding effect against GCR and SPE is the strongest during lower solar activities.

As overall **bounding case** for designing radiation shielding against GCR and SPE in deep space, one ideally considers the **most intensive solar minimum** (highest GCR intensities) as during the latter, the GCR dose rates are considerably higher opposed to during solar maximum (although the shielding effect is weaker during the latter). Once the passive shield has been optimized for GCR (solar minimum), effective shielding against SPEs should inherently be included as the latter's are fairly easy to shield against independent of the solar activity.

An additional study has been performed with the aim of determining the **thickness** of a material required **to reach** (worldwide) average **Earthly dose rates** in deep space caused by cosmic radiation. The results indicated that ~1300 g/cm² of Al and ~1000 g/cm² of PE would be required to reach the objective (~1 μSv/d).

As high-level conclusion, it can be stated that although light materials indeed have superior passive shielding characteristics for both GCR and SPE, it is unlikely that they will provide sufficient shielding to reduce the dose to acceptable levels within predefined weight constraints of the launchers. Hence, the **optimal** dose reduction **strategy** in deep space would be a combination of different approaches: passive shielding by **light materials** and a **reduction** in **transit time**, with the latter taking into account trajectory and timing.

The main conclusions formulated based on the results produced in this work were observed to be in line with literature, as far as relevant data was available.

2 Including secondary radiations produced by interactions of primary sources with the human body and shielding material.

LIST OF ABBREVIATIONS

ACE	Advance Composition Explorer
ALARA	As Low As Reasonably Achievable
AMS	Alpha Magnetic Spectrometer
ATIMA	ATomic Interaction with MAtter
AU	Astronomical Unit
BESS	Balloon-borne Experiment with Superconducting Spectrometer
BIRA-IASB	Belgisch Instituut voor Ruimte-Aeronomie-Institut royal d'Aéronomie Spatiale de Belgique (Royal Belgian Institute for Space Aeronomy)
BN(NT)	Boron Nitride (NanoTubes)
BON	Badhwar-O'Neill
CAPRICE	Cosmic AntiParticle Ring-Imaging Cerenkov Experiment
CLT	Central Limit Theorem
CME	Coronal Mass Ejection
CNT	Carbon NanoTube
CR	Cosmic Radiation
CREME	Cosmic Ray Effects on Micro-Electronics Code
CRIS	Cosmic Ray Isotope Spectrometer
DLR	Deutsches zentrum für Luft- und Raumfahrt (national center for aerospace, energy and transportation research of Germany)
EIT	Extreme ultraviolet Imaging Telescope
EPHIN	Electron Proton Helium INstrument
ESA	European Space Agency
EVA	ExtraVehicular Activity
eV	electronVolt
FLUKA	FLUktuierende KAskade (Fluctuating Cascade)
GCR	Galactic Cosmic Radiation
GEANT4	GEometry ANd Tracking version 4
GLEs	Ground-Level Events
GRAS	GEANT4 Radiation Analysis for Space

Gy	Gray
HCPs	Heavy Charged Particles
HEAO	High Energy Astrophysical Observatory
HZE	High Z (charge) high Energy
IAEA	International Atomic Energy Agency
ICRP	International Commission on Radiological Protection
ICRU	International Commission on Radiation Units and Measurements
IMAX	Isotope Matter-Antimatter eXperiment
IMP	Interplanetary Monitoring Platform
ISO	International Organization for Standardization
ISS	International Space Station
ISSN	International Sunspot Number
JAEA	Japan Atomic Energy Agency
JAM	Jet Aa microscopic transportation Model
JQMD	Jaeri Quantum Molecular Dynamics
KEK	Kō Enerugī Kasokuki Kenkyū Kikō (High Energy Accelerator Research Organization of Japan)
LaRC	Langley Research Center
LASCO	Large Angle and Spectrometric Coronagraph
LEO	Low Earth Orbit
LET	Linear Energy Transfer
LIS	Local Interstellar Spectrum
LNT	Linear Non-Threshold
MULASSIS	MUlti-LAyered Shielding SImulation Software
NASA	National Aeronautics and Space Administration
NCRP	National Council on Radiation Protection
NM	Neutron Monitor
NMTC	Nucleon-Meson Transport Code
OLTARIS	On-Line Tool for the Assessment of Radiation In Space
PAMELA	Payload for Antimatter Matter Exploration and Light-nuclei Astrophysics
PDF	Probability Density Function

PE	Polyethylene
PHITS	Particle and Heavy Ion Transport code System
QGSP BERT HP	Bertini High Precision Quark Gluon String Model
RBE	Relative Biological Effectiveness
RIST	Research organization for Information Science and Technology
SAA	South Atlantic Anomaly
SCK•CEN	StudieCentrum voor Kernenergie • Centre d'Etude de l'énergie nucléaire (Belgian Nuclear Research Centre)
SEP	Solar Energetic Particles
SI	Système International d'unités (International System of units)
SINP	Skobeltsyn Institute of Nuclear Physics
SOHO	SOlar and Heliospheric Observatory
SPE	Solar Particles Event
SPENVIS	SPace ENVironment Information System
Sv	Sievert
UNSCEAR	United Nations Scientific Committee on the Effects of Atomic Radiation
VRT	Variance Reduction Techniques

TABLE OF CONTENTS

1. INTRODUCTION

In order to gradually address the inherent complexity of space radiation shielding, a general introduction will be provided with the aim of pointing out the substantial differences between (ionizing) radiation (protection) on Earth and in space.

Upon touching these subjects, it will become very clear that advanced calculation methods are a requirement not only for the sake of mimicking and simulating the complex space radiation environment, but also for shielding optimization purposes.

After explaining the context and addressing the issues related to current methods for space radiation shielding (§1.1), the scope and its delimitation will be discussed in §1.2. The general structure of the thesis will be described in §1.3.

1.1. Context and problem statement

In addition to the considerable engineering challenges associated with unmanned space[3] missions, human spaceflight poses even greater challenges in limiting the negative health effects and hazards to humans. Among other important detrimental factors such as microgravity and psycho-social effects due to the confined living space associated with long-term space missions, the space radiation environment poses a substantial risk to the astronauts' health (Ref. [5]).

It is to be pointed out that the radiation environment in space is very different from that on Earth, both with respect to the various types of radiation involved and their intensities. The primary radiation field on the Earth's surface is composed of low-linear energy transfer (LET) radiations with small high-LET components, including neutrons from cosmic radiation and alpha particles from terrestrial radionuclides. The primary radiation fields in space include protons, alpha particles, heavy ions and electrons up to very high energies. Additional secondary radiations such as gammas, electrons, muons, neutrons, pions, collision and projectile fragments are produced by interaction of primary radiations with materials of the spacecraft and its equipment and with the body of the astronauts (Ref. [1] item 1).

Astronauts may work in low Earth orbits (LEOs) for extended periods of time or may be involved in deep space missions in which the conditions are exceptionally different from those on Earth. In fact, for deep space missions **outside** the **Earth's magnetosphere**, **ionising radiation** is recognised as the **key factor** through its impact on the crew's health and performance (Ref. [1] item 3). Hence, radiation exposure in space is of high concern, especially for long-term missions, due to its possible health consequences in terms of stochastic (e.g. cancer) and deterministic effects[4] (e.g. acute skin damage).

3 The term 'space' generally refers to the galactic space outside of the Earth's aviation altitudes (Ref. [1]).
4 As per Ref. [4], deterministic effects are mainly a consequence of intense SPEs (explained further).

In long-term missions, the exposure of astronauts will be higher than the annual limits recommended for exposure of workers on Earth. Publication 103 (Ref. [22]) states that '*Exceptional cases of cosmic radiation exposures, such as exposure in space travel, where doses may be significant and some type of control warranted, should be dealt with separately*'. Even though astronauts are exposed to ionising radiation during their occupational space activities, they are usually not classified as occupationally exposed in the general sense of the ICRP system for radiation protection of workers on Earth and aircraft crew[5]. Hence, for a specific mission, reference values for doses or risks may be selected at appropriate levels, but no dose limits may be applied. The **risk-related approach** for assessing the radiation exposure in space is strictly restricted to the special situation in space and should not be applied to any exposure situation on Earth (Ref. [1] item 3).

An illustrative dose rate comparison is provided below to underline the substantial differences in terms of exposure between the situation on Earth and in space.

In Belgium, the legal (effective) dose limit for occupationally exposed personnel is defined by the national authorities and is equal to 20 mSv over a period of 1 year (actually over a period of 12 consecutive sliding months to be correct), as per Ref. [9]. In terms of daily exposure, the yearly dose limit of 20 mSv can be converted to a value of ~0.05 mSv/d assuming a linear approach. For astronauts, on the other hand, the doses are a consequence of the extreme exposure situations in **space**, which typically generate daily exposure levels around **1 mSv/d** (Ref. [1] item 311). In other words, the daily exposure level in space is typically a factor ~20 higher than the daily exposure level in Belgium by assuming a continuous linear spread of the dose over a period of one year to reach the dose limit for occupationally exposed personnel in Belgium. In practice, the dose limit of 20 mSv/y is virtually never reached nor even approached in most situations. It can be concluded that even the typical exposure levels in space are exceptionally high compared to the (conservatively calculated) exposure levels on Earth (Belgium).

On **Earth**, radiation protection of workers and the primary dose limits defined are aimed to limit the probability on stochastic effects to acceptable levels compared with other health risks during human life, while simultaneously avoiding detriments caused by deterministic effects. The primary limits are defined in terms of doses[6,7] that can be assessed with sufficient precision for radiation protection applications, and not in terms of radiation risks, the value of which depends on many individual factors (e.g. age, sex, individual genetic properties). Especially at low exposure levels, knowledge on these risks is very limited and high uncertainties commonly arise. In addition to the limitation of doses and risks, the principle of optimisation is generally applied in radiation protection, which means that even below exposure limits, optimisation always needs to be considered and may even require further measures (Ref. [1] item 7).

5 The exposure of astronauts in space is considered by the ICRP as a special case of exposure and is defined as an existing exposure situation by the Commission (Ref. [1] item 3).

6 Effective dose and equivalent dose to the skin, hands, feet, and lens of the eye where specific limits have been defined for avoiding deterministic effects (Ref. [1] item 7).

7 The value of the effective dose is calculated by averaging organ equivalent doses over both sexes and using mean values of weighting factors obtained from epidemiological data, hence from large groups of exposed and unexposed persons (Ref. [1] item 7).

In **space**, in contrast to Earth, the situation is quite different; exposure of astronauts by space radiation cannot be avoided and prevention by shielding cannot fully be achieved (Ref. [1] item 8). Following the high exposure levels in space (1 mSv/d), it is clear that optimisation should be considered in space.

For space applications, simulations using radiation transport codes are essential for estimating the radiation doses that are likely to be received by the astronauts during future missions to space and in case when measurements are not feasible or non-existing. Radiation transport codes also play a crucial role in understanding the effects of **shielding** of radiation in space (Ref. [2] p47). Exactly for the latter purposes a radiation transport code (PHITS) will be used in this work.

From literature it is known that in deep space **Galactic Cosmic Radiation** (GCR) and **Solar Particle Events** (SPE) represent the most important primary sources of radiation in terms of dose contribution (Ref. [1] item 291, [32], [33]). **Secondary radiations** produced by interactions of primary radiation with matter can even so contribute significantly to the dose uptake (Ref. [1] item 56).

Furthermore, studies in literature (e.g. Ref. [2], [3], [4]) conclude that **aluminium**, a material typically used in spacecrafts, significantly reduces the exposure against SPE in function of the shielding thickness, while rather being **ineffective** or even counter-productive in terms of reducing exposure against **GCR**. Consequently, to account for all relevant sources of radiation in space, alternative materials should be investigated. Based on the interactions most likely to occur according to space radiation physics, literature suggests considering light hydrogenous materials for purposes related to space shielding optimisation (Ref. [1] item 254).

1.2. Scope and delimitation

Based on the context provided in §1.1, this work will focus on evaluating materials which may lead to **optimum shielding to GCR** and **SPE** since both sources have been identified as major primary sources of radiation in deep space. Because of its importance, **secondary radiations** will even so be taken into account.

Even though active shielding methods (electrostatic, magnetic, plasma) exist, they appear to be not mature enough for spaceflight (Ref. [29], [48]). Hence, focus will be put on evaluating **light materials** for **passive shielding** purposes only.

Focus will be put on optimizing passive shielding for **sheltering purposes** as the ICRP (Ref. [1] item 315) and the National Aeronautics and Space Administration (NASA) (Ref. [29]) state that the construction of a spacecraft should include areas, so-called storm shelters, at which the dose rates are lower than elsewhere in the spacecraft. This statement becomes even more important in long-duration space missions as in the latter space radiation exposure is recognised as the key factor affecting the astronauts health (Ref. [1] item 3).

Also, depending on the location with respect to the Earth’s magnetosphere, more particularly, inside or outside the Earth’s magnetosphere, the considered particle fluxes are treated differently.

As deep space missions are of interest in this work, particle fluxes from **outside Earth's magnetosphere** at a distance of **1 AU**[8] from the Sun will be considered (Ref. [2] p33-35). In fact, outside the Earth's magnetosphere the natural protection by the Earth's magnetic field is no more, leaving mission planning and radiation shielding as one of the few options for dose reduction (Ref. [1] item 18).

Information contained in the PhD work of Dr. Mrigakshi with title "*Galactic Cosmic Ray Exposure of Humans in Space – Influence of galactic cosmic ray models and shielding on dose calculations for low-Earth orbit and near-Earth interplanetary space*" (Ref. [2]) has extensively been used throughout this work as it particularly focused on enhancing the predictions of GCR exposure for humans in space. To fully grasp and cover all aspects related to space radiation shielding, many other references have been consulted as well throughout the elaboration of this work.

1.3. Structure of the thesis

A brief but sufficiently detailed overview of the space radiation environment will be provided in §2. It concludes with the types of radiation relevant for dose estimation and shielding optimisation.

Besides addressing the general aspects related to radiation protection in space, the importance and difficulties related to space radiation shielding will be described in §3 together with materials recommended for optimisation of shielding in space.

§4 will elaborate on the relevant dose quantities and summarizes the differences between the quantities used for radiation protection on Earth compared to those used in space. The risk based approach adopted by NASA will be discussed as well.

An overview of different GCR models available in literature will be provided in §5. These models will be compared among each other and to measurements based on information from literature. From this literature study, it will be defined which GCR model will be used as input for the Monte Carlo code PHITS.

The general methodology for evaluating shielding efficiencies will be described in §6, as well as the tool used for source term generation and the scripts developed for data treatment purposes. The Monte Carlo approach, the multi-purpose Monte Carlo code PHITS and the simulation input parameters will be addressed as well.

The specific methodology for GCR and SPE dose calculations applied in this work will be described in §7 together with an in-depth discussion of the results obtained by post-processing the output data.

Based on the data and results described in §6 and §7, a conclusion will be provided in §8 which takes into account all information described throughout this thesis.

Lastly, an outlook will be provided in §9 in which topics for potential future studies related to this work are discussed. Lastly, all references are summarized in §10.

[8] The astronomical unit 'AU' (or 'au' to be fully correct) is defined as exactly 149,597,870,700 m (about 150 billion meters). It is approximately the average distance between the Earth and the Sun (Ref. [18]).

2. RADIATION ENVIRONMENT IN SPACE

The radiation environment in space is a complex mixture of particles mostly from galactic and solar origin with a broad range of energies. Each source of radiation and their interactions by various mechanisms determine the actual radiation field at any given time and location within the heliosphere[9] (Ref. [1] items 12 and 17). Moreover, it is recognized by the ICRP that the basis for any measure in radiation protection, thus including radiological protection in space (§3), should always be knowledge of the radiation fields involved (Ref. [1] item 5).

The objective of this chapter is to provide a brief but sufficiently detailed overview of the space radiation environment. In a first step, the major primary and secondary sources of radiation in space will be addressed in §2.1 and §2.2, respectively. The radiation fields relevant for radiological protection in space will then be discussed in §2.3. To conclude, in §2.4 it will be justified which sources of radiation in space will be considered in this thesis.

2.1. Primary radiation fields in space

The three major primary sources of space radiation are identified and categorized by the ICRP to be the following (Ref. [1] item 19):

- Originating from outside of the heliosphere, Galactic Cosmic Radiation (**GCR**) continuously enters the heliosphere from all directions from outer space. Inside the heliosphere, radiation is continuously emitted by the Sun and is responsible for the creation of interplanetary magnetic fields, the so-called '**solar wind**';
- Solar Particle Events (**SPE**) are rare occasions in which unusually large pulses of energetic particles are emitted by the Sun, mostly protons and electrons with a small contribution of helium and heavy ions, and ejected into space by solar eruptions;
- Radiation belts created by bodies equipped with a magnetic moment such as the Earth. These **trapped radiation belts** can repel galactic and solar particles as well as secondary particles created through interaction of primary particles with the atmosphere, for example.

Even though the ICRP categorizes the different radiation fields in space in three major primary sources, a description of all four of them is provided in the following subchapters (§2.1.1 to §2.1.4). Secondary radiations will also briefly be discussed in §2.2 because of their particular importance in space dosimetry.

Note that the different radiation fields in space are described to the level of detail deemed relevant in order to comprehend and address the topics elaborated in the subsequent chapters of this thesis. For a complete description, dedicate literature should be consulted, such as, for instance, ICRP Publication 123 (Ref. [1]), which has extensively been used throughout these introductory chapters (§1 to §4).

[9] The heliosphere is defined as the space around the Sun and its planets that is filled by solar particles emitted from the Sun (the solar wind) and the corresponding solar magnetic field (Ref. [1]).

Before elaborating on the different radiation fields in space, a general description of the heliosphere and its direct impact on the space weather is provided with the intention of giving the reader a more global view on the topics yet to be discussed.

As shown in Figure 1 below, the Sun and its atmosphere consist of several zones from the inner core to the outer corona. Beyond the corona is the solar wind, which is an outward expansion of coronal plasma that extends well beyond the orbit of Pluto. This entire region of space influenced by the Sun is called the heliosphere.

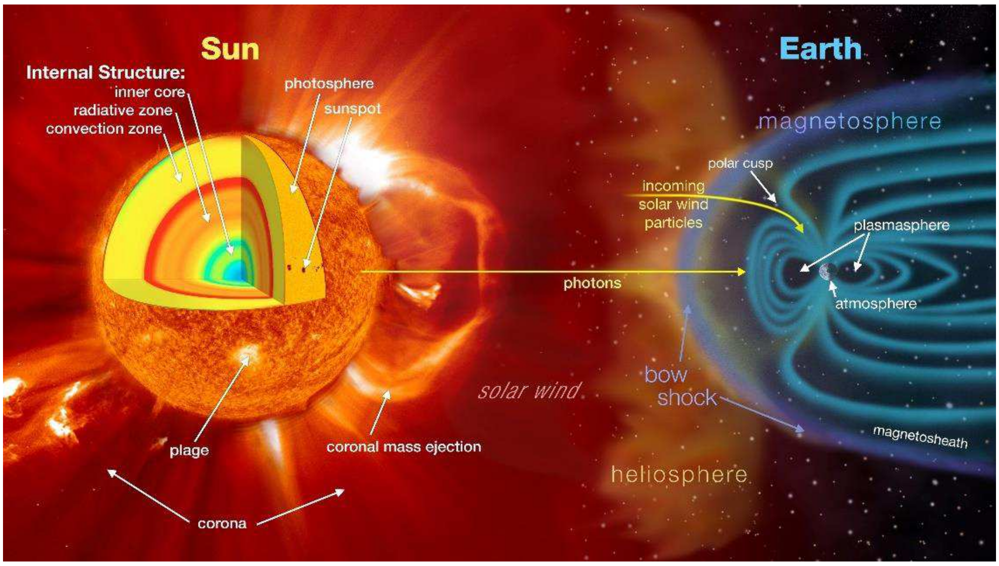

Figure 1: Illustration of the Sun-Earth interactions that influence space weather (Ref. [31])

Controlled by the Earth's magnetic field, the (spider shaped) magnetosphere acts as a natural shield essentially protecting the planet from solar wind. The shape of the Earth's magnetosphere is the direct result of being impacted by solar wind, compressed on its sunward side and elongated on the night-side, the magnetotail.

The shock wave where the solar wind encounters Earth's magnetosphere is called the bow shock, which slows and diverts the solar wind. Solar activity leads to solar eruptions, which includes such phenomena as sunspots[10], flares[11], prominences[12], and Coronal Mass Ejections[13] (CME) that influence space weather, or near-Earth environmental conditions (Ref. [31]).

[10] Sunspots are areas that appear dark on the surface of the Sun as they are cooler than other parts of the Sun's surface because they form at areas where magnetic fields are particularly strong. These magnetic fields are so strong that they keep some of the heat within the Sun from reaching the surface (Ref. [14]).

[11] Solar flares are intense bursts of radiation coming from the release of magnetic energy associated with sunspots and are our solar system's largest explosive events. They are seen as bright areas on the Sun and they can last from minutes to hours. Flares are also sites where particles (electrons, protons, and heavier particles) are accelerated (Ref. [13]).

[12] A solar prominence is a large, bright feature extending outward from the Sun's surface. Prominences are anchored to the Sun's surface in the photosphere, and extend outwards into the Sun's hot outer atmosphere, i.e. corona (Ref. [16]).

[13] At locations where the strong magnetic fields of the outer solar atmosphere close, the confined solar atmosphere can suddenly and violently release bubbles of gas and magnetic fields called Coronal Mass Ejections (CME). A large CME can contain a billion tons of matter that can be accelerated to several million miles per hour in a spectacular explosion. Solar material streams out through the interplanetary medium, impacting any planet or spacecraft in its path (Ref. [15]).

2.1.1. Galactic Cosmic Radiation (GCR)

Cosmic Radiation (CR) refers to radiation originating from the Sun (often called Solar Cosmic Radiation) and from radiation sources from outside the solar system. CR specifically originating from outside the solar system is commonly referred to as Galactic Cosmic Radiation (GCR) (§2.1 of Ref. [2]).

GCR can be defined as a stream of high-energy[14] charged particles, primarily in the hundreds of MeV to many GeV, ranging up to 10^{20} eV, continuously entering the heliosphere from outer space from all directions (Ref. [55]). It consists of ~83% protons (hydrogen nuclei), ~14% alpha particles, ~1% heavy ions[15] (the baryonic components), and ~2% electrons.

Although the exact mechanisms accelerating the charged particles are unknown, they most probably originate from supernova[16] explosions, neutron stars, pulsars[17], or other sources where high-energy phenomena are involved. Knowing that GCR particles are influenced by irregular interstellar magnetic fields, no profound data about the directional position of their sources is available (Ref. [1] item 23).

As shown in Figure 2a below, the GCR fluence rate is not constant in time but it varies between two extremes corresponding to maximum ('summer') and minimum ('winter') solar activity. In fact, the GCR fluence rate is anticorrelated to the solar activity during the 11-year sunspot cycle, as visualized in Figure 2b below, and the 22-year magnetic cycle of the Sun (Ref. [5]).

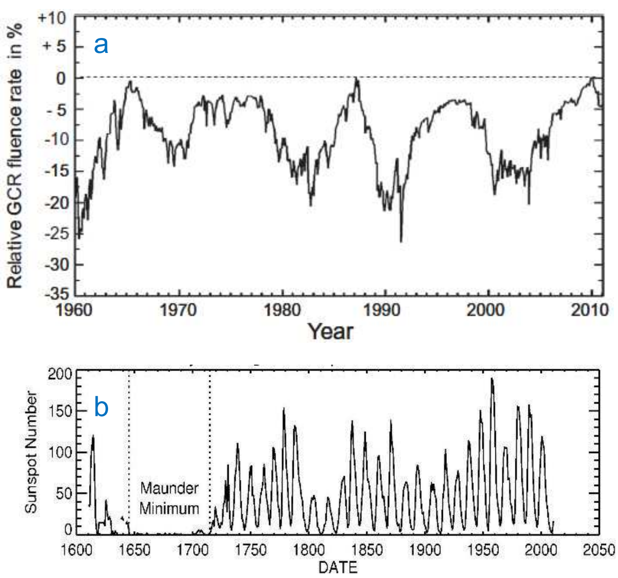

Figure 2: a) Relative GCR fluence rate in time (Ref. [1]), b) Yearly averaged sunspot number in time (Ref. [56])

For example, during the solar minimum in 2009, the GCR fluence rate reaches a maximum (Figure 2a) as the sunspot number reaches a minimum (Figure 2b).

14 In space radiation physics, energies are often expressed in MeV/u (AMeV). By doing so, all nuclei with the same value of energy per u (atomic mass unit) move with nearly the same velocity independent of their mass (Ref. [1] item 25).
15 Heavy ions or so-called 'high Z (charge) high energy' (HZE) particles are ions of elements heavier than He, i.e., Z > 2.
16 A supernova is defined as the largest explosion of a star that takes place at the end of a star's life cycle (Ref. [10]).
17 Most neutron stars are observed as pulsars. Pulsars are rotating neutron stars observed to have pulses of radiation at very regular intervals that typically range from milliseconds to seconds (Ref. [11]).

Knowing that solar modulations are defined by the variation of GCR over time and are caused by changes in the solar activity, the solar modulations can be monitored on Earth by measuring the fluence rate of secondary neutrons produced by interaction of primary GCR particles with nuclei of the Earth's atmosphere. This fluence rate has been measured over long periods by means of different ground-based stations using neutron monitors (NMs) (Ref. [1] item 27).

Coming back to the composition of the GCR, it may appear that the consideration of hydrogen (~85%) and helium nuclei (~14%) alone for the baryonic component (i.e. disregarding the electrons) might be sufficient for the GCR dose assessment as these particles comprise ~99% of the total baryonic component of GCR.

However, the fraction of heavy ions to the baryonic component (~1%) contributes significantly to the radiation exposure of astronauts as the extent of the biological damage is related to the energy deposition pattern on a cellular level (Ref. [2]). In fact, literature details that the influence of heavy ions on humans is often more significant than that of the protons and helium. Almost 50% of the human dose equivalent comes from ions with Z > 2 (Ref. [66]).

To explain these energy loss phenomena, an **intermezzo** on the different types of interactions of space radiation with matter is provided in subchapters §2.1.1.1 and §2.1.1.2, prefaced by a brief introduction. For more details on the most important radiation-matter interactions in space, reference is made to §2.2 of Ref. [2].

When GCR traverses through matter, it interacts with the constituting atoms and molecules through electromagnetic and nuclear forces. The interactions between GCR and a target (e.g. spacecraft material) produces a large variety of secondary particles (e.g. gamma radiation, electrons, muons, neutrons, pions and secondary protons and heavy ions). Neutrons and secondary ions are especially important for space applications as they can deposit large amounts of energy in the medium[18]. Other secondary particles such as electrons and photons contribute only a small fraction to the total exposure. Nevertheless, they can be of importance in radiation protection in space (Ref. [2] p18).

2.1.1.1. ELECTROMAGNETIC INTERACTIONS

While traveling through matter charged particles exert long-range Coulomb forces on electrons of the target atoms along their path and undergo inelastic scattering, thereby suffering energy loss as they penetrate deeper inside. The lost energy is transferred to the orbital electrons[19], causing ionization and excitation of the target atoms.

When the projectile protons or heavy ions interact with atomic electrons, they lose a very small fraction of their energy during a head-on single collision and are only slightly deflected. This kind of scattering is also known as Coulomb scattering. Thus, they travel mostly in nearly straight lines continuously transferring a small fraction of their energy during each collision with the electrons on their path.

---

[18] In fact, it is also important how the energy is deposited on the cellular level. For neutrons and heavy ions the energy deposition is more concentrated at the cellular level leading to more complex and more difficult to repair cell damage.

[19] The orbital electrons may sometimes gain sufficient energy from the projectile leaving the atom and induce secondary ionization of neighbouring atoms. Such electrons are often called δ-electrons or δ-rays. The range of δ-rays is however small compared to the charged ions so that ionizations occur close to the primary ion track.

For charged particles, the quantity stopping power is often used to determine the average energy loss per unit track length in the medium (usually expressed in MeV cm^{-1}) and is of fundamental importance in radiation dosimetry. There are three different kinds of stopping powers depending on the type of energy loss:

- Collision or electronic stopping power (associated with the inelastic collisions of the projectile ions with electrons which can lead to, e.g., ionization and excitation of target atoms and molecules);
- Radiation stopping power (associated with the emission of bremsstrahlung photons when typically electrons are decelerated by sharp deflections caused by their interaction with atomic nuclei of the medium);
- Nuclear stopping power (associated with the elastic collisions between the projectile ion and nuclei of the medium. It is only important for low energy heavy particles. When the projectile energy becomes higher, nuclear stopping is not important, and can be neglected in the calculations).

The description of the collision stopping power is particularly important for the transport of ions in matter as they suffer energy losses mainly due to ionization.

An expression of the collision stopping power of a uniform medium for relativistic heavy charged particles, $-\frac{dE}{dx}$, is given by the Bethe-Bloch formula.

The Bethe-Bloch formula essentially is the basic expression for the energy loss calculations:

$$-\frac{dE}{dx} = 2\pi N_a r_e^2 m_e c^2 \rho \frac{Z}{A} \frac{z^2}{\beta^2} \left[\ln\left(\frac{2m_e \gamma^2 v^2 T_{max}}{I^2} \right) - 2\beta^2 \right]$$

Where:

- N_a Avogadro’s number;
- r_e classical radius of electron;
- m_e mass of electron;
- c speed of light;
- ρ density of medium;
- Z charge number of medium;
- A mass number of medium;
- z charge of incoming particle;
- β $\frac{v}{c}$;
- γ $\frac{1}{\sqrt{1-\beta^2}}$;
- v velocity of the heavy ion projectile of mass M;
- T_{max} maximum energy transfer that occurs during a single head-on collision between a heavy ion projectile of mass M with velocity v and an orbital electron of mass m_e at rest;
- I mean excitation potential of medium.

From the Bethe-Bloch formula it is clear that the stopping power is dependent on properties of the incident ion type and its energy, and on the target material. It follows from the equation that with decreasing velocity and energy of the projectile the energy loss increases. As a result, a characteristic maximum in the energy deposition with depth curve is observed at the end of their path in the medium and is called the Bragg-peak.

Another factor to note is that the energy loss of a particle is proportional to the square of their charge z^2. This means that heavier ions lose energy in a given medium at a faster rate than the lighter ones which further indicates that they have shorter range (penetration depth) as well. The equation even so highlights the importance of the traversed medium in terms of energy loss of heavy ions. The energy loss is proportional to $\frac{Z}{A}$ which means that materials having high charge-to-mass ratio, e.g. hydrogen in comparison with aluminium, will lead to greater energy loss of the projectiles.

Depending on the energy level of the incoming photon and the atomic number of the target material Z, other well-known indirect electromagnetic interactions such as photoelectric effect, Compton scattering and pair production might occur which even so lead to energy loss. However, since the ICRP recognizes that there is no measurable contribution to radiation exposure by primary electromagnetic radiation (discussed in §2.3), is has been decided to not elaborate on (primary) photon interactions in this intermezzo. Nevertheless, secondary photons will be treated in the radiation transport calculations performed in this work (§6).

2.1.1.2. NUCLEAR INTERACTION

Unlike the quasi-continuous energy loss through electromagnetic interactions of a charged particle along its track, the energy loss via nuclear (strong) interactions occurs much less frequently. The latter can be explained by the significantly lower cross section of strong interactions. For charged particles, strong interactions can only take place if the energy of the incoming particle is higher than the repulsive coulomb forces exerted by other charged particles, known as the Coulomb barrier.

Strong interactions are dominant for heavy ions with energies above 100 MeV/nuc and are thus highly relevant for GCR nuclei interactions with the spacecraft and tissue. In fact, the main mechanism of energy loss of GCR heavy nuclei is through fragmentation. The latter process leads to the production of secondary particles which may further interact with the medium and lose energy. In such processes either the projectile or the target nucleus fragments into smaller nuclei and some nucleons. While the projectile fragments mostly preserve the velocity of the incident particle, the target fragments are slow relative to the incident particle.

Nuclear interactions can lead to the production of secondary neutrons which are of great importance as they are extremely penetrating and deposit large amounts of energy indirectly through the production of secondary charged particles due to nuclear interactions. Typical neutron interactions are the following: (n,γ), (n,p), (n,α), $(n, fragmentation)$.

Having this said, the **intermezzo** elaborated in §2.1.1.1 and §2.1.1.2 is considered as **closed**, continuing with the importance of the small fraction of heavy ions to the baryonic component (~1%) of GCR, as discussed in §2.1.1.

Based on the Bethe-Bloch formula provided in §2.1.1.1, it is clear that the small fraction of heavy ions to the baryonic component (~1%) contributes significantly to the radiation exposure of astronauts since the extent of the biological damage, which is directly related to the energy loss[20], is proportional to the square of charge of the particle, z^2. For different incoming particles, the proportionate energy loss factor due to ionization (inelastic scattering) is illustratively provided below:

- Proton (Z = 1) : $\mathrm{E_{loss}} \propto 1^2 = 1$;
- Alpha (Z = 2) : $\mathrm{E_{loss}} \propto 2^2 = 4$;
- Iron (Z = 26) : $\mathrm{E_{loss}} \propto 26^2 = 676$;
- Uranium (Z = 92) : $\mathrm{E_{loss}} \propto 92^2 = 8464$.

It can thus be concluded that the assessment of the radiation exposure from GCR heavy nuclei is important for radiation protection in space.

In conclusion, the contribution of lighter nuclei to the radiation exposure in space is substantial due to their large elemental abundances. Heavy ions, on the other hand, are much less abundant but they are of importance because of their higher biological effect related to the higher specific energy loss within a material, which is, as discussed above, proportional to the square of charge of the particle.

Heavy ions such as Fe are able to penetrate inside the spacesuits/crafts and can cause extensive cellular damage through interacting with the astronauts' bodies due to the large energy deposition along their densely ionizing tracks (Ref. [6], [8]).

Figure 3 below illustrates the relative contribution of GCR nuclei with 1 ≤ Z ≤ 26 and energies ranging from 10 MeV/nuc to 100 GeV/nuc to:

- The total particle fluxes integrated over energy (in black);
- The absorbed dose rates (dD/dt, in red);
- The dose equivalent rates (dH/dt, in blue).

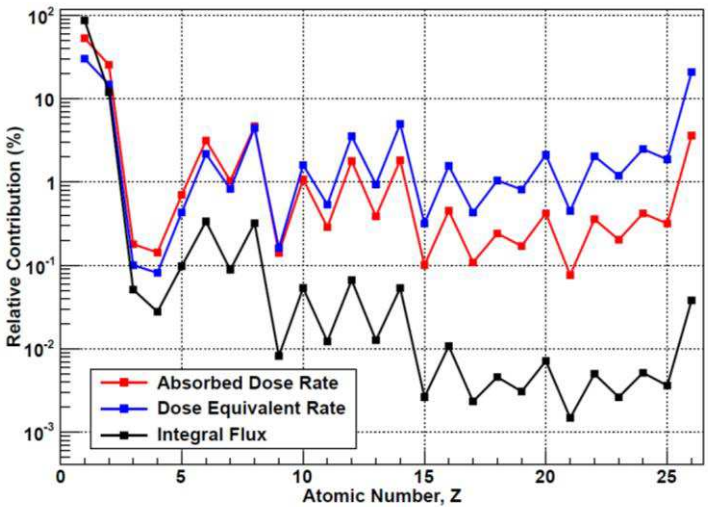

Figure 3: Relative GCR contribution to the total absorbed dose rate, dose equivalent rates and integrated flux (Ref. [2])

[20] The Bethe-Bloch formula gives energy loss per unit of length and thus shows that heavier ions deposit their energy on smaller length scales and therefore have more biological effect per unit of deposited macroscopic dose.

From literature, it has been shown that GCR nuclei with Z > 26 are usually ignored because they are much less abundant and have an insignificant dose contribution to the total exposure (§2.3.2. of Ref. [2], Ref. [6] and [8]).

Typical absorbed dose and dose equivalent rates for near-Earth interplanetary space[21] and International Space Station (ISS) orbit are provided in Figure 4a and Figure 4b below, respectively.

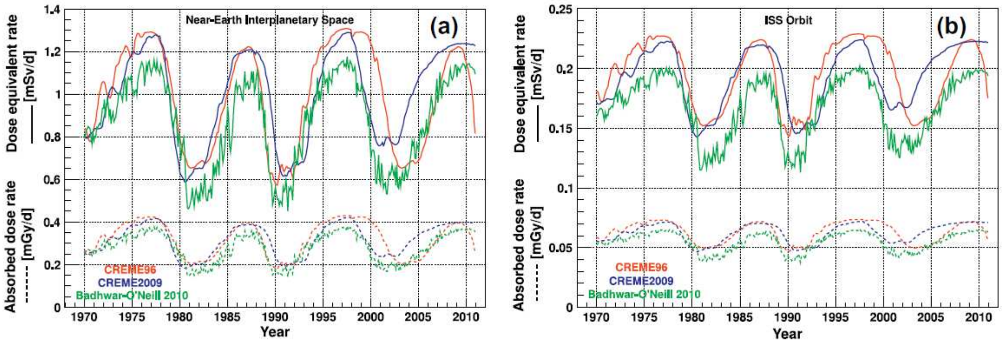

Figure 4: Absorbed dose and dose equivalent rates for near-Earth interplanetary space (a) and for ISS orbit (b) (Ref. [6])

As this work focuses on locations outside the Earth's magnetosphere, it is clear that the dose rates reported in Figure 4a are most relevant. The dose rates are calculated in an unshielded water sphere[22] using GCR spectra from different models. These GCR models will be addressed in §5.

To make the link to the solar cycle[23] and the GCR fluence rate, one can derive that, during the solar minimum in 2009 (Figure 2), when the solar activity is minimum and the GCR fluence rate reaches a maximum, the dose rates reach a maximum.

2.1.2. Solar wind

Solar winds are generally defined as streams of solar particles, mainly low-energy electrons and protons (between 100 eV and 3.5 keV), continuously emitted by the Sun into the heliosphere and are responsible for creating interplanetary magnetic fields. The intensity depends on the solar activity and varies with the solar cycle.

The intensities of the low-energy particles vary approximately between 10^{10} and 10^{12} particles cm^{-2} s^{-1} sr^{-1}. In terms of velocity, this particle stream is characterised by velocities between approximately 300 km s^{-1} and 800 km s^{-1} and more.

Within the inner heliosphere, the temporal variation of the solar wind influences the radiation exposure from GCR in space. In fact, when the solar activity is high, the solar wind is more dynamic and therefore more effective at impeding GCR penetration into the solar System. Hence, there is an anti-correlation between the sunspot number and the GCR intensity at Earth. The magnetic field based on the solar wind provides a similar shielding as the geomagnetic field (Ref. [1], [62]).

21 At a distance of 1 AU from the Sun outside the Earth's magnetosphere.
22 A water sphere with a radius of 25 cm was considered with the aim of mimicking the human body.
23 The solar cycle is defined as the variation of the solar activity between two extremes with a cycle time of approximately 11 years. The solar activity can be described by the number of observed sunspots (Ref. [1]).

2.1.3. Solar Particle Event (SPE)

A SPE can be defined as a rare event of probabilistic nature caused by an eruption at the surface of the Sun, leading to the acceleration of a large number of particles with huge variability in fluence rate and energy distribution.

It occurs when particles, mostly protons[24], emitted by the Sun become accelerated either close to the latter during a flare or in interplanetary space by CMEs. The Solar Energetic Particles (SEP) will escape into the interplanetary space and can spiral around the interplanetary magnetic field lines (Ref. [1] item 21).

The intensity (fluence rate), energy spectra, and angular distributions of SEP vary considerably with individual solar flares and are a function of time within any given event. A typical flare has a duration of about 1 to 4 days although longer duration flares have been observed. Normally, a flare’s intensity increases rapidly over the first few hours and then decreases (Ref. [58]).

Although solar protons normally have insufficient energy to penetrate the Earth's magnetic field, during extreme solar flares protons can be produced with sufficient energies to reach the Earth's magnetosphere around the poles. In fact, when solar protons enter the Earth's magnetosphere where the magnetic fields are stronger than solar magnetic fields, they are guided by the Earth's magnetic field into the polar regions where the majority of the Earth's magnetic field lines enter and exit.

In contrast to locations near or inside the Earth's magnetosphere, significant proton radiation exposure can be experienced by astronauts who are located outside of the protective shield of the Earth's magnetosphere. In fact, the ICRP states that SPEs are responsible for the most dramatic radiation events in terms of exposure of astronauts and have the ability to expose space crew to life-threateningly high doses (Ref. [1] item 30).

In the absence of shielding, strong SPEs can cause adverse skin reactions since protons above ~10 MeV can penetrate spacesuits and reach the skin or the eye lens. Depending on the particle intensities, they may induce erythema or give rise to late radiation cataracts within the lens of the eye. Symptoms as anorexia, fatigue, nausea, vomiting, and diarrhoea might also occur (Ref. [1] item 33).

Major SPEs are observed on Earth as random events with low frequency, typically one per month, and can be observed as ‘ground-level events’ (GLEs) by recording the count rate of secondary neutrons by means of terrestrial neutron monitors.

The ICRP reports that since 1955, five SPEs with intensities and energies large enough to jeopardise crew health behind normal or even enhanced spacecraft shielding have been observed (Ref. [1] item 34). The most intensive SPE recorded in observational history has occurred on November 4, 2003.

In fact, on May 18, 2004, NASA published an overview on the violent solar events of fall 2003 (Ref. [17]). The most relevant information on these events is quoted below accompanied by official footage captured by International Space Agencies:

[24] SPEs are mostly composed of protons with, in addition, about 10% He and < 1% heavier elements (Ref. [30]).

"…After a significant lull in its activity, the Sun unleashed a series of storms for a two-week period from October 22 to November 4, 2003, producing some of the most extreme events on record. The activity level was close to that of the maximum level of the current solar cycle, an 11-year period in which the Sun goes from stormy to quiet and back again…

…Scientists believe violent solar activity occurs when solar magnetic fields become strained and suddenly "snap" to a new configuration, like a rubber band that has been twisted to the breaking point. This releases tremendous energy, producing intense flashes of light and radiation called solar flares and massive eruptions of electrically charged gas called Coronal Mass Ejections (CMEs).This stormy solar weather occasionally disrupts satellites, power systems, and radio communications…

…A nest of twisted magnetic fields capable of generating explosive solar events typically arises around sunspots (relatively cool, dark regions on the Sun's visible surface) and is called an "active region"… Region 10486 was monstrous and produced the largest flare ever recorded in X-rays on November 4, 2003 before rotating behind the edge of the Sun. As the Sun continued to rotate, the regions came into view again and 10484 (renamed 10501) ejected a CME that caused the largest geomagnetic storm of the current cycle (solar cycle 23)…

Region 10486 has the unique distinction of launching CMEs whose shocks produced three "super particle" events. This has never happened in recorded history. (A super particle event is a measure of the intensity of the radiation from a solar event. An event is classified as such when solar-observing spacecraft detect more than 1,000 high-energy particles (10 MeV protons) per square centimeter per second in a given direction. More than 10 per second is considered hazardous.)"

Figure 5 below illustrates some footage of the extreme solar events occurred on November 4, 2003 (Credit to NASA and the European Space Agency (ESA)).

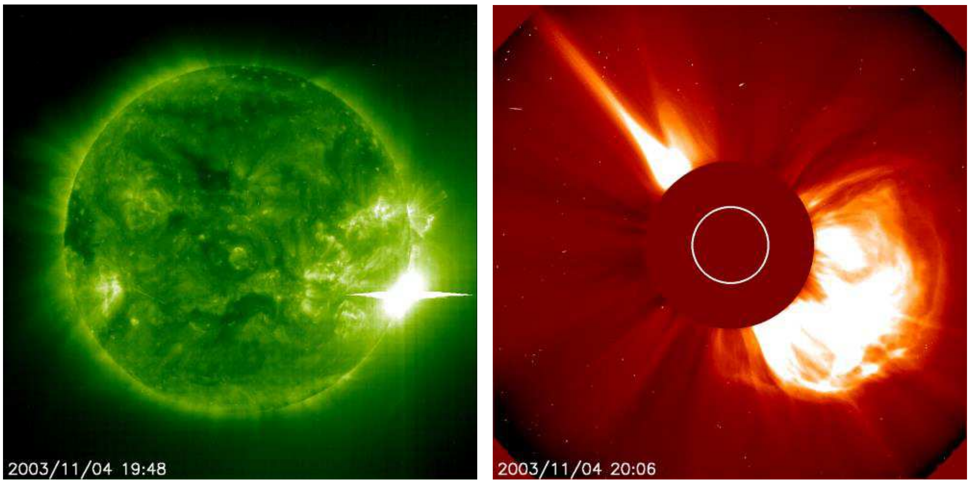

Figure 5: Picture of a false-colour image of the X-28 flare on November 4, 2003 (left) and the Coronal Mass Ejection associated with the November 4, 2003 X-28 flare (right) (Ref. [17])

The left sided picture illustrated in Figure 5 is a false-colour image of the X-28 flare on November 4, 2003 taken with the Solar and Heliospheric Observatory's (SOHO) Extreme ultraviolet Imaging Telescope (EIT). The flare is the white area near the bottom right of the image (the horizontal lines resulted when the flare's intense light saturated the EIT instrument). The flare came from Active Region 10486, and is the largest flare ever recorded in X-rays (Ref. [17]).

The right sided picture illustrated in Figure 5 shows the CME associated with the November 4, 2003 X-28 flare from Active Region 10486 and was the fastest yet observed. The picture was taken with SOHO's Large Angle and Spectrometric Coronagraph (LASCO) C2 instrument, which provides a close-up view of CMEs. The disk in the centre of the image blocks the Sun's direct light such that much fainter features in the solar atmosphere (corona) can be observed. The white circle on the disk represents the apparent size of the Sun in the image. The CME is the large white area at the lower right of the LASCO C2 disk (Ref. [17]).

When the Sun is very active, such as the periods near sunspot maxima, SPEs are able to deliver absorbed doses between 0.3 Gy and 3.0 Gy over a period of about 3 days (Ref. [58]). These significantly high absorbed doses are alarming and dose reduction techniques should therefore be considered to protect the astronauts in space. Fortunately, even though SEP can reach up to several GeV, they typically have an energy less than 150 MeV. Because of these relatively low energies, SPE radiation can substantially be shielded en route and nearly fully on the surface of Mars (Ref. [55]).

Ideally, for long-term missions the frequency and the proton energy distribution of SPEs should be considered. Due to its probabilistic nature, literature confirms that the capabilities for predicting SPEs and their strength are very limited making their treatment complex (Ref. [1] item 32). In fact, given the current level of knowledge of solar physics, it is not possible to forecast key SPE parameters with any degree of accuracy. These key parameters include, e.g., predicting the timing, magnitude, duration, and fluence rate of the SPE. The unpredictability of SPEs adds to their inherent radiation hazard (Ref. [55]).

The SPE spectral data sets considered in this work for shielding analysis will be described in §6.2.2.

2.1.4. Trapped radiation belts

The magnetosphere, i.e. the Earth's magnetic dipole field around the geomagnetic equator, is filled with charged particles, mainly trapped protons and electrons and some heavier ions, originating from GCR and solar winds.

These charged particles move in spirals along the geomagnetic field lines and are reflected back between the magnetic poles, forming trapped radiation belts where the density of electrons and protons is much higher than outside of these areas.

These belts are often referred to as 'Van Allen belts', the physicist who discovered this trapping phenomena (Ref. [1]).

An illustration of the trapped radiation belts is provided in Figure 6 below.

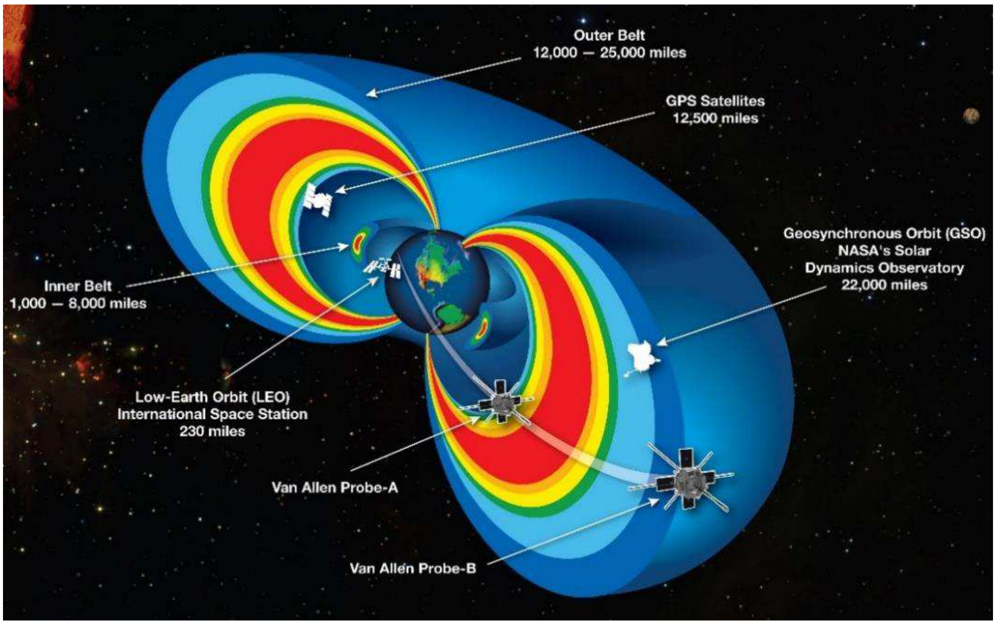

Figure 6: A cutaway model of the radiation belts with the 2 Van Allen Probes satellites flying through them (Ref. [20])

The trapped radiation belts extend over a distance from Earth from approximately 200 km to approximately 75,000 km around the geomagnetic equator and consist of electrons, protons, and some heavier ions ranging up to energies of 7 MeV, 700 MeV, and 50 MeV/u, respectively (Ref. [1]).

Different processes contribute to the filling of the different particles in the radiation belt; two main zones of captured particles are observed (Ref. [1] item 38):

- The inner belt is mainly formed by decaying secondary neutrons produced by interaction of GCR and solar winds with the atmosphere, giving rise to protons and electrons. The particle intensity in the centre of the inner belt is quite stable, especially with respect to protons. At the lower edge of the belt, electron and proton intensities may vary by a factor of 5 (Ref. [1] item 45). Due to the high proton fluence rates and energies, they are able to penetrate through shielding provided by walls and equipment of the spacecraft (Ref. [1] item 42). For most LEO space missions, protons are an important part of the radiation exposure inside the spacecraft (Ref. [1] item 45).
- The outer belt mainly consists of trapped solar particles, largely populated by electrons. The intensity may vary by a factor 6 – 16 (Ref. [1] item 45).

The Sun is the dominant primary source that feeds the trapped electron population in the outer belt. The trapped proton fluence in the inner belt, on the other hand, is higher during solar minimum conditions, i.e. during maximum GCR fluence rates.

The trapped radiation is modulated by the solar cycle; with increasing solar activity (decreasing GCR fluence rates), the proton intensity decreases, while the electron intensity increases (Ref. [1] item 45).

The two major mechanisms leading to energy loss of the trapped particles are the production of cyclotron radiation and the penetration of particles into the upper atmosphere near the geomagnetic mirror points (Ref. [1] item 38).

For the majority of space missions inside LEO, protons are an important part of the radiation exposure inside the spacecraft. Due to their higher energies and hence longer range, their total dose surpasses that of electrons at shielding thicknesses above ~0.3 g cm^{-2} Al. At lower shielding thicknesses (e.g. in case of extravehicular activities (EVAs)), the absorbed dose to the skin is dominated by the electron contribution, and may reach up to 10 mGy per day (Ref. [1] item 45).

In missions outside Earth's magnetosphere, such as a transit to Mars, the Earth's radiation belts will be crossed in a matter of minutes, meaning that its contribution to the astronauts' dose uptake will be rather small. In fact, depending on the exact path and the speed of the spacecraft[25], NASA estimates that a transit through the Van Allen belts will take less than an hour and that the corresponding total dose uptake will be less than 150 mGy (Ref. [57]).

2.2. Secondary radiation fields in space

As discussed in §2.1[26], essentially each primary source of radiation in space may lead to secondary radiations such as gamma radiation, electrons, muons, pions, neutrons and collision and projectile fragments. These secondary radiations can be produced by the interaction of primary radiations with the (Earth's) atmosphere, the structural materials of the spacecraft and its equipment, the spacesuits, and the body of the astronauts.

In 2016, Bilski et al. (Ref. [59]) characterized the contribution of different particle types to the GCR[27] dose vs. shielding thickness, as presented in Figure 7 below.

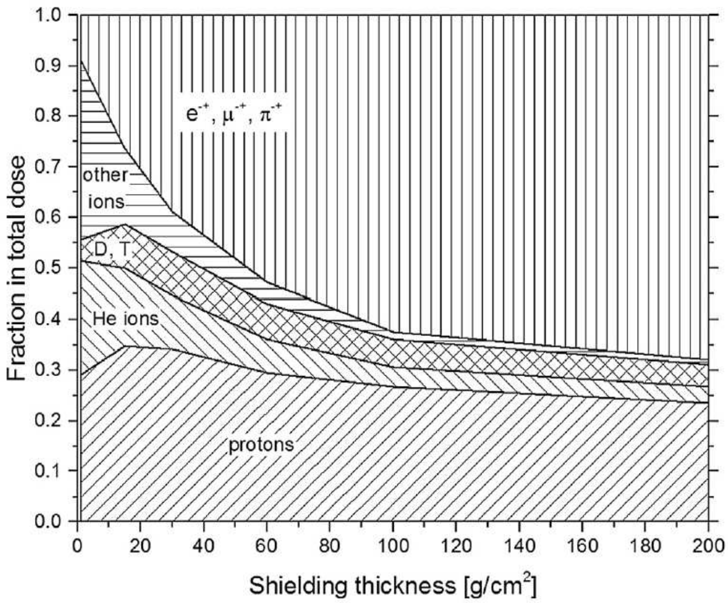

Figure 7: Contribution of different particle types to the GCR (solar maximum) dose vs. shielding thickness (Ref. [59])

[25] Typically about 25,000 km/hour (Ref. [57]).
[26] The creation of secondary particles through nuclear reactions has been addressed in §2.1.1.2.
[27] The calculation of the GCR component was based on the input spectra generated with the Matthïa model (Ref. [59]).

The particle energy spectra were calculated for realistic flight conditions of the ISS (inside LEOs) for solar minimum (2009) and solar maximum (2000) conditions. The interactions of the primary particles with the ISS were simulated with GEANT4 (GEometry ANd Tracking) using a shielding geometry derived from the mass distribution of the ISS Columbus Laboratory and several constant Al shields.

The study concluded that the Al shielding thickness has a significant influence on the composition of the radiation field caused by GCR behind shielding (Figure 7):

- For the lowest shielding thickness the radiation field is dominated by protons (~30% of dose) and other nuclei (~60%) being the primary constituents of GCR;
- With increasing shielding thickness the contribution of ions decreased and was replaced by lighter secondary particles such as electrons, muons and pions of low LET. The contribution of protons remains on approximately the same level.

Other studies reported that the contribution of secondary neutrons created by interaction of solar and galactic particles with the nuclei of the Earth's atmosphere is relatively low in LEOs. However, their contribution following interactions with the spacecraft and the astronaut's body appeared to be substantial (Ref. [1] item 47).

In terms of deep space, Ballarini et al. (Ref. [4]) made an effort to calculate doses in tissues/organs following exposure to the August 1972 SPE and to GCR[28] under different shielding conditions using the transport code FLUKA (FLUktuierende KAskade meaning Fluctuating Cascade). Contributions from secondary hadrons, in particular neutrons, with respect to primary particles were calculated to quantify the role of nuclear interactions occurring in the shield and in the human body. The main conclusions are listed below (exact numbers/figures are reported in Ref. [4]):

- In terms of SPE, it was concluded that for all doses[29] primary protons played the major role, although the contribution of secondary hadrons (including ions) produced by nuclear interaction was not negligible. As for secondary neutrons, it was observed that their contribution increased with increasing shielding. With no shielding only 1% of the secondary dose was due to neutrons. Behind 10 g/cm² Al the neutron dose accounted for ~20% of the dose from all secondaries.
- In terms of GCR, it was concluded that the role of nuclear reaction products (secondary particles) was found to increase with Al shielding thickness. With respect to all secondary particles produced in nuclear interactions, the neutron doses were found to be of the order of 10% the secondary particle doses.

In essence, it was concluded that nuclear reaction products (secondary particles) played a minor role for SPE doses, whereas they were important for GCR doses. Furthermore, it was observed that, depending on the shielding and on the organ location, neutrons accounted for up to 20% of the dose from secondaries.

Based on the above, it is clear that secondary radiations are important sources of radiation in space. In fact, the ICRP details that secondary radiation needs to be considered in particular in terms of space dosimetry (Ref. [1] item 56).

[28] The calculation of the GCR component was based on the input spectra generated with the BON model (Ref. [4]).
[29] Absorbed dose (Gy), dose equivalent (Sv) and biological dose (average number of induced 'Complex Lesions' per cell).

2.3. Radiation fields relevant for radiation protection in space

The previous chapters (§2.1 and §2.2) elaborated on different sources of radiation in space. It must however be noted that not all radiation fields in space are equally important in terms of dose uptake by the astronauts. More particularly, the ICRP specifically points out that the radiation fields relevant for radiation protection in space are **GCR**, **SPE**, and **secondary radiation** produced through interaction of space radiation with matter (Ref. [1] item 12).

Following this, it can be derived that solar winds and trapped radiation belts are of minor importance in terms of dose uptake, and this for the following reasons:

- Irrelevance of the **solar wind**:
  Solar wind particles (mainly protons and electrons), even when enhanced due to higher solar activity, do not contribute significantly to radiation exposure of humans due to their relatively low energy and hence their absorption in already very thin shielding materials (Ref. [1] item 12). More particularly, the particle energies are so low (for protons, between 100 eV and 3.5 keV) that they will be stopped within the first few microns of unshielded skin. They are, therefore, not of concern for radiation effects in humans (Ref. [1] item 28);
- Irrelevance of the **trapped radiation belts**:
  Although the ICRP recognizes that low-energy trapped heavy ions (< 50 MeV/u) are of no consequence for radiological protection of humans in space due to their limited penetration capacity (Ref. [1] item 38), it even so states that high-energy protons with high fluence rates are able to penetrate through shielding provided by the walls and spacecraft equipment (Ref. [1] item 42), making up an important part of the radiation exposure inside the spacecraft (Ref. [1] item 45). However, in missions outside the magnetosphere, which this thesis focuses on (§5), such as a transit to Mars, the Earth's radiation belts will be crossed in a manner of minutes and therefore their contribution to the astronauts' dose uptake, even when crossing the South Atlantic Anomaly (SAA)[30], is quite small (Ref. [1] item 18). Also, since trapped particles have much lower energies than GCR and solar energetic particles, the presence of even a few millimetres of aluminium shielding would result in a significant dose reduction (Ref. [30]).

For the sake of completeness, the ICRP even so recognizes that presently, there is no measurable contribution to radiation exposure by **primary electromagnetic ionising radiation**, such as from solar x-ray flares[31] or extreme gamma radiation bursts. This primary radiation source has therefore been ignored (Ref. [1] item 13).

Note that irradiation by **primary electrons** can also cause major health risks. This statement however is mostly only true during EVAs and during space travel inside the magnetosphere (especially within the outer radiation belt), which will both not be considered in this thesis (Ref. [1] item 14).

30 The SAA is an area where the radiation belt, and hence the trapped protons, comes closer to the Earth's surface due to a displacement of the magnetic dipole axes from the Earth's centre. This region accounts for a significant fraction of total exposure in LEOs (Ref. [1] item 46).

31 Solar flares are powerful bursts of radiation which cannot pass through Earth's atmosphere to physically affect humans on the ground. They can however disturb the atmosphere in the layer where communications signals travel (Ref. [19]).

2.4. Radiation fields considered in this thesis

With the explanations provided in §2.3 in mind, it has been chosen for this thesis to focus only on the most important primary sources of radiation in interplanetary space (at a distance of 1 AU from the Sun) in terms of radiation protection.

More particularly, this thesis solely focusses on **GCR** and **SPE** as primary sources of radiation in space while taking **secondary radiations** into account because of the following justified reasons:

- Literature studies (Ref. [32], [33]) confirm that although **SPEs** can increase the radiation exposure during short periods substantially, the largest fraction of the dose and, even more, of the dose equivalent during long-term missions, such as a mission to Mars, is expected to be contributed by **GCR**;
- As described in §2.1.3, **SPEs** have the potential to expose astronauts to life-threateningly high doses and are considered by the ICRP as the most dramatic radiation events (Ref. [1] item 30, 318). Although the dose reduction strongly depends on the proton energy, the ICRP recognizes that shielding can reduce effective doses caused by SPEs by factors of 2 to >10 (Ref. [1] item 260);
- Studies have shown that organ dose equivalents for many space missions are predominantly from **GCR** (Ref. [1] item 291, Ref. [2] p28). Although shielding to GCR is generally limited, the ICRP states that with the selection of optimised shielding material, a dose reduction of ~30% can be achieved at solar minimum and, to a lesser extent, at solar maximum (Ref. [1] item 260);
- As this thesis will focus on the radiation fields outside the magnetosphere (§5), **secondary particles** created by the interaction of solar and galactic particles with atmospheric nuclei are considered as irrelevant. Nevertheless, secondary radiations produced by interactions of primary sources with the human body and shielding material will be considered in the dose calculations as the ICRP specifically states that the contribution of the secondary radiations to the dose uptake in the human body needs to be considered in particular (Ref. [1] item 56).

Based on the justifications provided here above, it is clear that efficient shielding against **GCR** and **SPE** is crucial in space, especially during long-term deep space missions, and that the treatment of **secondary radiations** cannot be neglected.

Because of its stochastic nature and the fact that only five SPEs intense enough to jeopardise crew health have been monitored in ~65 years of time (§2.1.3), one could potentially opt to exclude the treatment of SPEs for shielding optimisation in space and only focus on GCR as primary source of radiation. However, in case shielding would be designed which is efficient for GCR but inefficient for SPEs, the outcome of the study and its applicability to space could deeply be questioned.

Consequently, this thesis aims to investigate materials and/or compounds which increase the shielding efficiency against GCR and SPE as they represent the most important sources of radiation in terms of dose contribution (Ref. [1] item 291, [8]).

Note that, as mentioned earlier (§1.2), in this work the particle fluxes from **outside Earth's magnetosphere** at a distance of **1 AU from the Sun** will be considered. The main reason for this choice is that most models currently available are limited to a distances of 1 AU from the Sun, as will be discussed in §5. A more theoretically sound justification of the use of this distance is provided below.

The following paragraphs are based on information obtained from Ref. [54], [55], and, without touching details, explain why the proton fluxes at a distances of 1 AU from the Sun, as provided by most models currently available, are a relatively fair estimate of the proton fluxes to be expected at Mars, located at a distances of 1.5 AU from the Sun. Indeed, the explanation provided below is for proton fluxes only, but it is known from literature that GCR and SPE environments are dominated by protons (Ref. [53]).

Extrapolation of Earth-based prediction methods to other location in space (e.g. for a Mars' mission) relies on some empirical data on the radial dependence of solar proton flux and fluence. For the simplicity, it is assumed that the maximum possible prompt solar proton flux would be at the position that is "well connected" to the solar flare source region. Using the intrinsic assumptions that the coronal particle intensity gradients control the particle flux observed around the Sun, it is possible to estimate the particle flux at any heliographic longitude.

The arguments used for extrapolation of the proton fluxes to other heliocentric distances rely on the assumption that the diffusion across magnetic field lines is negligible, and that the volume of the magnetic flux tube, as the distance from the Sun increases, expands in the manner expected from classical geometry. In this case, a power-law function of the form $\sim r^{-3}$ can be used to extrapolate to other distances (r is the radial distance from the Sun). In literature the probable effects of diffusion have been analyzed, and the preliminary estimate was that the power-law function of $\sim r^{-3.3}$ would be an appropriate factor.

Any distortions of the magnetic flux tubes are unknown so no accurate estimates can be performed. Hence, there is no consensus view on the proper method for extrapolating solar particle fluxes and fluences from 1 AU to other distances in the heliosphere. The sparse measurements that exist are from comparison of Earth-orbiting satellite proton fluxes compared with space-probe measurements of the same event in the energy range of 10 to 70 MeV[32] from 1 to 5 AU.

In a mission to Mars, for example, the radial distance will vary according to the spacecraft trajectory chosen, and the flux radial dependence and the SEP source locations are very important. As noted above, the flux of solar proton is expected to vary as a power law with radial distance from the Sun, and a power-law exponent of -3 would be expected from magnetic flux tube geometry. Since the radial distance to Mars is ~1.5 AU, then the flux at the orbit of Mars would be expected to be ~1/3 of the flux at 1 AU along the same spiral path. This variation should be contrasted with the average heliolongitudinal gradient of the order of magnitude per radian of heliocentric angular distance. A consideration of these expected variations suggests that the **proton prediction** problem for **Mars** is **not dramatically different from the Earth**. Hence, for the sake of convenience, the models currently available at a distances of 1 AU from the Sun will be used.

As mentioned in the introduction of this chapter (§2), knowledge about the radiation fields is key for any measure in radiological protection (Ref. [1] item 5). Having the space radiation fields defined, the next chapter (§3) will address the particularities related to radiation protection in space.

[32] Protons in this energy range are stopped by the vehicle hull and do not contribute significantly to astronaut dose. Data are required for proton energies greater than ~150 MeV where the contribution to crew dose is the greatest.

3. RADIATION PROTECTION IN SPACE

Since early years, several advisory bodies such as the International Atomic Energy Agency (IAEA), the International Commission on Radiological Protection (ICRP) and the International Commission on Radiation Units and Measurements (ICRU) made effort to define the term radiation protection as severe biological effects were observed as a consequence of ionizing radiation-matter (body) interactions.

The IAEA, for instance, defines the concept radiation or radiological protection as the protection of people from the effects of exposure to ionizing radiation, and the means for achieving this. It is concerned with controlling exposure to radiation and its effects. Even though the term radiation protection is, strictly speaking, restricted to the protection of humans, literature often extends its applicability to include the protection of non-human species or the environment (Ref. [24]).

On **Earth**, radiation protection generally refers to the protection of people and the environment from harmful effects of ionizing radiation. The objective is to reduce the exposure levels to ionizing radiation so that deterministic effects are avoided and the probability of developing stochastic effects is limited.

In fact, three general principles[33] of radiation protection have been developed with as fundamental safety objective[34] protecting people – individually and collectively – and the environment from harmful effects of ionizing radiation, and are defined as follows (Ref. [25]):

- **Justification** of activities: activities that give rise to radiation risks must yield an overall benefit;
- **Optimization** of protection: protection must be optimized to provide the highest level of safety that can reasonably be achieved;
- **Limitation** of risks to individuals (dose limits): measures for controlling radiation risks must ensure that no individual bears an unacceptable risk of harm.

In **space**, in contrary to Earth, the prime objective of radiation protection consists of reducing the radiation exposure of astronauts to a level at which the **individual health risks** are deemed acceptable (Ref. [1] item 311).

Consequently, in space, a more individually based dose/risk assessment should be performed because the number of astronauts exposed is very small compared with the number of occupationally exposed persons on Earth and as the doses to the astronauts are generally much higher than those received on Earth (Ref. [1] item 337).

Even though astronauts are exposed to ionising radiation during their occupation, they are usually not classified as occupationally exposed in the sense of the ICRP system for radiation protection of workers on Earth, meaning that for a mission, appropriate reference levels[35] may be selected, but no dose limits may be applied (Ref. [1] item 339). Nevertheless, due to the elevated exposure levels, assessment of radiation related risks is mandatory.

[33] In total, ten safety principles have been developed in order to achieve the fundamental safety objective (Ref. [25]). From these ten, three of them are commonly referred to the general safety principles.
[34] The fundamental safety objective applies to all activities and all stages over the lifetime of a radiation source (Ref. [25]).
[35] A reference level is defined as an action level, intervention level, investigation level or recording level (Ref. [24]).

The general safety principles used for radiation protection on Earth, justification, optimisation, and limitation, as defined earlier, are even so essential for radiation protection during space travel. However, operational radiation protection in space differs significantly from external radiation exposure on Earth. On Earth, doses to occupationally exposed workers are rather low and usually well below the annual limits defined in national regulations. For example, in Belgium, the effective dose limit for occupationally exposed personnel is defined at a value of 20 mSv over 12 consecutive sliding months (Ref. [26]). In many nuclear facilities, this dose limit is reduced to even lower values, for example to 10 mSv over 12 consecutive sliding months, for optimisation purposes. In space, however, due to the special radiation environment, the doses to astronauts can be extremely high, reaching doses up to (and beyond) 1 mSv per day (Ref. [1] item 311).

On Earth, radiation protection usually includes aspects related to the principles of ALARA, which stands for As Low As Reasonably Achievable taking into account economic and social factors (Ref. [24]). In fact, the ALARA principle is developed with particular view on reducing as much as possible the collective dose, in which the latter is defined as:

$$\text{Collective dose} = \sum \text{Individual dose} \quad [\text{man. mSv}]$$

In which:

$$\text{Individual dose} = \text{Dose rate} \times \text{exposure time} \quad [\text{mSv}]$$

Each activity for which exposure to a radiation risk is justified, different actors need to determine the best action(s) of prevention and protection. The collective dose can be decreased by acting on:

- The dose rate by:
  - Adding shielding;
  - Increasing the distance between the radioactive source(s) and the workers;
  - Performing pre-decontamination processes;
- The exposure time by:
  - Improving the intervention methodology;
  - Providing dedicated practical trainings to the workers.

Most often, ALARA studies deal with the time exposed to, the distance from and shielding of (a) radioactive source(s).

Apart from these key aspects, depending on the particular situation, it should even so be evaluated if ventilation systems should be installed for controlling airborne contamination, if zoning should be established to point out high radiation zones, if measurements should be foreseen and dosimeters should be worn to monitor the overall and individual exposure levels, respectively.

In space, contrary to Earth, only external radiation exposure to astronauts is to be considered as internal exposure is of very little relevance (Ref. [1] item 54). Hence, in space, nuclear ventilation systems for controlling radioactive contamination are of minor importance (apart from systems installed for habitable or other scientific purposes).

The concepts of radiation zoning and the increase of distance to the source are also considered as not directly applicable to exposure situations in a spacecraft. In space, astronauts are usually exposed to very intense omnidirectional radiation beams, making zoning, except for specific sheltering areas, little to not relevant. While shielding may result in less isotropic exposure at some particular locations, the quasi-continuous movement of astronauts within the spacecraft balances the situation. Except by significantly altering the spacecraft orbit/trajectory, it is clear that the distance to the space radiation source(s) cannot simply be increased. Also, distance is less relevant as the concerned particles hardly attenuate in free-space.

Once in space, the exposure time cannot easily be managed as the duration of the mission is often pre-planned and extreme solar outbursts might be detected too late to intervene. Hence, exercising spacewalks, preparing fast return routes, and optimizing protocols are essential tasks to be performed on Earth. In fact, the exposure time can only be influenced by faster propulsion systems (Ref. [53]).

Knowing that in space measurements[36] are mainly performed for the purpose of determining individual exposure levels, monitoring changes in the radiation fields (Ref. [1] item 149) and validating the models used for radiation transport calculations (Ref. [1] item 240), whilst dosimeters are worn to estimate the dose absorbed by astronauts, it should be clear that these measures are designed for surveillance, monitoring and registration purposes, and not for reducing the exposure level in terms of physical protection.

Based on the descriptions provide above and the fact that the ALARA principles are also applicable in space (Ref. [1] item 311), it leaves that **shielding** is basically the only parameter which can be controlled for purposes of dose manipulation in space. The ICRP recognizes the importance of shielding in space by indicating that the construction of a spacecraft should include sheltering areas at which the dose rates are lower than elsewhere in the spacecraft (Ref. [1] item 315).

With this in mind, the following subchapters will elaborate on the importance (§3.1) and difficulties (§3.2) related to space radiation shielding as well as on materials recommended to be used in space (§3.3) to increase the shielding efficiency.

3.1. Importance of shielding in space

As described in §2, the radiation environment in space is substantially different and much more complex than that on Earth, and, unfortunately, this complexity is also translated to the space radiation-matter interactions. Apart from SPEs, radiation exposure in space cannot simply be avoided by shielding (Ref. [1] item 3), as is often the case for exposure situations on Earth.

In fact, the radiation field inside a spacecraft depends on multiple factors in which the types and the amounts of shielding play a crucial role (Ref. [1] item 245). More particularly, the radiation field impacting the body of the astronauts is determined by the external radiation incident on the spacecraft, and the secondary radiation produced by the interactions with equipment inside and outside the spacecraft.

[36] Real-time measurements are however continuously performed in and/or around the spacecraft to have an instant idea on the radiation levels so astronauts can go to a more shielded location in case of e.g. a SPE.

The internal radiation field also varies with time due to variation of the external radiation and the exact location in the spacecraft due to the arrangement of the equipment and the shielding properties of the different walls and spacecraft components (Ref. [1] item 244).

The ICRP (Ref. [1]) states that the exposure of astronauts to radiation in space cannot be avoided, and that prevention by shielding cannot be achieved entirely. At the same time, it even so recognizes that **optimisation** of radiation protection measures (e.g. shielding) remains an important task, especially because doses to astronauts might exceed hundreds of mSv in long-term missions (Ref. [1] item 8).

In the same reference the ICRP states that "*As a first step, definition, procurement, and characterisation of candidate flexible materials to be used in future manned missions in LEOs and beyond are needed for inhabited structures. Computer codes are the tools to characterise such materials. The next step is improvement and validation of the models and tools for shielding analysis, by comparison with measurements*" (Ref. [1] item 260). The development of shielding requirements and strategies is thus important for optimisation purposes (Ref. [1] item 320). By selecting appropriate shielding materials, the shielding strategy can be optimized to minimize the dose contribution (Ref. [2] p29).

Although in theory the exposure of astronauts can be reduced by decreasing the exposure time and altering the location, shielding is currently the most important mitigating parameter in deep space exploration (e.g. on a mission to Mars) as the duration and location of space missions is often fixed prior to space flight.

For long-term space travels into near-Earth interplanetary space, ways to reduce the radiation exposure have to be found (Ref. [2] p130). A round trip to Mars is usually assumed to take up to a year or more. Hence, the shielding to be used must be appropriately optimized since literature has shown that the intense GCR exposure alone (i.e. neglecting other sources) already can induce very high doses (Ref. [2] p119). Unfortunately, some types/thicknesses of shielding appear to work counter-efficient due to the complex phenomena at high energy (§3.2).

3.2. Difficulties related to shielding in space

Based on the previous chapter (§3.1) it is very clear that effective shielding against space radiation is a crucial aspect for long-term (deep) space missions.

Unfortunately, designing effective shielding to space radiation is very complex due to the broad spectrum of different radiation types with very high energies and high penetrating abilities followed by the release of secondary radiations when primary radiation interacts with the shielding materials (Ref. [1] item 3). This phenomenon is illustrated in Figure 8 below.

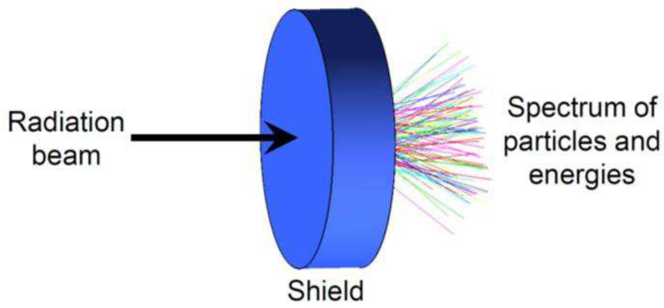

Figure 8: Illustration of a primary radiation beam interacting with a shield giving rise to secondary particles (Ref. [12])

In fact, to underline the level of complexity, it has been observed in literature that:

- A substantial number of neutrons, which are negligible as primary components of space radiation, might be produced with increasing shielding thickness and might therefore become a noticeable source of secondary radiation exposure (Ref. [1] item 256);
- The installation of passive shielding may cause an increased risk by increasing the dose equivalent from any generated secondary particles, and projectile and target fragments (including neutrons) (Ref. [1] item 320);
- Concrete and lead, materials often used for shielding purposes on Earth, have a response to GCR that is predicted to increase the dose with shielding depth due to the large production of neutrons and target fragments (Ref. [1] item 253);
- Aluminium, a typical type of material often used for shielding purposes in space, may in some cases be counter-efficient in shielding against GCR (Ref. [2] p130).

Moreover, a study has shown that during a flight, variable behaviours in dose rate with increasing shielding thickness was observed[37]. The results of the study clearly indicated the complexity of the issue of shielding against GCR and showed that it is not trivial to predict the variation of GCR exposure (dose rates) with a variable shielding thickness (Ref. [2] p27-30).

A detailed description of the effect of shielding on the dose is provided in Ref. [2] in which the different fundamental interaction processes of GCR with matter and the energy deposition characteristics are explained. The following two paragraphs summarize the basic principles based on the description given in Ref. [2].

As described in §2.1.1.1, heavy ions lose energy faster and are therefore stopped by thinner shielding compared with lighter ions because of their higher LET which is proportional to Z^2. This is true for energies below which the nuclear interactions are less likely to occur, and the ionization process dominates. However, when the energies are higher, such as for GCR, nuclear interactions can occur, giving rise to lighter nuclei which may penetrate deeper inside the shielding.

[37] The measured absorbed dose rates were 175.6, 167.2, 148.5 and 170.5 µGy/d and the dose equivalent rates were 614.4, 487.6, 617.2 and 540.5 µSv/d behind a shielding of 0, 17.145, 24.003 and 30.861 g cm^{-2}.

In fact, fragmentation is the main mechanism of energy loss of the GCR heavy nuclei (§2.1.1.2). The fragment nuclei are lighter than the incident nuclei and have a lower LET. Consequently, even though they are more penetrating and may yield higher absorbed doses, they have a lower biological effectiveness yielding a lower dose equivalent compared to the incident nuclei. On the other hand, if the incident high-LET nuclei interacts with shielding materials, the resulting lighter nuclei with higher quality factor may result in a higher dose equivalent (Ref. [2] p27-30).

Obviously, from practical point of view, requiring just one material which provides efficient shielding to all types of space radiation would be the ideal situation. In space, however, often combinations of multiple materials are used to optimize the shielding efficiency. In this case, the final shielding effectiveness depends on the geometry and the abundance of multiple materials used in the shielding. Detailed simulations remain essential for evaluating and designing a realistic spacecraft or space habitat. For example, simulations have shown that the shielding efficiency against GCR is rather poor for a wide variety of materials (Ref. [1] item 255).

3.3. Recommended shielding materials in space

It is well known from literature that most of the protection against radiation inside a spacecraft is currently provided by structural elements and equipment inside the spacecraft. The material most commonly used for shielding purposes is aluminium because of its attractive mechanical and structural properties, on one hand, and due to its relatively flat depth-dose equivalent responses, on the other hand. The fairly flat depth-dose equivalent responses for aluminium can be explained by the balance between the build-up of light particles and the attenuation of heavy ions (Ref. [1] item 253, 258).

In 2006, a study conducted on the role of primary and secondary particles in the framework of human exposure to GCR[38] and SPE[39] in deep space outside the geomagnetic field (Ref. [3]) revealed that the SPE absorbed doses dramatically decreased with increasing Al shielding thickness, and that mainly primary protons contributed to the total absorbed dose. The contribution of secondary particles[40] to SPE doses was almost negligible; only for thick shields (10 g cm^{-2},[41]) secondary neutrons produced through nuclear interactions in the shield were non-negligible, though still of minor importance. GCR absorbed doses remained roughly constant with increasing Al thickness due to the high energies of the primary particles. In contrast to SPE, GCR secondary particles, more particularly secondary neutrons produced by nuclear interactions in the shield, contributed significantly to the total absorbed dose.

Another study which evaluated the GCR and SPE organ doses in deep space by using different Al shielding thicknesses (Ref. [4]) based on the same geometries, GCR spectra and SPE data as considered in Ref. [3] essentially confirmed the same general conclusions as drawn in Ref. [3], as discussed above. Compared to Ref. [3], this study also calculated organ-averaged dose equivalents using the quality factors indicated in ICRP publication 60 (Ref. [21]).

38 The GCR spectra were taken from BON10 during solar minimum, considering incoming ions with $1 \leq Z \leq 28$ (Ref. [3]).
39 The time integral spectral proton fluence from the SPE of August 1972 was used (Ref. [3]).
40 The focus was put on neutrons because of their high biological effectiveness (Ref. [3]).
41 An areal density of ~10 g cm^{-2} is obtained by multiplying ρ_{Al} (~2.7 g cm^{-3}) by the considered Al thickness ~3.70 cm.

For SPE, it was concluded that the doses decreased dramatically with increasing shielding; in the range of 1-10 g cm^{-2}, the absorbed dose and dose equivalent fell from 8.20 Gy to 0.40 Gy and from 13.31 Sv to 0.62 Sv, respectively. For all doses, primary protons played the major role, although the contribution of secondary hadrons, including ions produced through nuclear interaction, was not negligible, especially for dose equivalent behind large shields. The contribution of secondary neutrons to the absorbed dose increased with increasing Al shielding thickness: with no shielding only 1% of the secondary dose was due to neutrons (produced in the body), while behind 10 g cm^{-2} Al the neutron dose accounted for about 20% of the dose from all secondaries. A similar trend was even so found for the dose equivalent.

For GCR, in contrast to SPE, it was found that the skin-averaged absorbed dose does not decrease with increasing Al shielding thickness. The skin-averaged dose equivalent showed a (slight) decrease starting from 2 g cm^{-2} Al due to projectile fragmentation.

The latter can give rise to charged particles with roughly the same velocity as the incident ion but lower charge, and thus lower LET and biological effectiveness. For each considered value of Al thickness, the relative contribution from ions with $Z \geq 3$ was found to be much larger for the skin-averaged dose equivalent than for the skin-averaged absorbed dose due to the higher quality factors of high-charge particles. The contribution of nuclear interactions was found to increase with Al thickness, and the relative contributions from nuclear reaction products to GCR doses were much higher with respect to the case of SPE doses. Lastly, the secondary neutron doses were found to be of the order of 10% of all secondary particle doses produced in nuclear interactions.

For more in depth information (exact numbers and graphical representation of the dose results, etc.), reference is made to Ref. [3] and [4].

A more recent study (Ref. [8]) calculated the GCR[42] exposure outside the Earth's magnetosphere for time periods starting from 1970 to the end of 2011 in order to investigate the increased exposure during the deep solar minimum between solar cycles 23 and 24 compared to the last three solar minima (SPE was neglected). The dose rates were calculated in a water sphere (surrogate for the human body) surrounded by aluminium shielding with areal densities of 0.3, 10 and 40 g cm^{-2} from August 1997 to October 2011 for near-Earth interplanetary space.

It was concluded that the absorbed dose rates calculated for an Al shield of 0.3 g cm^{-2} differed by less than 1% from those calculated in the target without shielding. The absorbed dose rates were found to increase for 10 and 40 g cm^{-2} Al shielding. The increase in absorbed dose rates was explained by the increase in secondary radiation like neutrons with increasing shielding thickness.

The variation of the dose equivalent rates with Al shielding, on the other hand, showed different behaviors with location and time, indicating that the influence of shielding on the dose rates is also dependent on the energy spectra of the GCR particles which changes with the solar activity. It was observed that in near-Earth interplanetary space the reduction in dose equivalent rate by adding 10 g cm^{-2} Al shielding was stronger during solar minimum periods than during solar maximum.

[42] The GCR spectra were taken from the Matthiä model, considering incoming ions with $1 \leq Z \leq 26$ (Ref. [3]).

By increasing the areal density from 10 to 40 g cm^{-2}, it was observed that the dose equivalent rate changed, on average, with ~4% over the considered time period. The quality factors (ratio of the dose equivalent to the absorbed dose rate) were found to decrease with increasing shielding thickness due to fragmentation.

In general it was found that the level of increase in both dose rates quantities from the peak exposure in 1997 to 2009 decreased with increasing Al shielding.

Other studies have shown that for Al shields a higher particle fluence at large LET-values was observed compared with other materials because of the production of secondary neutrons and charged particles inside the shield, which was reduced for materials containing hydrogen (Ref. [1] item 245). Hence, hydrogenous materials such as, e.g., polyethylene (PE) appeared to be more effective in terms of space radiation shielding than aluminium (Ref. [2] p30).

In fact, for space shielding purposes, the ICRP recommends using materials with **light constituent atoms** such as hydrogen since they are most efficient per mass of material at slowing down ions, attenuating heavy ion fluences through projectile fragmentation, and minimizing the build-up of neutrons and other target fragments produced directly from the atoms of the shielding material by nuclear interactions (Ref. [1] item 253).

As described in §2.1.1, the energy loss via ionization is proportional to the number of electrons per atom, Z/A, where Z is the charge number and A is the mass number. The energy loss per area of mass is thus proportional to $Z/(\rho A)$ where ρ is the density of the material. In fact, for a given area density and a given incident charged particle, the energy loss by ionization increases with the charge-to-mass ratio of the target nucleus, Z/A, while the fragmentation cross section per mass unit is proportional to $A^{-1/3}$. Hydrogen ($Z = 1$) is thus the most efficient material for shielding against (heavy) ions (Ref. [49]). **Materials abundant in loosely bonded hydrogen** atoms are also excellent candidates for efficient space radiation shielding (Ref. [1] item 254).

Studies in literature have shown that materials which increase the probability of nuclear interactions resulting in fragmentation of heavy GCR nuclei into smaller nuclei can be efficient per mass unit of material in slowing down heavy ions. This suggests that an efficient shielding material should have (Ref. [2] p29):

- A **low mean atomic mass**;
- As **few neutrons** as possible to reduce the production of secondary neutrons.

Even though of minor importance compared to protons, neutrons and heavy ions, primary and secondary electrons can also contribute to the dose uptake by the astronauts (§2.3). In contrast to protons and heavy ions, the relatively small mass of electrons causes them to be deflected easily by collisions with atomic electrons and nuclei. This in turn causes them to produce bremsstrahlung, which is much more penetrating than the electrons themselves. As Bremsstrahlung production is proportional to Z^2, light materials are also favourable for electron shielding (Ref. [29]).

This thesis will focus only on optimizing the shielding efficiency for **sheltering** (i.e. non-structural) purposes as the ICRP clearly indicates that the construction of a spacecraft should include sheltering areas at which the dose rates are lower than elsewhere in the spacecraft (Ref. [1] item 315). This statement becomes even more important in long-term deep space explorations since in the latter space radiation exposure is considered as the most crucial parameter affecting the astronauts health. The ICRP recognizes that the efficiency per mass unit is the only important endpoint when only focussing on sheltering inside a spacecraft (Ref. [1] item 258).

A PhD work dedicated to performing more reliable calculations of exposure from GCR in space (Ref. [2]) concluded that shielding studies are of particular interest since commonly used materials such as aluminium may work counter-efficient in terms of space radiation shielding. It also points out that other materials with low mean atomic mass should be investigated for use in spacecraft for long-duration flights (Ref. [2] p130). Also Ref. [4] concluded that testing shielding materials other than Al, such as polyethylene, should be carried out in the future. It is exactly the latter which will be investigated in this thesis.

Note that in fact, there are two general types of shielding applicable to protection against space radiation, more particularly active shielding and passive shielding. Active shielding uses electric or magnetic fields to deflect charged particles away from the spacecraft. In passive shielding a mass is installed between the radiation source and the receptor (target), whether they are humans or electronics.

NASA confirmed that active shielding's investigated in the past are electrostatic, magnetic, and plasma (Ref. [29]). Electrostatic shielding did not appear feasible due to the large fields and power levels required. Magnetic and plasma shielding appeared to be advantageous relative to passive material shielding under certain conditions depending on the size of the spacecraft and the degree of protection required. However, their application appeared to be not yet feasible as it required advancements in the field of superconductivity. Following this, NASA considered passive shielding as state of the art in 1970.

In 2014, a paper was published by Durante discussing different ways to enhance space radiation protection on a mission to Mars (Ref. [48]). Although ~45 years had passed since NASA published their recommendations on shielding in space (Ref. [29]), Durante's study performed in 2014 essentially came to the same main conclusion; among physical counter measures, passive shielding is the only one presently available. Active shielding, especially toroidal magnetic configurations are very promising, but still not mature enough for spaceflight. Following this, the focus of this thesis will be put on **passive shielding**.

The next chapter (§4) provides an overview of the different dose quantities and points out the differences between the quantities used for radiation protection on Earth (§4.1) compared to those used in space (§4.2).

4. QUANTITIES AND LIMITS USED FOR RADIATION PROTECTION

In a general sense, radiation protection refers to the protection of people and the environment against the harmful effects of ionizing radiation. It is concerned with controlling exposures to ionising radiation so that tissue reactions are prevented and the detriment from stochastic effects is limited to accepted levels.

On Earth, quantities have been developed for occupationally and publicly exposed situations based on low dose and low dose rates. For external irradiation on Earth, mainly exposure to low-LET radiation, such as photons, electrons and, depending on their energy range, neutrons are of concern within their most common (low-) energy ranges. In space, on the other hand, we are dealing with a broad spectrum of mainly high-LET radiation, such as protons, alpha particles and heavy ions with extremely high energies and dose rates, having the ability to penetrate deep into matter and produce secondary radiations. Because of these significant differences the radiation protection quantities developed specifically for applications on Earth might not be applicable anymore as such in space (Ref. [1]).

Following this, the aim of this chapter is to describe the different dose quantities and to provide a brief overview of the differences between the quantities used for radiation protection on Earth (§4.1) compared to those used in space (§4.2). The risk based approach adopted by NASA will be discussed in §4.2.

Note that humans can be exposed both externally (irradiation) as well as internally (contamination). As contamination is of very little relevance in space, this chapter focusses only on quantities for external radiation exposure (Ref. [1] item 54).

Throughout this chapter, information published by the ICRP on quantities used in radiological protection for assessing the radiation exposure of astronauts in space (§3 of Ref. [1]) has extensively been used because of its direct applicability.

4.1. Quantities used for radiation protection on Earth

Because of their fundamental differences, a clear separation will be made between physical (§4.1.1), protection (§4.1.2) and operational (§4.1.3) quantities.

4.1.1. Physical quantities

In fact, only one fundamental physical dose quantity, being the **absorbed dose**, D, has been defined by the ICRP as it can be applied to all types of ionising radiation and any irradiation geometry (Ref. [1] item 60).

The absorbed dose, D, is defined as the mean energy imparted by ionising radiation, $\mathrm{d}\bar{\varepsilon}$, to matter of mass $\mathrm{d}m$ per unit of mass, and can be written as follows:

$$D = \frac{\mathrm{d}\bar{\varepsilon}}{\mathrm{d}m}$$

The SI unit of the absorbed dose is J kg^{-1} and its special name is gray (Gy).

The absorbed dose accounts for all charged particles produced in or outside the specified volume. It is derived from the mean value of the stochastic quantity of energy imparted, ε, and does not reflect the random fluctuations of the interaction events in tissue.

In contrast to the protection quantities discussed in §4.1.2, the absorbed dose is a physical quantity which is actually measurable in practice by following dedicated primary standards.

Important to note is that the absorbed dose, D, only refers to the dose absorbed in one specific point in the human body (or considered object), making its direct use for general radiation protection purposes less relevant (Ref. [1] item 61).

4.1.2. Protection quantities

Protection quantities are essentially based on mean absorbed doses to the organs and tissues of the human body and can be related to the risks of ionising radiation exposure (Ref. [1] item 58).

In radiation protection, the main interest goes out to the absorbed dose averaged over an entire organ or tissue. Following this, in mixed radiation fields, R, the **mean absorbed dose in organs and tissues**, D_{T}, is defined as follows:

$$D_{\mathrm{T}} = \sum_{\mathrm{R}} D_{\mathrm{T,R}}$$

In fact, for low penetrating radiation, it is not fully correct to average the effects of ionization radiation over the entire considered organs/tissues as it would already be stopped by the upper skin layer, delivering no dose to deeper laying tissues. For radiation with sufficiently high penetrating ability, the mean absorbed dose in organs and tissues is however suitable for general radiation protection purposes (Ref. [1] item 64).

When using voxel phantoms[43], the mean absorbed doses in the organs or tissues are estimated from the energies deposited in the voxels assigned to each organ or tissue divided by the mass of the organ or tissue (Ref. [1] item 272).

By multiplying the mean absorbed dose in organs and tissues, D_{T}, by the radiation weighting factor, w_{R}, one obtains the **equivalent dose** in organs and tissues, H_{T}:

$$H_{\mathrm{T}} = \sum_{\mathrm{R}} w_{\mathrm{R}} D_{\mathrm{T,R}}$$

The SI unit of the equivalent dose is J kg^{-1} and its special name is sievert (Sv).

The radiation weighting factor, w_{R}, R referring to the different types of radiation[44], considers the differences in the radiobiological effectiveness of different radiations.

43 Voxel phantoms are anatomical models based on high-resolution scans and are intended to mimic the human anatomy with high precision. In most cases, reference male/female voxel phantoms are used. They consist of a large number of volume elements (voxels) and are currently the most detailed representation of the human anatomy (Ref. [1]).

44 In the case of neutrons, w_R refers to the energy of the neutrons.

Essentially, w_R is developed as different types of radiation can cause for the same absorbed dose different biological effects. For example, when a proton or an alpha particle traverses through the human body, the biological effect will be worse than if a gamma ray would pass through the body and deposit the same absorbed dose, independently from which organ or tissue it specifically passes through.

In fact, the radiation weighting factors are derived from radiobiological studies and are based on the concept 'relative biological effectiveness' (RBE). RBE is defined as the ratio of the absorbed dose due to low-LET reference radiation (most often gamma rays emitted by Co-60 or Cs-137 radioactive sources), to the absorbed dose due to the considered type of radiation which causes the same biological effect under identical irradiation conditions.

RBE studies conducted in radiobiology have proven to be very complex as they are influenced by a multitude of different factors such as the dose, the dose rate, the dose fractionation, the exposure conditions, the biological effect investigated, the tissue/organ exposed, etc. Therefore, for the same type of radiation there exist different RBE values, meaning that there are ranges of RBE for the same type of radiation. Nevertheless, the main focus for selecting RBE values is the induction of stochastic effects (cancer induction and hereditary effects).

Although RBE strongly depends on the linear energy transfer[45] (LET), studies have shown that it also depends on Z and the charge (especially for heavy ions). LET is defined as the mean energy lost by the charged particle by traveling a distance $\mathrm{d}l$ in matter[46], and can be written as follows:

$$L = \frac{\mathrm{d}E}{\mathrm{d}l}$$

The SI unit of LET is joule per metre (J m^{-1}), but it's often expressed in keV μm^{-1}.

Radiation where the energy transferred to matter by charged particles is below 10 keV μm^{-1} is referred to as low-LET radiation. Photons above ~15 keV, electrons, and muons are generally also referred to as low-LET radiations. In the same vain, radiation where the energy transferred to matter by charged particles is above 10 keV μm^{-1} is referred to as high-LET radiation. Neutrons, ions, and pions are generally also referred to as high-LET radiations (ICRP glossary).

While RBE values depend on the biological considered endpoint and on the dose and dose rate applied, the ICRP (Ref. [22]) has chosen to consider a single set of radiation weighting factors for defining the quantities used in radiation protection on Earth, and this based on data at low doses and dose rates.

Apart from neutrons, Table 1 below provides values of w_R for various types of radiation, either incident on the body or emitted by radionuclides inside the body. When neutrons travers through the human body, the radiation field can be altered by moderation, i.e. slowing down of the incident neutrons by consecutive scattering interactions, and secondary radiation from neutron reactions. Because of this, the values of w_R for neutrons follow a quasi-continuous energy-dependent distribution function, as illustrated in Figure 9 below. The latter function can be reconstructed based on the equations provided, in which the neutron energy, E_n, is given in MeV.

45 RBE-LET dependences are studied by focussing on the radiation effects in single cells and animal (Ref. [1] item 89).
46 Based on the definition of LET, it is clear that LET is closely related to the stopping power (§2.1.1.1).

Radiation type	Radiation weighting factor, w_R
Photons	1
Electrons and muons	1
Protons and charged pions	2
Alpha particles, fission fragments, heavy ions	20
Neutrons	A continuous curve as a function of neutron energy

Table 1: Radiation weighting factors, w_{R} (Ref. [22])

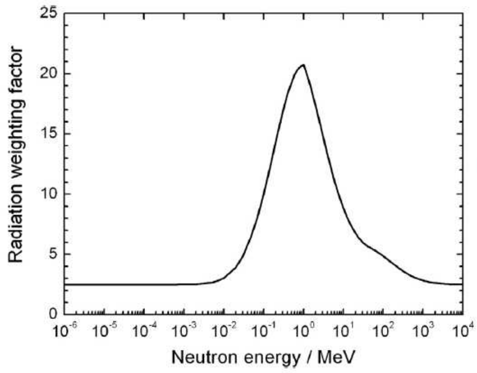

$$W_{\mathrm{R}} = \begin{cases} 2.5 + 18.2e^{-[\ln(E_n)]^2/6}, & E_n < 1\ \mathrm{MeV} \\ 5.0 + 17.0e^{-[\ln(2E_n)]^2/6}, & 1\ \mathrm{MeV} \leq E_n \leq 50\ \mathrm{MeV} \\ 2.5 + 3.25e^{-[\ln(0.04E_n)]^2/6}, & E_n > 50\ \mathrm{MeV} \end{cases}$$

Figure 9: Radiation weighting factor, w_{R}, for neutrons vs neutron energy and related set of equations (Ref. [22])

It is to be noted that the same radiation weighting factors are applied to all tissues and organs of the body, independent of the degradation of the primary radiation and the production of secondary radiations of different radiation quality.

To conclude, one could consider the different radiation weighting factors as mean factors representing the radiation quality averaged over the different tissues and organs of the body. Apart from neutrons (Figure 9), it might indeed seem that the approach based on a single values of w_{R} for each type of radiation (Table 1) is significantly oversimplified as certain, rather important, aspects are completely neglected (e.g. the energy of the concerned radiation). However, this approach is seen to provide sufficient precision for general applications in radiation protection.

Note that values of w_{R} are restricted to low doses and dose rates and should not be applied at higher doses where deterministic tissue reactions may occur.

in a last step, the **effective dose**, E, is obtained by multiplying the equivalent dose in organs and tissues, H_{T}, by the tissue weighting factor, w_{T}:

$$E = \sum_{\mathrm{T}} w_{\mathrm{T}} H_{\mathrm{T}}$$

In which H_{T} is equal to the mean value averaged over the male (M) and female (F) organ or tissue, and can be written as follows:

$$H_{\mathrm{T}} = 0.5\ (H_{\mathrm{T}}^{\mathrm{M}} + H_{\mathrm{T}}^{\mathrm{F}})$$

The SI unit of the effective dose is J kg^{-1} and its special name is sievert (Sv).

The tissue weighting factor, w_{T}, T referring to a specific organ or tissue, accounts for the change in radiosensitivity of different organs and tissues. More particularly, it represents the relative contribution of that organ or tissue to the total health detriment resulting from uniform irradiation of the body at low doses and dose rates.

As presented in Table 2 below, in total, 15 tissue weighting factors are developed and published in ICRP103 (Ref. [22]).

Organ/tissue	w_{T}	Total contribution
Lung, stomach, colon*, bone marrow, breast, remainder†	0.12	0.72
Gonads‡	0.08	0.08
Thyroid, oesophagus, bladder, liver	0.04	0.16
Bone surface, skin, brain, salivary glands	0.01	0.04

* The dose to the colon is taken to be the mass-weighted mean of upper large intestine (ULI) and lower large intestine (LLI) doses, as in the *Publication 60* (ICRP, 1991) formulation.

† The specified remainder tissues (14 in total, 13 for each sex) are: adrenals, extrathoracic tissue, gallbladder, heart, kidneys, lymphatic nodes, muscle, oral mucosa, pancreas, prostate (♂), small intestine, spleen, thymus, and uterus/cervix (♀).

‡ The w_{T} for gonads is applied to the mean of the doses to testes and ovaries.

Table 2: Tissue weighting factors, w_{T} (Ref. [22])

The summation of all tissue weighting factor is equal to one, meaning that in case of full body exposure the equivalent dose (Sv) is equal to the effective dose (Sv). Alternatively, it is clear that the effective dose calculated for a specific organ/tissue will always be smaller than the equivalent dose in organs and tissues.

The values of w_{T} are based on the detriment caused by stochastic effects after radiation exposure and on judgements. They represent mean values for humans averaged over all ages and both sexes (Ref. [1] item 69). Following this, the effective dose is not designed as a quantity considering individual properties of a specific person and should therefore not be applied for an assessment of radiation risk of an individual (Ref. [1] item 70). Consequently, the effective dose should only be used for comparative or optimization studies.

It is to be noted that D_{T}, H_{T}, and E are all so-called protection quantities and can only be obtained through calculations; they cannot be measured in practice. They are developed for radiation protection purposes and related to the risks of ionising radiation exposure.

Furthermore, the application of the protection quantities is restricted to low doses and low dose rates in which the linear non-threshold (LNT) model[47] is applicable. More particularly, for low doses and low dose rates, the area in which stochastic effects (cancer induction and hereditary effects) are important, the probability of the stochastic effects is proportional to the applied dose. At higher doses, when deterministic effects such as tissue reactions may occur, the LNT model is not an acceptable approximation. Tissue reactions always occur above a dose threshold, which depends on the type of tissue reaction (typically above 0.5–2 Gy).

47 The LNT model has been constructed based on high dose and dose rate neutron exposure of the surviving population following the Hiroshima-Nagasaki atom bomb explosion.

The LNT model is however not proven science and other models also exist, such as the supra- and sub linear models and the hormesis model. Nevertheless, the LNT model is widely accepted and applied for radiation protection purposes.

Lastly, it should be noted that near the threshold of the occurrence of deterministic effects, the unit Sv should never be used because the radiation weighting factors are only defined for low doses and low dose rates. In such particular cases, one should ideally use the unit Gy. Putting this in a general way, at high doses and dose rates, the equivalent dose and effective dose should not be used. Instead, the mean absorbed dose in organs/tissues, the maximum dose in organs/tissues, or the organ dose equivalent (depending on the available data, etc.) should be used.

A summary of the dose quantities for radiological protection, as recommended by ICRP103 (Ref. [22]), is provided in Figure 10 below:

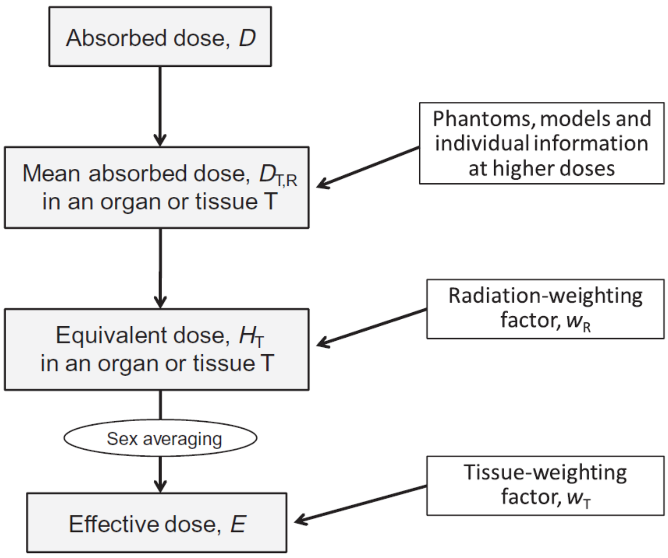

Figure 10: Dose quantities for radiological protection recommended by ICRP103 (Ref. [22])

4.1.3. Operational quantities

In contrast to the protection quantities, the operational quantities are specifically defined for use in measurements, enabling to make assessments of the effective dose or the mean dose in organs or tissues which are generally not measurable (Ref. [1] item 59).

The basis of the operational quantities is the dose equivalent, H, defined by:

$$H = QD$$

In which D equals to the absorbed dose at the point of interest in tissue, while Q represents the corresponding **mean quality factor** due to the charged particles at that point (Ref. [1] item 72). The mean quality factor is a dimensionless factor which reflects the relative biological effectiveness of high-LET radiation compared to low-LET radiation at low exposure levels.

Q is usually given by a function named the quality factor function $Q(L)$, where L is the unrestricted LET[48] in water. The quality factor at a point in tissue, is given by:

$$Q = \frac{1}{D}\int_{L=0}^{L=\infty} Q(L) D_L \mathrm{d}L$$

In which D is equal to the absorbed dose at that point, D_L reflects the distribution of D in unrestricted LET, L, at the point of interest, and $Q(L)$ represents the quality factor as a function of L. The integration must be performed over D_L, due to all charged particles, excluding their secondary electrons (ICRP glossary).

Essentially, $Q(L)$ characterizes the biological effectiveness of a charged particle, with L at a point of interest in tissue relative to the effectiveness of a reference radiation at this point. Q is defined by a function of L in water, not in tissue. RBE values provide the basis for the selection of a quality factor function used in the definition of the specific dose quantities in radiological protection (Ref. [1] item 100). The $Q(L)$[49] function results from radiobiological experiments conducted on cellular and molecular systems, and on results of animal experiments (Ref. [1] item 102).

Equivalently to the energy dependent distribution of w_{R} for neutrons (§4.1.2), for a given neutron exposure situation, the value of the quality factor depends on the position in the body and the mean radiation quality factor in organs and tissues of the body, which may change as a consequence of moderation. For each organ or tissue T, a tissue-mean radiation quality factor, Q_{T}, can be calculated as follows:

$$Q_{\mathrm{T}} = \frac{1}{m_{\mathrm{T}} D_{\mathrm{T}}} \int_{m_{\mathrm{T}}} \int_{L} Q(L) D_L \mathrm{d}L \mathrm{d}m$$

In which m_{T} represents the mass of the organ or tissue T.

The quality factor function $Q(L)$, with L for charged particles in water, can be obtained by means of the following parametrical set of equations (Ref. [21]):

$$Q(L) = \begin{cases} 1 & L < 10\ \mathrm{keV}\ \mu\mathrm{m}^{-1} \\ 0.32L - 2.210\ \mathrm{keV}\ \mu\mathrm{m}^{-1} \leq & L \leq 100\ \mathrm{keV}\ \mu\mathrm{m}^{-1} \\ 300/\sqrt{L} & L > 100\ \mathrm{keV}\ \mu\mathrm{m}^{-1} \end{cases}$$

In a last step, a mean quality factor averaged over the human body, Q_E, can be obtained considering the mean absorbed dose in organs and tissues, D_{T}, and the tissue weighting factors, w_{T}, and is given by the following formula:

$$Q_E = \sum_{\mathrm{T}} w_{\mathrm{T}} Q_{\mathrm{T}} D_{\mathrm{T}} \Big/ \sum_{\mathrm{T}} w_{\mathrm{T}} D_{\mathrm{T}}$$

Notice that for the calculation of Q_E the tissue-mean radiation quality factor, Q_{T}, only appears in the numerator.

The reason why the quality factor, Q, or actually the quality factor function, $Q(L)$, is of particular interest for radiation protection in space will be discussed in §4.2.2.

48 Unrestricted LET, L, means that the transfer energy includes the energies of all emitted delta electrons independent of their range (Ref. [1] item 88).

49 The $Q(L)$ function has been defined based on RBEmax data at low doses and, therefore, its application in radiation protection dosimetry is usually limited to the low-dose range (Ref. [1] item 138).

As described earlier, the operational quantities for area monitoring at a location in a radiation field are defined by the dose equivalent at a point in a simple phantom, the ICRU sphere. In fact, the sphere is hypothetical, a mathematical construct for determination of the values of the quantities for area monitoring. The sphere has a diameter of 30 cm and is composed of tissue-equivalent material, ICRU (soft) tissue with density 1 g cm^{-3}, mass composition 76.2% O, 11.1% C, 10.1% H, 2.6% N (Ref. [1] item 74). For radiation monitoring it well approximates the human body in terms of scattering and attenuation of the radiation fields under consideration.

The ICRU (Ref. [23]) has defined three distinct operational dose quantities:

- The ambient dose equivalent, $H^{*}(10)$;
- The directional dose equivalent, $H'(d, \Omega)$;
- The personal dose equivalent, $H_p(d)$.

The SI unit of the three operational dose quantities is joule per kilogram (J kg^{-1}), with special name sievert (Sv). Their definitions are provided below.

The **ambient dose equivalent**, $H^{*}(10)$, is used for assessing the effective dose by means of area monitoring, and is defined by the ICRU (Ref. [23]) as follows:

"*The ambient dose equivalent, H*(10), at a point in a radiation field, is the dose equivalent that would be produced by the corresponding expanded and aligned field[50] in the ICRU sphere at a depth of 10 mm on the radius vector opposing the direction of the aligned field*".

On Earth, the ambient dose equivalent provides a conservative estimate of the effective dose that a person would receive at that position (Ref. [1] item 76).

The **directional dose equivalent**, $H'(d, \Omega)$, is used for assessing dose to the skin, the extremities (hands, arms, feet), and the lens of the eye by means of area monitoring, and is defined by the ICRU (Ref. [23]) as follows:

"*The directional dose equivalent, $H'(d, \Omega)$, at a point in a radiation field, is the dose equivalent that would be produced by the corresponding expanded field in the ICRU sphere at a depth, d, on a radius in a specified direction, Ω*".

The **personal dose equivalent**, $H_p(d)$, is used to assess the individual external exposure by means of individual monitoring (usually personal dosimeters worn on the body), and is defined by the ICRU (Ref. [23]) as follows:

"*The personal dose equivalent, $H_p(d)$, is the dose equivalent in ICRU (soft) tissue at an appropriate depth, d, below a specified point on the human body*".

The specified point is usually given by the position where the personal dosimeter is worn. The following depths are recommended (Ref. [1] item 80):

- For assessing the effective dose : d = 10 mm;
- For assessing the equivalent dose to the skin, hands, and feet : d = 0.07 mm;
- For assessing the of dose to the lens of the eye : d = 3 mm.

50 An expanded and aligned field is defined as a field where the fluence and its energy distribution are the same as in the expanded field, but the fluence is unidirectional. In the latter, the expanded field is defined is a field where the fluence and its direction and energy distribution have the same values throughout the volume of interest as in the actual field at the point of reference (Ref. [1]).

In monitoring at low doses, the values of the operational dose quantities are taken as sufficiently accurate assessments of the effective dose or skin dose or dose to the lens of the eye, respectively, if their values are below the recommended limits for occupational exposure (Ref. [1] item 71).

Table 3 below provides an overview of the different operational quantities designed for area and individual monitoring of external exposures (Ref. [1] item 73).

Task	Operational quantities for:	
	Area monitoring	Individual monitoring
Control of effective dose	Ambient dose equivalent, $H*(10)$	Personal dose equivalent, $H_p(10)$
Control of doses to skin, hands, and feet	Directional dose equivalent, $H'(0.07, \Omega)$	Personal dose equivalent, $H_p(0.07)$
Control of doses to the lens of the eye	Directional dose equivalent, $H'(3, \Omega)$	Personal dose equivalent, $H_p(3)$

Table 3: Operational quantities for external exposure (Ref. [1])

4.2. Quantities used for radiation protection in space

As discussed in the introduction of this chapter (§4), the radiation environment in space strongly differs from the one on Earth. Obviously, the radiation environment on Earth has been considered to define the protection and operational quantities which are applied to exposure situations in daily life (i.e. on Earth). Following these facts, it is clear that the dose quantities developed for radiological protection on Earth are to be reconsidered for their application in space.

Because of their fundamental differences, again a clear separation will be made between physical (§4.2.1), protection (§4.2.2) and operational (§4.2.3) quantities.

4.2.1. Physical quantities

Since the **absorbed dose**, D, can be applied to all types of ionising radiation and irradiation geometries, as discussed in §4.1.1, the physical dose quantity, D, can also be used for dose calculations or measurements in space.

4.2.2. Protection quantities

Although the extremely low fluence rates of heavy ions might negatively impact the uncertainty on the dose averaged over various organs and tissues of the body, in general, the ICRP states that the concept of the **mean absorbed dose in organs and tissues**, D_{T}, is assumed to be applicable to astronauts in space, especially since the exposure of astronauts in space might be considered as omnidirectional (isotropic) because of their rather continuous movement (Ref. [1] item 119).

As described in §4.1.2, the equivalent dose used for radiation protection purposes on Earth can be obtained by multiplying the mean absorbed dose in organs and tissues, D_{T}, by the radiation weighting factor, w_{R}. Recall that, apart from neutrons, only a single value of w_{R} has been developed for each type of radiation.

Since the space environment is composed of different types of radiation with broad energy distributions up to extremely high particle energies (up to GeV/u), studies have been performed with the objective of verifying the correctness of using, apart from neutrons, also a single value of w_{R} for each type of radiation in space.

More particularly, studies have identified large differences between the radiation weighting factor, w_{R}, and the mean quality factor, Q_E, for proton energies below ~10 MeV. Protons below ~10 MeV, however, are low-penetrating radiation which are mainly stopped by the upper skin layer, thus contributing little to the effective dose in cosmic radiation fields in space (Ref. [1] item 107). At higher energies, the differences between the radiation weighting factor, w_{R}, and the mean quality factor, Q_E, are much lower and are less than 20% at proton energies above 1 GeV (Ref. [1] item 107). For example, at proton energies above 20 MeV, the mean quality factor is always situated between 1 and 2, at which the protons can be seen to be low-LET particles. (Ref. [1] item 108)

While the differences between the radiation weighting factor, w_{R}, and the mean quality factor, Q_E, is relatively small for high-energy protons as well as neutrons, the situation is substantially different for heavy ions (Ref. [1] item 109).

In fact, for heavy ions, the mean quality factor, Q_E, varies strongly with the type and energy of the ion, while the value of the radiation weighting factor, w_{R}, has been fixed at 20 (Table 1). More particularly, studies have shown that the value of the mean quality factor, Q_E, varies between ~2 and 24 depending on the type and energy of the ion. Furthermore, strong variations in the tissue-mean radiation quality factor, Q_{T}, have been observed depending on the position of the organ or tissue in the human body. Hence, selecting a single value of w_{R} for all heavy ions in space seems inappropriate for radiation protection purposes (Ref. [1] item 110).

Following this, in space, where high-energy heavy ions contribute significantly to the total dose in the body, a more realistic approach for radiation weighting should be chosen with a particular focus on heavy ions, since such strong deviations between Q_E and w_{R} are not observed for other types of radiation (Ref. [1] item 99).

Since the general use of a fixed weighting factor, w_{R}, of 20 for all heavy ions does not reflect the variations of RBE with type and energy of heavy ions, the ICRP and space agencies essentially suggest making use of the quality factor, Q, because of the better correlation between RBE and LET. The protection quantity which is obtained is named the **dose equivalent** in an organ or tissue T, and is defined as:

$$H_{\mathrm{T,Q}} = Q_{\mathrm{T}} D_{\mathrm{T}}$$

With the mean quality factor Q_{T} in an organ or tissue T for the given radiation field.

In case the quality factor function, $Q(L)$ is to be used, Q_{T} is calculated by:

$$Q_{\mathrm{T}} = \frac{1}{m_{\mathrm{T}} D_{\mathrm{T}}} \int_{m_{\mathrm{T}}} \int_{L=0}^{L=\infty} Q(L) D_L \,\mathrm{d}L \mathrm{d}m$$

With the mass, m_{T}, of the organ or tissue considered.

Based on the definition of effective dose, E, the **effective dose equivalent**, H_{E}, can be calculated by applying the tissue weighting factors, w_{T} presented in Table 2:

$$H_{\mathrm{E}} = \sum_{\mathrm{T}} w_{\mathrm{T}} H_{\mathrm{T,Q}}$$

In which $H_{\mathrm{T,Q}}$ is equal to the mean value averaged over the male (M) and female (F) phantom, and can be written as follows:

$$H_{\mathrm{T,Q}} = 0.5\,(H_{\mathrm{T,Q}}^{\mathrm{M}} + H_{\mathrm{T,Q}}^{\mathrm{F}})$$

In case individual effective dose equivalents would be needed for dose recording purposes, the following formulas are to be applied for males and females:

$$H_{\mathrm{E}}^{\mathrm{M}} = \sum_{\mathrm{T}} w_{\mathrm{T}} H_{\mathrm{T,Q}}^{\mathrm{M}}$$

$$H_{\mathrm{E}}^{\mathrm{F}} = \sum_{\mathrm{T}} w_{\mathrm{T}} H_{\mathrm{T,Q}}^{\mathrm{F}}$$

Similar to the effective dose which makes use of the same values of w_{T}, the quantity effective dose equivalent is inappropriate for risk assessments for individual male and female astronauts since w_{T} values are single values for both sexes and are based on data for persons of all ages including children (Ref. [1] item 126).

In summary, for radiation protection purposes in space, the quality factor, Q, is to be used instead of the radiation weighting factor, w_{R}, for determining the dose equivalent in an organ or tissue. The effective dose equivalent, on the other hand, can be determined by applying the tissue weighting factors, w_{T}, as presented in Table 2.

Notice also that on Earth, the radiological dose limits are developed with the aim of limiting the probability on stochastic effects and avoiding deterministic effects.

In space, however, deterministic effects (tissue reactions), especially to the lens of the eye or the skin, cannot be ignored because of the higher individual doses compared to the usual exposure situations on Earth (Ref. [1] item 117). In case that deterministic effects may occur (typically above a dose of 0.5 – 2 Gy), $H_{\mathrm{T,Q}}$ and H_{E} may give an indication of the radiation risks but should not generally be used for such assessments (Ref. [1] item 135). The reason for this is because the $Q(L)$ function has been defined based on $\mathrm{RBE}_{\mathrm{max}}$ data at low doses meaning that its application is limited to the low-dose range.

The ICRP points out that the mean absorbed dose in an organ or tissue, D_{T}, and the RBE weighted mean absorbed dose, RBE . D_{T}, when high-LET radiation is involved, are the appropriate quantities for assessing risks of deterministic effects at higher dose. The RBE value to be chosen may depend on the organ or tissue considered, the specific dose and dose rate, and on the type and severity of the tissue reaction considered (Ref. [1] item 136).

Lastly, in contrast to the low-energy environment on Earth, epidemiological data on cancer induction in humans from exposure to high-energy particles and heavy ions, which are abundantly present in space, are not available, and experimental data on cancer induction in animals are scarce (Ref. [1] item 90).

4.2.3. Operational quantities

As stated by the ICRP (Ref. [1]), radiation monitoring in a spacecraft and individual monitoring for each astronaut is a necessary measure for radiological protection in space and the assessment of mission doses of astronauts (Ref. [1] item 128).

On Earth, most strongly-penetrating external radiation fields consist of low-LET radiation, mostly X and gamma radiation or electrons, and in a few cases neutron irradiation is identified to be important. With this in mind, knowing that most area monitors used in radiological protection measure either photon or neutron doses, the operational dose quantities have been defined for applications on Earth.

Because of the specific radiation environment in space some concepts of dose quantities used on Earth should be revisited. For example, the operational quantity for area monitoring of penetrating radiation, which is based on the dose equivalent at 10 mm depth of the ICRU sphere in aligned fields, has been mainly designed on the basis of photon and neutron data for control of effective dose, and is limited in its application to radiation with energies where secondary charged particle equilibrium can be achieved at ~10 mm depth in tissue. This is not true for very-high-energy particles, which are abundantly present in space (Ref. [1] item 130), therefore not automatically providing a correct estimate of the dose in complex space radiation fields. For the latter situation, computer modelling of the exposure situations become very important in addition to measurements (Ref. [1] item 128).

Even though the ICRP does recognize that the applicability of $H^*(10)$ in space is fundamentally incorrect (due to the large spectrum of different types of particles of very high energies), no specific dose quantity for area and individual monitoring in space has been defined to date (Ref. [1] items 131, 133).

In fact, in space, monitoring is mainly performed for assessing the environmental radiation outside or inside a spacecraft, and for warning the astronauts in cases of intensive SPEs. Mainly properties such as particle fluences, LET distributions, and absorbed doses in detector materials are measured. These data are used as input or validation data for calculations of doses in body (Ref. [1] item 131).

To conclude, no specific operational quantities have been defined in space, so strictly speaking, the operational dose quantities used on Earth might as well be considered as valid in space.

4.3. Radiation exposure limits

On Earth, the typical yearly average dose uptake for people of the public is about 3.6 mSv, which is rather low. International Standards allow exposure to as much as 50 mSv a year for occupationally exposed personnel.

For spaceflight, the exposure limit is higher. The NASA limit for radiation exposure in LEO is 500 mSv/year. Note that the values are lower for younger astronauts, as presented in Table 4 below, since it is presumed that exposure to larger amounts of radiation early in their careers could present greater health risks (Ref. [60]).

Career whole-body exposure limits for NASA astronauts by age and gender

Age (years)	25	35	45	55
Male (mSv)	1500	2500	3250	4000
Female (mSv)	1000	1750	2500	3000

Table 4: Career exposure limits for NASA astronauts by age and gender (Ref. [60])

The career whole-body exposure limits are based on a maximum of 3% lifetime excess risk of (radiation induced) cancer mortality. As can be derived from Table 4 above, the total equivalent dose yielding this risk depends upon gender and age at the start of radiation exposure. Younger persons are assumed to have more life to live, thus a longer chance to develop subsequent health problems (Ref. [60]).

Note that the exposure limits provided in Table 4, which are based on report 132 of the National Council on Radiation Protection (NCRP) (Ref. [61]), only apply to activities in LEOs. At the time, no recommendations exist for planetary or deep space missions. Furthermore, the NCRP 132 risk estimates are subject to large uncertainties (e.g. due to the nature of SPEs). These uncertainties include limits of scientific knowledge, risk model limitations, and the lack of data to characterize the risk. The uncertainties can lead to shielding requirements that place significant limitations on design and mission duration (Ref. [58]).

Table 5 below compares the specific exposure limits between the general public and astronauts. The exposure limits are given depending on the exposure interval and on the radiation penetration depth (i.e. blood forming organs, eyes, skin).

	Depth of radiation penetration and exposure limits for astronauts and the general public (in mSv)			
	Exposure interval	**Blood forming organs (5 cm depth)**	**Eyes (0.3 cm depth)**	**Skin (0.01 cm depth)**
Astronauts	30 days	250	1000	1500
	Annual	500	2000	3000
	Career	1000-4000	4000	6000
General public	Annual	1	1500	50

Table 5: Depth of radiation penetration and exposure limits for astronauts and the general public (Ref. [60])

Table 6 below compares various missions and their durations with the observed radiation dose.

Mission type	Dose (mSv)
Space shuttle mission 41-C (8-day mission orbiting the Earth at 460 km)	5.59
Apollo 14 (9-day mission to the moon)	11.4
Skylab 4 (87-day mission orbiting the Earth at 473 km)	178
ISS mission (up to 6 months orbiting Earth at 353 km)	160
Estimated Mars mission (3 years)	1200

Table 6: Comparison of various missions and their durations with the observed radiation dose (Ref. [60])

Crews aboard the ISS receive an average of 80 mSv for a six-month stay at solar maximum and an average of 160 mSv for a six-month stay at solar minimum. On Earth, we receive an average of 2 mSv every year from background radiation alone (Ref. [60]).

More in-depth information on the radiation exposure limits in space can be found in §6.5 of Ref. [58] and in Ref. [61].

In the next chapter (§5) an overview will be provided of the different GCR models. These models will be compared among each other and to measurements based on a literature study (§5.1-5.2). From this literature study, it will be defined which GCR model will be used as input for the Monte Carlo code PHITS (§5.3).

5. GCR MODELS

As described in §2.4, GCR and SPE will be considered as primary radiation sources in deep space due to their importance in terms of dose contribution to the astronauts. Hence, materials and compounds will be investigated which can provide effective shielding against GCR and SPE. Note that this chapter solely focuses on GCR models. To limit the scope and avoiding the need of investigating the SPE models developed in literature, it has been chosen to consider SPE spectral data available from historical events. The (historical) SPE spectral data used for dose calculations and shielding optimisation will be described in §6.2.2.

GCR models are a necessary prerequisite for making predictions of the radiation exposure for future manned missions to space. The choice of the GCR model can affect the accuracy and the uncertainty of the dose estimations for a mission, which is demonstrated and concluded in Ref. [6] and [8]. Furthermore, since the model spectra can considerably influence the dose estimations, the choice of the model might also influence the selection of astronauts as the dose accumulated during previous spaceflights is considered as well (Ref. [6]).

Depending on the considered location with respect to the Earth's magnetosphere, more particularly, inside or outside the Earth's magnetosphere, the GCR particle fluxes are treated differently. Inside the Earth's magnetosphere, the GCR particle fluxes are attenuated as a result of the shielding provided by the Earth's magnetic field. The GCR models therefore must account for this geomagnetic shielding effect and transport the GCR particles accordingly to a specific orbit (Ref. [2] p33-35). As deep space missions are of interest, the focus will be put on **GCR particle fluxes outside the Earth's magnetosphere** at a distance of **1 AU** from the Sun.

Outside the Earth's magnetosphere, the natural protection by the Earth's magnetic field is no more, leaving only mission planning (which is most important prior to space flight) and shielding measures as a means of exposure reduction (Ref. [1] item 18). Furthermore, literature concluded that the increase in GCR exposure was more pronounced for locations outside the magnetosphere (Ref. [8]).

The aim of this chapter is to provide a brief overview of the different GCR models available and compare them among each other and to measurements based on information from literature (§5.1). From this literature study, it will be defined which GCR model will be used as input for the Monte Carlo code PHITS (§5.3).

5.1. Description and comparison of GCR models

A necessary requirement for an accurate estimation of the exposure level using computer simulations is a reliable description of the GCR spectra (Ref. [5] p1). More particularly, a description of the energy spectra of all relevant GCR particles for the time period and the location of interest (Ref. [2] p51).

Based on a literature study, it has been found that a multitude of scientific studies have been published (Ref. [2], [5], [6], [7], [8], [12], etc.) addressing topics related to GCR models for space exposure assessments. NASA published rather recently (2015) an overview of the GCR environment and the different models available (Ref. [12]). The latter NASA publication even so provides valuable information on the transport of radiation through shielding.

Information from Ref. [5] was of particular interest as the work aimed to compare GCR models and verify their applicability for exposure assessments of astronauts. In the latter, the CREME(96/2009), Badhwar-O'Neill 2010 and Burger-Usoskin (2005) models were compared with measurements to derive the most accurate model with the aim of reducing the uncertainties introduced by the models in the dose calculations (Ref. [2] p51). Since these four models were simultaneously discussed in Ref. [5], it has been chosen to address them collectively in §5.1.1. Valuable information retrieved from Ref. [6] has also been considered as Ref. [6] builds upon the results published in Ref. [5]. Due to the significant improvements compared to the Badhwar-O'Neill 2010 model, the updated Badhwar-O'Neill 2011 and 2014 models, which were not addressed in Ref. [5] and [6], are also discussed based on §5.1 of Ref. [2], and Ref. [40] and [12], respectively.

Information included in Ref. [7] was used to describe the so-called Matthiä/ACE – Matthiä/Oulu model which will be discussed in §5.1.2. In the latter, a model was presented which describes the GCR spectra based on a single free parameter derived from measurements (ACE or Oulu). The GCR spectra predicted by the model is compared to a comprehensive set of experimental data from literature. Valuable information retrieved from Ref. [8] has also been considered as Ref. [8] builds upon the results published in Ref. [7].

Lastly, a promising Russian model recently (2016) developed at the Skobeltsyn Institute of Nuclear Physics (SINP 2016) will be discussed in §5.1.3 based on Ref. [45], [46], and [47]. Although not elaborated in this work, a word on the SPENVIS (Space Environment Information System)/ISO15390 model is provided in §5.1.4.

As stated earlier, a comparison of GCR models is a prerequisite for selecting the most appropriate model to be used as input for the Monte Carlo code (§5.3). The comparison of different GCR models, as discussed in this chapter, fully relies on relevant information collected from literature studies, scientific papers published by space agencies, etc., as discussed here above.

Important to note is that the objective of this chapter is neither to elaborate on the physics behind each model nor to describe each measurement conducted, but to provide a brief overview of the different GCR models available and their agreement with measurements to identify and select the most appropriate model, i.e. the best agreement with measurements, for subsequently performing the simulations.

5.1.1. CREME, Badhwar-O'Neill, Burger-Usoskin

In Ref. [5], the CREME96/2009 and Badhwar-O'Neill 2010 models were selected due to their capability of describing GCR spectra of nuclei between $1 \leq Z \leq 26$ over an energy range from 10 to 10^5 MeV/nuc. The Burger-Usoskin (2005) model however is limited to describe only hydrogen and helium spectra.

5.1.1.1. DESCRIPTION OF CREME96/2009 MODELS

CREME96

CREME96 stands for Cosmic Ray Effects on Micro-Electronics Code updated in 1996. It was primarily designed to make radiation effect calculations on electronic systems and is easily accessible over the Internet. CREME96 applies the semi-empirical model developed by Nymmik et al. (Ref. [38], [64]) to describe GCR particle fluxes. The particle spectrum is calculated as a product of two functions: one describes the Local Interstellar Spectrum[51] (LIS), and the second describes the particle's modulation which is dependent on particle rigidity[52] and solar activity.

The differential energy distribution at 1 AU expressed in (s-m^2-sr-MeV/nuc)$^{-1}$ for the LIS, j_{lis}[53], of particle species i in the CREME96 model, is given by:

$$j_{lis}(R) = D_i \left(\frac{R}{GV}\right)^{-\gamma_i} \beta^{\alpha_i}$$

In which R is the rigidity of the particle in GV. D_i, γ_i, α_i are constant parameters for each particle species. D_i and γ_i are determined from high-energy experiments and α_i describes the form of the low energy region. β is the ratio of particle velocity to the speed of light in vacuum.

The modulation function (function indicating the strength of the solar modulation) is calculated by using the Wolf number W which is defined as:

$$W = k\,(10\,\mathrm{g} + f)$$

In which f is the number of individual sunspots, g is the number of sunspot groups, and k is an empirical observational factor depending on site of observation and the individual observer.

The CREME96 model describes GCR particle fluxes over energies from 10 to 10^5 MeV/nuc from Hydrogen up to Nickel for locations inside the magnetosphere and in near-Earth interplanetary space.

Although the CREME96 package is valid only from the year 1950 to 1997, it has been considered in Ref. [5] in order to estimate the accuracy of CREME96 and the reliability of estimations of the radiation exposure in space published in literature using this model for time periods after 1997.

CREME2009

CREME2009 is the latest version of the CREME package and is based on the GCR standard model described in ISO15390 (Ref. [28]) and the model by Nymmik et al. (Ref. [38]). The CREME2009 model uses 12-month averages of the Wolf numbers centred at the requested time instead of using the monthly averaged values as in the case of CREME96.

GCR particle spectra in the energy range from 10 to 10^5 MeV/nuc are described from Hydrogen up to Nickel from the year 1760 to present. The model is not able to provide estimates for particles at locations inside the magnetosphere.

51 Defined as the spectra of the nucleonic component of the GCR beyond the heliospheric modulation region (Ref. [5]).

52 The rigidity, R, of an ion is given by its momentum divided by its charge and is used for characterising the movement of a high-energy charged particle in a magnetic field in space (Ref. [1]).

53 j_{lis} represents the particle flux of the LIS.

5.1.1.2. DESCRIPTION OF BADHWAR-O'NEILL 2010 MODEL

The Badhwar-O'Neill 2010 (BON2010) model is a revision of a model which was first developed in the 1990s by G. D. Badhwar and P. M. O'Neill.

Unlike the CREME models describing the particle flux variation in the heliosphere semi-empirically, the BON2010 model uses the spherically symmetric Fokker-Planck equation that accounts for GCR propagation in the heliosphere due to diffusion, convection and adiabatic deceleration. A solution to this equation called the force-field solution resulted in a single deceleration parameter or the potential, ϕ, which describes the modulation of the particle spectra (Ref. [65]).

The modulation parameter in BON2010 is derived from the International Sunspot Number (ISSN) accounting for the time lag[54] of GCR flux variations relative to the solar activity. It is calibrated with GCR measurements from space missions.

The differential energy distribution of GCR particles at 1 AU expressed in (s-m^2-sr-MeV/nuc)$^{-1}$ for a given LIS, j_{lis}, is described in the model by:

$$j_{lis}(E) = J_0 \beta^{\delta} (E + E_0)^{-\gamma}$$

In which, E is the kinetic energy of the GCR particle in MeV/nuc; E_0 is the particle's rest mass per nucleon (938 MeV/nuc); β is particle speed relative to the speed of light; J_0, γ, and δ are parameters constant for each type of GCR particle and which are determined from various balloon and space measurements.

The BON2010 model describes the spectra of GCR nuclei in the energy range from 1 to 10^6 MeV/nuc and for elements from Hydrogen (Z = 1) to Plutonium (Z = 94) for near-Earth interplanetary space. The model does not provide spectra for locations inside the magnetosphere.

5.1.1.3. DESCRIPTION OF BURGER-USOSKIN MODEL

The Burger-Usoskin model also uses the force-field approximation of the cosmic ray modulation. The LIS, j_{lis}, of GCR hydrogen nuclei is described by:

$$j_{lis}(E) = \frac{1.9 \times 10^4 \cdot P(E)^{-2.78}}{1 + 0.4866 P(E)^{-2.51}}$$

$$P(E) = \sqrt{E(E + 2E_0)}$$

In which, E is the kinetic energy (in MeV/nuc) and E_0 = 938 MeV is the rest mass. The LIS of the helium nuclei is derived by approximating the ratio of helium to hydrogen particle number to 5% (i.e. scaling the equation of j_{lis} by 0.05). The local interstellar spectra together with the modulation parameter provided by Usoskin et al. (Ref. [39]) is applied in the force-field model to derive the energy spectra of the GCR hydrogen and helium particles at 1 AU.

The Burger-Usoskin model is limited to GCR ions with Z ≤ 2 and a constant ratio of He to H particle number in the LIS is assumed. Also, the reconstruction of the modulation parameter in the Burger-Usoskin model is based on neutron monitor count rates which are a direct measure of the GCR intensity.

[54] Lags can result from (1) rapid solar activity variations and (2) sign reversal of the heliospheric general magnetic field. The inertia-induced lags (1) can reach 1-2 years while the gradient particles drifts (2) can take months (Ref. [63]).

5.1.1.4. COMPARISON OF MODELS WITH MEASUREMENTS

Measurements

In Ref. [5], the fluxes derived from the models presented in §5.1.1.1-5.1.1.3 were compared with measurements to assess the accuracy of the models in terms of temporal variations and spectral shape[55]. GCR measurements were obtained from the following space and high-altitude balloon experiments (for details reference is made to Ref. [5]):

- Space experiments:
  - Advance Composition Explorer (ACE);
  - Payload for Antimatter Matter Exploration and Light-nuclei Astrophysics (PAMELA) experiment;
  - Electron Proton Helium Instrument (EPHIN);
  - Alpha Magnetic Spectrometer (AMS) experiment.
- Balloon-Borne Experiments:
  - Balloon-borne Experiment with a Superconducting Spectrometer (BESS);
  - Isotope Matter-Antimatter Experiment (IMAX);
  - Cosmic Antiparticle Ring-Imaging Cerenkov Experiment (CAPRICE-1).

Apart from the EPHIN space experiment, an overview of the space and balloon-borne experiments as stated above is provided in Figure 11[56] below:

Name	Flight	Time	Ions (Z)	Energy (GeV/n)	Data pts.
ACE/CRIS	Satellite	1998-present	5-28	0.05 – 0.5	8288
AMS	STS-91	1998	1, 2	0.1 – 200	58
ATIC-2	Balloon	2002	1, 2, 6, 8, 10,…,14, 26	4.6 – 10^3	55
BESS	Balloon	1997-2000, 2002	1, 2	0.2 – 22	300
CAPRICE	Balloon	1994, 1998	1, 2	0.15 – 350	93
CREAM-II	Balloon	2005	6-8, 10, 12, 14, 26	18 – 10^3	42
HEAO-3	Satellite	1979	4-28	0.62 – 35	331
IMAX	Balloon	1992	1, 2	0.18 – 208	56
IMP-8	Satellite	1974	6, 8, 10, 12, 14	0.05 – 1	53
LEAP	Balloon	1987	1, 2	0.18 – 80	41
MASS	Balloon	1991	1, 2	1.6 – 100	41
PAMELA	Satellite	2006-2009	1, 2	0.08 – 10^3	472
TRACER	Balloon	2003	8, 10, 12,…,20, 26	0.8 – 10^3	55
Lezniak	Balloon	1974	4-14, 16, 20, 26	0.35 – 52	131
Minagawa	Balloon	1975	26, 28	1.3 – 10	16
Muller	STS-51	1985	6, 8, 10, 12, 14	50 – 10^3	16
Simon	Balloon	1976	5-8	2.5 – 10^3	46

Figure 11: Overview of the various space and balloon-borne experiments (Ref. [29])

As a measure of the level of accuracy, the chi-square values were calculated from the comparison of the models against experimental data over the available energy ranges. The study was performed for the following elements: H, He, O and Fe. The first two nuclei represent the light GCR component, while O was taken as a representative for the mid-heavy and Fe for the heavy GCR component.

[55] For dosimetry purposes the GCR models should be able to describe the temporal variation of the GCR spectra related to their modulation during the solar cycle (Ref. [5]).

[56] The ACE/CRIS measurement is highlighted because of its exceptional high amount of data points, representing 82% of the data available.

Conclusions based on Ref. [5] and [6]

Temporal Variation of Integral Fluxes

In Ref. [5] it was concluded that for the times during which measurements were available the Burger-Usoskin model described the measurements most accurately. The CREME2009 model reproduced the measurements relatively well, except for the 2000-2002 solar maximum. Of all models discussed in Ref. [5], the BON2010 model was found to be the best model to describe the measurements of the heavier particles and showed good agreement with the helium data.

Differential Energy Distributions[57]

Based on the distributions for the selected time periods it was concluded in Ref. [5] that the BON2010 model described the spectrum of all the particles for the energy range above ~40 MeV/nuc more accurately than the CREME models. The H and He spectra from the Burger-Usoskin model were also noticeably well in line with the measurements.

Chi-Square Analysis

A chi-square test was performed in Ref. [5] to examine the accuracy of each model in comparison with measured data using the following formula:

$$\chi^2 = \frac{1}{N-1}\sum_{i=1}^{N}[f_{meas}(E_i) - f_{model}(E_i)]^2/\sigma_i^2$$

In which, $f_{meas}(E_i)$ and $f_{model}(E_i)$ are the measured and model flux at the measured energy i respectively, σ_i is the error of the measurement and N is the number of points measured in the spectrum.

Appendix 1 graphically illustrates[58] the Chi-square results calculated between the models and the available measurements for the GCR nuclei H, He, O and Fe, as per Ref. [5]. The following conclusions were drawn in Ref. [5] based upon the results included in Appendix 1:

- For H (plot a) and He (plot b)[59]:
  High chi-square values calculated for CREME96 relative to the other models during most of the times were observed indicating that the model produces the largest deviations in GCR flux spectrum with respect to the measurements. In general, it was concluded that all the models describe the measured H data inaccurately around the year 2000-2002. The same was true for the description of He spectra for the time in year 2000 but not for the time in 2002. The models, especially BON2010 and CREME96, can describe the He spectra relatively well for this time. On average, chi-square values for H nuclei showed to be the lowest from the BON2010 model whereas for He it showed to be the lowest from the Burger-Usoskin model.

57 The differential energy distribution of the GCR particle flux is defined as the number of particles per area, time, solid angle and particle energy (Ref. [6]).

58 The lines joining every point in the figures are added to clearly track plots for each model (Ref. [5]).

59 Due to the lack of H and He measurements for recent time periods, chi-square could be calculated only for 7 points in time for which the data was available (Ref. [5]).

- For O (plot c) and Fe (plot d)[60]:

  Calculated chi-square values were found to be similar for both particle spectra. The accuracy of the models was found to vary over different time periods. The incorrect description of the O and Fe spectra by all the models and the large deviation by CREME96 model with respect to the measurements around year 2000-2002 was also visible. CREME2009 and BON2010 models performed similarly during 1998 to 2000 and 2009 onwards in case of Fe spectra. From mid-2002 to mid-2003, the description of Fe spectra by the CREME96 model was in close agreement with the measurements in contrast to the other times where it showed an overestimation. The O spectra from the CREME2009 model also showed to be in good agreement with measurements for the time period from mid-1997 to 2000 and from 2006 to 2007. Similar to the trend of the CREME96 chi-square values for the Fe spectra, the differences between the measurements and the model fluxes were found to decrease from mid-2002 to mid-2003 for O spectra. The discrepancies in the CREME2009 and BON2010 models were also observed to reduce after 2010 while they remained high for the CREME96 model. The smallest value of the averaged chi-square for the BON2010 model with respect to the other models indicated that on average it described the GCR O and Fe spectra most accurately in comparison to the CREME models over the last 10 years. Only during some periods, the chi-square values of other models were slightly below BON2010.

Most important outcomes based on Ref. [5] and [6]

- Large discrepancies were observed between the measured and model spectra during several periods in the last decades (Ref. [6]):
  - During August 2000, CREME96 showed the largest differences of ~190% for H and ~100% for He fluxes integrated over the considered energy range in comparison to measurements;
  - CREME2009 showed large deviations from experiments by ~73% for H and ~44% for He;
  - BON2010 showed deviations from experiments by ~27% and ~18% for H and for He, respectively.
- For the H and He measurements investigated in Ref. [5] between July 1992 and August 2002, BON2010 showed the least deviation from the experimental data (Ref. [6]).
- BON2010 was found to be the most accurate GCR model in comparison to the CREME models for describing GCR spectra for heavy ions with the smallest chi-square for most of the periods in the last decade (Ref. [5]).
- For almost all time periods BON2010 showed the least deviation from measured data indicating that among the three models investigated in Ref. [5] it is the most accurate GCR model for the recent past (Ref. [6]).
- CREME96 should be used with caution after 1997 and calculations using this model should be interpreted carefully (Ref. [5]).
- All models showed limitations in describing the high GCR intensity observed around year 2009. The Burger-Usoskin model showed higher particle fluxes, overestimating the available data. The lack of H and He measurements made it difficult to accurately judge the discussed models (Ref. [5]).

60 Detailed GCR particle spectra were available due to continuous measurements on the ACE mission (Ref. [5]).

- The absorbed dose and dose equivalent rate have been calculated in Ref. [6] in an unshielded water sphere exposed to GCR intensities by using the models CREME96, CREME2009 and BON2010 (location outside the magnetosphere). Significant variations were observed in the calculated radiation exposure as a result of the differences in the GCR spectra by using the three models. It was however concluded that the results obtained with BON2010 can be assumed as the best estimate of the real values. The dose rates for the unusually deep solar minimum during period 2009-2010[61] were assumed to underestimate the real situation. The latter could however serve as a worst-case scenario for GCR exposure assessments.

5.1.1.5. DESCRIPTION OF UPDATED BADHWAR-O'NEILL 2011 MODEL

The Badhwar-O'Neill 2010 model (§5.1.1.2) was updated and released in 2012 as the Badhwar-O'Neill 2011 (BON2011) model. Since the BON2011 model was not considered in Ref. [5] and [6], the main features and conclusions are summarized below based on information provided in Ref. [42] and [2].

The model uses the spherically symmetric Fokker-Planck equation that accounts for cosmic ray propagation in the heliosphere due to diffusion, convection, and adiabatic deceleration. The boundary condition is the constant energy spectrum (LIS) for each GCR element at the outer edge of the heliosphere (~100 AU). The Fokker-Planck equation modulates the LIS to a given radius from the Sun, assuming steady-state heliosphere conditions.

BON2011 uses the ISSN rather than the actual GCR flux to determine the solar modulation parameter, ϕ, from a flight instrument. Actual spacecraft data is used to calibrate the sunspot number for periods where they overlap (Interplanetary Monitoring Platform-8 (IMP-8) from 1974 to 1997 and ACE from 1997 to present).

Parameter ϕ is directly associated with solar activity and determines the modulated GCR flux for any given time. Prior versions of BON used neutron monitor counts to determine ϕ (t) for periods when actual spacecraft instrument data were not available, such as periods prior to 1974. BON2011 uses the ISSN for all times. The ISSN is however not used directly. In a first step, account is taken for the time lag. Then the time delayed ISSN is calibrated by multiplying it by a constant.

One of the significant differences of BON2011 compared to its prior models is that the sunspot number coefficient for deriving the ϕ for heavier ions (Z > 1) is roughly half that used for protons (Z = 1) during the "plateau" solar minimum cycles. During "peaked" solar minimum cycles, the same coefficient is used for all Z = 1 to 28.

In essence, the BON2011 model is the only GCR model that utilizes all the GCR measurements between 1955 and 2012. It has an improved method of determining the solar modulation parameter and uses the ISSN in order to determine the solar modulation ϕ. It also has an improved time delay function. Information on the fit parameters of the LIS (J_0, δ, and γ) is provided in Ref. [42] in function of the energy range and ACE data.

[61] Period during which the largest increase in the GCR intensity in the past decades was observed (Ref. [6]).

The following main conclusions were drawn in Ref. [2] in terms of the agreement between the model spectra and the measured energy spectra and the influence on the dose rate:

- Model versus measured energy spectra:
  - For most of the time periods after the year 2001, BON2011 provided a more accurate description of the particle fluxes than BON2010. Unlike BON2010, BON2011 was able to describe the elevated GCR fluxes during the deep solar minimum between solar cycles 23 and 24 (around year 2009);
  - For most of the time periods investigated (1997-2012), BON2011 calculated higher particle fluxes in comparison to BON2010;
  - Compared to BON2011, the spectra from Matthiä/ACE (§5.1.2) showed a better agreement with measurements of H, He and heavy nuclei for most of the investigated time periods up to the year 2006;
  - Matthiä/ACE was able to describe the peak H fluxes observed in year 2009, however, it showed an underestimation for O and Fe which were described better by BON2011 in the investigated energy range;
  - For solar minimum (year 1998) and solar maximum periods (year 2000), the differences between the model and measured fluxes were smaller using BON2010 compared to BON2011;
  - Matthiä/ACE showed the best agreement with measurements during solar maximum period (2000) for all the selected nuclei (H, He, O, Fe);
  - During solar minimum period (1998) BON2011 showed a better agreement with O and Fe measurements whereas BON2010 performed better for the lighter nuclei;
  - H fluxes described by Matthiä/ACE were in agreement with measurements for all time periods except for the year 2008 wherein BON2011 showed a better agreement with measurements.

- Influence on the dose rates calculated using BON2010, 2011 and Matthiä/ACE for an unshielded water sphere located outside the magnetosphere close to Earth (time period from July 1997 to October 2011):
  - For most of the time periods BON2011 produced higher fluxes compared to BON2010, therefore also yielding higher dose values;
  - The dose rates calculated using BON2011 were higher in comparison with the values calculated using Matthiä/ACE for most of the time periods;
  - In general, the differences in the dose rate values calculated using different models are higher during periods of solar minimum.

In conclusion, the BON2011 model appears to be significantly better than its older model (BON2010) and showed a good agreement with measurements. BON2011 could also describe the increased GCR fluxes during the last deep solar minimum, showing even better agreement with measurement of heavy nuclei compared to Matthiä/ACE (Ref. [2] p127).

More details on the BON2011 model can be found in Ref. [42] and [2].

5.1.1.6. DESCRIPTION OF UPDATED BADHWAR-O'NEILL 2014 MODEL

In 2014, the Badhwar-O'Neill (BON) model received another update referred to as the Badhwar-O'Neill 2014 (BON2014) model. Since the BON2014 model was not considered in Ref. [5] and [6], the main features and conclusions are summarized below based on Ref. [40] and [12].

By using an updated GCR database and improved model fit parameters, the new BON model (BON2014) has significantly been improved over the previous BON models for describing the GCR radiation environment of interest to human space flight. More particularly, in BON2014, as opposed to the previous BON releases, the LIS parameters, J_0, δ, and γ (discussed in §5.1.1.2) have been modified based on a sensitivity study by using several metrics (details can be found in Ref. [41]). Based on the results of that study[62], the new LIS parameters were fitted to the GCR data in such a way that allowed evaluating a range of parameter combinations to minimize the uncertainty and relative difference between GCR measurements and the model.

In the past, the LIS parameters of the BON models were uniquely influenced by measurements from the Cosmic Ray Isotope Spectrometer (CRIS) onboard the ACE spacecraft. The CRIS instrument measures the flux of ions and their isotopes from boron to nickel, where the lowest and highest kinetic energy measurements are ion specific. CRIS provides kinetic energy of GCR isotopes between ~50 – 500 MeV/n (Figure 11). In BON2014, greater emphasis is placed on the higher kinetic energies, a region not covered by CRIS.

In Ref. [40] the BON2014 model was compared with GCR measurement data by evaluating the relative differences between both measurements and the model. Furthermore, the new BON2014 model was compared to the previous BON2011 model. Without going into detail, the following was concluded:

- The BON2011 model systematically overpredicts the GCR measurement data, whereas BON2014 provides a more balanced prediction. More importantly, the overall spread in the new model error was reduced from 23.7% (BON2011) to 13.0% (BON2014). At all energies, BON2014 was only a marginally improved fit to the hydrogen GCR data compared with BON2011;
- Overall, the BON2014 model has been improved significantly with respect to the previous models (BON2010/2011) both at low- and high-energy regions;
- The LIS parameters used by BON2014 slightly underpredict hydrogen GCR data for most of the years since ~1998 (beginning of a solar maximum).

In Ref. [12] NASA made a comparison between two well-known international GCR models. More particularly, GCR proton and alpha fluxes from the BON2014 and the Matthiä model (§5.1.2) were compared to PAMELA measurements.

Based on the results presented in Figure 12 below, it was concluded that the two GCR models tend to agree reasonably well at highest energies.

[62] It was shown that GCR ions with energies between 0.5 – 4.0 GeV/n account for most of the shielded effective dose.

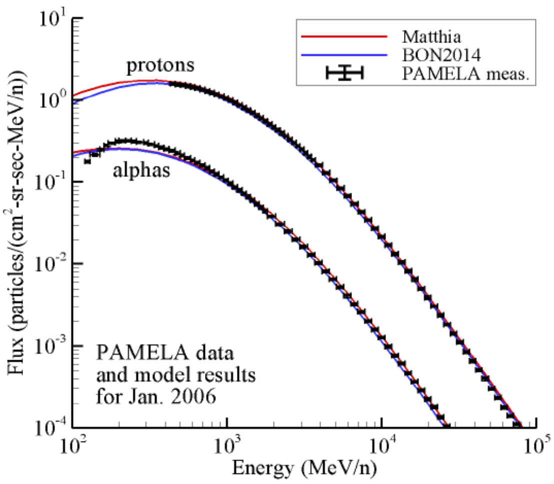

Figure 12: GCR proton and alpha fluxes from the BON2014 and the Matthiä model compared to PAMELA data (Ref. [12])

Furthermore, it was demonstrated that the exposures behind aluminium shielding were in good agreement if the BON2014 and the Matthiä GCR models were used. Figure 13 below illustrated this statement.

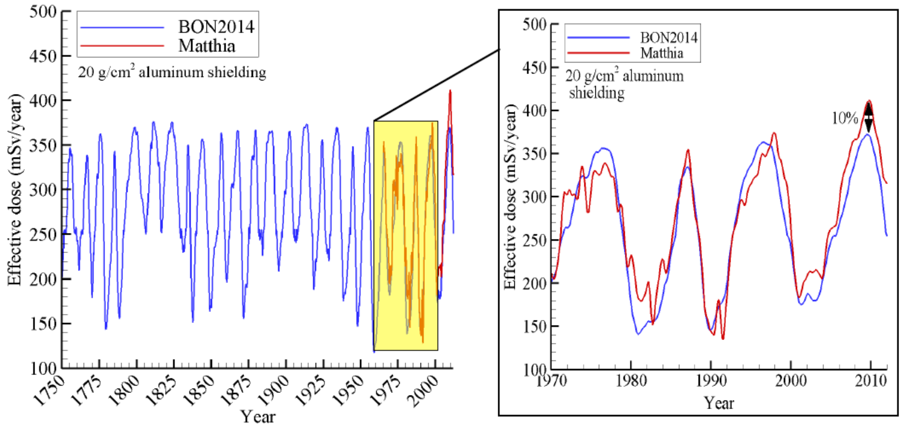

Figure 13: Effective dose versus time behind 20 g/cm^2 aluminium shielding (Ref. [12])

It was concluded that the effective dose behind 20 g/cm^2 Al shielding produced by the BON2014 and the Matthiä model were within 10% of each other, on average, over the past 40 years. The effective doses were computed as a weighted sum of tissue exposures in a detailed human model.

5.1.2. Matthiä/ACE – Matthiä/Oulu

5.1.2.1. DESCRIPTION OF THE MATTHIÄ/ACE – MATTHIÄ/OULU MODEL

GCR model

The Matthiä/ACE – Matthiä/Oulu model, hereafter referred to as the Matthiä model, has been derived from the GCR-ISO15390 model[63] (2004) which relates particle intensities to 12-month averages of the sunspot number.

In practice, the maximum and minimum average sunspot number during the solar cycle of interest are used together with the average sunspot number at the time of interest, taking into account a certain time lag between sunspot numbers and GCR intensities. Also, the time of the polar magnetic field reversal of the Sun in the solar cycle must be included in the ISO model. These quantities are however not easily derived and sometimes not even well defined[64]. Because of this, a new model was developed and described by Matthiä et al. (Ref. [7]) with the intention of eliminating the sunspot number and time of the field reversal dependencies. In fact, the latter two dependencies were replaced by a single free parameter based on experimental data. Based on information provided in Ref. [7], it will briefly be explained how the simplified Matthiä model is derived from the GCR-ISO model. For in depth information, reference is made to Ref. [7] and its including references.

The starting point of the GCR-ISO model is a description of the rigidity spectrum of the different nuclei:

$$\phi_i(R,t) \equiv \frac{dN}{dAdt'd\Omega dR}(R,t) = \frac{C_i \beta^{\alpha_i}}{R^{\gamma_i}}\left[\frac{R}{R+R_0(R,t)}\right]^{\Delta_i(R,t)}$$

In which:

- ϕ_i is the differential fluence rate or flux density of GCR particle type i with respect to particle rigidity R in GV at time t, i.e., number of particles N per area A, time t', solid angle Ω, and rigidity R;
- β is the ratio of particle speed to the speed of light;
- C_i, α_i, γ_i are fixed nuclei dependent parameters given by the ISO model (see Table 1 of Ref. [7]). C_i is expressed in (s sr m² GV)$^{-1}$. α_i, γ_i are dimensionless;
- $\Delta_i(R,t)$ and $R_0(R,t)$ describe the modulation of the GCR in the heliosphere.

At very large rigidities the part describing the modulation of the spectrum at lower rigidities, i.e. $\left[\frac{R}{R+R_0(R,t)}\right]^{\Delta_i(R,t)}$, and parameter β approach unity, meaning that the rigidity spectrum can be described by a pure power law:

$$\phi_i = C_i R^{-\gamma_i}$$

R_0 is a function of the mean sunspot or Wolf number W:

$$R_0(R,t) = 0.37 + 3 \cdot 10^{-4} \cdot \Big(W\big(t, \Delta t(R,t)\big)\Big)^{1.45}$$

[63] For detailed information on the GCR-ISO15390 model, reference is made to Ref. [28].

[64] For instance in the time period close to the end of a solar cycle and the beginning of the subsequent or in the ongoing cycle prior to the magnetic field reversal (Ref. [7]).

In the ISO model the mean sunspot number, i.e. $W\big(t, \Delta t(R,t)\big)$, is calculated by considering a rigidity dependent time lag Δt between the sunspot number and the GCR intensity at Earth. In Ref. [7], however, parameter W is treated as a rigidity independent free parameter which is to be derived by a fitting procedure based on GCR measurements and neutron monitor count rates (explained later).

The exponent Δ_i in the modulation term of the ISO model is described as a function of the rigidity, the time and the mean sunspot number. Δ_i however, can also be approximated by a linear function of W. During periods of very small-time lag between the sunspot number and the GCR intensity, the numerical value of W is expected to be similar to the sunspot number.

By inserting the expression of $R_0(R,t)$ in the rigidity spectrum, i.e. $\phi_i(R,t)$, by replacing Δ_i with the following assumed linear relationship:

$$\Delta = b \cdot W + c$$

and by assuming a rigidity independent W, the following description of the rigidity spectrum is obtained:

$$\phi_i(R,t) = \frac{C_i \beta^{\alpha_i}}{R^{\gamma_i}} \left[\frac{R}{R + (0.37 + 3 \cdot 10^{-4} \cdot W(t)^{1.45})}\right]^{b \cdot W(t) + c}$$

Hence, the rigidity spectrum can be described with the single, time- or modulation-dependent parameter W, and two constant parameters b and c (detailed below).

Based on the latter expression, the differential fluence rate with respect to energy or flux density F_i can then be calculated as follows:

$$F_i(E,t) \equiv \frac{dN}{dAdtd\Omega dE}(E,t) = \phi_i(R(E),t) \frac{A_i}{|Z_i|} \frac{1}{\beta}$$

$$= \frac{C_i \beta^{\alpha_i}}{R(E)^{\gamma_i}} \left[\frac{R(E)}{R(E) + (0.37 + 3 \cdot 10^{-4} \cdot W(t)^{1.45})}\right]^{b \cdot W(t) + c} \frac{A_i}{|Z_i|} \frac{1}{\beta}$$

In which:

- F_i is the differential fluence rate or flux density of particle i with respect to energy E at time t;
- A_i and Z_i are the mass number and atomic number of GCR nucleus i.

The fundamental difference between the ISO model and its simplified version, i.e. the Matthiä model, is the description of the solar modulation effect. More precisely, the modulation effect in the Matthiä model is described by a single free parameter assuming that b and c are modulation independent C^{t} parameters. The single free parameter, W, has been derived from measurements of GCR carbon fluxes by the CRIS on-board the ACE between August 1997 and April 2012. By establishing a linear relationship between the model parameter derived from ACE data and the count rate of the Oulu neutron monitor, W can be estimated until the year 1964. The determination of b, c and W is briefly explained below based on Ref. [7].

Determination of model parameters

As described above, to estimate the modulated GCR spectra at Earth, the single free parameter, W, must be determined. For this purpose, the particle flux density, $F_i(E,t)$, was fitted to experimental GCR carbon[65] data obtained from the CRIS on-board the ACE spacecraft.

The data used for the analysis were averages of the carbon flux over one Bartels rotation (27 days) and cover the period between August 14th 1997 and April 2nd 2012, which is a total number of 198 Bartels rotations. The parameters b and c of the model were derived by performing a minimization procedure[66] from which the relationship between W and expression $\Delta = b \cdot W + c$ could be derived.

The minimization procedure led to the following expression of Δ:

$$\Delta = 0.02 \cdot W + 4.7$$

Indicating that parameters b and c are equal to 0.02 and 4.7, respectively[67].

By inserting the expression $\Delta = 0.02 \cdot W + 4.7$ in $F_i(E,t)$ a description of the GCR fluxes dependent only on the single parameter W is obtained. Values of W derived from ACE carbon data between August 1997 and April 2012[68] can be found in Table 1 of Ref. [7].

In Ref. [7], efforts were made in order to extend the temporal validity of the model. For the latter purpose, the Oulu neutron monitor count rates were selected as a second source of information on the GCR intensity. Since the neutron count rates are a measure of the GCR intensity, a strong correlation between parameter W and the neutron count rates could be assumed.

A description of W as a function of the neutron count rate cr (counts/min) can be obtained by fitting the ACE carbon data (W_{ACE}) and the Oulu neutron count rates averaged over the same Bartels rotation with a polynomial of the first degree.

The following linear expression of W based on Oulu data is obtained:

$$W_{Oulu} = -0.093 \cdot cr + 638.7$$

5.1.2.2. COMPARISON WITH MEASUREMENTS

Measurements and conclusions based on Ref. [7] and [8]

A comparison to a large set of measurements, including a wide range of energies for several GCR nuclei, has been performed in Ref. [7] to validate the model. More particularly, measured data of the ACE/CRIS detector for GCR nuclei C[69], O, Si and Fe was compared to the predictions of the model using W_{ACE}. The agreement between the model predictions and the ACE measurements showed to be very good for all solar modulation conditions[70] and for all ions.

65 GCR carbon data was found to be appropriate to determine the model parameters due to its relatively high abundance. Also, the energy range of carbon measured by CRIS was well suited for investigating the solar modulation (Ref. [7]).
66 More details about the minimization procedure are provided in Ref. [7].
67 Although the solution for b and c is not necessarily unique, it led to very good agreement with measurements (Ref. [7]).
68 Using the same data set of ACE/CRIS C data, it is possible to derive W between August 1997 and present (Ref. [7]).
69 The data of C was used in the fitting procedure to obtain W. The spectra of O, Si, Fe are derived from this W (Ref. [7]).
70 The lowest modulation (W_{ACE} = 0.0) leading to the maximum GCR flux was reached at the end of 2009 (Ref. [7]).

The mean absolute deviation between the model predictions and the ACE data averaged over the period between 1997 and 2012 was calculated to be 5% for C, 7% for Si and Fe, and 9% for O. A comparison of the model predictions based on W_{Oulu} revealed similar good agreement for the three modulations in years 2009, 2006 and 2004.

The values predicted with the ISO model, the BON2010 model and the Matthiä model were also compared to ACE iron data to investigate their agreement with experimental data. A strong disagreement was observed between the measured ACE data and the values predicted with the ISO model and the BON2010 model, especially for very strong modulations corresponding to low GCR intensities. The same behaviour was observed for the other nuclei (C, O, and Si).

Because the data provided by ACE/CRIS is restricted to heavier elements and energies below a few 100 MeV, the values predicted with the three models were also compared to experimental balloon data from BESS and from the High Energy Astrophysical Observatory-3-C2 (HEAO-3-C2), for H and He, and for C and Fe, respectively, for energies between 100 MeV/n and 20 GeV/n and above. The following was concluded:

- A good agreement was observed between experimental data from BESS and the Matthiä model for both weak and strong modulation conditions. Deviations were observed between experimental data from BESS and both the ISO and BON10 models;
- For intermediate modulations all three models described the experimental data from HEAO-3-C2 accurately;
- In general, the Matthiä model gave rise to significantly smaller deviations from experimental data compared to the ISO model and the BON10 model.

Most important outcomes based on Ref. [7] and [8]

- Requiring input on the average sunspot number for GCR spectra calculations, as described in the ISO standard, showed to be difficult and the resulting GCR intensities showed to disagree with experimental data (Ref. [7]).
- During solar activity extremes the Matthiä model agreed much better with ACE and balloon data than the ISO and BON10 models (Ref. [7]).
- The Matthiä model did not show similar disagreements to experimental data during the recent solar minimum as was observed for other models (discussed in §5.1.1.4) (Ref. [7]).
- The Matthiä model deviated for most of the experimental conditions on average by ~10% or less. The GCR-ISO model, on the other hand, showed significant discrepancies compared to measurements (several tens of percent) (Ref. [7]).
- The Matthiä model offers a significant improvement in the description of the intensity of the modulated GCR close to Earth (Ref. [7]).
- In Ref. [8], the increase in GCR exposure outside the Earth's magnetosphere was investigated during the last solar minima. The exposure was estimated in terms of absorbed dose and dose equivalent rates between 1970 and 2011 in order to examine the relative change in the dose quantities. The Matthiä model was employed as it was shown that other models (§5.1.1.4) were not able to describe the increased GCR intensity and the increase in dose during 2008–2010. The dose rates were calculated in a water sphere (surrogate for the body) either unshielded or surrounded by Al shielding of 0.3, 10 or 40 g cm^{-2}.

The following conclusions were drawn (Ref. [8]):

- The dose rate correlates with the GCR intensity and is anti-correlated to the solar activity;
- The exposure was the largest during the solar minimum periods when the GCR flux reached its peak values (1977, 1986, 1997, 2009). The estimated doses using ACE and Oulu data in the Matthiä model were very similar;
- The level of increase in the dose rates from the peak exposures in 1997 to 2009 is found to reduce with shielding;
- The dose values in 2009 were estimated for an unshielded water sphere by applying the CREME96/2009, BON10 and Matthiä (ACE and Oulu) models. It was found that the application of the CREME96/2009 and BON10 models resulted in lower dose rates with respect to the values calculated using the Matthiä model. It was also observed that the BON2010 model gave rise to the largest difference in dose values compared to the doses estimated by the Matthiä models[71];
- The differences in the dose rates calculated with the various GCR models for the recent solar minimum showed that the selection of the GCR model plays an important role in the estimation of the radiation exposure;
- It was concluded that the GCR exposure between the years 2008 and 2010 is expected to have been the highest since the beginning of the space age. The dose estimations made for this period could serve as a reference for the worst-case GCR exposure scenario in terms of manned spaceflight to destinations close to Earth.

5.1.3. SINP 2016

5.1.3.1. DESCRIPTION OF THE SINP 2016 MODEL

In 2016, a promising Russian GCR model has been developed at the Skobeltsyn Institute of Nuclear Physics (SINP 2016) which is since then in use by the Russian space agency, ROSCOSMOS. Without touching the mathematical expressions and diving deep into the selected experimental data for developing the model, a summary of the model's main features is provided below based on Ref. [45].

Most empirical models currently available, such as the ISO15390, Burger-Usoskin, and Matthiä models, are designed to estimate GCR particle fluxes in interplanetary space at a heliocentric distance of about 1 AU (in Earth's orbit).

The new SINP 2016 empirical model, on the other hand, can estimate long-term variations in GCR particle fluxes in the interplanetary space at the ecliptic plane (with particle energies from ~80 to 10^5 MeV/nucleon and particle charge from H to Ni), taking into account changes in solar activity and heliocentric distance from the Sun r (from 1 to ~70 AU). The model was developed based on experimental fluxes of GCR protons, helium, and heavy charged particles (HCPs) measured by different instruments from 1973 up to 2015 (overview of experiments provided in Table 1 of Ref. [45]).

[71] For near-Earth interplanetary space the dose rates from CREME96, CREME2009 and BON2010 were respectively ~16%, ~14%, and ~21% lower than the values calculated using the Matthiä/ACE model (Ref. [8]).

To calculate the particle energy spectra in interplanetary space the SINP model provides parametric formulas by generalizing experimental data since 1973. The formulas convert the power law energy spectrum of the interstellar flux of GCR particles to energy spectrum in heliosphere by using a modulation function which allows accounting for change of the GCR interstellar spectrum. This approach does not require information on the GCR LIS in contrast to other models, such as the ISO15390, Burger-Usoskin, and Matthiä models.

Without elaborating on the specificities related to the model development (i.e. the modulation function, modulation potential, sunspot number, time delays due to odd and even cycles, etc.) it was shown that the accuracy of the model on a large-term scale (at or higher than the duration of the solar cycle) does not exceed the error of the experimental data (~±20%). The model error can however be higher during increase of solar activity and near the solar maxima due to the unexpected fluctuations in the heliospheric medium by stochastic processes in the Sun.

5.1.3.2. COMPARISON WITH MEASUREMENTS

Results included in Ref. [46] and [47] were used to investigate the agreement of SINP 2016 with experimental data. In fact, the data included in these references were particularly interesting as they compared the GCR models[72] used by NASA (BON2014), ROSCOSMOS (ISO15390, SINP 2016) and ESA (DLR[73] i.e. Matthiä) to recent data from the AMS measured from the ISS. The latter space experiment is particularly important as it is making new high precision measurements of H and heavy ions from ~400 MeV/n to ~1 TeV/n, an energy range with only limited coverage up to now.

The recent AMS data included measurements for hydrogen flux and helium flux integrated over three years between May 19, 2011 and November 26, 2013 and the boron to carbon flux ratio integrated over six years between May 19, 2011 and May 26, 2016.

The AMS data is typically given as a function of rigidity, R, whereas GCR models are usually a function of kinetic energy, T. A conversion is thus required to obtain the desired unit. Also, to meaningfully compare the models with AMS data, it is required to similarly integrate the GCR spectra produced by each model within the AMS energy bins. For more information on both these aspects reference is made to Ref. [46].

Measurements and conclusions based on Ref. [46] and [47]

Hydrogen

Figure 14 illustrates the ratio of each model results divided by AMS data (top) and plots fluxes on a linear scale to emphasize the low energy part of the spectrum as these are most important for space radiation protection (bottom).

[72] Computer codes were used for the BON2014, SINP and DLR models, whereas the ISO model results were obtained by running the code on the SPENVIS web site, which did not provide fluxes for energies above 100 GeV/n.
[73] The Matthiä model (§5.1.2) was developed at the Deutsches zentrum für Luft- und Raumfahrt (DLR).

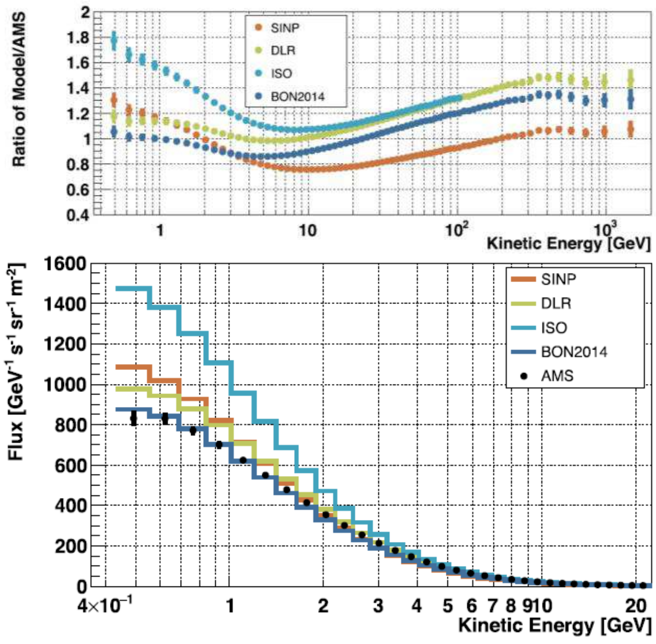

Figure 14: Ratio of model results divided by AMS data (top), linear plot of fluxes at low energies (bottom) (Ref. [46])

Main observations for H:

- At lower energies, the ratio (Figure 14, top) and linear plots (Figure 14, bottom) show that the BON2014 and DLR models are best matched to data;
- Below ~2 GeV, the BON2014 model reproduces the data closely;
- The DLR model matches the data very well between ~2–20 GeV;
- The SINP model first over-predicts and then systematically under-predicts the data across the energy spectrum;
- The ISO model systematically overpredicts across the entire energy range;
- All models fail in the very high energy region, particularly above ~30 GeV. Fortunately, this region does not significantly impact space radiation exposure.

Helium

Figure 15 illustrates the ratio of each model results divided by AMS data (top) and plots fluxes on a linear scale to emphasize the low energy part of the spectrum as these are most important for space radiation protection (bottom).

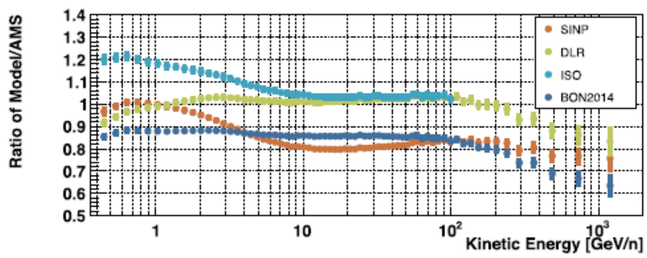

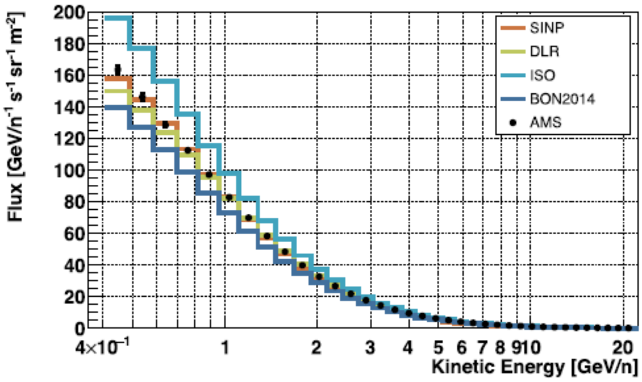

Figure 15: Ratio of model results divided by AMS data (top), linear plot of fluxes at low energies (bottom) (Ref. [46])

Main observations for He:

- The DLR model reproduces best the data across the entire energy spectrum;
- The SINP model performs well below ~2 GeV/n. It under-predicts the remaining part of the He spectrum;
- The ISO model overestimates the spectrum below ~10 GeV/n. It matches the data fairly well between ~10–100 GeV/n;
- The BON2014 model produces a spectral shape similar to data (Figure 15 top). It is however consistently ~13% too low across the entire energy range;
- All models fail in the very high energy region (unimportant for space radiation).

B to C flux ratio

Figure 16 illustrates the AMS measurements of the B to C flux ratio compared to model results (top) and plots the model results divided by data (bottom).

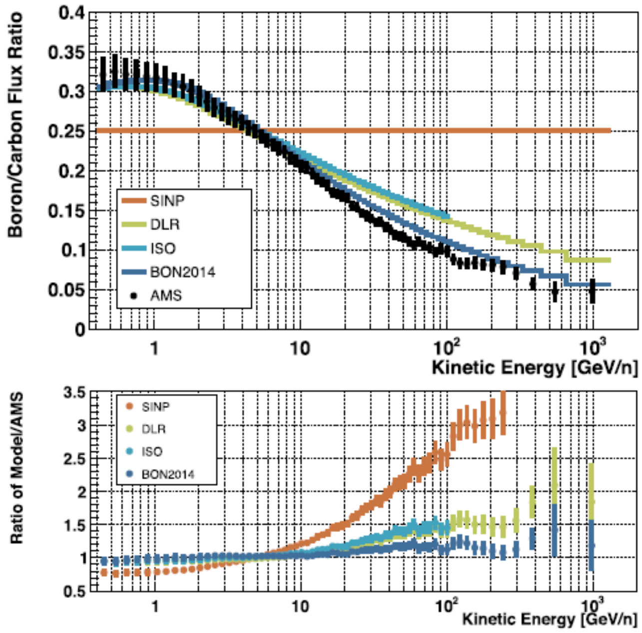

Figure 16: AMS data of B/C flux ratio compared to model results (top), model results divided by data (bottom) (Ref. [46])

Main observations for B to C flux ratio:

- The ISO and DLR models give comparable results, with slight under-prediction of data at low energy and slight overprediction at high energy;
- BON2014 reproduces the data very well, especially below 10 GeV/n where it falls within the measurement uncertainties;
- In the SINP model, all ion spectra are based on the helium flux scaled by a constant value, therefore SINP cannot be used to study ratios between different heavy ions as it will yield a constant value at all energies.

Comparison based on the absolute relative difference and chi-square (χ^2)[74]

Based on absolute relative difference and chi-square analyses, presented in Table 1 and Table 2 of Ref. [46], respectively, the following was concluded:

- Hydrogen:

  The lowest energy part of the hydrogen spectrum (< 1.5 GeV) was by far best represented by the BON2014 model. At the middle energies between 1.5–4 and 4–20 GeV, the DLR model was the closest to data. The BON2014 model was the best performer above 4 GeV and across the spectrum;
- Helium:

  The AMS He spectrum is best represented by the DLR model. The SINP model does a better job only at the lowest energies <1.5 GeV/n, where it follows the data closely before systematically underestimating the data;
- B to C ratio:

  The B/C ratio is best reproduced by the BON2014 model, except in the range of 1.5–4 GeV/n where the ISO model transitions from underestimating to overestimating the data. Below 4 GeV/n, while BON2014 is best, both DLR and ISO models are reasonable representations of the data.

Most important outcomes based on Ref. [46]

- The AMS H spectrum integrated over three years was best represented by BON2014 over the full energy spectrum and below 1.5 GeV. However, DLR better predicted the data for energies between 1.5–20 GeV. Thus, the best choice of model for H depends on the energy range of interest.
- The AMS He spectrum integrated over three years was best reproduced by the DLR model over all energies, except for <1.5 GeV/n where the SINP model follows the data closely. The DLR model was also good in this lowest energy range.
- The AMS B/C ratio integrated over six years was very well matched by the BON2014 model across the spectrum.
- For dosimetry studies, the H spectrum is best represented by the DLR and/or BON2014 model. The DLR model excellently reproduces AMS He spectra, while the BON2014 model is the most accurate for the B/C ratio.

[74] More information on the concepts of the absolute relative difference and χ^2 can be found in §4.4. of Ref. [46].

5.1.4. SPENVIS/ISO15390

The SPENVIS/ISO15390 model has not been included in the comparison of the GCR models since Ref. [2] stated that the model was found to perform similar to the CREME2009 model which is also based on the ISO15390 model and showed severe discrepancies especially for the solar maximum period (Ref. [2] p127).

5.2. Overview of GCR models

An overview of the different models describing GCR spectra outside the Earth's magnetosphere at a distance of 1 AU from the Sun (and beyond for SINP 2016) is provided in Appendix 2 (Ref. [2] p35).

The overview includes the following models: CREME96/2009, BON2010/2011, BON2014, Burger-Usoskin, Matthiä/ACE, Matthiä/Oulu, SPENVIS/ISO15390, and SINP 2016. The model type, the origin of the modulation function, the location, the energy range, the particle type, the validity period, the means of GCR spectra generation and the user-friendliness are summarized for each model.

5.3. GCR model considered as input for PHITS

Based on the information provided in §5.1 and §5.2, it can be concluded that the GCR spectra generated by the most recent models, being **BON2014** (§5.1.1.6), **Matthiä** (§5.1.2.2) and **SINP 2016** (§5.1.3), are in **good agreement** with data from **measurements** compared to other (superseded) GCR models.

Since Ref. [2] concludes that, based on the Matthiä model, the largest contribution to dose comes from particle energies ranging from 1 to 10 GeV/nuc, and that Ref. [46] indicates that, based on the NASA and Matthiä models, 90% of the effective dose behind shielding is induced by GCR with energies above 500 MeV/n, it is concluded that the Matthiä and BON2014 models are best fit for the work to be performed in this thesis (in accordance with §5.1.3.2).

Although both these models are made accessible by NASA through the On-Line Tool for the Assessment of Radiation In Space[75] (OLTARIS), in this work only the GCR spectra generated by the **Matthiä model** (§6.2) has been used as input for PHITS (§6) as both models perform equally well (§5.1.3.2). Also, because of time constraints only one GCR model could be considered.

It was required to develop scripts[76] in an intermediate step to allow converting the output of the selected GCR model to the source input format for the PHITS code.

In the next chapter (§6) the methodology applied and data considered for the dose assessment will be addressed.

[75] More details on this particular tool will be provided in §6.2.
[76] The scripts will be detailed in §6.3.

6. METHODOLOGY FOR DOSE ASSESSMENT

Generally, two different procedures may be applied for the assessment of doses in a target, namely by calculations or by measurements combined with calculations. Radiation field parameters outside or inside a spacecraft may be determined by measurements or by calculations, and then doses in a target may be calculated using particle **transport codes**. There are two possibilities in performing this task. One may either assess the radiation field parameters near to an astronaut and then apply fluence to dose conversion coefficients for all particles involved for the assessment of the doses, or one can calculate the doses using the radiation field data outside of the spacecraft and a code that combines radiation transport in the spacecraft and in the human body (Ref. [1] item 263).

Alternatively, absorbed dose or dose equivalent may be measured near to the target, and these values may be directly correlated to doses in the human body. This is the usual procedure performed in individual dosimetry on Earth, where the reading of an individual dosimeter for strongly-penetrating radiation is taken to be a sufficiently precise value of effective dose for the purpose of usual radiological protection. In space, however, this method is difficult because of the very complex radiation field which varies with time and position within a spacecraft. No single device is able to fulfil this task, and a set of different detectors may be necessary for the assessment of dose equivalent, or effective dose equivalent. The location and orientation of a person within the spacecraft can introduce variations in doses due to the anisotropic spacecraft shielding distributions, which can be important for solar protons. In any case, particle transport calculations need to be performed to verify the appropriateness for the foreseen task/mission (Ref. [1] item 264).

When performing simulations, the real scenario is modelled by transport codes. It is a powerful method for understanding complex physical systems by studying the influence of various parameters. For space applications simulations are essential, especially for estimating the doses that are expected to be received by astronauts during future space missions and in the case when measurements are not feasible or have not yet been made. They also play an important role in **understanding the effect of shielding** on the radiation exposure.

Unfortunately, uncertainties are introduced because the models used in numerical calculations are approximations of the reality (Ref. [2] p31). More particularly, the precision of the simulated results directly depends on the validity of the physical models used in the transport code, the level of detail of the target geometry and its environment, and on the models specifying the composition and spectra of the different components of the radiation field (Ref. [5]). Although beyond the scope of this work, it should also be clear that experimental data are key for the validation of the models used in computer simulation (Ref. [2] p31).

The aim of this chapter is to discuss the methodology applied and data considered for dose assessment. In a first step, the general approach to evaluate the shielding efficiency will be described in §6.1. The tool used for source term generation will be addressed in §6.2 together with the GCR/SPE spectral data considered in this work. The scripts developed for data processing will briefly be described in §6.3. Lastly, the Monte Carlo code and the input parameters will be discussed in §6.4.

6.1. General approach

In general, simulation of radiation exposure requires a description of the radiation field, materials and geometries of the target and its surroundings, the physics of particle interactions and methods to transport the radiation in the target volumes. For estimating the exposure in space, models describing the energy spectra, the target, the shielding and a radiation transport code are thus required (Ref. [2] p32).

Essentially, in the process of space radiation shielding, there are three main stages:

- The modelling stage wherein the GCR and SPE spectra of the relevant particles are calculated for a location outside the magnetosphere (1 AU);
- The simulation stage wherein the setup is defined and the target is irradiated isotropically by relevant GCR and SPE particles;
- The data post-processing stage wherein the shielding efficiency is evaluated.

Figure 17 below provides a schematic diagram illustrating the procedure applied to evaluate the shielding efficiency (case of the use of OLTARIS and PHITS).

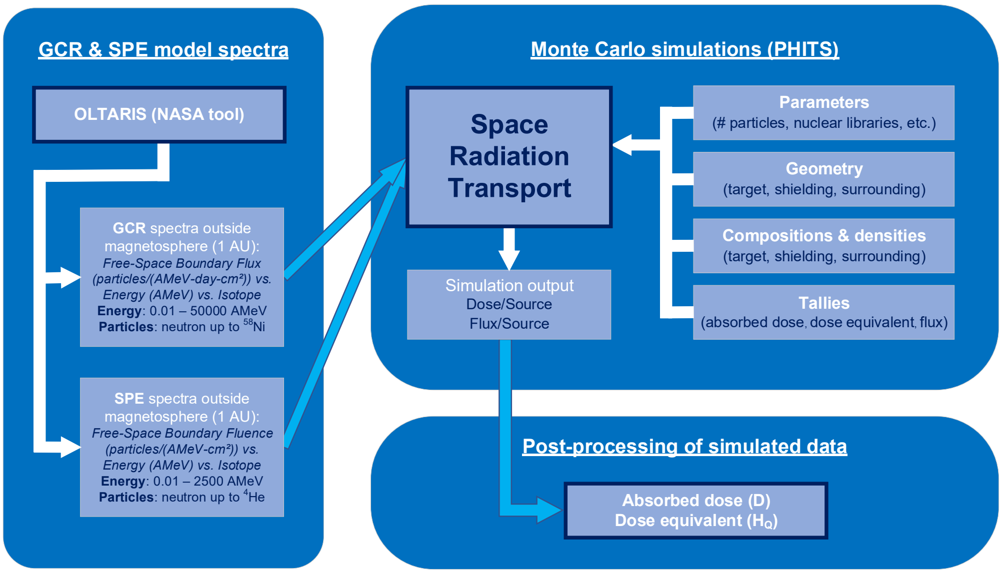

Figure 17: Schematic diagram illustrating the procedure applied to evaluate the shielding efficiency

As indicated in Figure 17 above, the radiation transport code PHITS was selected in this work. Being a general multi-purpose Monte Carlo code, PHITS is not able to provide GCR and SPE spectra. These spectra are obtained from a tool called OLTARIS which is developed by NASA (illustrated on the left side in Figure 17).

Unfortunately, OTARIS generates GCR and SPE spectra in a format which is not directly importable in PHITS as such. For this reason, Matlab scripts have been developed to generate source input data in a format compatible with PHITS.

The following chapters will describe the considered GCR and SPE spectra (§6.2), the Matlab scripts developed (§6.3), and the simulation input parameters (§6.4), prefixed by an introduction on the Monte Carlo approach and a word on PHITS.

6.2. OLTARIS source term tool

The On-Line Tool for the Assessment of Radiation In Space[77] (OLTARIS) has been used to generate the relevant source terms (GCR and SPE spectral data) in space.

OLTARIS is a World Wide Web based tool developed by the NASA which can be used to assess the effects of space radiation on humans and electronics in e.g. spacecrafts, habitats, rovers, and spacesuits. Although the OLTARIS tool is free, it can only be accessed through a registration process.

The OLTARIS architecture is subdivided in two main parts, the website, in which the users interact through a browser, and the execution environment, where the computations are performed.

Figure 18 below schematically presents the OLTARIS program flow[78].

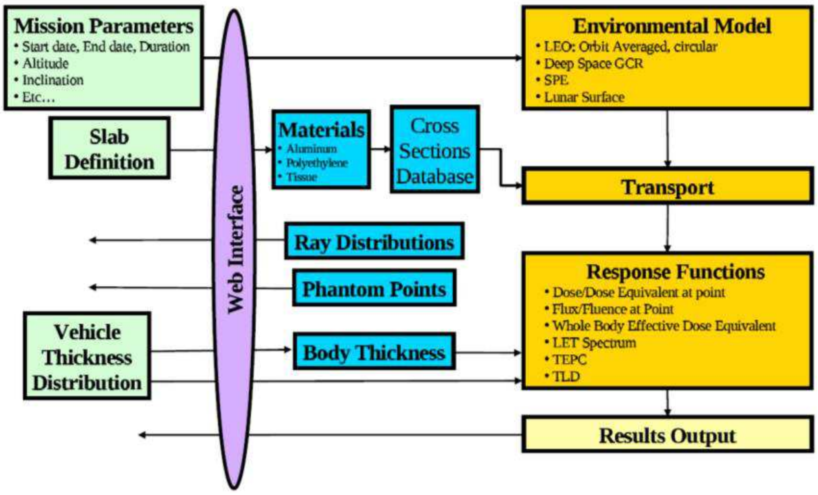

Figure 18: Program Flow for OLTARIS (Ref. [43])

The green boxes indicate data to be supplied by the user. In this work, the mission parameters defining the external radiation environment were most important. The blue boxes indicate data that the user can either download from the web server or data used in the calculations and stored on the execution host. The gold boxes represent the computations performed on the execution host and consist of three modules: the environmental model, particle transport, and the response functions (Ref. [43]).

The following environments are currently available in OLTARIS:

- **GCR**: Free Space 1 AU, Lunar Surface, Mars Surface;
- **SPE**: Free Space 1 AU, Lunar Surface, Mars Surface;
- Earth Orbit / Trajectories;
- Europa Mission.

77 https://oltaris.nasa.gov/
78 Note that although the figure is an extract from an older OLTARIS version, the fundamentals remain valid.

For GCR the following models are made available: BON2010, BON2014, Matthiä, and SINP 2016. In terms of SPE, one can choose between eleven historical SPEs or implement a user defined SPE. The two environments Earth Orbit / Trajectories and Europa Mission are not discussed as they are not used in this work.

The GCR and SPE environments used in this work are discussed in the following subchapters. Reference is made to the OLTARIS website for more information on the tool and its features.

6.2.1. GCR spectral data

OLTARIS has been used to obtain the spectral data from the three most recent GCR models, being BON2014, Matthiä, and SINP 2016, and this for all the solar activities made available in the tool.

Table 7 summarizes the historical solar minima and maxima available in OLTARIS.

	Solar activities available in OLTARIS				
Min	1965	1977	1987	1997	2010
Max	1970	1982	1991	2001	/

Table 7: Overview of historical solar minima and maxima available in OLTARIS

Besides the GCR model and the solar activity, the mission duration is a free input parameter to be defined in OLTARIS. In this work, it has been decided to consider a fixed mission duration of 10 days[79].

In total, 27 spectra[80] were extracted from OLTARIS by combining the three different GCR models with the nine solar activities available. Each spectra provides for 59 particles (Table 8) the Free-Space Boundary Flux (particles/(AMeV-day-cm²)) in function of the energy (AMeV), with energy ranging from 0.01 – 50 000 AMeV.

Particles available in OLTARIS

^{1}n	^{1}H	^{2}H	^{3}H	^{3}He	^{4}He	^{6}Li	^{7}Li	^{8}Be	^{9}Be
^{10}B	^{11}B	^{12}C	^{13}C	^{14}N	^{15}N	^{16}O	^{17}O	^{18}F	^{19}F
^{20}Ne	^{21}Ne	^{22}Ne	^{23}Na	^{24}Mg	^{25}Mg	^{26}Mg	^{27}Al	^{28}Si	^{29}P
^{30}S	^{31}S	^{32}S	^{33}Cl	^{34}Ar	^{35}Cl	^{36}Ar	^{37}K	^{38}Ar	^{39}K
^{40}Ca	^{41}Ca	^{42}Ca	^{43}Sc	^{44}Ti	^{45}Ti	^{46}Ti	^{47}Ti	^{48}V	^{49}V
^{50}Cr	^{51}Cr	^{52}Cr	^{53}Mn	^{54}Mn	^{55}Fe	^{56}Fe	^{57}Co	^{58}Ni	

Table 8: Particles for which the spectral GCR data is provided by OLTARIS

79 In fact, the mission duration has no influence on the spectral data used in this work (i.e., the mission duration is irrelevant).
80 Free-Space Boundary Flux (particles/(AMeV-day-cm²)) vs. Energy (AMeV) vs. Isotope.

Note that, as the radiation transport calculations will be performed by means of PHITS, it is only in our interest to use OLTARIS for obtaining the so-called Free-Space Boundary Flux (particles/(AMeV-day-cm²)) vs. Energy (AMeV) vs. Isotope. In this context, "Free-Space" refers to the unshielded boundary flux in space (void) which is independent of the considered volume, material and mission duration. In fact, OLTARIS can also perform dose calculations and shielding analyses but as it is less flexible and less realistic than PHITS, it was not used for this purpose.

Knowing that for each GCR model all solar activities available were considered and that each spectra provides information on 58 different particles, one can derive that in total 1566 (3 x 9 x 58) plots were obtained.

Because of this huge amount of data, it has been chosen to only explicitly illustrate the plot of ^{1}H (proton) in function of each solar activity available, this by using the Matthiä model (Figure 19). This choice can be justified knowing that ^{1}H is the most abundant particle in space, while the Matthiä model showed excellent agreement with measurements. Nonetheless, each plot was analyzed for determining which spectra will be considered as source input for the radiation transport calculations.

Figure 19 below illustrates the spectral proton data as provided by OLTARIS.

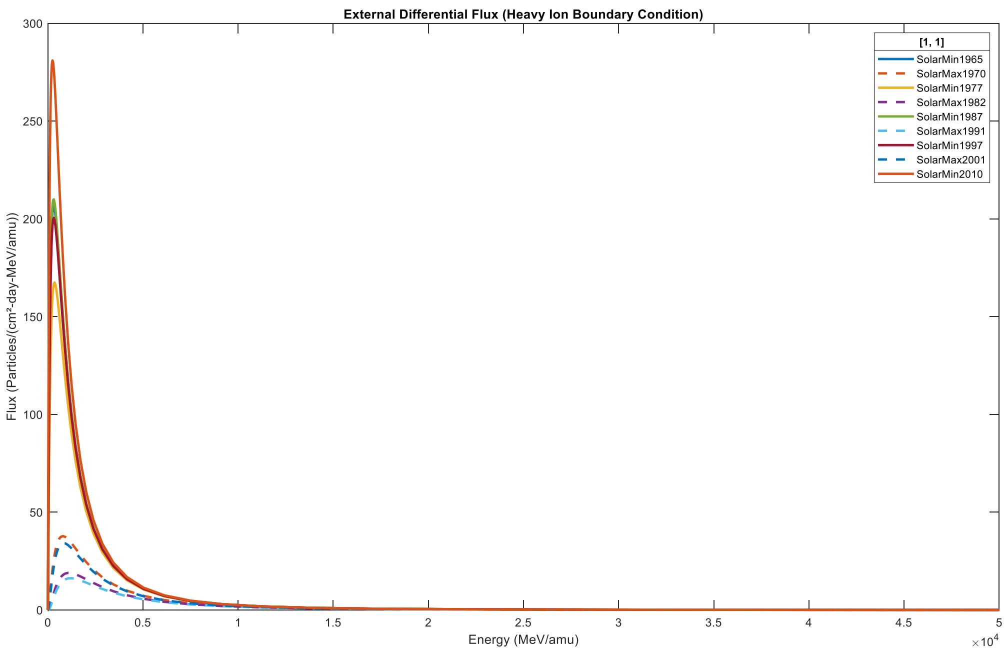

Figure 19: Illustration of the spectral proton data as provided by OLTARIS (Matthiä model)

Drawing meaningful conclusions based on Figure 19 is rather impossible knowing that valuable information is not visualized due to the choice of the axis. Because of this, Figure 20 below provides the same information as illustrated in Figure 19 but on a loglog scale.

In fact, for the evaluation of the shielding efficiency, we are mostly interested in the relative (or fractional) dose reduction rather than in the absolute dose reduction. Consequently, the shape of the different spectral curves is much more important than their actual magnitudes. Following this, all the curves have been normalized in order to analyse their shape (flux distribution in function of the energy). Figure 21 below illustrates the normalized spectral proton data.

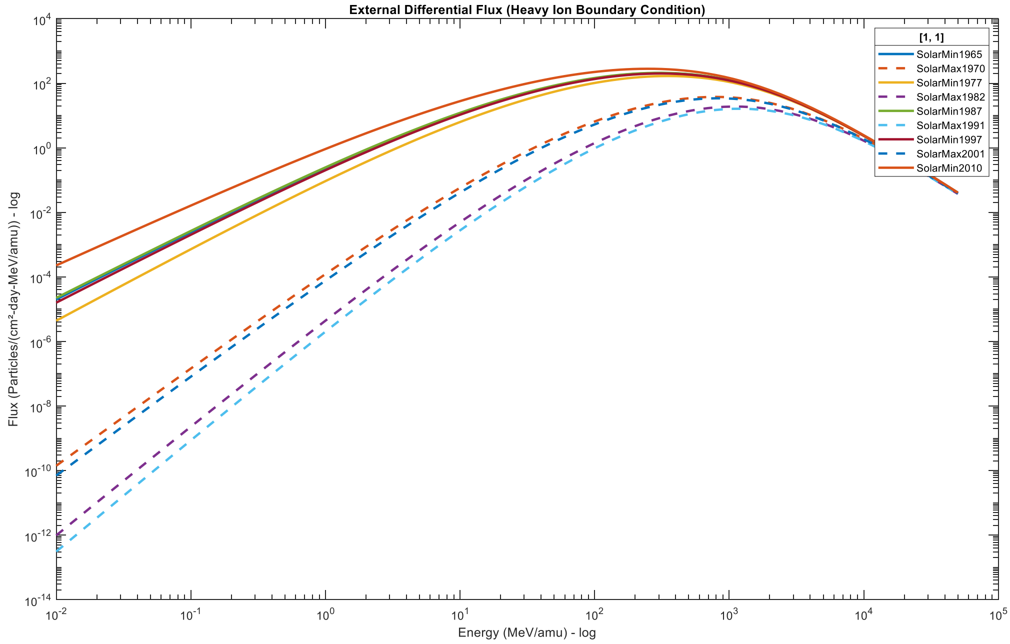

Figure 20: Illustration of the spectral proton data on loglog scale (Matthiä model)

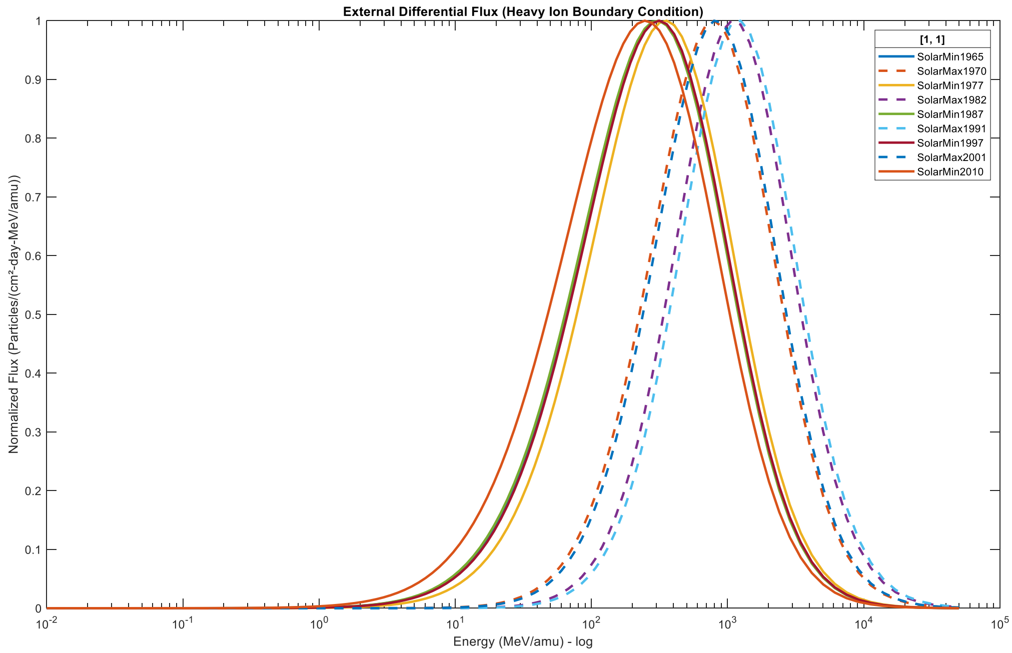

Figure 21: Illustration of the normalized spectral proton data (Matthiä model)

Based on the shape of the curves illustrated in Figure 21, it was evaluated which spectra are to be selected as source input for the radiation transport calculations. For illustrational purposes, Figure 22 below illustrated the same graph as plotted in Figure 21 but with a zoom on the different peaks.

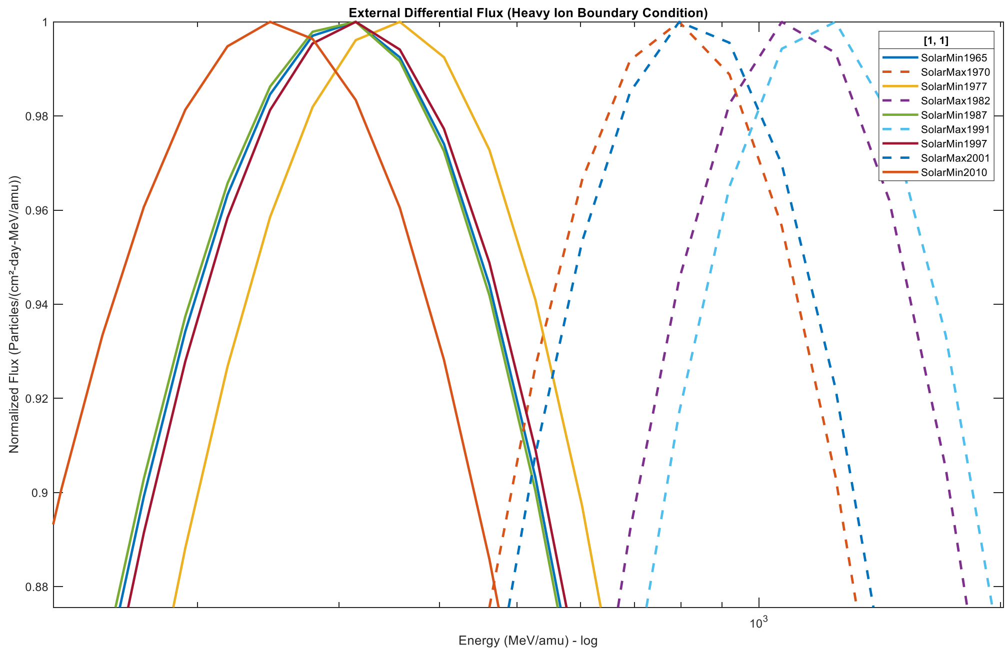

Figure 22: Zoomed illustration of the normalized spectral proton data (Matthiä model)

With the aim of enveloping the different spectral shapes, it was chosen to consider the following solar activities as input for the Monte Carlo simulations (Table 9):

	Selected solar activities
Min	2010
Max	2001

Table 9: Selected solar activities used as input for the Monte Carlo simulations

Indeed, the Solar Min of 2010 is enveloping the lower energy range. Although the Solar Max of 1991 is the enveloping case for the higher energy range, it has been chosen to consider the Solar Max of 2001 since its flux is higher (Figure 20) and because it is the most recent data available, which should increase its reliability.

The validity of this conclusion was verified for all spectral GCR data available (i.e. for the three GCR models and for all particles). The outcome of the analysis showed that these two solar activities indeed tend to envelope the spectral shapes of other data (other models and other particles). For completeness, Appendix 3 visualizes the spectral data of all solar activities for ^{1}H, ^{4}He and ^{56}Fe, and this for the three GCR models (BON2014, Matthiä, and SINP 2016).

Based on Figure 22, it is directly noticeable that the normalized Solar Min curves are shifted towards lower energies compared to the normalized Solar Max curves. This can be explained knowing that during Solar Max (i.e. lowest GCR intensity), the solar modulation reaches a maximum, basically sweeping out a large part of the low energy particles present in the solar spectra.

6.2.2. SPE spectral data

As described in §2.1.3, performing accurate predictions of future SPEs is complex due to its stochastic nature. Because of this, studies involving SPEs often fall back on historical data. Also in this work spectral data constructed based upon historical SPEs were considered. The following SPEs are available in OLTARIS (Table 10):

	SPEs available in OLTARIS
SPE 1	September 1859 (Carrington - September 1989 hard fit)
SPE 2	September 1859 (Carrington - March 1991 soft fit)
SPE 3	February 1956 (Webber)
SPE 4	February 1956 (LaRC)
SPE 5	November 1960
SPE 6	August 1972 (LaRC)
SPE 7	August 1972 (King)
SPE 8	August 1989
SPE 9	September 1989
SPE 10	October 1989
SPE 11	Sum of October 1989 Tylka Band fits

Table 10: Overview of historical SPEs available in OLTARIS

In total, 11 spectra[81] were extracted from OLTARIS. Each spectra provides for 6 particles (Table 11) the Free-Space Boundary Fluence (particles/(AMeV-cm²)) in function of the energy (AMeV), with energy ranging from 0.01 – 2500 AMeV.

Particles available in OLTARIS

^{1}n	^{1}H	^{2}H	^{3}H	^{3}He	^{4}He

Table 11: Particles for which the spectral SPE data is provided by OLTARIS

Note that, as the radiation transport calculations will be performed by means of PHITS, it is only in our interest to use OLTARIS for obtaining the so-called Free-Space Boundary Fluence (particles/(AMeV-cm²)) vs. Energy (AMeV) vs. Isotope. In this context, “Free-Space” refers to the unshielded boundary fluence in space (void) which is independent of the considered volume and material. As for GCR (§6.2.1), OLTARIS was thus not used for performing shielding analyses.

Knowing that all SPEs were considered and that each spectra provides information on 6 different particles, one can derive that in total 66 plots were obtained. Even though 6 particles are listed in OLTARIS, only data for ^{1}H (proton) was available. Hence, the ^{1}H spectral data from all SPEs are visualized in Figure 23 below.

81 Free-Space Boundary Fluence (particles/(AMeV-cm²)) vs. Energy (AMeV) vs. Isotope.

In fact, for the evaluation of the shielding efficiency, we are mostly interested in the relative (or fractional) dose reduction rather than in the absolute dose reduction. Consequently, the shape of the different spectral curves is more important than their actual magnitudes. Following this, all the curves have been normalized in order to analyse their shape (fluence distribution in function of the energy). Figure 24 below illustrates the normalized spectral proton data.

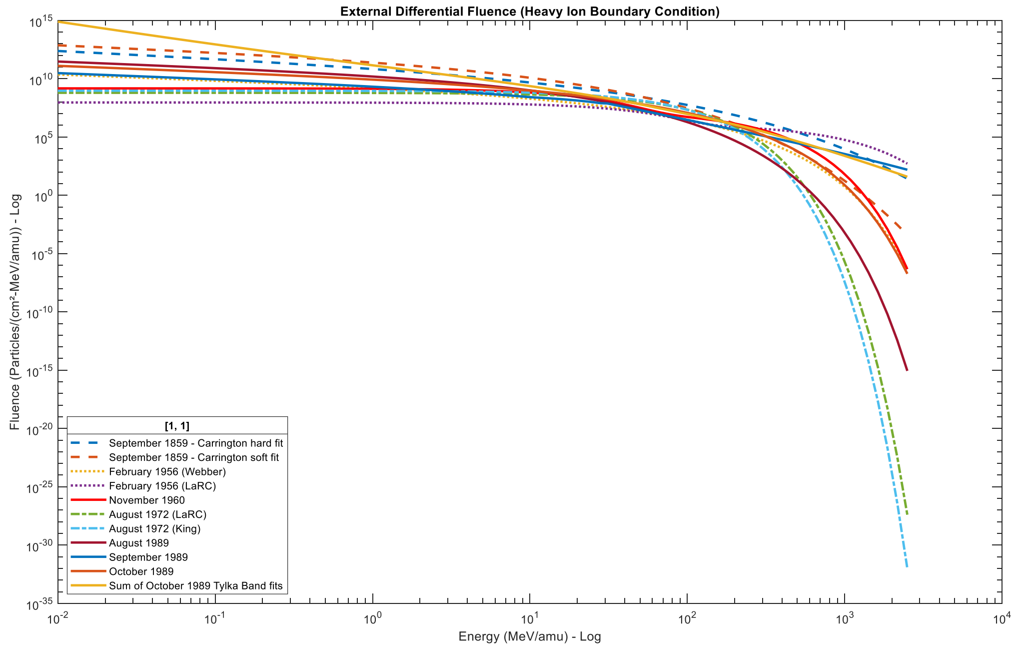

Figure 23: Illustration of the spectral proton data on loglog scale

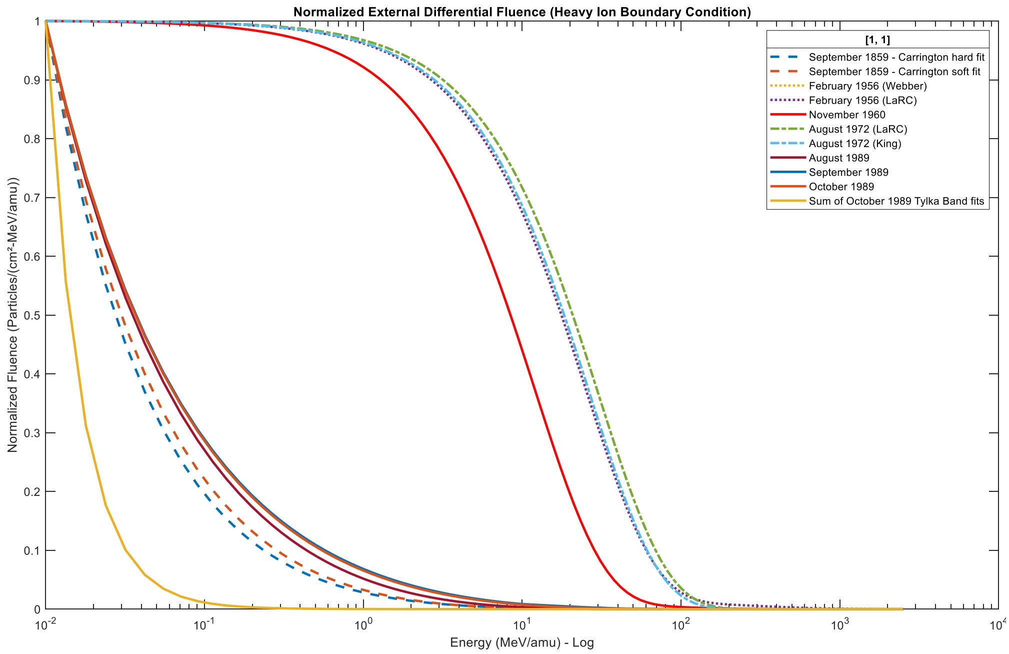

Figure 24: Illustration of the normalized spectral proton data

Based on the shape of the curves illustrated in Figure 24, it was evaluated which spectra are to be selected as source input for the radiation transport calculations.

With the aim of enveloping the different spectral shapes, it was chosen to consider the following SPEs as input for the Monte Carlo simulations (Table 12):

	Selected SPEs
SPE 6	August 1972 (LaRC)
SPE 11	Sum of October 1989 Tylka Band fits

Table 12: Enveloping SPEs used as input for the Monte Carlo simulations

Clearly, the SPEs of August 1972 (LaRC) and October 1989 (Tylka Band fits) envelope the different spectral shapes (Figure 24). Besides being an enveloping case, the SPE of October 1989 (Tylka Band fits) also has the highest total (i.e. energy integrated) fluence (Figure 23).

6.3. MATLAB interfaces

As discussed earlier, multiple Matlab scripts have been developed mainly for data treatment purposes. An overview of these scripts is provided in Table 13 below:

	Matlab scripts developed
GCR	(1) Script for transferring data from OLTARIS to Matlab/Excel
	(2) Script for analysing the GCR spectra from 3 GCR models
	(3) Script for analysing the enveloping GCR source data
	(4) Script for transferring source term data from OLTARIS to PHITS
	(5) Script for importing results produced by PHITS to Matlab
SPE	(1) Script for transferring data from OLTARIS to Matlab/Excel
	(3) Script for analysing the enveloping SPE source data
	(4) Script for transferring source term data from OLTARIS to PHITS
	(5) Script for importing results produced by PHITS to Matlab

Table 13: Overview of Matlab scripts developed for data processing purposes

Based on Table 13, it is directly noticeable that a clear separation has been made between scripts developed for GCR and SPE data treatment purposes, and this in the pre-processing as well as in the post-processing phase.

This approach has been adopted for the following justifiable reasons:

- The output of OLTARIS (i.e. fluxes for GCR and fluences for SPE) is presented in a slightly different order for GCR compared to SPE. Hence, OLTARIS output data required to be imported in Matlab in a slightly different away;
- The analyses of GCR data was different compared to SPE data since for GCR three models needed to be intercompared using different solar activities (for 59 particles), while for SPE eleven events were compared for only one particle;
- PHITS required a modified source input format for GCR compared to SPE due to differences in the (normalisation of the) source term distribution.

Nevertheless, one could have indeed developed only one extended over coupling script which would have been able to treat both GCR and SPE data. However, it has been chosen not to do so to avoid errors during the code development phase as well as during the usage of the code for data processing purposes.

Furthermore, based on Table 13, one can notice that an additional script has been developed for GCR compared to SPE, being script (2) which has the purpose of analysing the GCR spectra from three GCR models. The reason for this is obvious since only for GCR there are three distinct space radiation models from which the user can choose (BON2014, Matthiä, SINP 2016). For SPEs, one can only select between different historical events; not between different calculation models.

Without going into details in terms of coding, the basic functions and main purpose of each script is briefly described below (applicable for GCR and SPE):

(1) Scripts for transferring data from OLTARIS to Matlab/Excel
OLTARIS has the ability to export spectral data in the format of a text (.txt) file. Besides spectral data (fluxes/fluences in function of energy), this text file also contains information less relevant for radiation transport purposes such as, e.g., the date of file creation, the name of the (data generation) job, the version number of the NASA Fortran code, etc. More importantly, the spectral data of the particles involved are provided in an unorganized fashion and lack important simulation parameters needed for direct use in PHITS. An example of an OLTARIS output file is provided in Appendix 4. Generic easy-to-use scripts have been written to automate the process of importing the spectral data generated by OLTARIS in Matlab in a desired fashion. The scripts can visualize all spectral data and have the ability to export all imported OLTARIS data to an Excel format (values and plots).

(2) Script for analysing the GCR spectra from 3 GCR models
As mentioned earlier, this script has been developed to intercompare the spectral output generated by the different GCR models (not applicable to SPE). Indeed, different GCR models lead to differences in terms of spectral shape and magnitude. By considering a particular solar activity, this script visualizes exactly the latter.

(3) Scripts for analysing the enveloping GCR source data
New scripts have been developed to identify which spectra (representing the space source term) will effectively be considered as source input data for PHITS. Some graphical outputs generated by means of these scripts are included in chapters §6.2.1–6.2.2 (e.g. normalized spectral ^1H data).

(4) Script for transferring source term data from OLTARIS to PHITS
As described in (1), the spectral data generated by OLTARIS are provided in an undesired fashion and lack important simulation parameters needed for direct use in PHITS. Hence, new scripts have been developed which export the source data to a format directly readable by PHITS (.txt format). This step is fully automated and reduces significantly the time needed to implement the source term in a correct way. For example, in PHITS, the GCR source term contains more than 3000 lines to be written in a specific format. It is clear that the probability on potential human errors is reduced significantly by automating this process. An example of a source term dataset to be imported in PHITS, as generated by the scripts, is provided in Appendix 5 (the source term dataset is limited to two pages only as the entire dataset would occupy 47 pages).

(5) Script for transferring results produced by PHITS to Matlab
A large amount of output data needed to be analyzed upon finalization of the simulations. Hence, scripts have been developed to extract relevant data from the simulation output files for data post-processing purposes in Matlab. An example of a PHITS output file (i.e. tally results) is provided in Appendix 6.

Indeed, the scripts used in the framework of this work were developed with caution and thoroughly verified/validated as they treated a huge part of the data flow.

In the absence of automated scripts this work would have occupied a tremendous amount of time for importing/exporting data, and for data analyses. Furthermore, once the correct functioning of a script is confirmed, most of the human errors are avoided during data transferring processes (i.e. copy/paste errors are excluded).

Lastly, note that all scrips are developed in a user-friendly way in the sense that no coding during data processing is required. This was achieved by ensuring that the user is only required to select the concerned input files and choose the desired output formats.

6.4. Monte Carlo code

Precise predictions of the radiation environment inside space vehicles and inside the human body are essential when planning for long-term deep space missions. Since these predictions include complex geometries as well as the contributions from many different types of radiation, including neutrons, 3D Monte Carlo codes with precise physics models are needed (Ref. [34]).

This chapter aims to provide a general introduction on the Monte Carlo approach (§6.4.1) as well as a word on the Monte Carlo code PHITS considered in this work (§6.4.2). The main focus will be put on the simulation input parameters (§6.4.3).

6.4.1. The Monte Carlo approach

Because the approach itself reaches far beyond the scope of this work, the aim of this subchapter is not to provide in-depth information on the Monte Carlo method, but rather to highlight its fundamentals and its most important features in terms of radiation transport. Information relevant for this work has been extracted from the book "*Exploring Monte Carlo Methods*" (Ref. [44]).

6.4.1.1. INTRODUCTION

The analysis technique called Monte Carlo is, in essence, a methodology to use sample means to estimate population means and has been developed at the time that digital computers were far from being invented.

In fact, the foundations of the Monte Carlo approach, which were initially referred to as statistical sampling, were laid in the 17th century by gifted mathematicians within the Bernoulli family. Their key work was put further by many successors in subsequent years. Although this approach was developed as far as ~330 years[82] ago, Monte Carlo became a practical analysis technique only in the mid-twentieth century, with the invention of digital computers. Once pseudorandom numbers[83] could be generated and long summations could be computed, it became evident that the Monte Carlo formalism was a great tool for estimating the behaviour of neutrons and other radiation particles. Neutrons were of particular interest in the mid-twentieth century because of the effort to construct nuclear weapons. Just as the space program 20 years later gave great impetus to computing and materials research, so too the nuclear weapons program gave great impetus to the Monte Carlo method as a numerical procedure. In fact, it was during efforts to design and test the hydrogen bomb that Monte Carlo got its name[84].

In the "games of chance", popular at the Monte Carlo (Monaco, France) gambling centres, the "house" assures itself, by a very small bias in the rules of each game, that it will win when averaged over many players. However, any individual player has a chance to win in any game, providing the motivation and allure to play.

[82] In 1689, the original statement of the law of large numbers, on which Monte Carlo is based, was produced (Ref. [44]).
[83] A pseudorandom number generator is a deterministic algorithm that, given the previous numbers (usually just the last number) in the sequence, the next number can be efficiently calculated.
[84] The name Monte Carlo originates from one of the mathematicians interest in "game of chances" who later published a paper titled "The Monte Carlo Method" (Metropolis and Ulam, 1949).

In a Monte Carlo simulation, an individual history can go anywhere in the problem space, meaning that all possibilities and their consequences can occur; however, it is assured that if enough histories are run (a large enough sample is chosen) and the game is played correctly, the game converges toward the desired result. In this sense, the name Monte Carlo indeed captures the concept appropriately.

In its simplest form, Monte Carlo turns bits into meaningful rational numbers. Run an experiment that leads to either success (one) or failure (zero). Repeat the experiment N times. Call N the number of histories or trials. Then divide the number of successes S by the number of trials. There are $N + 1$ possible outcomes $(0, 1/N, 2/N, \ldots, N/N = 1)$. If N is large, then the quantity S/N gives a good approximation to the average or expected value of the experiment. In this form, each history is a bit (a zero or a one) and the result is a rational number.

Monte Carlo is, in essence, a powerful form of quadrature or numerical integration in which finite summations are used to estimate definite integrals. Although Monte Carlo is inherently involved with the concept of probability, it can be applied, with much success, to problems that have no apparent connection with probabilistic phenomena. It is particularly valuable when considering multidimensional integrals where it generally outperforms traditional quadrature methods. Monte Carlo also can be applied to a great variety of problems for which the integral formulation is not posed explicitly. Often, the complex mathematics needed in many analytical applications can be avoided entirely by simulation.

It can be concluded that Monte Carlo methods provide extremely powerful ways to address realistic problems which are very hard or even impossible to solve by analytic techniques. Today, with the widespread availability of powerful computers, Monte Carlo methods are widely used in a multitude of disciplines which require quantitative analysis.

6.4.1.2. FUNDAMENTALS

Monte Carlo is based on two fundamental statistical results, being the law of large numbers and the central limit theorem. Leaving most of the mathematics besides, both fundamentals are briefly described in the following paragraphs.

The heart of a Monte Carlo analysis is to obtain an estimate of an expected value such as:

$$\langle z \rangle = \int_a^b z(x) f(x) dx$$

If one forms the estimate:

$$\bar{z} = \frac{1}{N} \sum_{i=1}^{N} z(x_i)$$

where the x_i are suitably sampled from $f(x)$, the law of large numbers states that, as long as the mean exists and the variance is bounded:

$$\lim_{N \to \infty} \bar{z} = \langle z \rangle$$

This law states that eventually the normalized summation $\bar{z}$ approaches the expected value $\langle z\rangle$. Here, the quadrature nodes x_i are "sampled" from the probability density function[85] (PDF) $f(x)$ and the quadrature weights are equal to $1/(Nf(x_i))$.

The law of large numbers provides a prescription for determining the nodes and weights of a Monte Carlo quadrature scheme for estimating well-defined definite integrals. It however does not indicate how large N must be in practice. The answer to this question is provided by the central limit theorem (CLT).

The CLT is a general and powerful theorem which can be expressed as follows:

$$\lim_{N\to\infty} \text{Prob}\left\{\frac{|\bar{z}-\langle z\rangle|}{\sigma(z)/\sqrt{N}} \leq \lambda\right\} = \frac{1}{\sqrt{2\pi}}\int_{-\lambda}^{\lambda} e^{-u^2/2}du$$

The right side of this formula is called the confidence coefficient. The parameter λ is the number of standard deviations[86], from the mean, over which the unit normal is integrated to obtain the confidence coefficient.

In words, the CLT provides the following insights:

- The CLT indicates that the asymptotic distribution of $(\bar{z}-\langle z\rangle)/\left[\sigma(z)/\sqrt{N}\right]$ is a unit normal distribution or, equivalently, $\bar{z}$ is asymptotically distributed as a normal distribution[87] with mean $\mu = \langle z\rangle$ and standard deviation $\sigma(z)/\sqrt{N}$;
- Nothing is said about the distribution function used to generate the N samples of z, from which the random variable $\bar{z}$ is formed. No matter what the distribution is, provided it has a finite variance[88], the sample mean $\bar{z}$ has an approximately normal distribution for large samples. The restriction to distributions with finite variance is of little practical consequence because, in almost all practical situations, the variance is finite;
- As $\lambda \to 0$, the right side of the CLT formula approaches zero. Thus, the sample mean $\bar{z}$ approaches the true mean $\langle z\rangle$ as $N \to \infty$, a result that corroborates the law of large numbers;
- The CLT provides a practical way to estimate the uncertainty in a Monte Carlo estimate of $\langle z\rangle$, because the sample standard deviation, $s(z) = \sqrt{s^2(z)}$, can be used to estimate the population standard deviation $\sigma(z)$ of the CLT formula.

The CLT provides an estimate of the uncertainty in the estimated expected value. Most important, it states that the uncertainty in the estimated expected value is proportional to $1/\sqrt{N}$, where N is the number of histories or samples of $f(x)$. If the number of histories is quadrupled, the uncertainty in the estimate of the sample mean is halved.

85 A PDF specifies the probability per unit of x, so that $f(x)$ has units that are the inverse of the units of x. For a single continuous variable it is a non-negative function defined on an interval. The integral over that interval is unity.

86 The square root of the variance is called the standard deviation σ, thus $\sigma = \sqrt{\sigma^2(x)}$.

87 The normal distribution, also often called the Gaussian distribution, has the PDF $f(x) = (1/\sqrt{2\pi}\sigma)\, e^{-(\mu-x)^2/(2\sigma^2)}$ with $-\infty < x < \infty$. The mean μ and variance σ^2 are the parameters of this distribution.

88 The variance describes the spread of the random variable x from the mean and is defined as $\sigma^2(x) \equiv \langle[x-\langle x\rangle]^2\rangle$.

In summary, the CLT guarantees that the deviation of the sample mean from the true mean approaches zero as $N \to \infty$. The quantity $\sigma(z)/\sqrt{N}$ provides a measure of the deviation of the sample mean from the population mean after N samples. Use of the sample standard deviation $s(z)$, to approximate the population standard deviation $\sigma(z)$, allows the construction of a confidence interval about $\bar{z}$ that has a specified probability of containing the true unknown mean. As the sample size N increases, this confidence interval, the width of which is proportional to $1/\sqrt{N}$, becomes progressively smaller.

In conclusion, one of the important features of Monte Carlo is that not only can one obtain an estimate of an expected value (by the law of large numbers) but also one can obtain an estimate of the uncertainty in the estimate (by the central limit theorem). Thus, at the end of a Monte Carlo simulation, one can have an idea not only of what the answer is but also of how good the estimate of the answer is.

Before discussing the application of Monte Carlo to radiation transport (§6.4.1.3), it is reminded that in many complex problems an estimate is sought of some mean value in which the underlying PDF $f(x)$ is not known a priori. The PDF however can be estimated numerically by performing simulations. Monte Carlo simulations that numerically mimic the actual physical processes involved are called analog Monte Carlo simulations. In many problems, however, such analog simulations are computationally impractical as enormous numbers of simulated particle histories need to be constructed to obtain even a few scores. Nevertheless, Monte Carlo simulations can still be used effectively by introducing so-called “biases” into the simulation. Biases basically allow more particles to reach the target and the tally adjustments give correct tally values, thereby requiring fewer particle histories to obtain statistically meaningful results compared to analog simulations.

6.4.1.3. MONTE CARLO IN RADIATION TRANSPORT

A Monte Carlo radiation transport calculation simulates a finite number N of particle histories by sampling from the appropriate PDFs governing the various events that may happen to a particle from its birth by a source to its eventual demise by, for example, being absorbed or escaping through the boundary. A history begins by randomly selecting a particle’s initial position, energy, and direction from the PDFs that describe the sources for the problem. As the particle travels on various legs of its trajectory, sampling is performed to determine random values for distance to the next interaction, type of interaction, scattering angle, energy change, and so on.

While charged particles such as protons and heavy ions continuously loose a small part of their energy along their pathway through matter, uncharged particles like neutrons and photons basically travel in straight lines between interactions. On some interactions, secondary particles are created, such as, for example, neutrons from fission reactions or X-rays from photoelectric interactions. These secondary particles are “banked” and their initial energies, interaction positions, and travel directions recorded. After the original particle finishes its history, these secondary banked particles are processed sequentially to create a history for each.

After each history is terminated or its interactions are determined, its contribution z_i is added to the tally being used to estimate the quantity of interest such as, for example, average flux in a cell, probability of escape, energy deposited in a cell, current through a surface, or other quantities related to the radiation field.

Note that to calculate the absorbed dose in a certain volume the energy deposited for each step in the volume is summed up and divided by the mass of the volume. To calculate the dose equivalent in the volume the deposited energy for each step is then multiplied by the quality factor, which is calculated by applying the Q-LET relationship (Ref. [6]), as discussed in §4.1.3.

After N histories, the estimate of $\langle z \rangle$ is expressed as follows:

$$\langle z \rangle \cong \bar{z} = \frac{1}{N}\sum_{i=1}^{N} z_i$$

Such analog simulations mimics the stochastic events that befall an actual particle if the problem were converted to an equivalent experiment. In such calculations, very few of the histories contribute anything to the tally of interest. For example, if the probability of a neutron incident on a thick shield eventually reaching the other side is 1 in 10^9, then in analog simulations only 1 out of 10^9 histories, on average, terminate on the back side of the shield. For such problems, it is recommended to implement variance reduction techniques (VRT) and perform nonanalog Monte Carlo calculations (as discussed in §6.4.1.2).

The following aspects, being crucial parts of basically any Monte Carlo simulations, will briefly be discussed in the following paragraphs:

- Geometry;
- Sources;
- Path-length;
- Type of collision;
- Particle weights;
- Score and tallies;
- Variance reduction and nonanalog methods.

Geometry

The three-dimensional space in which the simulated histories are constructed is usually assumed to be composed of contiguous homogeneous volumes or cells, each cell being bounded by one or more surfaces (or portions of surfaces). A cell can be a void or composed of any homogeneous material. All of the three-dimensional space must belong to some cell; there can be no “holes” where a particle would become “lost”. Although not necessary, the geometry of the problem is often surrounded by a problem boundary, usually far from tally regions. The cell containing all space beyond the problem boundary is the “graveyard” of which the purpose is to “kill” any particle that enters it, thereby saving time by not tracking particles beyond the boundary and that have negligible chance of contributing to the tally. Constructing an effective but efficient geometry model for a particular problem is a matter of skill and experience on the modeler’s part.

Sources

Each particle history is begun by sampling from the spatial, energy, and angular distribution of the source to determine the starting position, energy, and direction of each particle history.

The source may be specified explicitly (a fixed-source problem) or calculated by the simulation itself (an eigenvalue problem). In the latter case, initial simulations are used to estimate the spatial distribution of sources such as a fission source and the resulting equilibrium distribution in a critical system.

Sources in a transport calculation can be distributed over many regions, be localized to a few cells, or be singular sources such as point, line, and plane sources. The energy of particles emitted by the sources can consist of a discrete set of energies (typical of gamma rays produced by radioactive decay) or have a continuous distribution of energies (such as neutrons produced by spontaneous fission). While many sources emit radiation isotropically, some sources can be anisotropic (such as a beam of radiation from a reactor beam port). To start a particle history, one must sample from the appropriate spatial, energy, and angular distributions. These three distributions are often interrelated.

Path-length

The distance a particle travels before interacting is a random variable. The path length s of each leg of a particle's history is estimated from its PDF $f(s) = \mu e^{-\mu s}$, where μ is the total interaction coefficient. Because μ generally varies from region to region and because a track segment may span multiple regions, the PDF for travel distance is expressed in terms of mean-free-path lengths $\lambda \equiv \mu s$. Thus, the distance to the next collision, in mean-free-path lengths, has a PDF $f(\lambda) = e^{-\lambda}$and is independent of the medium. The length of each track segment is then obtained by sampling from an exponential distribution.

Type of collision

At the end of a path segment, the particle undergoes an interaction with the material in the current cell (if the collision site is outside the problem boundary, the history is terminated, tallies are updated, and a new source particle history is started). The probability that the particle with energy E interacts with species j in a reaction of type i is:

$$p_i^j = \frac{\mu_i^j(E)}{\sum_i \sum_j \mu_i^j(E)}$$

In which the summations are over all species in the cell and over all possible reaction types.

If the reaction is one in which no particle of the type being tracked emerges from the interaction, the particle is absorbed and the history ends. If more than one particle of the type being considered results from the interaction, the energy and direction of all but one are "banked" for later processing and one particle continues the presented history.

Particle weights

The efficiency of a Monte Carlo transport calculation depends both on the speed with which the calculation can be made and the variance of the result. The speed is, to a large extent, controlled by the hardware and, to a lesser extent, by the computer programmer and the operating system. The variance is controlled mainly by the type of tally used and the number of particles that contribute to the tally.

In strict analog simulations, the only way to reduce the variance of a tally is to run more histories. But this brute-force approach only reduces the variance as $1/N$. A better way to increase the precision of the tally is to use nonanalog techniques to force more particles to the regions of phase space where particles are more likely to score without increasing (and perhaps decreasing) the sampling in less important regions of phase space.

In nonanalog Monte Carlo simulations, on the other hand, the scoring of the particles reaching the tally region or detector must be modified from just the sum of the particles' scores to the sum of the particles' weighted scores. In this way, unbiased results can be achieved with less computing time, if proper variance reduction methods are used, compared to an analog calculation producing the same results and precision.

Score and tallies

After a particle history ends or, more usually, after a particle leaves a cell, its contribution to the score (or tally) is added to the running score of interest. Almost anything of interest that depends on the radiation field can be estimated from the particle histories used in a Monte Carlo simulation.

Variance reduction and nonanalog methods

To define the efficiency of a Monte Carlo calculation, one must take into account both speed and variance. The speed is, to a large extent, determined by the hardware. Of course, the skill of the programmer and the operating system of the computer also determine speed. More important is the variance of the result of a calculation and ways to minimize it. The power of Monte Carlo depends on using many nonanalog techniques to reduce the variance of the estimator.

For detailed information on the application of Monte Carlo to radiation transport simulations, reference is made to Ref. [44][89] (§10 of Ref. [44] in particular).

6.4.2. Particle and heavy ion transport code PHITS

Particle and heavy ion transport codes are essential tools in designing and studying the radiation effects in, for example, accelerator facilities and spacecrafts. Exactly for the latter reason, the multi-purpose Monte Carlo code PHITS[90,91] (Particle and Heavy Ion Transport code System) has been developed[92].

PHITS can transport nearly all particles, including neutrons, protons, heavy ions, photons, and electrons, over wide energy ranges using various nuclear reaction models and data libraries. It is written in Fortran language and can be executed on almost all computers. All components of PHITS such as its source, executable and data-library files are assembled in one package and are distributed to many countries via dedicated databanks and research platforms (Ref. [36]).

[89] The scope of this reference, at least §9-10 of Ref. [44], is limited to neutral particles such as neutrons and photons.
[90] http://phits.jaea.go.jp (Ref. [27]).
[91] PHITS is based on the NMTC/JAM.3 models (Ref. [27]).
[92] PHITS was developed in collaboration with several institutes including Japan Atomic Energy Agency (JAEA), Research Organization for Information Science and Technology (RIST), High Energy Accelerator Research Organization (KEK), and Chalmers University of Technology (Ref. [27]).

The physical processes treated in PHITS can be divided in two different categories, namely transport processes and collision processes (Ref. [35]):

- In the transport process, PHITS can simulate a motion under external fields such as magnetic and gravitational fields. In absence of external fields, neutral particles move along a straight trajectory with constant energy up to the next collision point. Charged particles and heavy ions, on the other hand, interact multiple times with electrons in the material losing energy and changing the direction. PHITS treats ionization processes not as collision but as a transport process under an external field. The average dE/dx is given by the charge density of the material and the momentum of the particle taking into account the fluctuations of the energy loss and the angular deviation;
- The second category is the collision with the nucleus of the material. In addition to the collision, the decay of the particle is considered as a process. The total reaction cross section, or the lifetime of the particle, is an essential quantity to determine the mean free path of the transport particle. According to the mean free path, PHITS chooses the next collision point using the Monte Carlo method. To generate the secondary particles of the collision, information is needed on the final states of the collision. For neutron induced reactions in the low energy region, PHITS uses the cross sections from Evaluated Nuclear Data libraries. For high energy neutrons and other particles, the JAM4 and JQMD5 models have been incorporated to simulate the particle induced reactions up to 200 GeV and the nucleus-nucleus collisions, respectively.

As PHITS can determine the energy of charged particles emitted from low-energy neutron-induced nuclear reactions using the event generator mode in combination with nuclear data libraries, it can perform direct calculations of dose equivalent in organs or tissues which cannot be calculated by using the conventional kerma approximation. The accuracy of PHITS for specific use in space dosimetry was well verified by calculating neutron spectra inside the space shuttle and doses inside anthropomorphic phantoms using simplified geometries of spacecraft (Ref. [1]). An example specifically related to space applications is provided below.

As described in Ref. [35], a shielding problem of a spacecraft has been evaluated by means of PHITS. Trapped and GCR protons, albedo neutrons from the Earth's atmosphere, and heavy ion with charges up to 28 and energy up to 100 GeV/u were considered as source particles. The spectrum of albedo neutrons was also calculated by means of PHITS by simulating the earth atmosphere based on the charge particles spectra outside of the earth. The calculated neutron spectra in an imaginary vessel were compared with orbit-averaged data from measurements. An excellent agreement was observed between the calculated and experimental results, particularly for neutron energies above 1 MeV which is very important in the evaluation of dose for astronauts.

More information on PHITS, including its latest developments and improvements, can be found in the following reference: [34], [35], [36], [37].

Having discussed the Monte Carlo approach (§6.4.1) and the multi-purpose Monte Carlo code PHITS (§6.4.2), the next chapter (§6.4.3) will elaborate on the input parameters considered for radiation transport calculations by means of PHITS.

6.4.3. Input parameters for modelling in PHITS

This chapter describes the modelling input parameters considered in PHITS. The following aspects are discussed in the order as presented below:

- Geometry (§6.4.3.1);
- Shielding materials (§6.4.3.2);
- Source terms (§6.4.3.3);
- Material compositions, densities and shielding thicknesses (§6.4.3.4);
- Parameter section (§6.4.3.5);
- Tallies (§6.4.3.6).

6.4.3.1. GEOMETRY

In space, spherical and anthropomorphic phantoms are typically used to measure dose distributions in the human body. For numerical dose calculations, spherical phantoms[93] are however easier to model and require less computational time in comparison with human voxel phantoms.

In fact, Matthiä et al. (Ref. [8]) investigated the applicability of a water sphere of radius 20 cm as a surrogate for anthropomorphic phantoms and estimated organ doses for isotropic irradiation from GCR in LEO. By comparing the calculated organ absorbed dose and dose equivalent rates in the spherical and voxel phantoms, it was found that these quantities differed by less than 5% and 11%, respectively.

Hence, in this work, a homogenised[94] spherical water phantom with a fixed radius of 25 cm was used as a surrogate for the human body (cf. Ref. [8], [30]). Figure 25 below provides a 2D view of the unshielded water sphere and its surroundings.

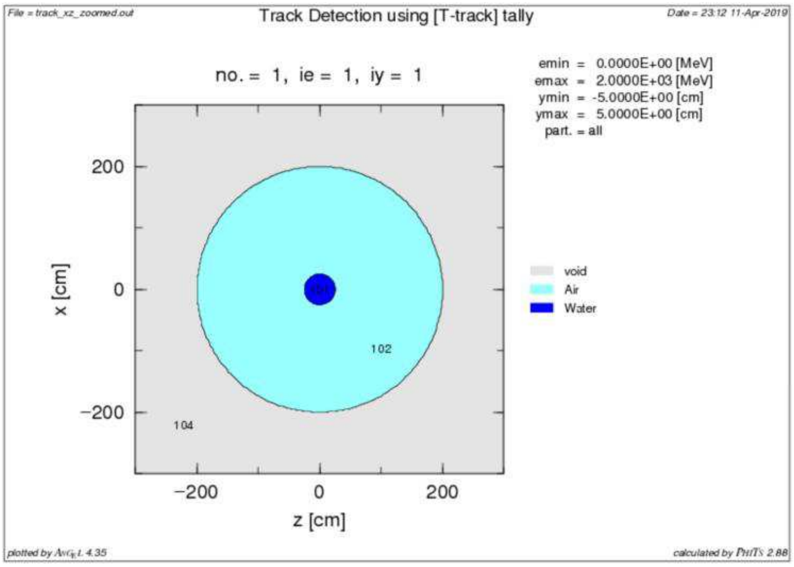

Figure 25: 2D view of the unshielded water sphere and its surroundings as modelled in PHITS

[93] Organ doses from spherical phantoms can be derived from computed values at points inside the sphere where the mean shielding equals the mean shielding of the organs inside the human body (Ref. [8]).

[94] Constant density distribution (discussed in §6.4.3.4).

As illustrated in Figure 25 above, the spherical water phantom (radius 25 cm) is surrounded by a spherical volume of air with a radius of 200 cm, representing the habitable area inside the spacecraft. The empty space environment outside of the spacecraft is defined as void.

The objective of this work consists of evaluating the shielding efficiency of different materials against GCR and SPE. Hence, shielding is to be positioned in between the air volume and the space environment (void). In PHITS, the spherical shields are coded considering a fixed inner radius of 200 cm while varying the outer radius in function of the desired thickness. Hence, the shielding thickness is calculated as the difference between both radii. Figure 26 below illustrates the setup considering a spherical Al shield with a thickness of 14.82 cm (i.e. outer radius of 214.82 cm).

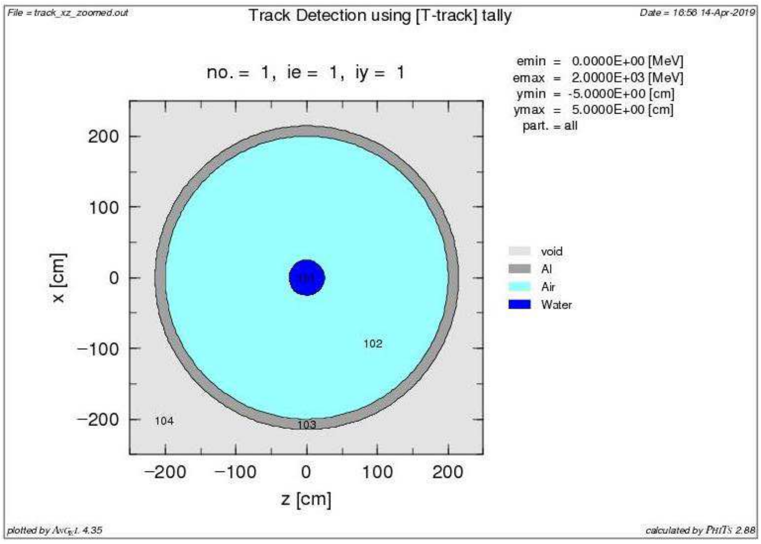

Figure 26: Example of a geometrical setup considering a spherical Al shield with a thickness of 14.82 cm

For illustrational purposes, Figure 28 below provides a 3D view of Figure 26.

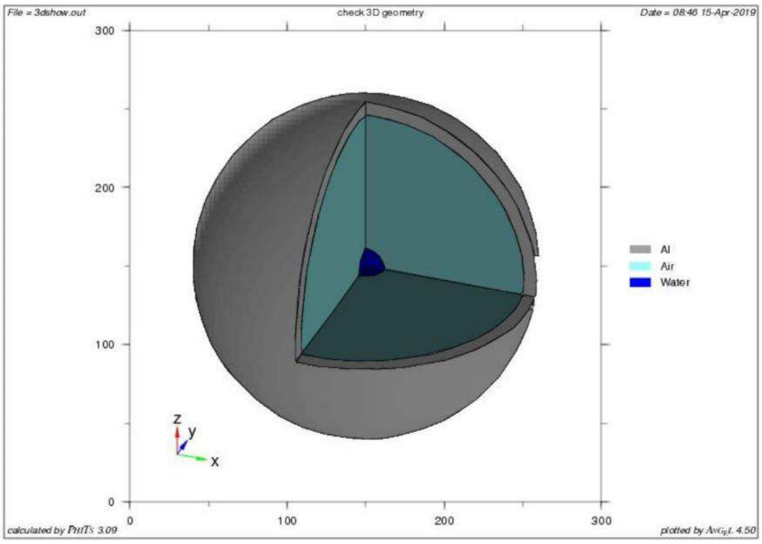

Figure 27: 3D representation of Figure 26

Note that for intellectual and proprietary reasons, no PHITS input files have been appended to this work. The author and/or mentors (SCK•CEN) can be contacted to obtain specific information on the actual PHITS input files used in this work.

6.4.3.2. SHIELDING MATERIALS

As extensively discussed in §3.3, in the past, mainly Al has been considered as material to shield against the radiation fields prevailing in space.

However, for space shielding purposes, it is recommended to use materials with **light constituent atoms** such as hydrogen since they are most efficient per mass of material at slowing down ions, attenuating heavy ion fluences through projectile fragmentation, and minimizing the build-up of neutrons and other target fragments produced directly from the atoms of the shielding material by nuclear interactions.

Hence, this thesis will focus on investigating the shielding efficiency against GCR and SPE by considered the following shielding materials (Table 14):

Category	Material	Justification of choice
Non-light material	Aluminium	Reference non-light material
Light materials	Liquid H	• Theoretically the best shielding (Ref. [49]) • Not practicable (Ref. [49]) – difficult to store and explosion risk
	Liquid H_2O	• Theoretically yields good shielding • Practically more feasible than H
	Non-borated polyethylene	• High practical usage • Higher Z_{eff} decreases the efficiency
	Borated polyethylene	• High practical usage • Compared to non-borated PE, the high thermal neutron σ_{abs} of B might capture the slowed down secondary neutrons (Ref. [49])
Compound	Outwards: 50% Aluminium Inwards: 50% Borated-PE	• Al is considered to shield against SPE • Borated-PE is considered to shield against GCR and slow down (PE) and capture (B) secondary neutrons

Table 14: Shielding materials considered in this work

Having the shielding materials defined, it should be noted that there exists a subtle difference in expressing the shielding materials in space as compared to on Earth.

On Earth, shielding is often expressed by the density (g cm^{-3}) of the material. For space applications, shielding is typically expressed as an areal density (g cm^{-2}), corresponding to the density integrated over the thickness of the shielding. For H_2O (density 1 g cm^{-3}), the numerical value of the areal density in g cm^{-2} is equivalent to the shielding thickness in cm. For materials with a higher density, the shielding thickness is smaller, and vice versa. In fact, the shielding efficiency is related to the mass of the traversed material rather than to its geometrical thickness, making the areal density a preferred parameter. For example, the thickness of an Al layer (2.7 g cm^{-3}) would only be ~1/3 of that of water with the same areal density.

In literature (Ref. [3], [4], [8], [30], [50]), the areal densities as presented in Table 15 below are often considered since most of them correspond to typical shielding structures considered in space travel:

Areal density	Shielding structure
0.3 g cm^{-2}	Light spacesuit
1 g cm^{-2}	Nominal spacesuit
2 g cm^{-2}	Lightly shielded spacecraft
5 g cm^{-2}	Nominal spacecraft
10 g cm^{-2}	SPE storm shelter (min)
20 g cm^{-2}	SPE storm shelter (max)
40 g cm^{-2}	/

Table 15: Overview of areal densities typically considered in space travel

Based on the densities of the shielding materials (described in §6.4.3.4) one can easily calculate which thickness of a certain material is required to obtain the areal densities, as defined in Table 15 above. The thicknesses of the shielding materials (expressed in cm) as considered in PHITS will be reported in §6.4.3.4.

6.4.3.3. SOURCE TERMS

The source term (i.e. spectral) data considered as input for the radiation transport calculations has been discussed in §6.2. A summary is provided below:

- **GCR** (§6.2.1 – Table 9):
  - Solar Min: 2010;
  - Solar Max: 2001.
- **SPE** (§6.2.2 – Table 12):
  - August 1972 (LaRC);
  - Sum of October 1989 Tylka Band fits.

The following source parameters were considered:

- In terms of geometry, the radiation source has a spherical shape (s-type = 10) and is positioned closely around (at 1 cm from) the thickest shield of the considered shielding material, hence fully enveloping the shield, the target and the air in between (no off-set in the X, Y or Z-direction). The inner and outer radius of the source are equal, implying that the source has no thickness;
- The source terms, as provided by OLTARIS, are (Free-Space) fluxes (GCR) or fluences (SPE) in function of the energy. Hence, the source terms are defined as differential probabilities in function of the energy bins (e-type = 21);
- In terms of direction of the emitted source particles (parameter “Dir” in PHITS), there are four options available in PHITS and presented in Table 16 below.

	Emission of source particles
Dir = all	Isotropic – inwards and outwards direction
Dir = -all	Isotropic – only inwards direction
Dir = 1	From the centre with normal line – outwards direction
Dir = -1	From the centre with normal line – inwards direction

Table 16: Directions of the emitted source particles available in PHITS

Figure 28 below illustrates the different options in terms of directional particle emission (Table 16) for an unshielded water sphere (source type is irrelevant). The location of the spherical source is indicated by the dashed circle (dark blue).

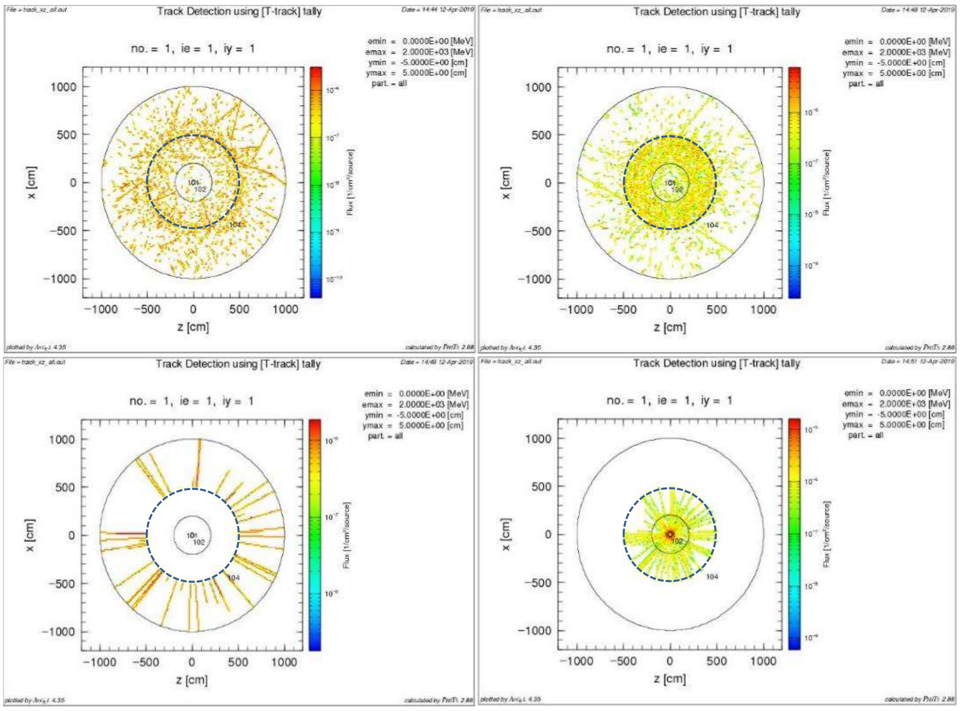

Figure 28: Top left: Dir = all – Top right: Dir = -all – Bottom left: Dir = 1 – Bottom right: Dir = -1

Note that in the actual transport calculations, the source is positioned closely around (at 1 cm from) the thickest shield of the considered shielding material. In Figure 28 above, the source has been fixed at a radial distance of 500 cm as otherwise the particle tracks could not have been visualized as clearly.

It is clear that the options Dir = all and Dir = 1 are not desired because:

- If Dir = all, a large amount of particles will be emitted isotropically in directions which will not contribute to the scoring of the dose in the water sphere. Also, the simulation time is significant while the statics are rather poor;
- If Dir = 1, all particles will be emitted from the centre with normal line, but in opposite direction of the water sphere (target). This is obviously not desired.

Consequently, the options Dir = -all and Dir = -1 are most favourable:

- Dir = -all is most desired as this scenario is best in line with the actual space environment (i.e. fully isotropic emission of particles). The drawback of this option is that the simulation time, especially in the case of GCR, could be considerably high while the statistics could be rather poor.
- Dir = -1 provides better statistics within shorter simulation times compared to Dir = -all as all the primary particles are forced to be emitted on a normal line in the direction of the centre of the water sphere. Nevertheless, due to the forced particle emission, the representativeness of the results is strongly questionable. Additionally, all emitted sources particles would cross exactly the same amount of shielding material, which also happens to represent the thinnest shielding. Although one might refer to this scenario as conservative, it is, due to its features, rather considered as meaningless in this work.

Hence, based on the reasoning as provided here above, the option Dir = -all has been selected for all simulations performed in the framework of this work.

6.4.3.4. MATERIAL COMPOSITIONS, DENSITIES AND SHIELDING THICKNESSES

The geometrical setup of the target, its surrounding environment and the shielding materials considered have been discussed in §6.4.3.1 and §6.4.3.2.

To distinguish between the different types of materials, it is required to define their chemical compositions and densities as these characteristics influence the types of interaction occurring.

Table 17, Table 18 and Table 19 tabulate the chemical compositions and densities of the target, the surroundings and shielding materials, respectively.

Material	Composition (weight %)		Density (g cm^{-3})	Reference
Water sphere	H O	0.111894 0.888106	1.00000	Standard value

Table 17: Chemical composition and density of the target material

Material	Composition (weight %)		Density (g cm^{-3})	Reference
Air	^{12}C ^{14}N ^{16}O ^{40}Ar	0.000124 0.755267 0.231781 0.012827	1.20479E-3	[51]
Void	/		/	/

Table 18: Chemical compositions and densities of the surrounding environment

Material	Composition (weight %)		Density (g cm^{-3})	Reference
Aluminium	Al	1.000000	2.69890	[51]
Liquid H	H	1.000000	0.07085	[52]
Liquid H_2O	H O	0.111894 0.888106	0.99821	[51]
Non-borated polyethylene	H C	0.143716 0.856284	0.93000	[51]
Borated polyethylene	H B C	0.125355 0.100000 0.774645	1.00000	[51]
Outwards: 50% Aluminium Inwards: 50% Borated-PE	Al H B C	1.000000 0.125355 0.100000 0.774645	Al: 2.69890 B-PE: 1.00000	[51]

Table 19: Chemical compositions and densities of the shielding materials

Based on the material densities (Table 19) and the areal densities (Table 15), the shielding thicknesses (cm) of the different shielding materials can be calculated. The results are presented in Table 20 below.

	Shielding thickness (cm)						
Areal density (g cm^{-2})	**Al**	**Liquid H**	**Liquid H_2O**	**Non-B PE**	**B PE**	**50% Al**	**50% PE-B**
0.3	0.11	4.23	0.30	0.32	0.30	0.06	0.15
1.0	0.37	14.11	1.00	1.08	1.00	0.19	0.50
2.0	0.74	28.23	2.00	2.15	2.00	0.37	1.00
5.0	1.85	70.57	5.01	5.38	5.00	0.93	2.50
10.0	3.71	141.14	10.02	10.75	10.00	1.85	5.00
20.0	7.41	282.29	20.04	21.51	20.00	3.71	10.00
40.0	14.82	564.57	40.07	43.01	40.00	7.41	20.00

Table 20: Shielding thicknesses (cm) of the different shielding materials

Together with the geometrical and the source data, the data presented in Table 17, Table 18, Table 19 and Table 20 were used to prepare the different input files.

A two-dimensional view of the compound made up out of 50% aluminium and 50% borated polyethylene and its surroundings, as modelled in PHITS, is visualized in Figure 29 below as the latter can be seen as a special case compared to the other non-compound materials. In the example, thicknesses for an areal density of 40 g cm^{-2} are illustrated, i.e. 7.41 cm Al and 20 cm Borated-PE.

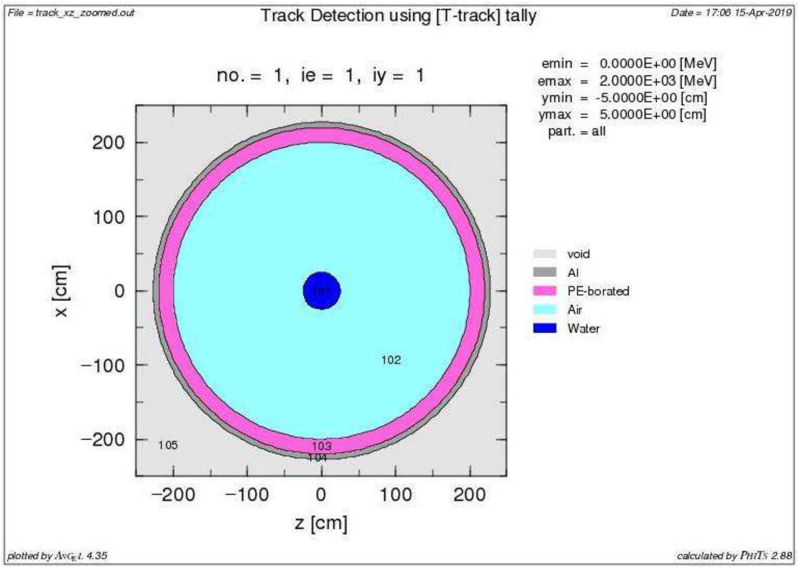

Figure 29: 2D view of the compound (50% Al – 50% B-PE) with areal density of 40 g cm^{-2} as modelled in PHITS

6.4.3.5. PARAMETER SECTION

The main objective of the parameter section is to define:

- The simulation mode;
- The number of particles/batches;
- The nuclear libraries;
- The modelling parameters (nuclear reaction models, particle transport, etc.).

Indeed, it is clear that the choice of the parameters strongly impact the simulations in terms of results, accuracy, computational time, etc. It is therefore of paramount importance that all the parameters relevant for radiation transport calculations in a space environment are included in this section.

Without stepping into detail, the following nuclear physics models were activated in each PHITS simulation performed in this work (also for benchmarking purposes as will be described in §7.2): ATIMA (charged particles and nucleus interactions), Sato's nucleon-nucleus collisions, photo-nuclear reactions, coulomb diffusion (i.e. angular straggling), muon capture and muon-induced nuclear reactions, γ decay for residual nuclei, low energy neutron interactions, JQMD-2.0. Elaborating on the parameters and explaining the physics behind each model is considered to be out of scope of this work. Note that some modelling parameters have been defined based on 'trial and error' (with physics reasoning) and have been optimized during the GCR/SPE benchmarking phase (§7.2). Once optimized, the parameters have been fixed for each PHITS simulation performed. Lastly, in each PHITS simulation a cutoff energy of 1 MeV/u for all source particles was considered (except for GCR benchmarking as will be described in §7.2.1).

As mentioned earlier, for intellectual and proprietary reasons, no PHITS input files have been appended to this work. The author and/or SCK•CEN can be contacted to obtain specific information on the parameters used in this work.

6.4.3.6. TALLIES

In PHITS, tallies are mainly used for the following two reasons:

- Performing a geometry check (in 2D or 3D);
- Scoring a certain quantity such as, e.g., dose, flux, LET, etc.

Although in PHITS the user can select between many different types of tallies, the following tallies have been used in the framework of this work:

- [T – Track]
  This tally is used to provide information on the fluence inside the water sphere. The track length is evaluated each time a particle pass through the specified region and the sum of the track lengths, expressed in cm, is scored. Particle fluence in the unit 1/cm²/source is determined from the scored track lengths divided by the volume of the region and the number of source particles. This tally can also generate 2D views of the geometrical setup while tracking the particle fluxes, such as illustrated in Figure 25.
- [T – 3Dshow]
  This tally is used to generate a 3D view of the geometrical setup. As shown in Figure 27, the so-called “eye point” has been defined such that the inner part of the geometry (i.e. the target) is visualized.
- [T – Deposit]
  This tally is used to score dose quantities expressed in dose/simulated particle. The main advantage of this tally is that it can directly output the dose equivalent which is calculated based on the deposited energies and the $Q(L)$ relationship (discussed in §4.1.3). The drawback of this tally is that it can only score energy losses of charged particles and nuclei. Hence, by means of this tally, it cannot explicitly be demonstrated that, for example, the secondary neutrons produced by interaction of primary particles with the shield are (to a certain extent) slowed down and captured by the borated polyethylene. Nevertheless, the energy deposition of all (secondary) uncharged particles is included in the total dose scored since the uncharged particles transfer a part of their energy to charged particles, in which the latter is responsible for dose deposition. Consequently, the energy deposited by uncharged particles is taken into account by tracking their secondary particles.

The most important tallies defined in the PHITS input files are listed below:

- [T – Deposit]: scoring total D_T due to all particles;
- [T – Deposit]: scoring D_T distribution in function of depth in the water sphere;
- [T – Deposit]: scoring total $H_{T,Q}$ due to all particles;
- [T – Deposit]: scoring $H_{T,Q}$ distribution in function of depth in the water sphere;
- [T – Track]: scoring the fluence inside the water sphere.

7. EVALUATION OF SHIELDING EFFICIENCY

Evaluating the shielding efficiency of light (hydrogenous) materials against GCR and SPE is paramount for extended human presence in interplanetary space. The need for such studies increased significantly in the past years since many space agencies report to schedule extended trips beyond the Earth's magnetosphere in the near future. For manned space missions, it is essential to estimate the dose equivalent to evaluate the potential impact on the crew's health and performance.

The aim of this chapter is to evaluate the shielding efficiency of different materials against GCR and SPE. In a first step, the methodology for dose calculations will be addressed (§7.1). Next, it will be shown that the GCR and SPE radiation transport calculations performed in this work are benchmarked (§7.2). The outcome of the actual transport calculations will subsequently be discussed (§7.3), followed by a discussion on the thickness of a material required to reach Earthly dose rates in deep space (§7.4). Lastly, some general insights will be provided to better situate the results produced in this work (§7.5).

7.1. Methodology for dose calculation

In order to obtain dose results, it is required to post-process the data outputted by PHITS and OLTARIS. Note that while PHITS is used to perform the actual transport calculations (based on the input parameters described §6.4.3), OLTARIS is used to normalize the PHITS outputs to the model free-space boundary flux/fluence.

The following subchapters describe the approach followed to calculate the dose rate and the dose for GCR (§7.1.1) and SPE (§7.1.2), respectively.

7.1.1. GCR dose rate calculation

The following data obtained from PHITS and OLTARIS were used for calculating the GCR absorbed dose rate inside the **unshielded** water sphere:

Tally [T – Deposit]

$$\frac{D_{Total}\ (Gy)}{Simulated\ particle}$$

Tally [T – Track]

$$\frac{Flux_{Total}\ (1/cm^2)}{Simulated\ particle}$$

OLTARIS output

$$\frac{\#\ particles}{cm^2 - day - \frac{MeV}{amu}}$$

It is clear that the dose rate can be obtained as follows:

$$Dose\ rate\ (Gy/d) = \frac{\frac{D_{Total}\ (Gy)}{Simulated\ particle}}{\frac{Flux_{Total}\ (1/cm^2)}{Simulated\ particle}} * \sum_{j=1}^{m}\left[\sum_{i=1}^{n}\left(\frac{\#\ particles}{cm^2 - day - \frac{MeV}{amu}}\right)_i * \left(\left(\frac{MeV}{amu}\right)_i - \left(\frac{MeV}{amu}\right)_{i-1}\right)\right]$$

In which:

- i = energies as outputted by OLTARIS;
- j = particles as outputted by OLTARIS.

The latter formula can be rewritten as:

$$Dose\ rate\ (Gy/d) = \frac{D_{Total}\ (Gy)}{Flux_{Total}\ (1/cm^2)} * \frac{Total\ \#\ particles}{cm^2 - day}$$

Resulting in:

$$Dose\ rate\ (Gy/d) = \frac{D_{Total}\ (Gy) *\ Total\ \#\ particles}{day}$$

Note that this calculation methodology is only applied for the unshielded sphere. For the configurations in which the target (water sphere) is **shielded**, the calculations are performed relative with respect to the unshielded configuration[95]:

$$Dose\ rate\ (Gy/d)_{Shield\ N} = \frac{Dose\ rate\ (Gy/d)_{Unshielded}}{\left(\frac{D_{Total}\ (Gy)}{Simulated\ particle}\right)_{Unshielded}} * \left(\frac{D_{Total}\ (Gy)}{Simulated\ particle}\right)_{Shield\ N}$$

The same methodology was applied to obtain the GCR dose equivalent rate inside the water sphere by replacing $D_{Total}\ (Gy)$ by $H_{Total}\ (Sv)$ in the first formula of §7.1.1.

Notice that the dose results are expressed as dose rates when dealing with GCR. This makes sense as GCR is responsible for the permanent background radiation in space. In space, the dose (equivalent) rates are typically expressed in mGy/d (mSv/d) while on Earth they are usually expressed in mGy/h (mSv/h).

PHITS automatically provides the relative error (i.e. statistical uncertainty) of each quantity tallied, being the total dose and the total flux. These relative errors were then converted into absolute errors by means of the formulas presented below.

Absolute error $_{\text{Unshielded}}$:

$$Dose\ rate\ \left(\frac{Gy/Sv}{d}\right)_{Unshielded} * \sqrt{(Rel.\,error)^2_{\left(\frac{D_{Total}/H_{Total}}{Sim.\ particle}\right)_{Unshielded}} + (Rel.\,error)^2_{\left(\frac{Flux_{Total}}{Sim.\ particle}\right)_{Unshielded}}}$$

Absolute error $_{\text{Shielded}}$:

$$Dose\ rate\ \left(\frac{Gy/Sv}{d}\right)_{Shielded} * \sqrt{(Rel.\,error)^2_{\left(\frac{D_{Total}/H_{Total}}{Sim.\ particle}\right)_{Unshielded}} + (Rel.\,error)^2_{\left(\frac{Flux_{Total}}{Sim.\ particle}\right)_{Unshielded}} + (Rel.\,error)^2_{\left(\frac{D_{Total}/H_{Total}}{Sim.\ particle}\right)_{Shielded}}}$$

95 This approach simplifies the dose calculation efforts.

7.1.2. SPE dose calculation

The following data obtained from PHITS and OLTARIS were used for calculating the SPE absorbed dose inside the **unshielded** water sphere:

Tally [T – Deposit]	Tally [T – Track]	OLTARIS output
$\frac{D_{Total}\ (Gy)}{Simulated\ particle}$	$\frac{Flux_{Total}\ (1/cm^2)}{Simulated\ particle}$	$\frac{\#\ particles}{cm^2 - \frac{MeV}{amu}}$

It is clear that the dose can be obtained as follows:

$$Dose\ (Gy) = \frac{\frac{D_{Total}\ (Gy)}{Simulated\ particle}}{\frac{Flux_{Total}\ (1/cm^2)}{Simulated\ particle}} * \left[\sum_{i=1}^{n} \left(\frac{\#\ particles}{cm^2 - \frac{MeV}{amu}}\right)_i * \left(\left(\frac{MeV}{amu}\right)_i - \left(\frac{MeV}{amu}\right)_{i-1}\right)\right]$$

In which:

- i = energies as outputted by OLTARIS;
- There is no need to mention j as only data from ^1H is outputted by OLTARIS.

The latter formula can be rewritten as:

$$Dose\ (Gy) = \frac{D_{Total}\ (Gy)}{Flux_{Total}\ (1/cm^2)} * \frac{Total\ \#\ particles}{cm^2}$$

Resulting in:

$$Dose\ (Gy) = D_{Total}\ (Gy) * \ Total\ \#\ particles$$

Note that this calculation methodology is only applied for the unshielded sphere. For the configurations in which the target (water sphere) is **shielded**, the calculations are performed relative with respect to the unshielded configuration[96]:

$$Dose\ (Gy)_{Shield\ N} = \frac{Dose\ (Gy)_{Unshielded}}{\left(\frac{D_{Total}\ (Gy)}{Simulated\ particle}\right)_{Unshielded}} * \left(\frac{D_{Total}\ (Gy)}{Simulated\ particle}\right)_{Shield\ N}$$

The same methodology was applied to obtain the SPE dose equivalent inside the water sphere by replacing $D_{Total}\ (Gy)$ by $H_{Total}\ (Sv)$ in the first formula of §7.1.2.

Notice that the dose results are expressed as doses when dealing with SPE. This can be explained by the fact that SPEs last for a few hours or days, giving rise to an exposure limited in time.

[96] This approach simplifies the dose calculation efforts.

PHITS automatically provides the relative error (i.e. statistical uncertainty) of each quantity tallied, being the total dose and the total flux. These relative errors were then converted into absolute errors by means of the formulas presented below.

Absolute error $_{\text{Unshielded}}$:

$$Dose\ (Gy/Sv)_{Unshielded} * \sqrt{(Rel.error)^2_{\left(\frac{D_{Total}/H_{Total}}{Sim.\ particle}\right)_{Unshielded}} + (Rel.error)^2_{\left(\frac{Flux_{Total}}{Sim.\ particle}\right)_{Unshielded}}}$$

Absolute error $_{\text{Shielded}}$:

$$Dose\ (Gy/Sv)_{Shielded} * \sqrt{(Rel.error)^2_{\left(\frac{D_{Total}/H_{Total}}{Sim.\ particle}\right)_{Unshielded}} + (Rel.error)^2_{\left(\frac{Flux_{Total}}{Sim.\ particle}\right)_{Unshielded}} + (Rel.error)^2_{\left(\frac{D_{Total}/H_{Total}}{Sim.\ particle}\right)_{Shielded}}}$$

7.2. Benchmarking

As discussed in §6, the precision of the simulated results depends on the validity of the physical models used in the transport code, the level of detail of the target geometry and its environment, and on the models specifying the composition and spectra of the different components of the radiation field.

It is therefore crucial to validate the correctness of the developed PHITS transport codes and the methodology used for dose calculations (§7.1) by benchmarking the output to literature or to validated dose calculation tools. Subchapters §7.2.1 and §7.2.2 will describe the benchmarking process for GCR and SPE, respectively.

7.2.1. GCR

For GCR, the dose (equivalent) rates obtained by post-processing the PHITS and OLTARIS outputs were benchmarked to the dose (equivalent) rates extracted from Figure 30 below, which originates from Ref. [8] (Figure 4 of Ref. [8]).

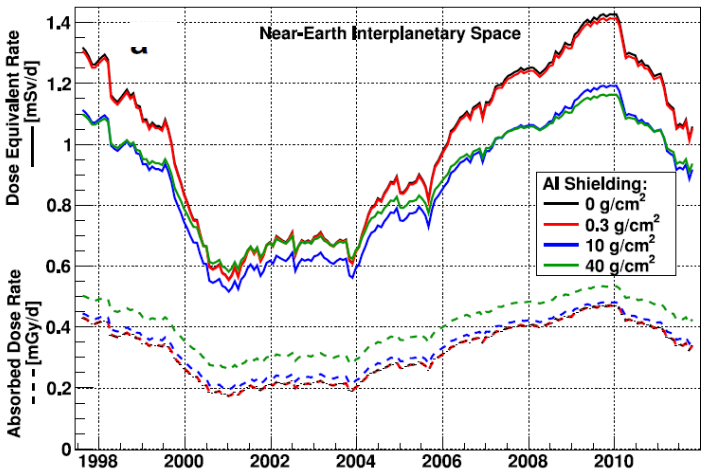

Figure 30: Absorbed dose rates (dashed lines) and dose equivalent rates (solid lines) in a water sphere with varying shield thicknesses for near-Earth interplanetary space, calculated by applying the Matthïa/ACE model (Ref. [8])

Indeed, in Figure 30, the dose (equivalent) rates are provided for different years. However, for benchmarking purposes, only the data corresponding to the Solar Min of 2010 and the Solar Max of 2001 were considered (cf. §6.4.3.3).

Ref. [8] was used for benchmarking purposes since the setup considered for the radiation transport calculations was similar to the one considered in this work. The main modelling parameters considered in Ref. [8] are summarized below:

- In terms of geometry, a spherical water phantom with a radius of 25 cm was used as a surrogate for the human body to estimate the radiation exposure;
- The dose quantities were calculated over the entire water sphere. To calculate the absorbed dose, the summation of the energy deposited at each step along a particle's trajectory in the sphere was divided by its mass, and to calculate the dose equivalent, the summation of the energy deposited weighted by the quality factor for each step was divided by the mass of the sphere;
- Ions ranging from H to Fe were isotropically emitted from a spherical radiation source inwards onto the water sphere with and without Al shielding;
- A cutoff energy of 10 MeV/u was considered for all source particles;
- The spherical shields employed entirely surrounded the target sphere with an outer radius of 50 cm with varying thicknesses corresponding to areal densities 0.3, 10, and 40 g/cm². The space between the Al shield and the target is air;
- The Matthiä model (§5.1.2) generated the spectra of the relevant particles.

Some noteworthy differences in terms of the setup were even so observed:

- In Ref. [8], the Monte Carlo transport code GEANT4 was used for performing the radiation transport calculations. In this work, PHITS (§6.4.2) was used for the latter purpose;
- In Ref. [8], the following physics models were activated: QGSP_BERT_HP, emstandard_opt3, JQMD/JAM. The physics models activated in this work are defined in §6.4.3.5. In contrast to the cutoff energy stated in §6.4.3.5 (1 MeV/u), a cutoff energy of 10 MeV/u was considered in PHITS for all source particles to be better in line with the setup considered in Ref. [8];
- In Ref. [8], it is likely that the source code of the Matthiä model (§5.1.2) was used to generated the GCR spectra while in this work the Matthiä GCR spectra were generated by and extracted from OLTARIS;
- In Ref. [8], the source particles (ions) range from H to Fe while in this work the source particles (ions) range from H to Ni. Also, in Ref. [8] it is not specified at which position the source is situated (e.g. at 1 cm from the outer shield, etc.);
- In Ref. [8], the shielding **outer** radius is fixed and equal to 50 cm while in this work the shielding **inner** radius is fixed and equal to 200 cm. Consequently, in Ref. [8] the shields are added in the inwards direction (towards the target), while in this work the shields are added in the outwards direction (towards the void). Hence, in Ref. [8], the volume of air in between the shield and the target reduces with increasing shielding thickness while in this work the air remains constant. The disadvantage of the approach adopted in this work is that particles could more easily 'get lost' in the larger air volume compared to the setup in Ref. [8]. Note however that in this work it was chosen to consider shields with a fixed inner radius (200 cm) since the fixed volume of air in between the target and the shields represents the fixed habitable area inside the spacecraft.

Because the geometry in terms of the considered volume of air and the approach of inwardly introducing shields are remarkably different than those adopted in this work, it has been chosen, solely for benchmarking purposes, to align the geometry and shielding approach adopted in this work to the latter's considered in Ref. [8].

Figure 31 below illustrates the geometrical setup defined in PHITS, as considered in Ref. [8]. More particularly, Figure 31 illustrates the scenario in which 40 g/cm² of Al shielding was inwardly employed (i.e. direction towards the target). Note that 40 g/cm² of Al corresponds to a thickness of ~14.82 cm, giving rise to an air gap of ~10.18 cm (50 cm (fixed outer radius) – 25 cm (water sphere) – 14.82 cm (Al)).

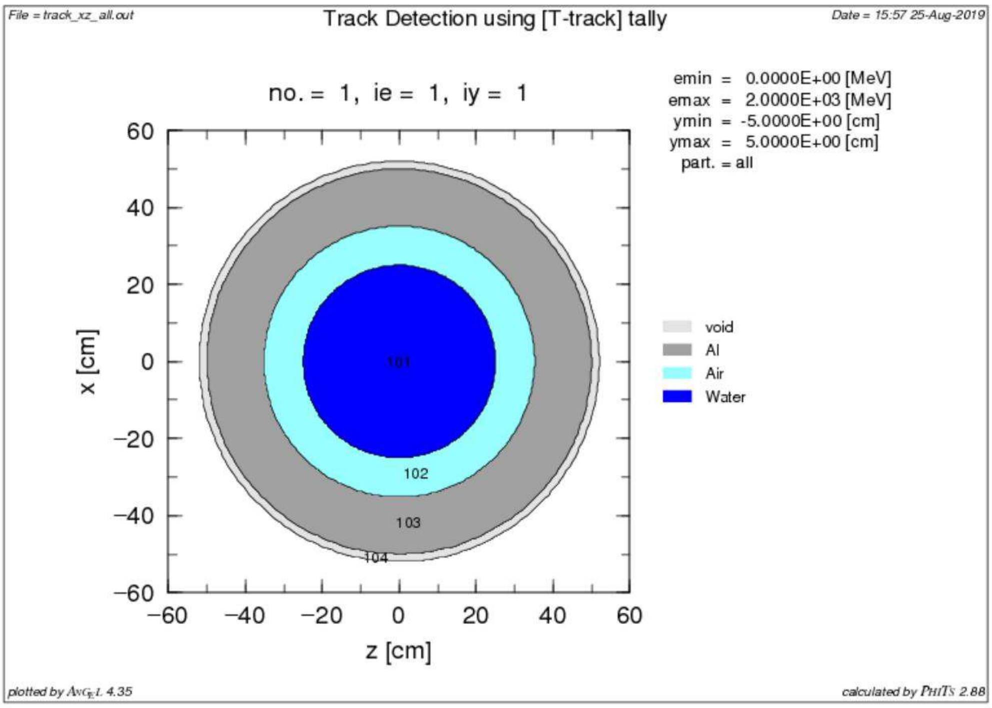

Figure 31: Geometrical setup as defined in Ref. [8] for the configuration with 40 g/cm² of Al shielding

As in Ref. [8] the position of the spherical radiation source was not defined, it was chosen to fix the latter on a radial distance of 51 cm from the center (outwardly at 1 cm from the shield and inwardly at 1 cm from the outer void). Furthermore, the amount of source particles considered in Ref. [8] was not defined. Hence, in PHITS, 1E6 source particles were used to have a good balance between the statistics (largest Monte Carlo rel. error < 5%) and the computational time (< 5 h).

Results

Figure 32 (Solar Min 2010) and Figure 33 (Solar Max 2001) below plot the dose (equivalent) rates obtained by post-processing the PHITS and OLTARIS outputs (solid lines) and by extracting the latter's for the same areal densities from Figure 30 (dotted lines). Indeed, only four data points (shielding configurations) could be extracted from Ref. [8], as can be derived from Figure 30.

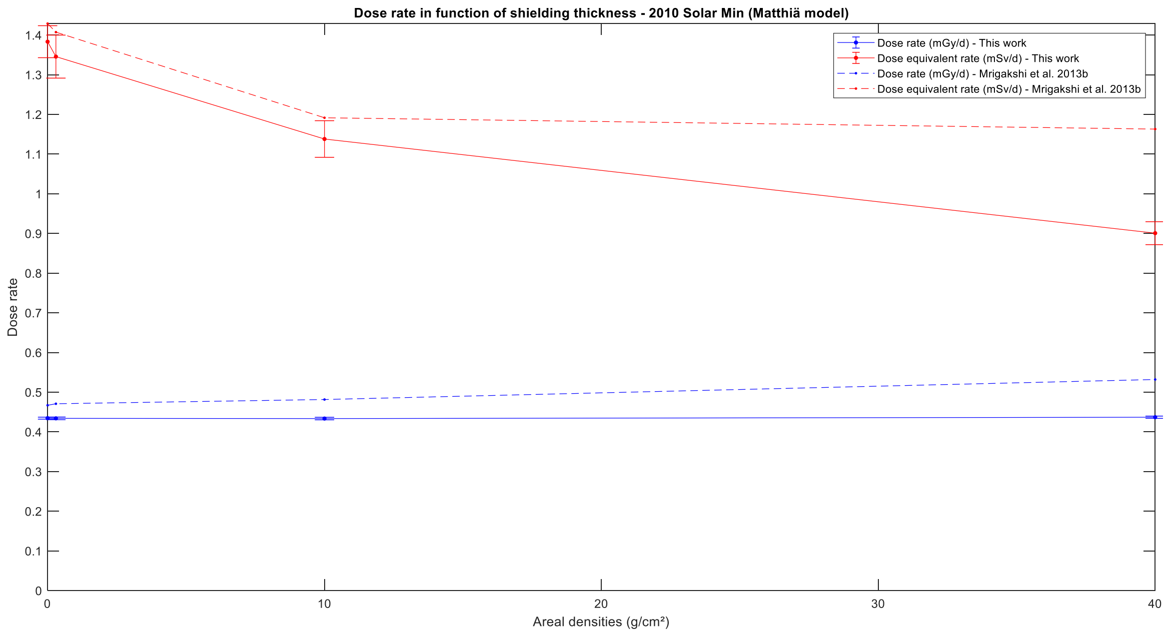

Figure 32: $\dot{D}$ (mGy/d) and $\dot{H}$ (mSv/d) for Al shielding obtained by post-processing the PHITS and OLTARIS outputs (solid lines) and by extracting data from Figure 30 of Ref. [8] (dotted lines) for the 2010 Solar Min

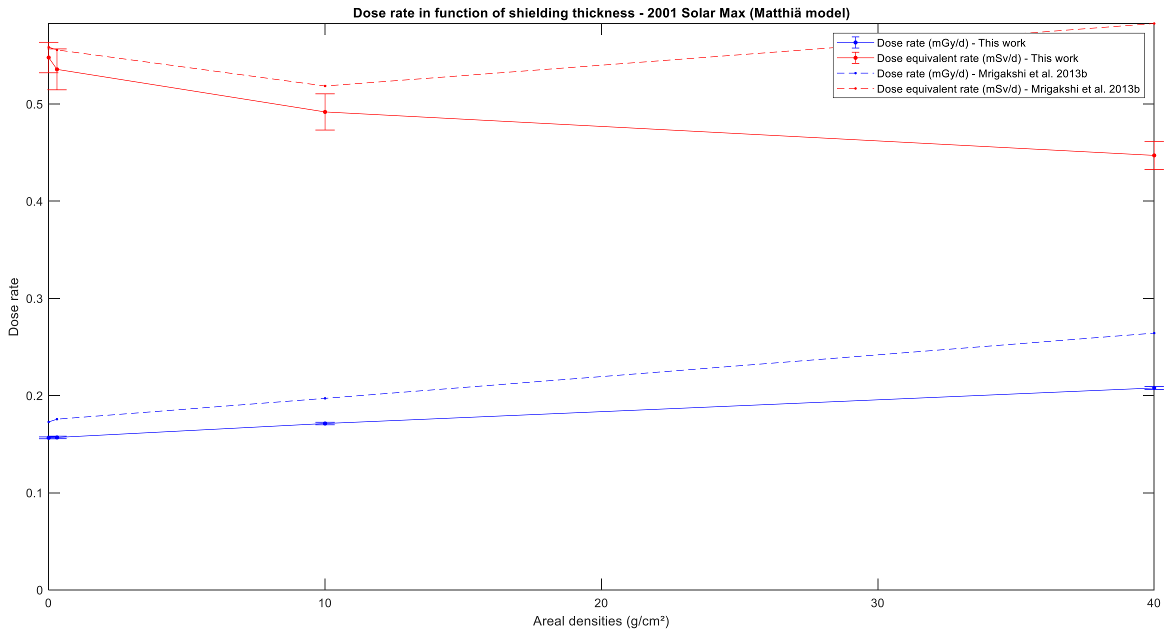

Figure 33: $\dot{D}$ (mGy/d) and $\dot{H}$ (mSv/d) for Al shielding obtained by post-processing the PHITS and OLTARIS outputs (solid lines) and by extracting data from Figure 30 of Ref. [8] (dotted lines) for the 2001 Solar Max

Table 21 (Solar Min 2010) and Table 22 (Solar Max 2001) below tabulate the numerical values of the dose (equivalent) rates for the four data points available (deviation relative to the results extracted from Ref. [8]). Based on Figure 32 and Figure 33 above, it can be observed that the error bars (absolute errors) on the dose quantities are small and thus not explicitly tabulated in Table 21 and Table 22. The absorbed dose rate ($\dot{D}$) and the dose equivalent rate ($\dot{H}$) are given in mGy/d and mSv/d, respectively, while the quality factor (Q) is dimensionless.

	Results produced in this work			Results extracted from Ref. [8]			Deviation rel. to Ref. [8] (%)		
g/cm²	$\dot{D}$	$\dot{H}$	Q	$\dot{D}$	$\dot{H}$	Q	$\dot{D}$	$\dot{H}$	Q
0	4.35E-01	1.38E+00	3.18E+00	4.67E-01	1.43E+00	3.06E+00	7	3	4
0.3	4.34E-01	1.35E+00	3.10E+00	4.71E-01	1.41E+00	2.99E+00	8	4	4
10.0	4.34E-01	1.14E+00	2.63E+00	4.82E-01	1.19E+00	2.47E+00	10	4	6
40.0	4.37E-01	9.01E-01	2.06E+00	5.32E-01	1.16E+00	2.19E+00	18	23	6

Table 21: Summary of $\dot{D}$ (mGy/d), $\dot{H}$ (mSv/d) and Q for the Solar Min of 2010

	Results produced in this work			Results extracted from Ref. [8]			Deviation rel. to Ref. [8] (%)		
g/cm²	$\dot{D}$	$\dot{H}$	Q	$\dot{D}$	$\dot{H}$	Q	$\dot{D}$	$\dot{H}$	Q
0	1.57E-01	5.48E-01	3.50E+00	1.73E-01	5.59E-01	3.23E+00	9	2	8
0.3	1.57E-01	5.36E-01	3.41E+00	1.76E-01	5.56E-01	3.16E+00	11	4	8
10.0	1.71E-01	4.92E-01	2.87E+00	1.97E-01	5.19E-01	2.63E+00	13	5	9
40.0	2.08E-01	4.47E-01	2.15E+00	2.64E-01	5.83E-01	2.21E+00	21	23	2

Table 22: Summary of $\dot{D}$ (mGy/d), $\dot{H}$ (mSv/d) and Q for the Solar Max of 2001

Conclusions

The dose (equivalent) rates obtained by post-processing the PHITS and OLTARIS outputs are well in line with the latter's extracted from Figure 30 (Ref. [8]). The same holds true for the derived quality factors. Considering the differences in the setup (as discussed above), the following conclusions are drawn (Solar Min/Max):

- Similar trends are observed for $\dot{D}$ and for $\dot{H}$ (Figure 32, Figure 33);
- Small deviations[97] are observed for $\dot{D}$, $\dot{H}$ and Q (Table 21, Table 22);

The results for the Solar Min of 2010 appear to be better in line with literature (Ref. [8]) than those for the Solar Max of 2001. Nevertheless, the general conclusions are valid for the Solar Min of 2010 and for the Solar Max of 2001.

These satisfying results give rise to a high level of confidence in terms of:

- Definition of the complex multi-source source term in PHITS;
- Selection of the parameter settings (reaction models, etc.) in PHITS;
- Definition of the geometry and the (shielding) materials in PHITS;
- Application of a methodology for converting the tally output provided by PHITS (dose/source and flux/source) to absolute dose rates.

[97] The amount of source particles considered per simulation significantly impacts the error bars (solid curves). Due to time constrains, it was concluded that the results are sufficiently accurate for this work (largest Monte Carlo rel. error < 5%). Note that no error bars are plotted on the dashed curves as no errors are provided in Figure 30 (Ref. [8]).

7.2.2. SPE

For SPE, in contrast to GCR (§7.2.1), no literature was found which considered a setup similar to the one considered in this work (§6.4.3.1).

Because of this, it was attempted to use OLTARIS for performing dose calculations in function of different shielding thicknesses. These results could then be used for benchmarking purposes. Unfortunately, the results produced with OLTARIS were incomparable to the results produced by PHITS as OLTARIS is only able to score the dose in a tissue equivalent point (of undocumented radius[98]) while in this work the dose is scored in a water sphere with a radius of 25 cm. Multiple attempts were made to reconstruct the point-geometry as considered by OLTARIS using PHITS, but without desirable results[99]. The fact that multiple parameters used by OLTARS were not known (e.g. target/source geometry, source distance/particles, physics models) could explain the poor agreement. Also, the fact that the setup considered in this work required significant modifications in an attempt to mimic OLTARIS led us further away from the situation actually to be benchmarked.

Like NASA developed OLTARIS (§6.2), ESA even so developed a free online tool called SPENVIS[100] (SPace ENVironment Information System) that can model the space environment and its effects. The big advantage of SPENVIS over OLTARIS is that in SPENVIS the geometry considered in this work could be reconstructed.

The SPENVIS tool can be used to perform radiation shielding analyses in space by means of two built-in GEANT4-based simulation platforms called "MULASSIS" (Multi-Layered Shielding Simulation Software) and "GRAS" (GEANT4 Radiation Analysis for Space)[101]. A brief description of both platforms is provided below (details are provided on their website):

- MULASSIS enables to define a multi-layered 1D shield and an incident particle source. Using the GEANT4 toolkit, it can simulate radiation transport through the 1D geometry, treating both electromagnetic and nuclear interactions. Upon completion of the simulation, MULASSIS can provide, among other features, the energy deposition or ionizing dose in the selected layer(s);
- GRAS is a GEANT4-based toolkit that can perform space radiation analyses for 3D geometries. More specifically, GRAS enables to define a multi-volume 3D geometry (MULASSIS-like geometries could also be defined) and incident particle sources. GRAS can simulate radiation transport through a 3D geometry, treating both electromagnetic and nuclear interactions. Upon completion of the simulation, GRAS can provide, among other features, the energy deposition or ionizing dose in the selected layer(s).

Based on the description above, it is clear that the setup in GRAS is more in line with the setup coded in PHITS since the geometries are both three-dimensional.

98 Despite that NASA was contacted multiple times in an attempt to better understand the setup considered in OLTARIS.
99 The most desirable results were obtained for the unshielded tissue equivalent sphere with r = 1 nm in which deviations of ~12% and ~25% from OLTARIS were observed for the absorbed dose and the dose equivalent, respectively.
100 https://www.spenvis.oma.be/
101 MULASSIS and GRAS can both be executed remotely without the need of locally installing GEANT4 and without the need of having the MULASSIS and GRAS source codes.

Nevertheless, the dose results produced by GRAS (3D) as well as by MULASSIS (1D) will be used for benchmarking purposes (i.e. comparison to the dose results obtained by post-processing the PHITS and OLTARIS outputs). As stated earlier, SPENVIS can reconstruct the same geometry[102] as coded in PHITS (§6.4.3.1).

In terms of SPE spectral data, SPENVIS is only equipped with the 1972 King SPE. Because of this, although other SPE data will be used for evaluating the shielding efficiency (defined in §6.4.3.3), PHITS simulations were performed using the 1972 King SPE spectral data specifically for benchmarking purposes. Furthermore, the PHITS simulations were performed with the 1972 King SPE data extracted from OLTARIS, but also with the 1972 King SPE data extracted from SPENVIS. Using both datasets as source input in PHITS allows to demonstrate that both source terms (should) give rise to very similar dose results. The spectral data from NASA (OLTARIS) and ESA (SPENVIS) both only consider a proton as source particle. The inwardly emitting isotropic source was positioned at the same location in PHITS as in GRAS[103] (radially at 240 cm from the center). Because of SPENVIS server time restrictions, the same amount of source particles considered in PHITS could not be used in GRAS and in MULASSIS. The highest amount of source particles were selected for the GRAS (1E5) and MULASSIS (1E7) simulations, while the PHITS simulations were performed with 1E8 particles (so that the rel. errors < 5%).

In GRAS and MULASSIS, it is not possible (at least not through the web interface) to manually adapt all modelling parameters to those considered in PHITS (e.g. reaction models, cutoff energies, etc.). The physics models activated in this work are defined in §6.4.3.5. A cutoff energy of 1 MeV/u was considered in PHITS for all source particles as defined in §6.4.3.5. Lastly, note that while PHITS was used as radiation transport code in this work, SPENVIS (GRAS and MULASSIS) makes use of the GEANT4 framework.

The benchmarking is performed against different thicknesses of aluminium. More particularly against Al shields with areal densities of 0.3, 1, 2, 5, 10, 20, 40 g/cm².

Lastly, GRAS and MULASSIS could only be used to calculate the absorbed dose, no information on the dose equivalent could be obtained (at least not as 'normal' (non-advanced) user through the web interface). This was not considered as an issue since it was demonstrated for GCR (§7.2.1) that PHITS is able to correctly reconstruct the dose equivalent rates based on the quality factors.

Results

Figure 34 below plots the doses obtained by post-processing the PHITS and OLTARIS outputs using the OLTARIS (blue) and SPENVIS (cyan) source terms, and the doses by running the MULASSIS (green) and GRAS (pink) simulations both using the SPENVIS source terms.

[102] Based on email correspondence with the SPENVIS support team, it was confirmed that the geometry reconstructed in SPENVIS (MULASSIS and GRAS) is equal to the geometry considered in PHITS.

[103] The source in MULASSIS was positioned immediately around each shield and could not be changed.

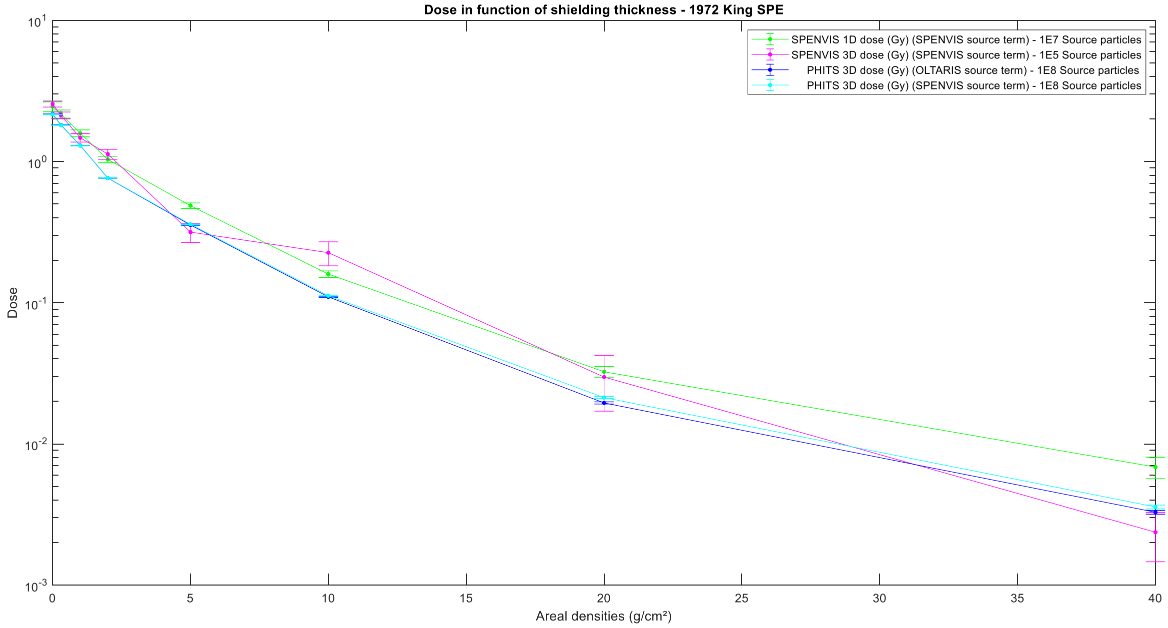

Figure 34: D (Gy) obtained by post-processing the PHITS and OLTARIS outputs using the OLTARIS (blue) and SPENVIS (cyan) source terms, and by running the MULASSIS (green) and GRAS (pink) simulations with SPENVIS source terms

Note that in Figure 34 above the doses were plotted on a log scale following the strong dose reduction with increasing shielding thickness (areal density). Hence, the error bars are indeed asymmetrical with respect to their dose values.

As stated earlier (and as mentioned in the legend of Figure 34), a different amount of source particles were used for the GRAS (1E5), MULASSIS (1E7) and PHITS (1E8) simulations. Following this, the magnitudes of the error bars (absolute error values) are expected to be different, being the largest for the GRAS simulations (pink curve) and the smallest for the PHITS simulations (blue and cyan curves), which is exactly what is observed in Figure 34 above.

Table 23 below tabulates the numerical values of the absorbed doses. The PHITS simulations were performed with the SPE spectral data extracted from OLTARIS. The absorbed doses (D) are expressed in Gy.

	Absorbed dose (Gy)			Deviation PHITS rel. to MULASSIS and GRAS (%)	
g/cm²	PHITS	MULASSIS	GRAS	MULASSIS	GRAS
0	2.17E+00	2.45E+00	2.55E+00	11	15
0.3	1.81E+00	2.17E+00	2.12E+00	16	15
1.0	1.30E+00	1.58E+00	1.47E+00	18	12
2.0	7.64E-01	1.03E+00	1.13E+00	26	32
5.0	3.55E-01	4.87E-01	3.16E-01	27	12
10.0	1.10E-01	1.59E-01	2.26E-01	31	51
20.0	1.95E-02	3.24E-02	2.97E-02	40	34
40.0	3.28E-03	6.86E-03	2.37E-03	52	39

Table 23: Summary of D (Gy) for the King 1972 SPE with OLTARIS source term

Table 24 below tabulates the numerical values of the absorbed doses. The PHITS simulations were performed with the SPE spectral data extracted from SPENVIS. The absorbed doses (D) are expressed in Gy.

	Absorbed dose (Gy)			Deviation PHITS rel. to MULASSIS and GRAS (%)	
g/cm²	PHITS	MULASSIS	GRAS	MULASSIS	GRAS
0	2.16E+00	2.45E+00	2.55E+00	12	16
0.3	1.81E+00	2.17E+00	2.12E+00	17	15
1.0	1.30E+00	1.58E+00	1.47E+00	18	12
2.0	7.65E-01	1.03E+00	1.13E+00	26	32
5.0	3.59E-01	4.87E-01	3.16E-01	26	14
10.0	1.12E-01	1.59E-01	2.26E-01	30	50
20.0	2.13E-02	3.24E-02	2.97E-02	34	28
40.0	3.58E-03	6.86E-03	2.37E-03	48	51

Table 24: Summary of D (Gy) for the King 1972 SPE with SPENVIS source term

Conclusions

The dose results obtained by post-processing the PHITS and OLTARIS/SPENVIS outputs, using the spectral data from OLTARIS and SPENVIS, are in line with the doses simulated by MULASSIS and GRAS using the SPENVIS source terms.

Considering the differences in modelling between PHITS, MULASSIS, and GRAS (source particles, modelling parameters, transport codes, etc.), the following main conclusions are drawn:

- Similar trends are observed for the absorbed doses (Figure 34);
- Small deviations are observed for the absorbed doses for 0 g/cm² (Table 23, Table 24). The unshielded doses are the most important as for thicker shields the source particles in MULASSIS/GRAS should be increased (1E8 cf. PHITS).

Indeed, the amount of source particles considered strongly influences the results (notice the magnitude of the error bars on Figure 34). The significant error bars observed on the GRAS simulations (pink curve) originate from the fact that the least amount of source particles (compared to MULASSIS and PHITS) could be generated. It is expected that when running GRAS simulations with more source particles, the GRAS results would be even better in line with the PHITS results. This statement was confirmed by running one GRAS simulation for the unshielded configuration (least computationally intense) with 1E6 source particles (OLTARIS source term). When generating 1E6 source particles, GRAS yielded an absorbed dose of 2.513E+00, while with 1E5 source particles GRAS yielded an absorbed dose of 2.555E+00 (Table 23). Hence, the deviation between PHITS and GRAS is reduced from 15% with 1E5 source particles (Table 23) to 13% with 1E6 source particles. Furthermore, the relative error outputted by GRAS is reduced from ~5% with 1E5 source particles to ~2% with 1E6 source particles. Especially for thicker shields, it is expected that GRAS would be better in line with PHITS since the rel. errors outputted by GRAS (1E5 source particles) are significant for thicker shields.

Additionally, for most shielding thicknesses, the deviations observed between the 3D PHITS results (using both source terms) and the 3D GRAS results are smaller than the deviations observed between the 3D PHITS results (using both source terms) and the 1D MULASSIS results. This observation is indeed well in line with expectations since PHITS and GRAS both perform 3D transport calculations.

Lastly, it is shown that the 1972 King SPE spectral data (source terms) extracted from NASA (OLTARIS) and from ESA (SPENVIS) yield very similar dose results (blue and cyan curves in Figure 34), which is indeed in line with expectations.

These satisfying results give rise to a sufficient level of confidence in terms of:

- Definition of the (OLTARIS and SPENVIS) source term(s) in PHITS;
- Selection of the parameter settings (nuclear libraries, etc.) in PHITS;
- Definition of the geometry and the (shielding) materials in PHITS;
- Application of a methodology for converting the tally output provided by PHITS (dose/source and flux/source) to absolute doses.

7.3. Outcome of radiation transport calculations

In this chapter, the outcome of the radiation transport calculations will be presented based on the input and the methodology described in §6.4.3 and §7.1, respectively.

In an attempt to balance the statistical uncertainties with manageable simulation times (Monte Carlo efficiency), it was chosen to perform transport calculations with 1E7 and 1E8 source particles for GCR and SPE, respectively.

In a first step, the absolute doses will be provided in §7.3.1. Based on the latter, the dose reduction factors and the shielding efficiencies will be provided in §7.3.2 and §7.3.3, respectively. The results will be discussed in §7.3.4.

7.3.1. Absolute doses

The absolute doses refer to the absolute dose rate (GCR) and dose (SPE) results obtained by post-processing the PHITS and OLTARIS outputs.

7.3.1.1. GCR

Table 25 and Table 26 below provide the absolute GCR dose rates for each areal density considered for the 2010 Solar Min and the 2001 Solar Max, respectively.

The absolute error (%), as calculated per §7.1.1, is provided for each value. The latter is colored red when exceeding the limit of 10% (unreliability criteria).

	Absolute dose rates – Solar minimum of 2010 (Matthiä)					
Areal density (g cm^{-2})	**Al**	**Liquid H**	**Liquid H_2O**	**Non-B PE**	**B PE**	**50% Al 50% PE-B**
0	4.36E-01 (1%) 1.35E+00 (4%)	4.37E-01 (3%) 1.36E+00 (13%)	4.36E-01 (1%) 1.35E+00 (4%)	4.34E-01 (1%) 1.35E+00 (4%)	4.36E-01 (1%) 1.35E+00 (4%)	4.34E-01 (1%) 1.32E+00 (4%)
0.3	4.35E-01 (1%) 1.34E+00 (5%)	4.31E-01 (4%) 1.24E+00 (17%)	4.35E-01 (1%) 1.32E+00 (6%)	4.35E-01 (1%) 1.32E+00 (6%)	4.35E-01 (1%) 1.33E+00 (6%)	4.32E-01 (1%) 1.26E+00 (5%)
1.0	4.36E-01 (1%) 1.34E+00 (5%)	4.31E-01 (4%) 1.21E+00 (17%)	4.32E-01 (1%) 1.28E+00 (6%)	4.31E-01 (1%) 1.25E+00 (6%)	4.32E-01 (1%) 1.27E+00 (6%)	4.34E-01 (1%) 1.31E+00 (6%)
2.0	4.31E-01 (1%) 1.29E+00 (5%)	4.12E-01 (3%) 9.72E-01 (15%)	4.28E-01 (1%) 1.23E+00 (6%)	4.28E-01 (1%) 1.26E+00 (6%)	4.28E-01 (1%) 1.22E+00 (6%)	4.33E-01 (1%) 1.29E+00 (6%)
5.0	4.36E-01 (1%) 1.20E+00 (5%)	4.12E-01 (3%) 8.71E-01 (14%)	4.27E-01 (1%) 1.11E+00 (6%)	4.27E-01 (1%) 1.10E+00 (6%)	4.27E-01 (1%) 1.10E+00 (6%)	4.31E-01 (1%) 1.17E+00 (5%)
10.0	4.38E-01 (1%) 1.13E+00 (5%)	4.15E-01 (3%) 7.97E-01 (13%)	4.30E-01 (1%) 1.07E+00 (6%)	4.26E-01 (1%) 9.83E-01 (5%)	4.25E-01 (1%) 9.85E-01 (5%)	4.30E-01 (1%) 1.06E+00 (5%)
20.0	4.43E-01 (1%) 1.10E+00 (5%)	4.16E-01 (3%) 7.76E-01 (13%)	4.32E-01 (1%) 9.33E-01 (5%)	4.28E-01 (1%) 8.94E-01 (5%)	4.27E-01 (1%) 8.91E-01 (5%)	4.32E-01 (1%) 9.58E-01 (4%)
40.0	4.46E-01 (1%) 1.01E+00 (4%)	4.01E-01 (3%) 7.29E-01 (13%)	4.32E-01 (1%) 8.65E-01 (5%)	4.28E-01 (1%) 8.26E-01 (4%)	4.30E-01 (1%) 8.47E-01 (5%)	4.30E-01 (1%) 8.69E-01 (4%)

Table 25: $\dot{D}$ (mGy/d) and $\dot{H}$ (mSv/d) are given by the upper and lower values, respectively, followed by its absolute error (%) for the solar minimum of 2010 (Matthiä)

Areal density (g cm^{-2})	Al	Liquid H	Liquid H_2O	Non-B PE	B PE	50% Al 50% PE-B
	Absolute dose rates – Solar maximum of 2001 (Matthiä)					
0	1.58E-01 (1%) 5.41E-01 (3%)	1.57E-01 (3%) 5.40E-01 (11%)	1.56E-01 (1%) 5.07E-01 (4%)	1.56E-01 (1%) 5.05E-01 (4%)	1.56E-01 (1%) 5.09E-01 (4%)	1.57E-01 (1%) 5.34E-01 (4%)
0.3	1.58E-01 (1%) 5.39E-01 (5%)	1.61E-01 (4%) 5.89E-01 (17%)	1.57E-01 (1%) 5.04E-01 (5%)	1.57E-01 (1%) 5.21E-01 (5%)	1.57E-01 (1%) 5.09E-01 (5%)	1.57E-01 (1%) 5.18E-01 (5%)
1.0	1.59E-01 (1%) 5.32E-01 (5%)	1.60E-01 (4%) 5.20E-01 (16%)	1.58E-01 (1%) 5.12E-01 (5%)	1.58E-01 (1%) 5.17E-01 (5%)	1.58E-01 (1%) 5.01E-01 (5%)	1.59E-01 (1%) 5.37E-01 (5%)
2.0	1.60E-01 (1%) 5.24E-01 (5%)	1.61E-01 (4%) 5.48E-01 (16%)	1.59E-01 (1%) 4.96E-01 (5%)	1.59E-01 (1%) 5.08E-01 (5%)	1.58E-01 (1%) 4.82E-01 (5%)	1.59E-01 (1%) 5.07E-01 (5%)
5.0	1.65E-01 (1%) 5.12E-01 (5%)	1.62E-01 (4%) 4.48E-01 (16%)	1.63E-01 (1%) 4.81E-01 (5%)	1.63E-01 (1%) 4.85E-01 (5%)	1.62E-01 (1%) 4.66E-01 (5%)	1.63E-01 (1%) 4.74E-01 (5%)
10.0	1.72E-01 (1%) 4.77E-01 (5%)	1.66E-01 (3%) 3.44E-01 (12%)	1.69E-01 (1%) 4.34E-01 (5%)	1.69E-01 (1%) 4.26E-01 (5%)	1.69E-01 (1%) 4.15E-01 (5%)	1.70E-01 (1%) 4.52E-01 (5%)
20.0	1.87E-01 (1%) 4.72E-01 (4%)	1.83E-01 (3%) 3.47E-01 (11%)	1.82E-01 (1%) 4.06E-01 (4%)	1.82E-01 (1%) 3.94E-01 (4%)	1.82E-01 (1%) 3.96E-01 (4%)	1.83E-01 (1%) 4.26E-01 (4%)
40.0	2.09E-01 (1%) 4.84E-01 (4%)	2.02E-01 (3%) 3.72E-01 (11%)	2.05E-01 (1%) 4.12E-01 (4%)	2.05E-01 (1%) 4.05E-01 (4%)	2.05E-01 (1%) 4.14E-01 (4%)	2.03E-01 (1%) 4.20E-01 (4%)

Table 26: $\dot{D}$ (mGy/d) and $\dot{H}$ (mSv/d) are given by the upper and lower values, respectively, followed by its absolute error (%) for the solar maximum of 2001 (Matthiä)

In order to more easily interpret the data included in Table 25 and Table 26 above, Figure 35 and Figure 36 below plot the absolute GCR dose rates for each areal density considered for the 2010 Solar Min and the 2001 Solar Max, respectively.

The error bars visualized on the plots correspond to the absolute errors as given in Table 25 and Table 26 above.

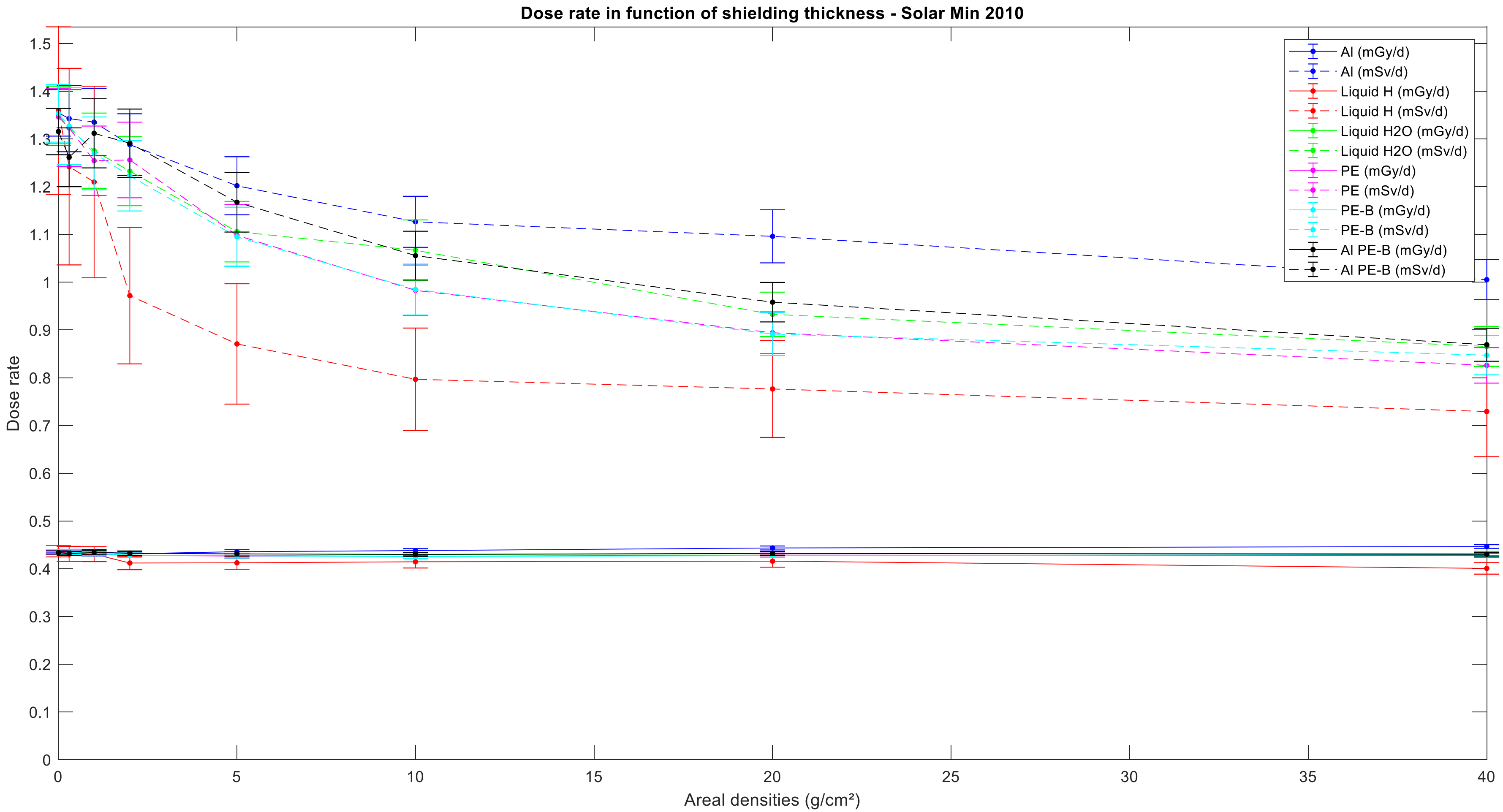

Figure 35: Absolute GCR dose rates for the solar minimum of 2010 (Matthiä)

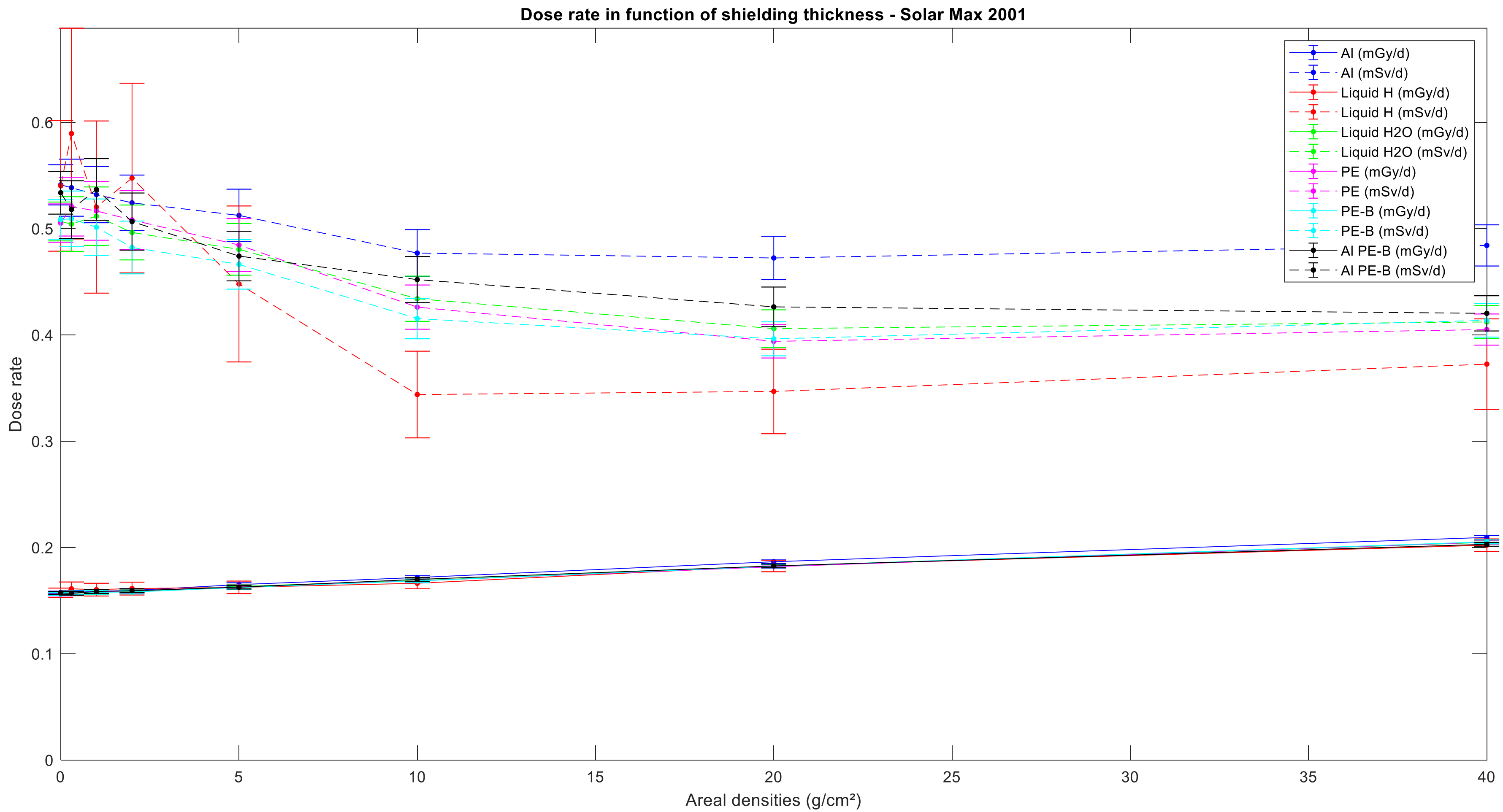

Figure 36: Absolute GCR dose rates for the solar maximum of 2001 (Matthiä)

7.3.1.2. SPE

Table 27 and Table 28 below provide the absolute doses for each areal density considered for the August 1972 (LaRC) SPE and the Sum of October 1989 Tylka Band fits SPE, respectively.

The absolute error (%), as calculated per §7.1.2, is provided for each value. The latter is colored red when exceeding the limit of 10% (unreliability criteria).

	Absolute doses – August 1972 (LaRC) SPE					
Areal density (g cm^{-2})	**Al**	**Liquid H**	**Liquid H_2O**	**Non-B PE**	**B PE**	**50% Al 50% PE-B**
0	1.91E+00 (0%) 2.90E+00 (0%)	1.92E+00 (0%) 2.91E+00 (0%)	1.91E+00 (0%) 2.90E+00 (0%)	1.91E+00 (0%) 2.90E+00 (0%)	1.91E+00 (0%) 2.90E+00 (0%)	1.91E+00 (0%) 2.90E+00 (0%)
0.3	1.65E+00 (0%) 2.45E+00 (0%)	1.32E+00 (1%) 1.92E+00 (1%)	1.57E+00 (0%) 2.33E+00 (0%)	1.56E+00 (0%) 2.30E+00 (0%)	1.56E+00 (0%) 2.31E+00 (0%)	1.59E+00 (0%) 2.37E+00 (0%)
1.0	1.23E+00 (0%) 1.81E+00 (0%)	7.13E-01 (1%) 1.01E+00 (1%)	1.10E+00 (0%) 1.60E+00 (0%)	1.07E+00 (0%) 1.54E+00 (0%)	1.08E+00 (0%) 1.57E+00 (0%)	1.15E+00 (0%) 1.67E+00 (0%)
2.0	7.69E-01 (0%) 1.11E+00 (0%)	3.44E-01 (1%) 4.81E-01 (1%)	6.59E-01 (0%) 9.39E-01 (0%)	6.52E-01 (0%) 9.28E-01 (0%)	6.70E-01 (0%) 9.54E-01 (0%)	7.90E-01 (0%) 1.14E+00 (0%)
5.0	4.01E-01 (0%) 5.78E-01 (0%)	8.18E-02 (3%) 1.10E-01 (3%)	2.83E-01 (0%) 4.03E-01 (0%)	2.61E-01 (0%) 3.70E-01 (0%)	2.71E-01 (0%) 3.85E-01 (0%)	3.26E-01 (0%) 4.69E-01 (0%)
10.0	1.43E-01 (1%) 2.16E-01 (1%)	1.27E-02 (7%) 1.75E-02 (8%)	8.34E-02 (1%) 1.23E-01 (1%)	7.34E-02 (1%) 1.07E-01 (1%)	7.83E-02 (1%) 1.15E-01 (1%)	1.06E-01 (1%) 1.60E-01 (1%)
20.0	3.13E-02 (1%) 6.10E-02 (1%)	6.45E-04 (29%) 1.41E-03 (42%)	1.35E-02 (2%) 2.42E-02 (2%)	1.07E-02 (2%) 1.93E-02 (2%)	1.19E-02 (2%) 2.19E-02 (2%)	1.96E-02 (1%) 3.85E-02 (1%)
40.0	5.09E-03 (2%) 2.17E-02 (2%)	/ /	1.54E-03 (4%) 5.14E-03 (5%)	1.08E-03 (6%) 3.52E-03 (6%)	1.26E-03 (5%) 4.41E-03 (5%)	2.74E-03 (3%) 1.04E-02 (3%)

Table 27: D (Gy) and H (Sv) are given by the upper and lower values, respectively, followed by its absolute error (%) for the August 1972 (LaRC) SPE

	Absolute doses – Sum of October 1989 Tylka Band fits SPE					
Areal density (g cm^{-2})	**Al**	**Liquid H**	**Liquid H_2O**	**Non-B PE**	**B PE**	**50% Al 50% PE-B**
0	1.13E+02 (4%) 1.99E+02 (4%)	1.17E+02 (14%) 1.92E+02 (12%)	1.08E+02 (4%) 1.85E+02 (4%)	1.10E+02 (5%) 1.89E+02 (4%)	1.08E+02 (4%) 1.86E+02 (4%)	1.12E+02 (4%) 1.93E+02 (4%)
0.3	8.49E+01 (6%) 1.32E+02 (6%)	6.62E+01 (25%) 1.09E+02 (26%)	7.49E+01 (7%) 1.17E+02 (7%)	7.33E+01 (7%) 1.14E+02 (7%)	7.51E+01 (7%) 1.16E+02 (7%)	7.90E+01 (7%) 1.24E+02 (7%)
1.0	5.78E+01 (7%) 8.52E+01 (8%)	3.39E+01 (36%) 4.13E+01 (34%)	4.47E+01 (9%) 6.74E+01 (10%)	4.35E+01 (9%) 6.16E+01 (9%)	4.35E+01 (9%) 6.52E+01 (10%)	4.89E+01 (8%) 7.27E+01 (9%)
2.0	3.18E+01 (10%) 4.82E+01 (11%)	2.14E+01 (49%) 2.45E+01 (47%)	2.84E+01 (12%) 4.32E+01 (16%)	2.67E+01 (12%) 4.02E+01 (15%)	2.79E+01 (12%) 4.04E+01 (14%)	3.48E+01 (10%) 4.91E+01 (12%)
5.0	2.01E+01 (13%) 2.69E+01 (13%)	1.12E+01 (74%) 3.04E+01 (80%)	1.58E+01 (17%) 2.67E+01 (21%)	1.41E+01 (20%) 2.00E+01 (23%)	1.33E+01 (18%) 1.91E+01 (20%)	1.60E+01 (16%) 2.34E+01 (19%)
10.0	1.26E+01 (17%) 1.72E+01 (18%)	4.38E+00 (101%) 4.99E+00 (101%)	9.43E+00 (23%) 1.13E+01 (23%)	7.61E+00 (25%) 1.05E+01 (25%)	8.32E+00 (26%) 1.45E+01 (31%)	1.10E+01 (20%) 1.38E+01 (19%)
20.0	6.00E+00 (25%) 9.41E+00 (25%)	3.59E+00 (101%) 3.59E+00 (101%)	5.58E+00 (31%) 6.83E+00 (30%)	4.00E+00 (33%) 6.83E+00 (40%)	3.98E+00 (33%) 5.50E+00 (31%)	5.76E+00 (30%) 1.06E+01 (37%)
40.0	2.68E+00 (42%) 5.09E+00 (30%)	3.85E+00 (101%) 4.46E+00 (101%)	2.72E+00 (55%) 2.91E+00 (53%)	1.45E+00 (71%) 1.59E+00 (69%)	2.30E+00 (53%) 2.90E+00 (53%)	3.45E+00 (43%) 4.30E+00 (38%)

Table 28: D (Gy) and H (Sv) are given by the upper and lower values, respectively, followed by its absolute error (%) for the Sum of October 1989 Tylka Band fits SPE

In order to more easily interpret the data included in Table 27 and Table 28 above, Figure 37 and Figure 38 below plot the absolute doses for each areal density considered for the August 1972 (LaRC) SPE and the Sum of October 1989 Tylka Band fits SPE, respectively.

The error bars visualized on the plots correspond to the absolute errors as given in Table 27 and Table 28 above.

Important remark

For the Sum of October 1989 Tylka Band fits SPE (Table 28), high absolute errors are observed above 1 g/cm^2[104] for both D and H, making the results unreliable[105]. The reason for these high absolute errors compared to those for the August 1972 (LaRC) SPE (Table 27) follows from the energy distribution. From Figure 23, one can observe that the fluences of the Sum of October 1989 Tylka Band fits SPE are much higher than of the August 1972 (LaRC) SPE over nearly the full energy range (except between ~20 and ~150 MeV/u). Hence, the Sum of October 1989 Tylka Band fits SPE is harder to shield against. In order to decrease the uncertainties, transport calculations with more source particles (> 1E8) should be performed. Due to time restrictions, new transport calculations could not be performed.

Due to the unreliability of the Sum of October 1989 Tylka Band fits SPE results (Table 28), neither the dose reduction factors nor the shielding efficiencies have been calculated for the latter SPE.

[104] For liquid H, high absolute errors are observed even below 1 g/cm^2.

[105] Monte Carlo results with statistical uncertainties above 5-10% have little to no meaning. A statistical uncertainty of 50% does not imply that the result with good statistics will be within a range of 50% (it can differ even an order of magnitude).

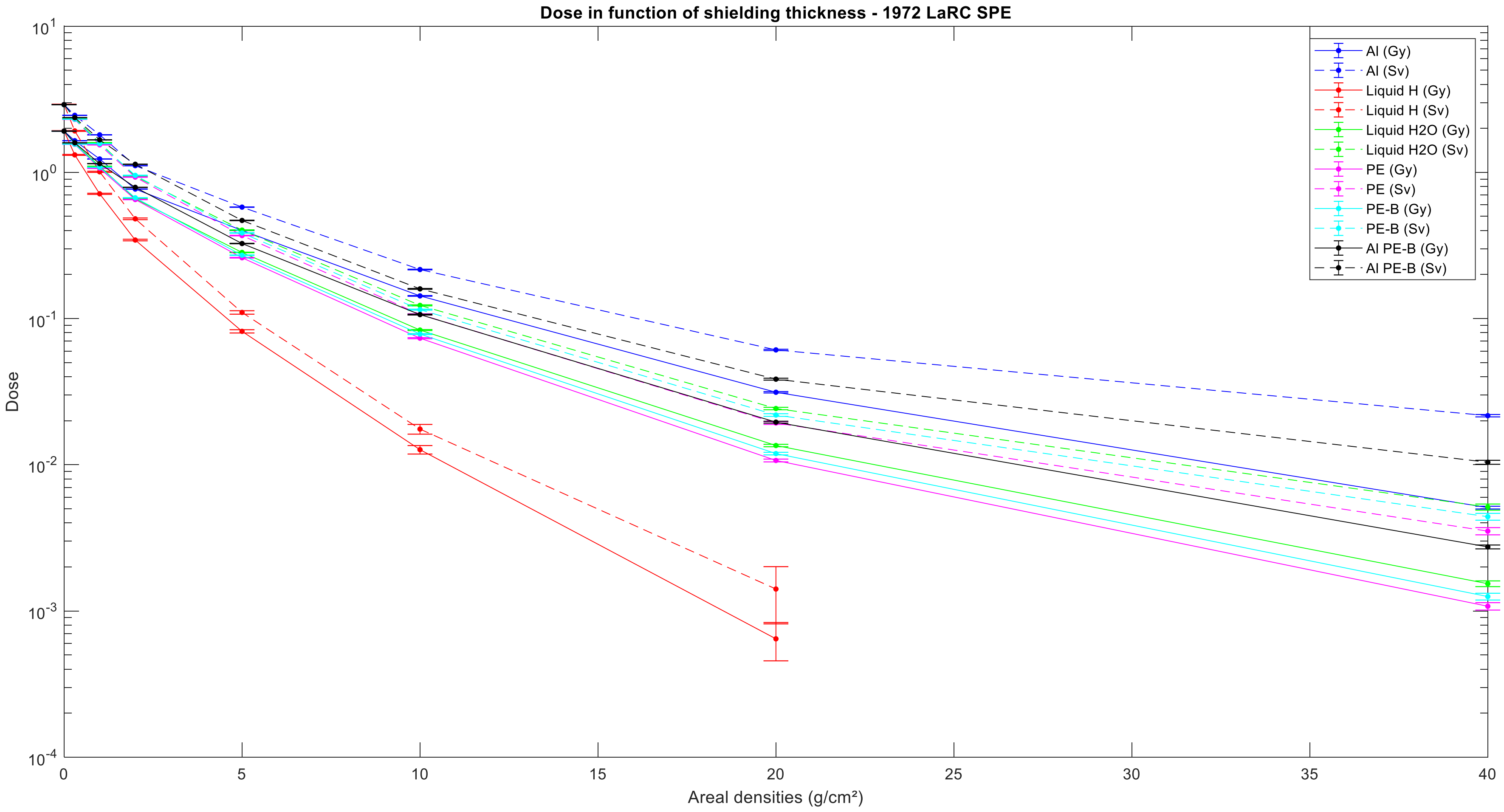

Figure 37: Absolute doses for the August 1972 (LaRC) SPE

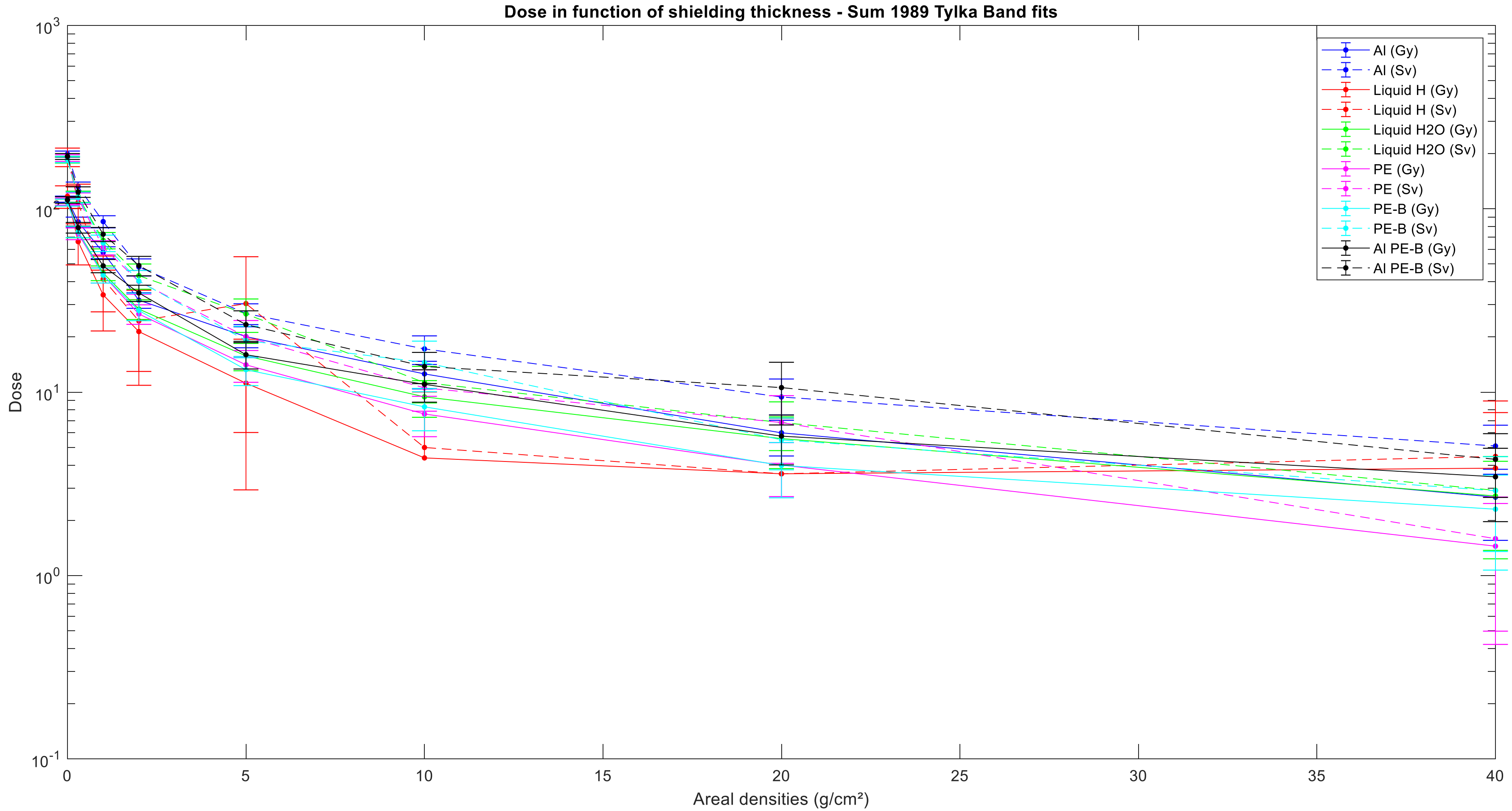

Figure 38: Absolute doses for the Sum of October 1989 Tylka Band fits SPE

7.3.2. Dose reduction factors

The dose reduction factors express the performance of the shielded configurations relative to the unshielded configuration by increasing the shielding thickness of the material (e.g. 1 g/cm² of Al relative to its unshielded configuration).

7.3.2.1. GCR

Table 29 and Table 30 below provide the dose reduction factors for each areal density considered for the 2010 Solar Min and the 2001 Solar Max, respectively.

A combined absolute error[106] (%) is provided for each value. The latter is colored red when exceeding the limit of 10% (unreliability criteria).

	Dose reduction factors – Solar minimum of 2010 (Matthiä)					
Areal density (g cm^{-2})	**Al**	**Liquid H**	**Liquid H_2O**	**Non-B PE**	**B PE**	**50% Al 50% PE-B**
0	1 1	1 1	1 1	1 1	1 1	1 1
0.3	9.97E-01 (1%) 9.91E-01 (6%)	9.87E-01 (5%) 9.14E-01 (21%)	9.99E-01 (1%) 9.80E-01 (8%)	1.00E+00 (1%) 9.83E-01 (8%)	9.98E-01 (1%) 9.80E-01 (8%)	9.96E-01 (1%) 9.59E-01 (6%)
1.0	9.99E-01 (1%) 9.86E-01 (6%)	9.85E-01 (5%) 8.90E-01 (21%)	9.92E-01 (1%) 9.45E-01 (8%)	9.92E-01 (1%) 9.32E-01 (7%)	9.91E-01 (1%) 9.38E-01 (7%)	1.00E+00 (1%) 9.97E-01 (7%)
2.0	9.88E-01 (1%) 9.51E-01 (6%)	9.43E-01 (4%) 7.15E-01 (20%)	9.84E-01 (1%) 9.13E-01 (7%)	9.86E-01 (1%) 9.33E-01 (8%)	9.83E-01 (1%) 9.03E-01 (7%)	9.97E-01 (1%) 9.81E-01 (7%)
5.0	9.98E-01 (1%) 8.87E-01 (6%)	9.44E-01 (4%) 6.41E-01 (19%)	9.81E-01 (1%) 8.19E-01 (7%)	9.82E-01 (1%) 8.16E-01 (7%)	9.80E-01 (1%) 8.09E-01 (7%)	9.93E-01 (1%) 8.87E-01 (6%)
10.0	1.00E+00 (1%) 8.32E-01 (6%)	9.49E-01 (4%) 5.86E-01 (19%)	9.86E-01 (1%) 7.90E-01 (7%)	9.81E-01 (1%) 7.30E-01 (7%)	9.76E-01 (1%) 7.27E-01 (7%)	9.91E-01 (1%) 8.03E-01 (6%)
20.0	1.02E+00 (1%) 8.09E-01 (6%)	9.52E-01 (4%) 5.71E-01 (18%)	9.91E-01 (1%) 6.91E-01 (7%)	9.86E-01 (1%) 6.64E-01 (7%)	9.81E-01 (1%) 6.58E-01 (7%)	9.96E-01 (1%) 7.28E-01 (6%)
40.0	1.02E+00 (1%) 7.42E-01 (6%)	9.17E-01 (4%) 5.36E-01 (18%)	9.92E-01 (1%) 6.41E-01 (7%)	9.85E-01 (1%) 6.13E-01 (6%)	9.86E-01 (1%) 6.26E-01 (7%)	9.91E-01 (1%) 6.61E-01 (5%)

Table 29: Dose reduction factors relative to the unshielded configuration for $\dot{D}$ (upper value) and $\dot{H}$ (lower value), followed by its combined absolute error (%) for the solar minimum of 2010 (Matthiä)

[106] $Combined\ Abs.error = dose\ reduction\ factor * \sqrt{(Abs.error/dose\ rate)^2_{Unshielded} + (Abs.error/dose\ rate)^2_{Shielded}}$

	Dose reduction factors – Solar maximum of 2001 (Matthiä)					
Areal density (g cm^{-2})	**Al**	**Liquid H**	**Liquid H_2O**	**Non-B PE**	**B PE**	**50% Al 50% PE-B**
0	1 1	1 1	1 1	1 1	1 1	1 1
0.3	1.00E+00 (1%) 9.95E-01 (6%)	1.02E+00 (5%) 1.09E+00 (20%)	1.00E+00 (1%) 9.95E-01 (6%)	1.01E+00 (1%) 1.03E+00 (6%)	1.01E+00 (1%) 1.00E+00 (6%)	9.98E-01 (1%) 9.70E-01 (6%)
1.0	1.01E+00 (1%) 9.83E-01 (6%)	1.02E+00 (5%) 9.63E-01 (19%)	1.01E+00 (1%) 1.01E+00 (6%)	1.02E+00 (1%) 1.02E+00 (6%)	1.01E+00 (1%) 9.86E-01 (6%)	1.01E+00 (1%) 1.01E+00 (7%)
2.0	1.01E+00 (1%) 9.69E-01 (6%)	1.02E+00 (5%) 1.01E+00 (20%)	1.02E+00 (1%) 9.80E-01 (6%)	1.02E+00 (1%) 1.01E+00 (7%)	1.01E+00 (1%) 9.48E-01 (6%)	1.01E+00 (1%) 9.49E-01 (7%)
5.0	1.05E+00 (1%) 9.47E-01 (6%)	1.03E+00 (5%) 8.29E-01 (20%)	1.05E+00 (1%) 9.48E-01 (6%)	1.05E+00 (1%) 9.59E-01 (6%)	1.04E+00 (1%) 9.17E-01 (6%)	1.03E+00 (1%) 8.88E-01 (6%)
10.0	1.09E+00 (1%) 8.81E-01 (6%)	1.06E+00 (4%) 6.37E-01 (16%)	1.08E+00 (1%) 8.57E-01 (6%)	1.08E+00 (1%) 8.44E-01 (6%)	1.08E+00 (1%) 8.17E-01 (6%)	1.08E+00 (1%) 8.47E-01 (6%)
20.0	1.18E+00 (1%) 8.73E-01 (6%)	1.16E+00 (4%) 6.42E-01 (16%)	1.17E+00 (1%) 8.01E-01 (6%)	1.17E+00 (1%) 7.80E-01 (5%)	1.17E+00 (1%) 7.79E-01 (5%)	1.16E+00 (1%) 7.99E-01 (6%)
40.0	1.33E+00 (1%) 8.95E-01 (5%)	1.28E+00 (4%) 6.89E-01 (16%)	1.31E+00 (1%) 8.13E-01 (5%)	1.32E+00 (1%) 8.02E-01 (5%)	1.32E+00 (1%) 8.13E-01 (5%)	1.29E+00 (1%) 7.87E-01 (5%)

Table 30: Dose reduction factors relative to the unshielded configuration for $\dot{D}$ (upper value) and $\dot{H}$ (lower value), followed by its combined absolute error (%) for the solar maximum of 2001 (Matthiä)

In order to more easily interpret the data included in Table 29 and Table 30 above, Figure 39 and Figure 40 below plot the dose reduction factors for each areal density considered for the 2010 Solar Min and the 2001 Solar Max, respectively (the absolute errors are not visualized).

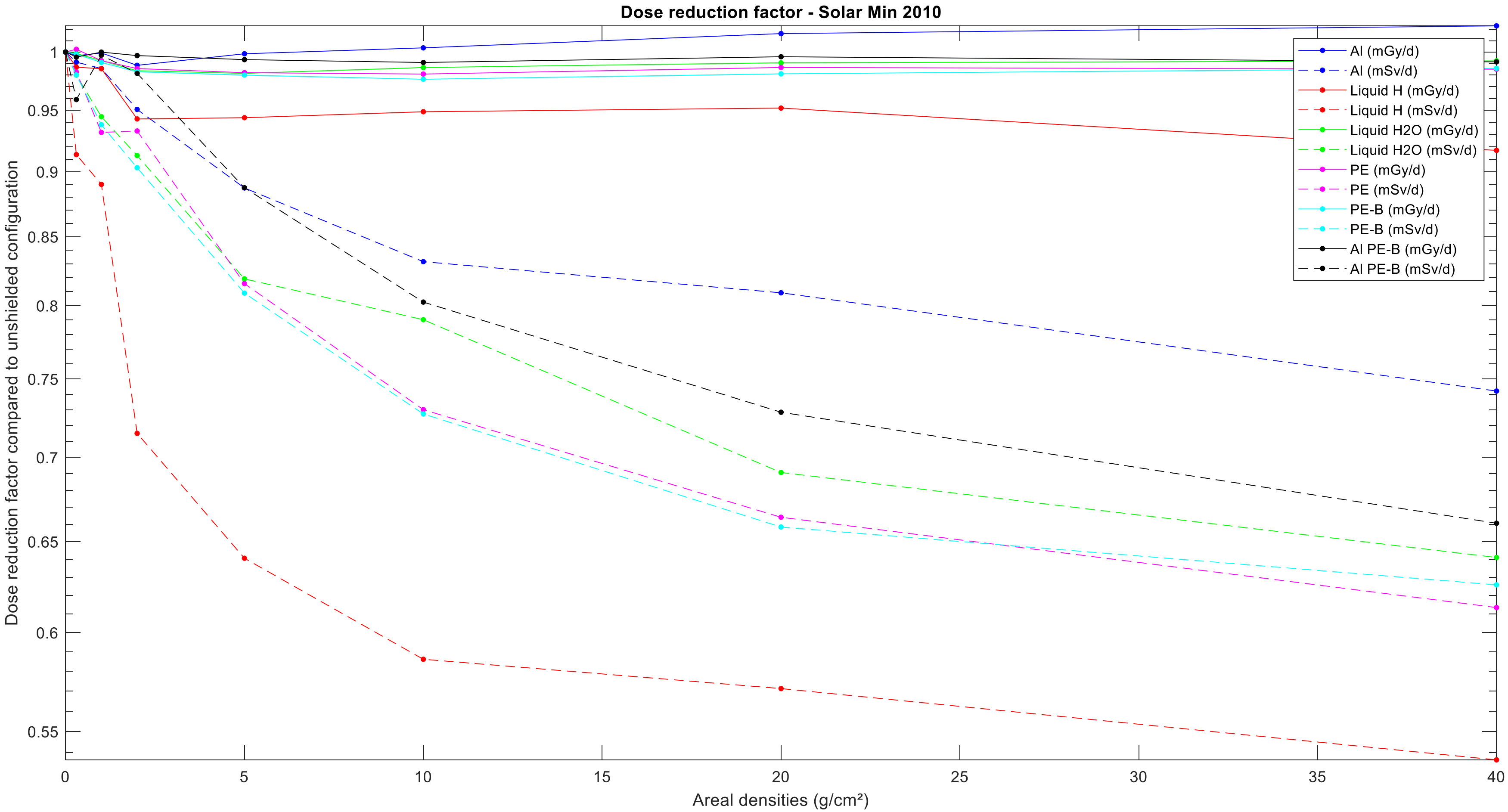

Figure 39: Dose reduction factors against GCR for the solar minimum of 2010 (Matthiä)

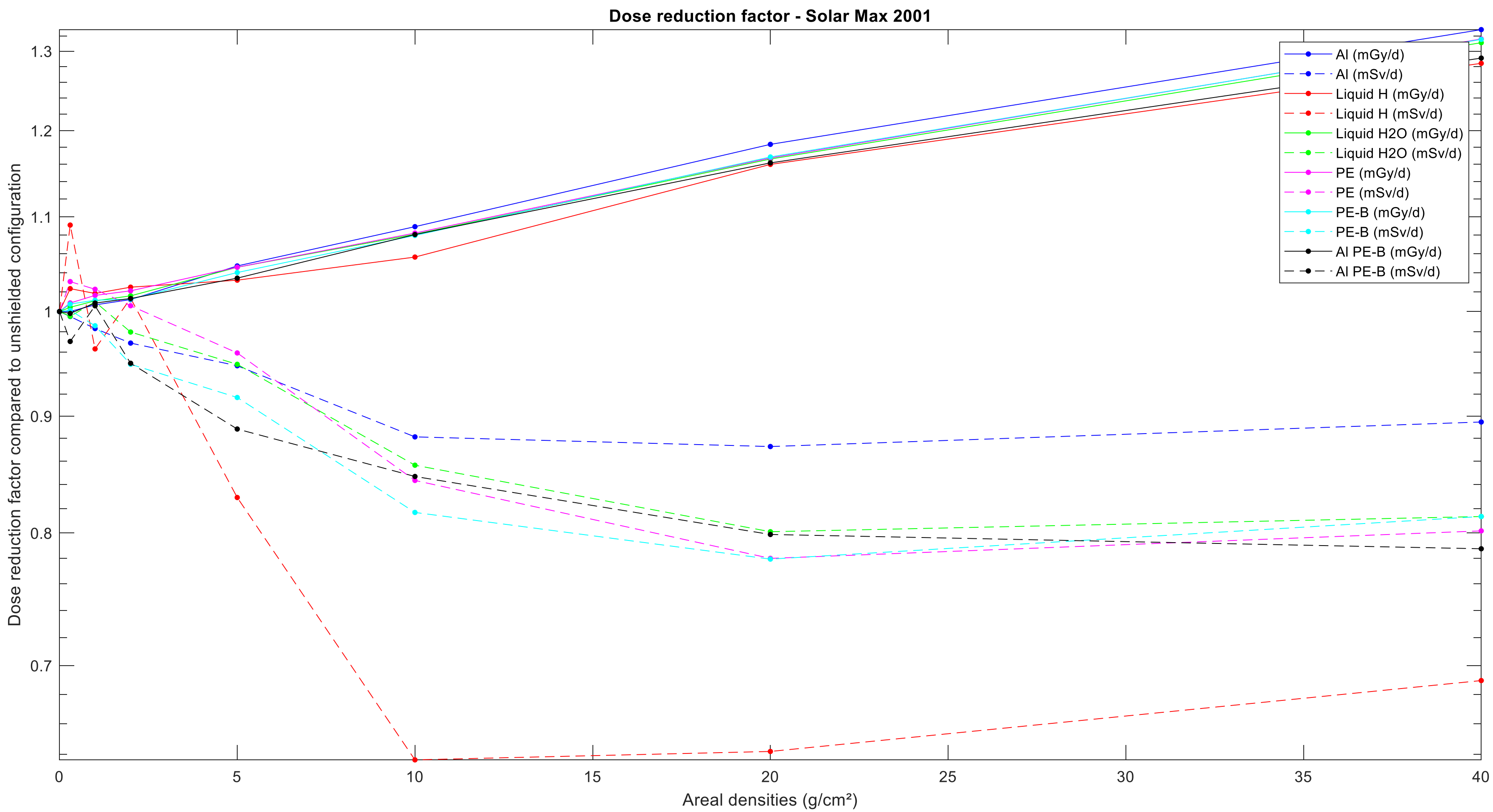

Figure 40: Dose reduction factors against GCR for the solar maximum of 2001 (Matthiä)

7.3.2.2. SPE

Table 31 below provides the dose reduction factors for each areal density considered for the August 1972 (LaRC) SPE.

A combined absolute error[107] (%) is provided for each value. The latter is colored red when exceeding the limit of 10% (unreliability criteria).

	Dose reduction factors – August 1972 (LaRC) SPE					
Areal density (g cm^{-2})	**Al**	**Liquid H**	**Liquid H_2O**	**Non-B PE**	**B PE**	**50% Al 50% PE-B**
0	1 1	1 1	1 1	1 1	1 1	1 1
0.3	8.60E-01 (0%) 8.45E-01 (0%)	6.86E-01 (1%) 6.60E-01 (1%)	8.21E-01 (0%) 8.02E-01 (0%)	8.13E-01 (0%) 7.93E-01 (0%)	8.16E-01 (0%) 7.96E-01 (0%)	8.32E-01 (0%) 8.15E-01 (0%)
1.0	6.45E-01 (0%) 6.22E-01 (0%)	3.71E-01 (1%) 3.46E-01 (1%)	5.75E-01 (0%) 5.50E-01 (0%)	5.57E-01 (0%) 5.31E-01 (0%)	5.66E-01 (0%) 5.40E-01 (0%)	5.99E-01 (0%) 5.74E-01 (0%)
2.0	4.02E-01 (0%) 3.82E-01 (0%)	1.79E-01 (1%) 1.65E-01 (1%)	3.44E-01 (0%) 3.24E-01 (0%)	3.41E-01 (0%) 3.20E-01 (0%)	3.50E-01 (0%) 3.28E-01 (0%)	4.13E-01 (0%) 3.91E-01 (0%)
5.0	2.10E-01 (0%) 1.99E-01 (0%)	4.26E-02 (3%) 3.78E-02 (3%)	1.48E-01 (0%) 1.39E-01 (0%)	1.36E-01 (0%) 1.27E-01 (0%)	1.42E-01 (0%) 1.33E-01 (0%)	1.70E-01 (0%) 1.61E-01 (0%)
10.0	7.47E-02 (1%) 7.45E-02 (1%)	6.60E-03 (7%) 6.02E-03 (8%)	4.36E-02 (1%) 4.24E-02 (1%)	3.83E-02 (1%) 3.68E-02 (1%)	4.09E-02 (1%) 3.96E-02 (1%)	5.56E-02 (1%) 5.50E-02 (1%)
20.0	1.64E-02 (1%) 2.10E-02 (1%)	3.36E-04 (29%) 4.85E-04 (42%)	7.08E-03 (2%) 8.35E-03 (2%)	5.59E-03 (2%) 6.65E-03 (2%)	6.23E-03 (2%) 7.54E-03 (2%)	1.02E-02 (2%) 1.33E-02 (1%)
40.0	2.66E-03 (2%) 7.46E-03 (2%)	/ /	8.03E-04 (4%) 1.77E-03 (5%)	5.63E-04 (6%) 1.21E-03 (6%)	6.56E-04 (5%) 1.52E-03 (5%)	1.43E-03 (3%) 3.58E-03 (3%)

Table 31: Dose reduction factors relative to the unshielded configuration for D (upper value) and H (lower value), followed by its combined absolute error (%) for the August 1972 (LaRC) SPE

In order to more easily interpret the data included in Table 31 above, Figure 41 below plots the dose reduction factors for each areal density considered for the August 1972 (LaRC) SPE (the absolute errors are not visualized).

[107] $Combined\ Abs.error = dose\ reduction\ factor * \sqrt{(Abs.error/dose)^2_{Unshielded} + (Abs.error/dose)^2_{Shielded}}$

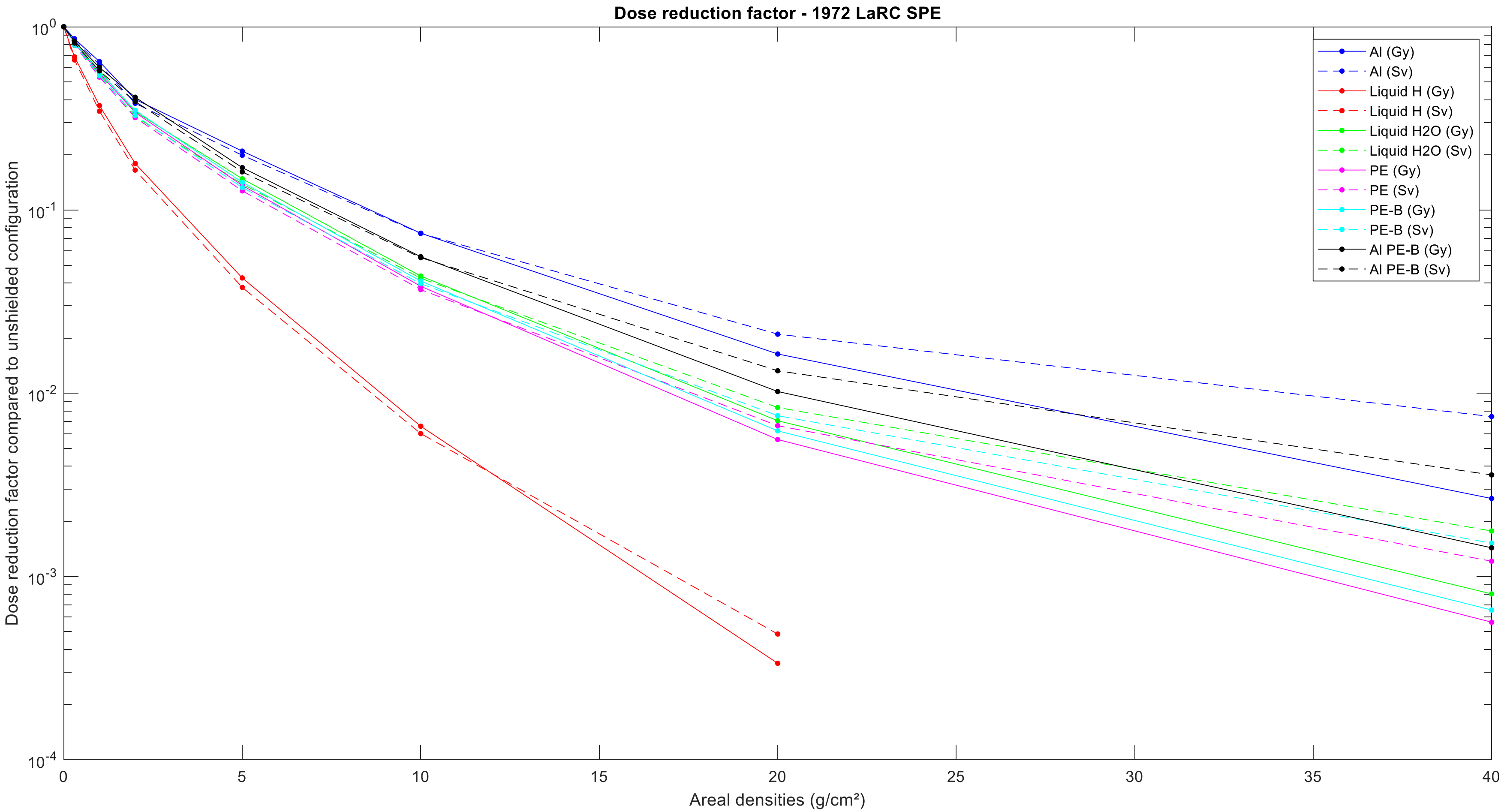

Figure 41: Dose reduction factors against the August 1972 (LaRC) SPE

7.3.3. Shielding efficiencies

The shielding efficiencies express the performance (dose reduction factor) of light materials relative and normalized to the performance of Al (reference material) considering the same shielding thickness (e.g. 1 g/cm² of liquid H relative and normalized to 1 g/cm² of Al).

7.3.3.1. GCR

Table 32 and Table 33 below provide the shielding efficiencies for each areal density considered for the 2010 Solar Min and the 2001 Solar Max, respectively.

A combined absolute error[108] (%) is provided for each value. The latter is colored red when exceeding the limit of 10% (unreliability criteria).

		Shielding efficiencies – Solar minimum of 2010 (Matthiä)				
Areal density (g cm^{-2})	**Al** (reference)	**Liquid H**	**Liquid H_2O**	**Non-B PE**	**B PE**	**50% Al 50% PE-B**
0.3	1 1	1.01E+00 (4%) 1.08E+00 (17%)	1.00E+00 (2%) 1.01E+00 (8%)	9.99E-01 (2%) 1.01E+00 (8%)	1.00E+00 (2%) 1.01E+00 (8%)	1.01E+00 (1%) 1.06E+00 (7%)
1.0	1 1	1.01E+00 (4%) 1.10E+00 (17%)	1.01E+00 (2%) 1.05E+00 (8%)	1.01E+00 (2%) 1.06E+00 (8%)	1.01E+00 (2%) 1.05E+00 (8%)	1.00E+00 (1%) 1.02E+00 (8%)
2.0	1 1	1.05E+00 (4%) 1.33E+00 (16%)	1.01E+00 (2%) 1.04E+00 (8%)	1.01E+00 (2%) 1.03E+00 (8%)	1.01E+00 (2%) 1.05E+00 (8%)	9.97E-01 (1%) 9.98E-01 (7%)
5.0	1 1	1.06E+00 (3%) 1.38E+00 (15%)	1.02E+00 (1%) 1.09E+00 (8%)	1.02E+00 (1%) 1.09E+00 (8%)	1.02E+00 (1%) 1.10E+00 (8%)	1.01E+00 (1%) 1.03E+00 (7%)
10.0	1 1	1.06E+00 (3%) 1.41E+00 (14%)	1.02E+00 (1%) 1.06E+00 (8%)	1.03E+00 (1%) 1.15E+00 (7%)	1.03E+00 (1%) 1.14E+00 (7%)	1.02E+00 (1%) 1.07E+00 (7%)
20.0	1 1	1.07E+00 (3%) 1.41E+00 (14%)	1.03E+00 (1%) 1.18E+00 (7%)	1.03E+00 (1%) 1.23E+00 (7%)	1.04E+00 (1%) 1.23E+00 (7%)	1.03E+00 (1%) 1.14E+00 (7%)
40.0	1 1	1.11E+00 (3%) 1.38E+00 (14%)	1.03E+00 (1%) 1.16E+00 (6%)	1.04E+00 (1%) 1.22E+00 (6%)	1.04E+00 (1%) 1.19E+00 (6%)	1.04E+00 (1%) 1.16E+00 (6%)

Table 32: Shielding efficiencies relative and normalized to Al for $\dot{D}$ (upper value) and $\dot{H}$ (lower value), followed by its combined absolute error (%) for the solar minimum of 2010 (Matthiä)

108 $Combined\ Abs.error = shielding\ efficiency * \sqrt{(Abs.error/dose\ rate)^2_{Al} + (Abs.error/dose\ rate)^2_{Other\ materials}}$

	Shielding efficiencies – Solar maximum of 2001 (Matthiä)					
Areal density (g cm^{-2})	**Al** (reference)	**Liquid H**	**Liquid H_2O**	**Non-B PE**	**B PE**	**50% Al 50% PE-B**
0.3	1 1	9.79E-01 (4%) 9.14E-01 (18%)	1.01E+00 (2%) 1.07E+00 (7%)	1.00E+00 (2%) 1.03E+00 (7%)	1.00E+00 (2%) 1.06E+00 (7%)	1.00E+00 (2%) 1.04E+00 (7%)
1.0	1 1	9.90E-01 (4%) 1.02E+00 (16%)	1.01E+00 (2%) 1.04E+00 (7%)	1.00E+00 (2%) 1.03E+00 (7%)	1.01E+00 (2%) 1.06E+00 (7%)	1.00E+00 (2%) 9.91E-01 (7%)
2.0	1 1	9.89E-01 (4%) 9.57E-01 (17%)	1.01E+00 (2%) 1.06E+00 (7%)	1.00E+00 (2%) 1.03E+00 (7%)	1.01E+00 (2%) 1.09E+00 (7%)	1.00E+00 (2%) 1.03E+00 (7%)
5.0	1 1	1.02E+00 (4%) 1.14E+00 (17%)	1.01E+00 (2%) 1.07E+00 (7%)	1.01E+00 (2%) 1.06E+00 (7%)	1.02E+00 (1%) 1.10E+00 (7%)	1.02E+00 (1%) 1.08E+00 (7%)
10.0	1 1	1.03E+00 (3%) 1.39E+00 (13%)	1.02E+00 (1%) 1.10E+00 (7%)	1.02E+00 (1%) 1.12E+00 (7%)	1.02E+00 (1%) 1.15E+00 (7%)	1.01E+00 (1%) 1.06E+00 (7%)
20.0	1 1	1.02E+00 (3%) 1.36E+00 (12%)	1.02E+00 (1%) 1.16E+00 (6%)	1.03E+00 (1%) 1.20E+00 (6%)	1.02E+00 (1%) 1.19E+00 (6%)	1.02E+00 (1%) 1.11E+00 (6%)
40.0	1 1	1.04E+00 (3%) 1.30E+00 (12%)	1.02E+00 (1%) 1.17E+00 (5%)	1.02E+00 (1%) 1.20E+00 (5%)	1.02E+00 (1%) 1.17E+00 (6%)	1.03E+00 (1%) 1.15E+00 (6%)

Table 33: Shielding efficiencies relative and normalized to Al for $\dot{D}$ (upper value) and $\dot{H}$ (lower value), followed by its combined absolute error (%) for the solar maximum of 2001 (Matthiä)

In order to more easily interpret the data included in Table 32 and Table 33 above, Figure 42 and Figure 43 below plot the shielding efficiencies for each areal density considered for the 2010 Solar Min and the 2001 Solar Max, respectively (the absolute errors are not visualized).

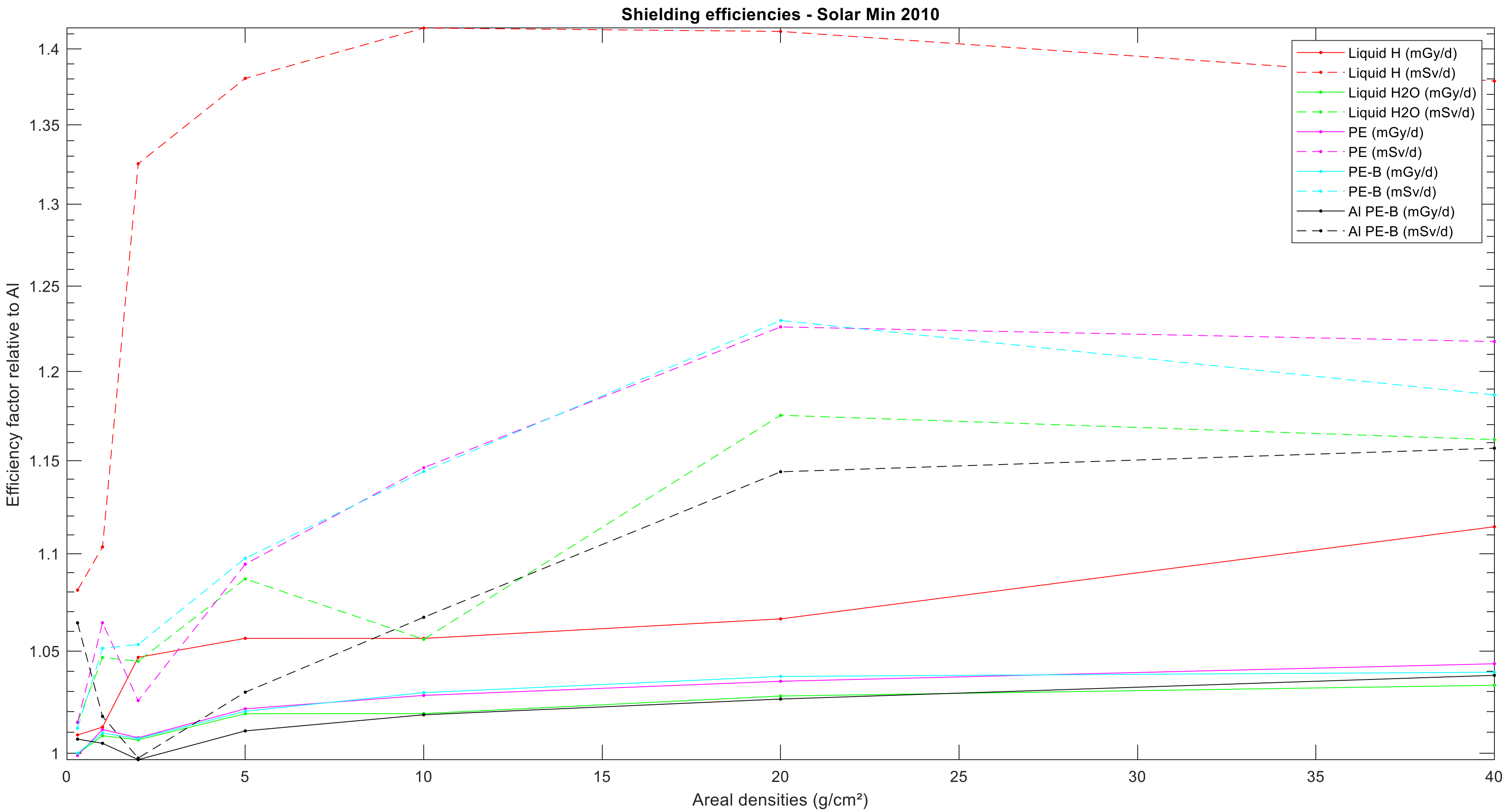

Figure 42: Shielding efficiencies relative and normalized to Al – GCR solar minimum of 2010 (Matthiä)

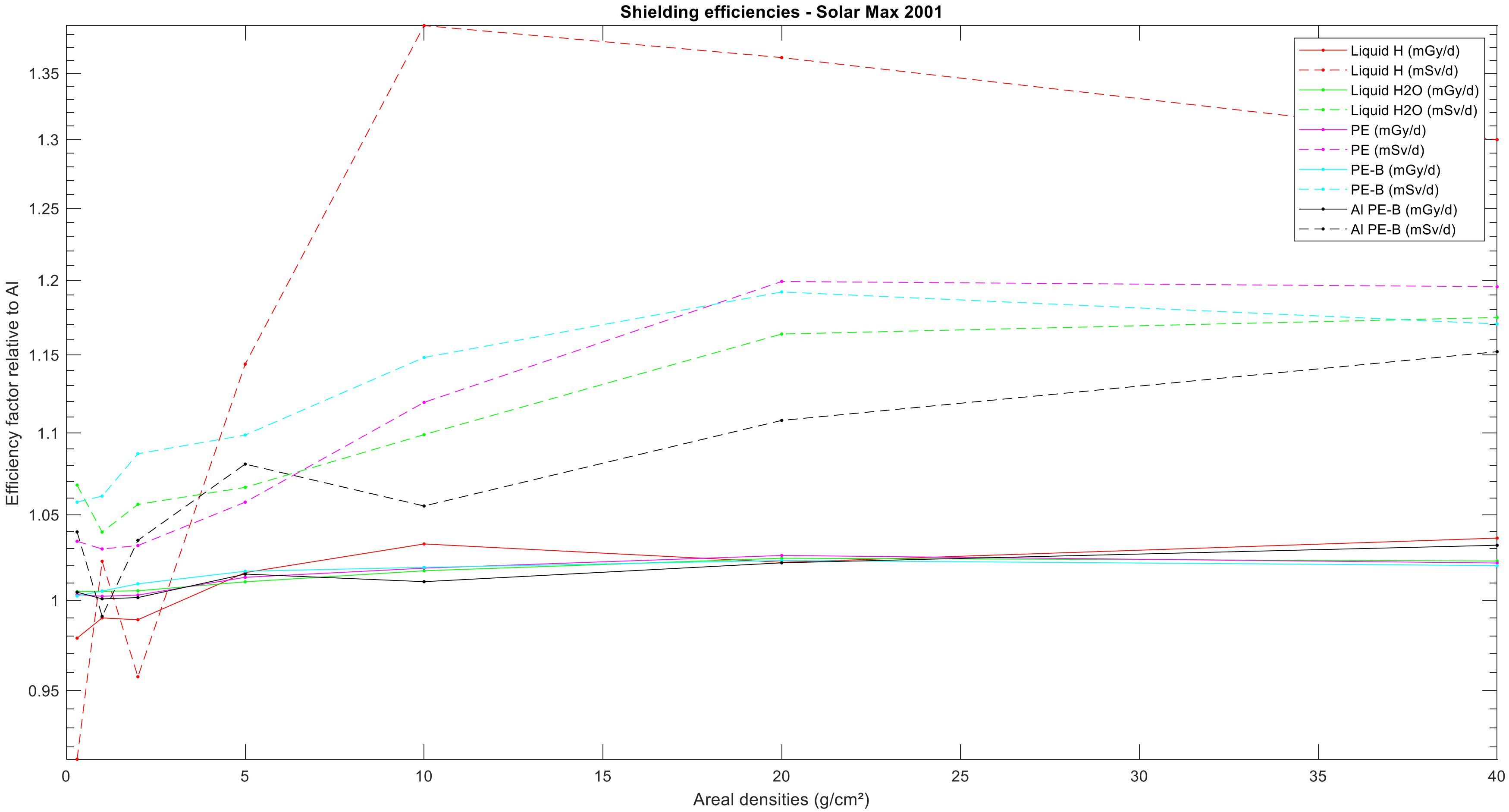

Figure 43: Shielding efficiencies relative and normalized to Al – GCR solar maximum of 2001 (Matthiä)

7.3.3.2. SPE

Table 34 below provides the shielding efficiencies for each areal density considered for the August 1972 (LaRC) SPE.

A combined absolute error[109] (%) is provided for each value. The latter is colored red when exceeding the limit of 10% (unreliability criteria).

		Shielding efficiencies – August 1972 (LaRC) SPE				
Areal density (g cm^{-2})	**Al** (reference)	**Liquid H**	**Liquid H_2O**	**Non-B PE**	**B PE**	**50% Al 50% PE-B**
0.3	1 1	1.25E+00 (1%) 1.28E+00 (1%)	1.05E+00 (0%) 1.05E+00 (0%)	1.06E+00 (0%) 1.07E+00 (0%)	1.05E+00 (0%) 1.06E+00 (0%)	1.03E+00 (0%) 1.04E+00 (0%)
1.0	1 1	1.73E+00 (1%) 1.79E+00 (1%)	1.12E+00 (0%) 1.13E+00 (0%)	1.16E+00 (0%) 1.17E+00 (0%)	1.14E+00 (0%) 1.15E+00 (0%)	1.08E+00 (0%) 1.08E+00 (0%)
2.0	1 1	2.23E+00 (1%) 2.31E+00 (1%)	1.17E+00 (0%) 1.18E+00 (0%)	1.18E+00 (0%) 1.20E+00 (0%)	1.15E+00 (0%) 1.17E+00 (0%)	9.73E-01 (0%) 9.78E-01 (0%)
5.0	1 1	4.90E+00 (3%) 5.25E+00 (3%)	1.41E+00 (1%) 1.44E+00 (1%)	1.54E+00 (1%) 1.56E+00 (1%)	1.48E+00 (1%) 1.50E+00 (1%)	1.23E+00 (0%) 1.23E+00 (1%)
10.0	1 1	1.13E+01 (7%) 1.23E+01 (8%)	1.71E+00 (1%) 1.76E+00 (1%)	1.95E+00 (1%) 2.03E+00 (1%)	1.82E+00 (1%) 1.88E+00 (1%)	1.34E+00 (1%) 1.36E+00 (1%)
20.0	1 1	4.86E+01 (29%) 4.32E+01 (42%)	2.31E+00 (2%) 2.52E+00 (2%)	2.93E+00 (2%) 3.16E+00 (2%)	2.63E+00 (2%) 2.79E+00 (2%)	1.60E+00 (2%) 1.59E+00 (2%)
40.0	1 1	/ /	3.32E+00 (5%) 4.22E+00 (5%)	4.73E+00 (6%) 6.16E+00 (6%)	4.06E+00 (6%) 4.91E+00 (6%)	1.86E+00 (4%) 2.08E+00 (4%)

Table 34: Shielding efficiencies relative and normalized to Al for D (upper value) and H (lower value), followed by its combined absolute error (%) for the August 1972 (LaRC) SPE

In order to more easily interpret the data included in Table 34 above, Figure 44 below plots the shielding efficiencies for each areal density considered for the August 1972 (LaRC) SPE (the absolute errors are not visualized).

[109] $Combined\ Abs.error = shielding\ efficiency * \sqrt{(Abs.error/dose)^2{}_{Al} + (Abs.error/dose)^2{}_{other\ materials}}$

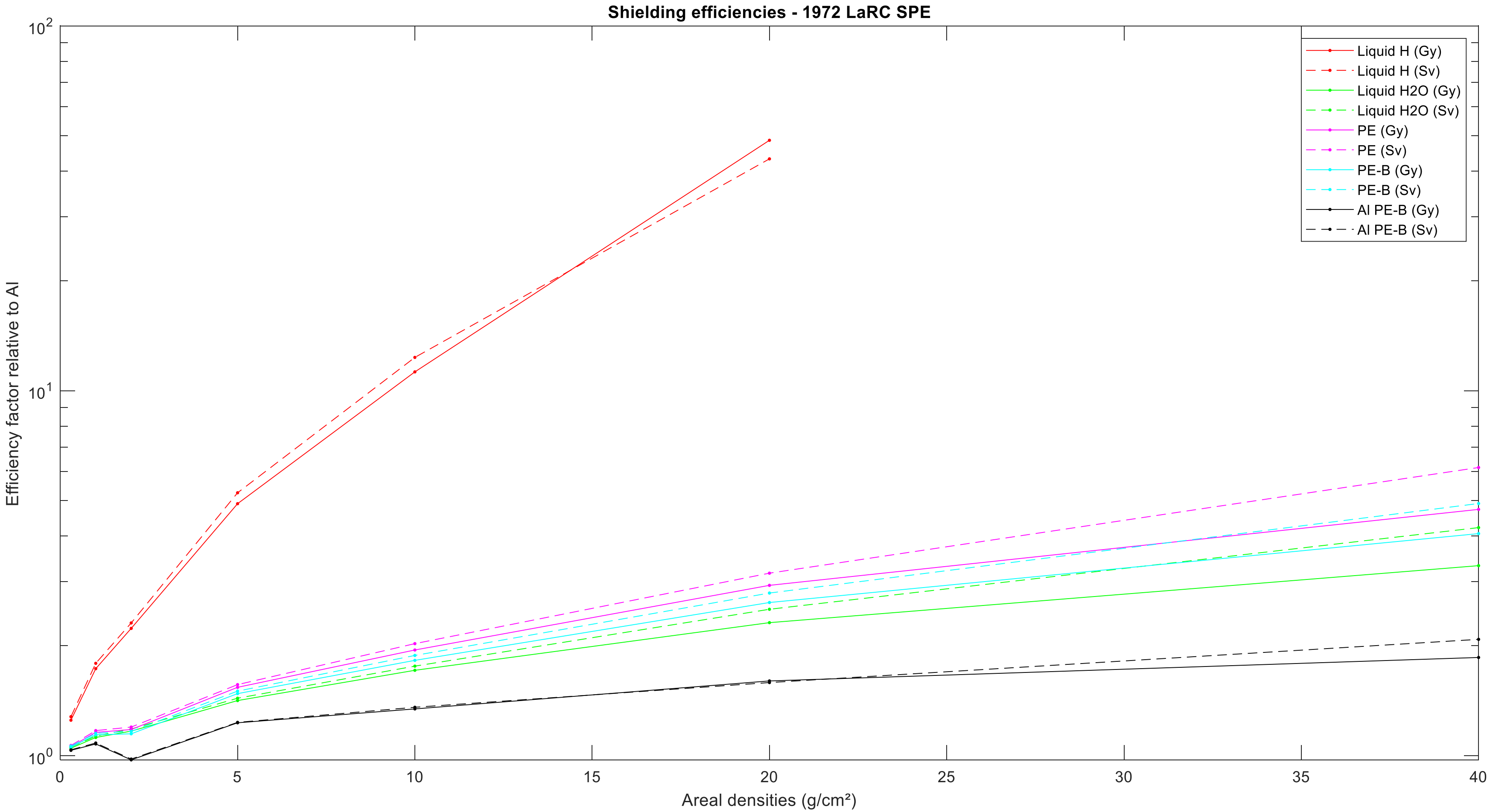

Figure 44: Shielding efficiencies relative and normalized to Al – August 1972 (LaRC) SPE

7.3.4. Discussion of results

7.3.4.1. GCR

Solar Min 2010

From the **absolute dose rates** (Table 25 and Figure 35), it can be concluded that:

- The absorbed dose rates are situated between 4.34E-01 and 4.37E-01 mGy/d for 0 g/cm². For the thickest shields (40 g/cm²), the latter's are situated between 4.01E-01 and 4.46E-01 mGy/d;
- The dose equivalent rates are situated between 1.32E+00 and 1.36E+00 mSv/d for 0 g/cm². For the thickest shields (40 g/cm²), the latter's are situated between 8.26E-01 and 1.01E+00 mSv/d (neglecting liquid H due to high uncertainties);
- All quality factors (ratio of the dose equivalent to the absorbed dose rates) are well-situated between ~2 and ~3 (not explicitly presented in Table 25);
- Note that for 0 g/cm², the dose rates should have the same numerical values as no shield introduced. Based on Table 25, one can however observe minor (negligible) differences in the dose rates at 0 g/cm². This likely follows from the fact that for each shielding material, the source is positioned at a fixed distance of 1 cm from the thickest shield of the concerned material (e.g. at 215.82 cm for Al while at 765.57 cm for liquid H). These differences give rise to slight differences in angular distribution and can therefore affect the unshielded dose rates (they will however converge if the amount of source particles increases);
- The absolute errors on the absorbed dose rates range between 1% and 4% for all materials and all thicknesses. The absolute errors on the dose equivalent rates range between 4% and 17% for all materials and all thicknesses. Indeed, the absolute errors on the dose equivalent rates are larger than those on the absorbed dose rates. This is likely due to the PHITS calculation mechanism of the quality factors which are then used to convert the absorbed dose rates into dose equivalent rates (based on RBE-LET relations as described in §4.1.3);
- It is noticeable that for the same material, the absolute errors first increase and then decrease with increasing shielding thickness (especially for the absolute errors on the dose equivalent rates). The increase noticed at first likely results from the fact that less particles are able to reach the target with increasing shielding thickness. The decrease afterwards could be due to the fact that, with increasing shielding thickness, the shield is positioned closer to the fixed source, hence decreasing the probability of particles escaping from the system without any interactions (i.e. without dose contribution to the target). Note that as the combined absolute errors of the dose reduction factors and the shielding efficiencies are derived from the absolute errors of the absolute dose rates, the combined absolute errors will not be discussed further.

From the **dose reduction factors** (Table 29 and Figure 39), it can be concluded that:

- For all materials, the absorbed dose rate reduction factors are nearly equal to 1 with increasing shielding thickness (i.e. virtually no reduction) due to the high energies of the primary particles. This is not true for liquid H, where a maximum absorbed dose rate reduction factor of 9.17E-01 is observed at 40 g/cm².

For Al, absorbed dose rate reduction factors higher than 1 are observed above 5 g/cm², indicating its counter effectiveness. In fact, as described in §3.3, it is known that GCR secondary particles, more particularly secondary neutrons, produced by nuclear interactions in the Al shield contribute significantly to the total absorbed dose rate with increasing shielding thickness, which can explain this counter effective effect;

- For all materials, the dose equivalent rate reduction factors are below 1 due to the introduction of shielding. In fact, it is observed that with increasing shielding thickness, the dose equivalent rate reduction factors decrease for all materials (except for non-B PE at 2 g/cm² and for the compound of Al B-PE at 1 g/cm²). The steepest reductions are observed at low shielding thicknesses. This effect flattens out above 10 g/cm² for all the materials. The effect of the decreasing dose equivalent rates with increasing shielding thickness is likely caused by nuclear interactions resulting in fragmentations of the heavy ion projectiles. As described in §3.3, this process can give rise to charged particles with roughly the same velocity as the incident ion but lower charge, and thus lower LET and biological effectiveness, resulting in lower quality factors;
- In general, the (absorbed) dose (equivalent) rate reduction factors are the lowest (best) for liquid H and the highest (worst) for Al (see further).

From the **shielding efficiencies** (Table 32 and Figure 42), it can be concluded that:

- For all shielding thicknesses, Liquid H yields the best shielding efficiency while the compound Al PE-B generally yields the worst shielding efficiency and this for both the absorbed dose and the dose equivalent rates. This observation is well in line with expectations, since materials with the lowest (effective) atomic number should provide the most efficient (heavy) ion shielding (§3.3);
- In general, it is observed that, with increasing shielding thickness, the 2nd to 4th best shielding materials are non-B PE, B PE and liquid H_2O. Based on this observation, it seems that although boron was added to the PE with the aim of decreasing the dose rates by absorbing the secondary neutrons produced in the shields, its presence rather works counter effectively because it increases the effective atomic number. Furthermore, it could also be that the secondary neutrons produced are not sufficiently thermalized by the PE, thereby reducing the effectiveness of the boron (as boron has a high thermal neutron absorption cross section). Note that the shielding efficiencies with and without B in the PE are very close to one another;
- For each material, the shielding efficiencies generally increase with increasing shielding thickness. This effect is especially true for the absorbed dose rates, and slightly less pronounced (fluctuating) for the dose equivalent rates.

Solar Max 2001

From the **absolute dose rates** (Table 26 and Figure 36), it can be concluded that:

- The absorbed dose rates are situated between 1.56E-01 and 1.58E-01 mGy/d for 0 g/cm². For the thickest shields (40 g/cm²), the latter's are situated between 2.02E-01 and 2.09E-01 mGy/d;
- The dose equivalent rates are situated between 5.05E-01 and 5.41E-01 mSv/d for 0 g/cm². For the thickest shields (40 g/cm²), the latter's are situated between 4.05E-01 and 4.84E-01 mSv/d (neglecting liquid H due to high uncertainties);

- All quality factors (ratio of the dose equivalent to the absorbed dose rates) are well-situated between ~2 and ~4 (not explicitly presented in Table 26);
- Note that for 0 g/cm², the dose rates should have the same numerical values as no shield is introduced. Based on Table 26, one can however observe minor (negligible) differences in the dose rates at 0 g/cm². This likely follows from the fact that for each shielding material, the source is positioned at a fixed distance of 1 cm from the thickest shield of the concerned material (e.g. at 215.82 cm for Al while at 765.57 cm for liquid H). These differences give rise to slight differences in angular distribution and can therefore affect the unshielded dose rates (they will however converge if the amount of source particles increases);
- The absolute errors on the absorbed dose rates range between 1% and 4% for all materials and all thicknesses. The absolute errors on the dose equivalent rates range between 3% and 17% for all materials and all thicknesses. Indeed, the absolute errors on the dose equivalent rates are larger than those on the absorbed dose rates. This is likely due to the PHITS calculation mechanism of the quality factors which are then used to convert the absorbed dose rates into dose equivalent rates (based on RBE-LET relations as described in §4.1.3);
- It is noticeable that for the same material, the absolute errors first increase and then decrease with increasing shielding thickness (especially for the absolute errors on the dose equivalent rates). The increase noticed at first likely results from the fact that less particles are able to reach the target with increasing shielding thickness. The decrease afterwards could be due to the fact that, with increasing shielding thickness, the shield is positioned closer to the fixed source, hence decreasing the probability of particles escaping from the system without any interactions (i.e. without dose contribution to the target). Note that as the combined absolute errors of the dose reduction factors and the shielding efficiencies are derived from the absolute errors of the absolute dose rates, the combined absolute errors will not be discussed further.

From the **dose reduction factors** (Table 30 and Figure 40), it can be concluded that:

- For all materials, except for the Al PE-B compound at 0.3 g/cm², the absorbed dose rate reduction factors are higher than 1 and increase with increasing shielding thickness, indicating their counter effectiveness. The most probable reason for this is that, compared to solar minimum, the fluxes of the primary source particles are lower but shifted to higher energies during solar maximum (Figure 20, Figure 22), giving rise to more secondaries by nuclear interactions in the shields. Indeed, secondary particles, especially secondary neutrons, can contribute significantly to the total absorbed dose rate with increasing shielding thickness (as described in §3.3), which explains this counter effective effect;
- For most materials, slightly different behaviours are observed for the dose equivalent rate reduction factors with increasing shielding thickness: For Al, the reduction factors decrease up to 20 g/cm² followed by a slight increase at 40 g/cm². For liquid H, alternating increases and decreases of the reduction factors are observed up to 5 g/cm² followed by a decrease at 10 g/cm² and increases up to 40 g/cm². For PE and B-PE, at first an increase is observed, following by decreasing reduction factors up to 20 g/cm², and an increase at 40 g/cm². For liquid H_2O and the Al B-PE compound, the reduction factors decrease and increase up to 1 g/cm² followed by decreases up to 20 g/cm²;

At 40 g/cm², an increase of the reduction factor is observed for liquid H_2O and a decrease for the Al B-PE compound. More importantly, besides the trends, it is observed that from 5 g/cm², for all materials, the reduction factors are below 1, pointing out their effectiveness, and that the latter's decrease with increasing shielding thickness (i.e. improving the effectiveness) up to 20 g/cm² (except for liquid H) after which they increase slightly (except for the Al PE-B compound). The general trend of decreasing dose equivalent rate reduction factors with increasing shielding thickness up to 20 g/cm² is most likely caused by nuclear fragmentation reactions in the shield (as explained earlier). The increase at 40 g/cm² could originate from the creation of more and more secondaries;

- From 5 g/cm², the (absorbed) dose (equivalent) rate reduction factors are the lowest (best) for liquid H and the highest (worst) for Al (see further).

From the **shielding efficiencies** (Table 33 and Figure 43), it can be concluded that:

- In terms of the shielding efficiency for the absorbed dose rates, up to 5 g/cm², B-PE performs the best, except at 0.3 g/cm² at which liquid H_2O performs better. From 10 g/cm², liquid H performs the best, except at 20 g/cm² at which PE performs better. Up to 2 g/cm², liquid H performs the worst. For 5 g/cm², liquid H_2O performs the worst. The Al B-PE compound performs the worst for 10 and 20 g/cm². At 40 g/cm², B-PE appears to perform the worst. In terms of the shielding efficiency for the dose equivalent rates, up to 2 g/cm², B-PE performs the best, except at 0.3 g/cm² at which liquid H_2O performs better. From 5 g/cm², liquid H performs the best. Up to 2 g/cm², liquid H performs the worst, except at 1 g/cm² at which the Al B-PE compound performs the worst. At 5 g/cm², PE performs the worst. From 10 g/cm², the Al B-PE compound performs the worst;
- In general, it can be concluded that below 5 g/cm², B-PE performs the best and liquid H the worst for both the absorbed dose and the dose equivalent rates. Above 5 g/cm², it can generally be concluded that liquid H performs the best (especially for the dose equivalent rates) and the Al B-PE compound the worst (especially for the dose equivalent rates) for both the absorbed dose and the dose equivalent rates. These general observations, at least above 5 g/cm², are in line with expectations, since materials with the lowest (effective) atomic number should provide the most efficient (heavy) ion shielding (§3.3);
- Up to 10 g/cm², with the exception of the shielding efficiency of the absorbed dose rate at 0.3 g/cm², it is observed that B-PE yields slightly higher shielding efficiencies than PE for both the absorbed dose and the dose equivalent rates. Above 10 g/cm², PE appears to perform better than B-PE for both the absorbed dose and the dose equivalent rates. This observation seems to point out that, above 10 g/cm², boron works counter effectively due to the increased effective atomic number (or since the secondary neutrons produced are not sufficiently thermalized by the PE). Note that the shielding efficiencies with and without B in the PE are very close to one another;
- For each material, the shielding efficiencies generally increase with increasing shielding thickness. This overall effect is observed to be more pronounced for the absorbed dose rates than for the dose equivalent rates.

The discussions above did not explicitly take into account the magnitude of the absolute errors. Hence, the overall trends/observations can be considered as valid, but the numerical values must be interpreted with care (especially for liquid H).

General discussion on GCR

As expected, the magnitudes of the absolute (absorbed) dose (equivalent) rates are the highest during solar minimum and the lowest during solar maximum. For the unshielded configurations, the absorbed dose rates and dose equivalent rates are, respectively, factors ~2.8 and ~2.6 higher when comparing solar minimum to solar maximum. For the thickest shielding configurations (40 g/cm²), these factors are reduced to ~2.1 and ~2.0, respectively (averaged over all shielding materials). For all configurations considered (thicknesses and materials), the quality factors are well-situated between ~2 and ~4 during both solar activities.

During solar minimum, it is overall observed that the absorbed dose rates remain nearly constant while the dose equivalent rates decrease with increasing thickness for all materials. During solar maximum, on the other hand, it is overall observed that the absorbed dose rates increase with increasing thickness for all materials while the dose equivalent rates generally decrease (though less than during solar minimum) up to a certain thickness and then slightly increase for all materials. This "Solar activity – Dose rate behaviour" likely follows from the fact that, compared to solar minimum, the fluxes of the primary GCR particles during solar maximum are lower but shifted to considerably higher energies (§6.2.1), making them harder to shield and producing more secondaries which can contribute to the dose rate. In fact, as discussed in §3.3, the influence of shielding on the dose rates is also dependent on the energy spectra of the GCR particles which changes with solar activity. More particularly, a study for near-Earth interplanetary space pointed out that the reduction in dose equivalent rate by adding a certain thickness of Al was stronger during solar minimum opposed to during solar maximum (Ref. [8]). This solar activity effect has also been observed in this work.

In terms of shielding efficiency, it is generally observed that for both solar activities Liquid H yields the best shielding efficiency (above 5 g/cm² for solar maximum) while the compound Al PE-B generally yields the worst shielding efficiency with increasing shielding thickness, and this for both the absorbed dose and the dose equivalent rates. This observation is well in line with expectations, since materials with the lowest (effective) atomic number should provide the most efficient (heavy) ion shielding (§3.3).

In terms of using PE with or without B, it was observed that during solar minimum boron rather worked counter effectively while during solar maximum the opposite effect was observed up to 10 g/cm², above which boron also appeared to work counter effectively. The overall counter effectiveness of the addition of boron (with increasing thickness) could be due to the increased (effective) atomic number of the PE. These observations with/without B were however not strongly pronounced.

Lastly, in terms of material, the highest errors were clearly observed for liquid H. This likely results from its superior shielding effect and the fact that for liquid H the source is located the furthest from the target, both decreasing the probability of particles reaching the target. In terms of doses, the highest errors were observed for the dose equivalent rates which likely follows from the calculation mechanism of the quality factors.

7.3.4.2. SPE

August 1972 (LaRC) SPE

From the **absolute doses** (Table 27 and Figure 37), it can be concluded that:

- The absorbed doses are situated between 1.91E+00 and 1.92E+00 Gy for 0 g/cm². For the thickest shields (20 g/cm² for liquid H and 40 g/cm² for the other materials), the latter's are situated between 1.08E-03 and 5.09E-03 Gy (liquid H was neglected due to high uncertainties);
- The dose equivalents are situated between 2.90E+00 and 2.91E+00 Sv for 0 g/cm². For the thickest shields (20 g/cm² for liquid H and 40 g/cm² for the other materials), the latter's are situated between 3.52E-03 and 2.17E-02 Sv (liquid H was neglected due to high uncertainties);
- All quality factors (ratio of the dose equivalents to the absorbed doses) are well-situated between ~1 and ~4 (not explicitly presented in Table 27);
- Note that for 0 g/cm², the dose rates should have the same numerical values as no shield is introduced. Based on Table 27, one can however observe minor (negligible) differences in the dose rates at 0 g/cm². This likely follows from the fact that for each shielding material, the source is positioned at a fixed distance of 1 cm from the thickest shield of the concerned material (e.g. at 215.82 cm for Al while at 765.57 cm for liquid H). These differences give rise to slight differences in angular distribution and can therefore affect the unshielded dose rates (they will however converge if the amount of source particles increases);
- The absolute errors on the absorbed doses range between 0% and 6% for all materials and all thicknesses (apart from liquid H where a maximum absolute error of 29% is observed). The absolute errors on the dose equivalents range between 0% and 6% for all materials and all thicknesses (apart from liquid H where a maximum absolute error of 42% is observed). The large absolute errors particularly on liquid H most likely result from its superior shielding effect compared to the other materials and the fact that the source is located much further from the target, both causing that much less particles are able to reach the target. The absolute errors on both doses are similar for all materials which likely follows from the fact that no or negligible nuclear fragmentation reactions occur (compared to GCR). For liquid H, it is observed that, above 5 g/cm², the absolute errors on the dose equivalents are larger than those on the absorbed doses which is likely due to the PHITS calculation mechanism of the quality factors which are used to convert the absorbed doses into dose equivalents (based on RBE-LET relations as described in §4.1.3). Note that at 20 g/cm², both dose results for liquid H are unreliable due to the high uncertainties;
- It is noticeable that for the same material, the absolute errors increase with increasing shielding thickness. This increase most likely results from the fact that much less particles are able to reach the target with increasing shielding thickness. For SPE, the shielding effect appears to be more important than the geometrical effect (position of the shield with respect to the target) as was observed for GCR. Note that as the combined absolute errors of the dose reduction factors and the shielding efficiencies are derived from the absolute errors of the absolute doses, the combined absolute errors will not be discussed further.

From the **dose reduction factors** (Table 31 and Figure 41), it can be concluded that:

- For all materials, the absorbed dose and dose equivalent reduction factors are below 1 due to the introduction of shielding. Moreover, it is observed that with increasing shielding thickness, both dose reduction factors strongly decrease for all materials, pointing out the effectiveness of the shield and the rather low importance of secondary particles. Note that above 10 g/cm² (thick shields), it is observed that for all materials, the dose equivalent reduction factors become higher (i.e. worse) than the absorbed dose reduction factors, which could be explained by the secondary particles (likely predominantly neutrons) produced through nuclear interactions in the shields. These observation are fully in line with studies performed in literature (with Al only), as discussed in §3.3;
- In general, the (absorbed) dose (equivalent) reduction factors are the lowest (best) for liquid H and the highest (worst) for Al (see further).

From the **shielding efficiencies** (Table 34 and Figure 44), it can be concluded that:

- For all shielding thicknesses, Liquid H yields the best shielding efficiency while the compound Al PE-B yields the worst shielding efficiency and this for both the absorbed doses and the dose equivalents. This observation is well in line with expectations, since materials with the lowest (effective) atomic number should provide the most efficient shielding against ions (§3.3);
- It is observed that, for all shielding thicknesses, the 2nd to 4th best shielding materials are non-B PE, B PE and liquid H_2O (except at 2 g/cm², at which liquid H_2O appears to perform better than B PE). Based on this observation, it seems that although boron was added to the PE with the aim of decreasing the doses by absorbing the secondary neutrons produced in the shields, its presence rather works counter effectively as it increases the effective atomic number. Furthermore, it could also be that the secondary neutrons produced are not sufficiently thermalized by the PE, thereby reducing the effectiveness of the boron (as boron has a high thermal neutron absorption cross section). Note that the shielding efficiencies with and without B in the PE are very close to one another up to 10 g/cm², above which non-B PE performs noticeably better;
- For each material, the shielding efficiencies increase with increasing shielding thickness and this for both the absorbed doses and dose equivalents (except for the Al PE-B compound at 2 g/cm²).

The discussions above did not explicitly take into account the magnitude of the absolute errors. Hence, the overall trends/observations can be considered as valid, but the numerical values must be interpreted with care (especially for liquid H).

Sum of October 1989 Tylka Band fits SPE

As discussed in §7.3.1.2, due to the general unreliability of the doses (Table 28), neither the dose reduction factors nor the shielding efficiencies were calculated for the Sum of October 1989 Tylka Band fits SPE. No results are thus discussed for the latter SPE.

General discussion on SPE

In contrast to the reliable results obtained for the August 1972 (LaRC) SPE, the Sum of October 1989 Tylka Band fits SPE yielded unreliable results above 1 g/cm² (§7.3.1.2). Nevertheless, up to 1 g/cm², it was observed that the magnitudes of the absolute absorbed doses and dose equivalents are the highest for the Sum of October 1989 Tylka Band fits SPE. For 0 g/cm², the absorbed doses and dose equivalents are, respectively, factors ~58.8 and ~66.1 higher when comparing the Sum of October 1989 Tylka Band fits SPE to the August 1972 (LaRC) SPE.

The following main observations are made for the August 1972 (LaRC) SPE:

- The quality factors are well-situated between ~1 and ~4 for all configurations considered (thicknesses and materials);
- The absorbed doses and dose equivalents drastically decrease with increasing shielding thickness and this for all materials, pointing out the effectiveness of the shields and the low importance of secondary particles. These observation are well in line with studies performed in literature (Ref. [3], [4]), as discussed in §3.3;
- In terms of shielding efficiency, Liquid H yields the best shielding efficiency while the compound Al PE-B generally yields the worst shielding efficiency with increasing shielding thickness, and this for both the absorbed dose and the dose equivalent. This observation is well in line with expectations, as materials with the lowest (effective) atomic number should provide the most efficient (heavy) ion shielding (§3.3);
- In terms of using PE with or without B, boron rather worked counter effectively. The overall counter effectiveness of the addition of boron could be due to the increased (effective) atomic number of PE. These overall observations with/without boron were however not strongly pronounced, except at thicker shields (i.e. above 10 g/cm²), at which non-B PE performed noticeably better than the PE with boron;
- The highest absolute errors were observed for liquid H. This likely results from its superior shielding effect causing significantly less particles reaching the target. Overall, the absolute errors on both doses were observed to be similar.

The Sum of October 1989 Tylka Band fits SPE was discarded following the overall unreliability of the dose results (Table 28), hence no further analyses were done.

7.3.4.3. GCR AND SPE

Based on the discussions of GCR and SPE as provided in §7.3.4.1 and §7.3.4.2, respectively, the following main **conclusions** in terms of shielding can be drawn.

Neglecting the fact that GCR is expressed as a dose rate and SPEs as a dose, it is directly noticeable that the orders of dose magnitudes are completely different for both space radiation components. More particularly, unshielded, GCR doses are typically situated in the orders of mGy and mSv (per day) while SPE doses can range up to hundreds of Gy's and Sv's. Nevertheless, it has been observed that, clearly, **SPEs** are much **easier** to **shield** against compared to **GCR**.

This can be explained by the fact that, on one hand, the SPE particle spectrum mainly (in this work exclusively) consists of energic protons compared to the GCR particle spectrum which consists of particles ranging from protons up to Ni ions, and on the other hand, that, compared to GCR, the SPE particle spectrum is pushed to much higher intensities but shifted to significantly lower energies (e.g. compare Figure 20 to Figure 23). Energetic GCR heavy ions have the tendency to fragment, producing lighter dose-contributing secondary charged particles, an effect which is not observed for SPEs. Because of these reasons, SPE particles are generally much easier to shield against compared to GCR particles.

Light materials have shown to have superior (passive) shielding characteristics to aluminum for both GCR and SPE due to the high hydrogen content[110]. In fact, in terms of shielding efficiency, it has been observed that for both GCR and SPE, **Liquid H** overall yields the **best** shielding efficiency while the compound **Al PE-B** generally yields the **worst** shielding efficiency with increasing shielding thickness, and this for both the absorbed dose (rates) and the dose equivalent (rates).

Furthermore, although the results were generally not strongly pronounced, it has been observed that adding **boron** to the PE generally works **counter effectively** for both the absorbed dose (rates) and the dose equivalent (rates) as it increases the (effective) atomic number of the PE.

Based on the above, it can be concluded that, fortunately, light materials provide effective radiation shielding against the moderately intensive but permanent GCR, as well as against the stochastic but brutally intensive SPEs. These **observations** are well **in line with** the conclusions drawn by **NASA** as they have demonstrated that the higher the overall hydrogen content of the material, the better the radiation shielding effectiveness against both GCR and SPE (Ref. [67]).

Besides passive **shielding** (materials and thicknesses), it has been observed that the decrease of the dose (rate) also **depends on** the **solar activity**. For GCR, the shielding effect showed to be stronger during solar minimum opposed to during solar maximum. For SPEs, the shielding effect showed to be stronger during “less intensive” (i.e. lower fluences) solar outbursts[111]. Hence, one can conclude that for GCR and SPE, the shielding effect is the strongest during lower solar activities.

As overall **bounding case** for designing radiation shielding for GCR and SPE in deep space, one ideally considers the **most intensive solar minimum** as during the latter, the GCR dose rates are considerably higher opposed to during solar maximum (although the shielding effect is weaker during the latter). Once the passive shield has been optimized for GCR (solar minimum), effective shielding against SPEs should inherently be included as the latter’s are fairly easy to shield against independent of the solar activity.

[110] Note that both GCR and SPE environments are dominated by protons (Ref. [53]).
[111] This statement is supported by dose results up to thicknesses of 1 g/cm² only (reliable statistics for both SPEs).

7.4. Earthly dose rates in deep space

In the framework of radiation protection, one could ask which thickness of a material would be required in space[112] in order to reach dose rates typically encountered on Earth as the sole consequence of the permanent cosmic background radiation.

Following this, the aim of this chapter is to determine which thickness of a material is required in deep space to reach the average Earthly dose rates solely due to cosmic radiation. In order to evaluate this scenario, a target dose rate of ~1 μSv/d will be considered as the UNSCEAR (United Nations Scientific Committee on the Effects of Atomic Radiation) reported that the (worldwide) annual average dose particularly due to cosmic radiation is equal to 0.39 mSv (Ref. [68]).

To obtain such low dose rates in deep space, it is required to introduce significant amounts of shielding to drastically decrease the permanent background radiation. When using such thick shields, the simulation time can easily take up several days for producing desirable Monte Carlo statistics[113]. However, as indicational rather than accurate values are in our interest for this particular study, higher statistical errors were accepted (the relative errors can be reduced by increasing the initial amount of source particles considered).

The input data used for this Earthly dose rate analysis will be described in §7.4.1 while the results will be discussed in §7.4.2.

Note that this additional analysis has only been performed for the permanent GCR since effective shielding against GCR has shown to be also effective against SPE.

7.4.1. Input parameters for modelling in PHITS

In terms of geometry, the same setup as defined in §6.4.3.1 was considered.

As shielding materials, Al and PE were considered. Al was chosen as it represents a non-light reference material, while PE represents a light material which can fairly easily be used in practice compared to, for example, liquid H or liquid H_2O.

As spectral data, the solar minimum of 2010 (Matthiä model) was considered (highest dose rates cf. §7.3.4.1). The amount of source particles was fixed at 1E7.

The same material compositions and densities, parameter section and tallies as defined in §6.4.3.4, §6.4.3.5, and §6.4.3.6, respectively, were considered.

Since it was initially not known which areal density would yield Earthly dose rates in deep space, multiple radiation transport calculations were performed for both Al and PE. The results are presented below (§7.4.2).

7.4.2. Outcome of radiation transport calculations

Figure 45 and Figure 46 below plot the dose equivalent rates in function of the areal density for Al and PE, respectively. The error bars are visualized on the plots.

[112] At a distance of 1 AU from the Sun.
[113] Reliable Monte Carlo statistics are often defined by the criteria in which the rel. error (statistical uncertainty) < 10%.

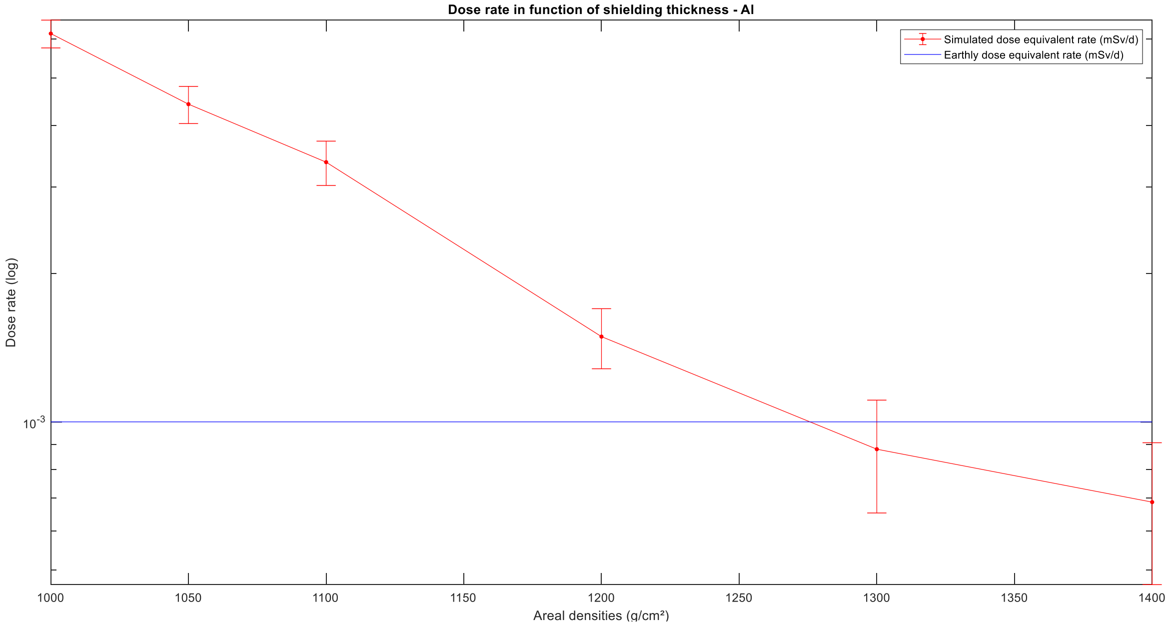

Figure 45: Dose equivalent rates in function of areal density for Al

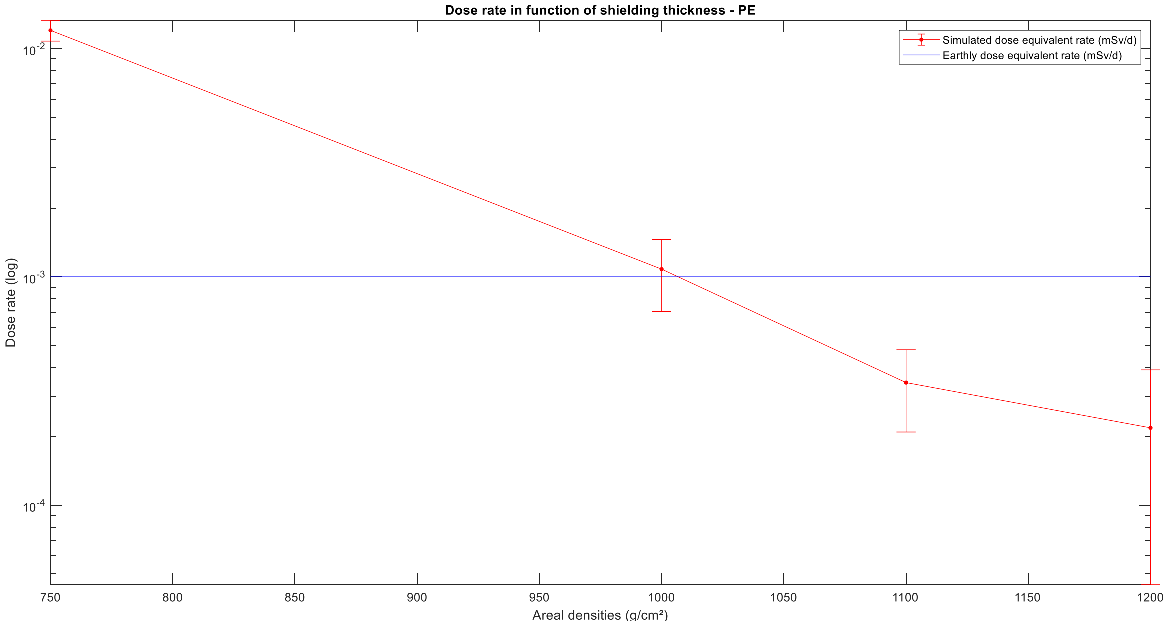

Figure 46: Dose equivalent rates in function of areal density for PE

Based on the results above, it can be concluded that **~1300 g/cm²** (~482 cm) of **Al** and **~1000 g/cm²** (~1075 cm) of **PE** would be required to reach the (worldwide average) Earthly cosmic background radiation (~1 μSv/d).

It must however be noted that the simulation times were significant to obtain the results provided above. For example, for Al, it took ~7 days to obtain the dose rate results at 1300 g/cm² with an absolute error of 26%, while for PE, it took ~4 days to obtain the dose rate results at 1000 g/cm² with an absolute error of 35%.

Following the long simulation times, ideally, VRT (§6.4.1.3) should be implemented in PHITS[114] with the objective of speeding up the simulation time without affecting the average value of the physical quantities tallied (dose/source and flux/source).

As a reminder, the main idea behind VRT is to split the incoming particle in more particles by reducing their weight. For example, if the incoming particle is doubled, their weight will be reduced by half. This process will not affect the average value of the physical quantities and can thus be introduced safely. Note that in case of many source particles, the average quantities will always converge to the same values using VRT. With a given number of source particles, the convergence will however be different between each technique and how it is used.

For studies on Earth, VRT are typically used to simulate the transport of neutrons through a shield (e.g. through the walls of the reactor pit). In such cases, VRT are implemented fairly easily by considering a certain amount of importance regions in which the importance increases with a factor ~2 between adjacent regions.

Following the undesired results[115] of multiple attempts, it has been concluded that implementing VRT in the complex space environment using the geometrical setup as defined in §7.4.1 is not straightforward. Indeed, a large fraction of the ions are stopped in the thick shield when attempting to reach Earthly dose rates in deep space (especially heavy ions, cf. §2.1.1.1). Only particles with sufficiently high energies are expected to have ranges which can penetrate through the shield. Furthermore, geometrical issues arise when using thick shields. For example, for 1000 g/cm² (370.37 cm) of Al, the source is positioned at a radial distance of 571.37 cm from the center while the target has a comparatively small radius of 25 cm, as illustrated in Figure 47 below (the source is not visualized).

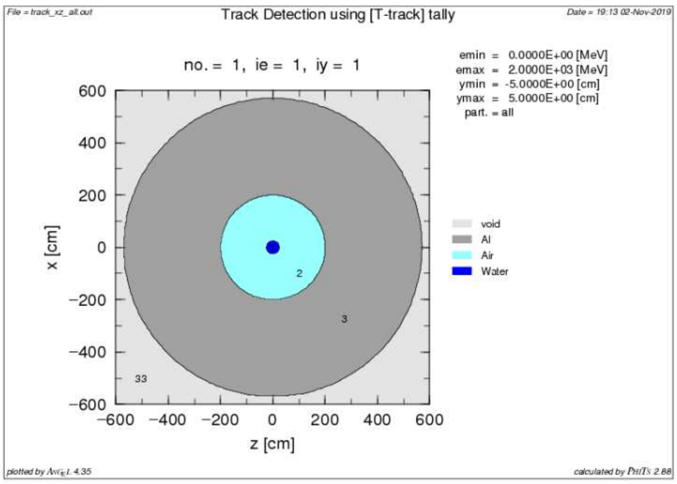

Figure 47: Illustration of the geometrical setup using 1000 g/cm² (370.37 cm) of Al shielding

Hence, even if a small fraction of particles would succeed in penetrating through the shield and reach the air volume, the probability that these particles will reach and deposit a dose in the small water sphere is small. Due to time restrictions and the fact that overall satisfying indicational values were obtained without VRT, further optimization of VRT was not performed (discussed as future work in §9).

[114] In PHITS, three VRT are available: forced collision, weight window (energy range), and importance function.
[115] Long simulation times and/or high Monte Carlo relative errors (i.e. poor Monte Carlo efficiencies).

7.5. General insights

In the previous chapters, the outcome of the radiation transport calculations have been discussed. In this chapter, particularities and practical considerations in the framework of space radiation protection will be addressed in order to better situate the results produced in this work.

7.5.1. Reliability of results and comparison of codes

In literature there is a lack of knowledge/data on heavy ions, high-energy charged particles, and on cross-sectional data for light fragments and neutrons which can impair the overall reliability of the results produced (Ref. [1]):

(90) *For neutrons and alpha particles, a broad range of experimental data for many different biological endpoints exists, including data from animals; however, the situation for high-energy charged particles is more problematic. Epidemiological data on cancer induction in humans from exposure to high-energy particles and heavy ions are not available, and experimental data on cancer induction in animals are scarce. Most RBE data for high-energy protons and heavy ions have been obtained from experiments with cells at high doses (>1 Gy) and high dose rates which are of particular interest for heavy-ion radiotherapy applications, with only a few studies of tumours in mice*.

(338) *The physics at the basis of the particle transport and cross-sectional data tables must be improved to further develop the computational methods. There is a lack of experimental cross section data for light fragments and neutrons. Codes need to be improved to treat all primary and secondary cascades including photons, protons, light ions, heavy ions, mesons, and electromagnetic cascades. The nuclear interaction database needs to be updated, especially for neutrons and light ions*.

Hence, the absolute dose results produced in this work should be interpreted with caution, even if reliable Monte Carlo outputs were obtained.

In terms of comparing different Monte Carlo codes, it is not straightforward to point out exact differences between different transport codes (e.g. PHITS vs. GEANT4). In order to do so, one should thoroughly analyse the transport codes and compare the underlying physics models, cross-sectional libraries, etc. Such analyses were therefore considered as out of scope for this work. Nevertheless, overall satisfying agreements between different transport codes were observed.

7.5.2. Practicability of light materials

While space vehicles are constructed largely of Al, light materials such as H_2O and PE have shown to have superior (passive) shielding characteristics to Al.

However, in terms of practical use, it must be noted that H_2O is a liquid and not a structural material. Hence, H_2O could only be considered as part of the shielding concept as it is a required consumable for all human exploration missions. PE, on the other hand, is a solid material but it does not have the required strength and thermal stability for space applications. PE also has outgassing and flammability issues and should be encapsulated for many applications (Ref. [67]).

As practical material, the NASA believes that crystalline boron nitride nanotubes[116] (BNNT) are ideal shielding materials as they can hold much H. Also their structural needs have been verified and confirmed. NASA studies have indicated that H with BNNT may offer excellent shielding effectiveness against GCR and SPE. When spacecraft wall thicknesses and forms of materials are considered, NASA points out that boron nitride (BN) materials perform better than liquid H and H_2O. BN with 5% of H has shown to perform better than state-of-the-art PE (Ref. [67]). Future studies should be performed using such novel materials (discussed in §9).

Irrespectively of the material choice, adding mass solely for shielding purposes is considered as unpalatable due to the limited launch capabilities and the mass inherently required to sustain astronauts for long periods of time in space. Hence, alternative shielding options have been studied (Ref. [58]). Compacted astronaut waste, for example, is an attractive alternative since no additional mass would be required. For this, NASA is developing "Heat Melt Compactor technology" with the aim of constructing a device that can compact waste, recover water from the waste, and produce a stable tile suitable for radiation shielding. The aim is to use Heat Melt Compactor material instead of PE as shielding as it requires no dedicated mass solely for radiation shielding purposes. Preliminary studies demonstrated that the (hypothetical) Heat Melt Compactor material exhibits favorable radiation shielding characteristics as they were shown to be similar to PE (Ref. [58]).

7.5.3. Optimal dose reduction strategy

Among the physical counter measures, passive shielding is the only one presently available. Even though novel shielding materials could lead to a significant dose reduction, it is unlikely that they will provide sufficient passive shielding to reduce the dose to acceptable levels within the weight constraints of the launchers.

Nevertheless, independent of the materials chosen, one could try to optimize the passive protection by altering the spacecraft's internals (rearranging the interiors) and/or by improving the intrinsic radiation hardness of critical components. Active shielding methods, on the other hand, are very promising but have shown to be not mature yet. According to literature (Ref. [48], [55]), the optimal solution to the space radiation problem, as well as to other health risks related to microgravity and confinement, would be the reduction of the space transit time. This could be achieved by using nuclear propulsions (potentially a combination of thermal and electric nuclear power). Major developments are however required in this field.

Indeed, and as pointed out in Ref. [48], the first travelers to Mars will likely benefit from a combination of different approaches: passive shielding using light materials (including a SPE storm shelter) and a reduced transit time, with the latter taking into account trajectory and timing (at solar minimum the probability on SPEs is reduced while at solar maximum the constant GCR exposure is reduced). Active shielding and nuclear propulsions are possibilities for future space missions. The use of so-called radio-protective drugs are also being investigated (Ref. [30]).

[116] BNNT has a molecular nanotube structure and has a density of 1.3 – 1.4 g/cm³ (Ref. [67]).

8. CONCLUSIONS

8.1. Context

This work focused on performing radiation transport calculations for optimizing the shielding efficiency against GCR and SPE at a distance of 1 AU from the Sun with the aim of reducing the astronauts' dose uptake during long-duration deep space explorations missions.

The effect of shielding on the dose (rate) has been investigated for liquid H, liquid H_2O, non-borated polyethylene, borated polyethylene and a compound consisting of aluminium and borated polyethylene (light materials). Plain aluminium, being a non-light material, was used as a reference material (for benchmarking purposes).

Enveloping and/or worst-case GCR and SPE spectral data (source terms) were considered in the radiation transport calculations. The simulations were performed for each source term individually (i.e. separately for GCR and SPE). This was done because the moment of occurrence of both radiation components is different in time. GCR is continuously present in space (dose rate), while SPE radiation only lasts for a few hours or days and virtually gives rise to an instant exposure (dose). Hence, the spectral data was integrated over different time intervals.

A realistic three-dimensional setup was considered for the geometries as well as for the source term distributions and this for all shielding configurations analyzed.

GCR dose rates were benchmarked against a GEANT4-based study performed in literature while SPE doses were benchmarked against a GEANT4-based tool developed by ESA. The results confirmed the reliability of the radiation transport calculations and the dose (rate) calculation methodology.

8.2. Outcome

Based on the results obtained by evaluating the dose reduction and the shielding efficiency of different **light materials** against GCR and SPE[117] at a distance of 1 AU from the Sun (outside the Earth's magnetosphere), it has been observed that light materials have **superior** (passive) shielding characteristics to aluminium for both GCR and SPE because of the high hydrogen content[118].

In fact, in terms of shielding efficiency, it has been observed that for both GCR and SPE, **Liquid H** overall yields the **best** shielding efficiency while the compound **Al PE-B** generally yields the **worst** shielding efficiency with increasing shielding thickness (among the materials evaluated), and this for both the absorbed dose (rates) and the dose equivalent (rates).

[117] Including secondary radiations produced by interactions of primary sources with the human body and shielding material.
[118] Note that both GCR and SPE environments are dominated by protons (Ref. [53]).

The effectiveness of the addition of **boron**, a material with a high thermal neutron absorption cross section, to a shield of polyethylene has also been evaluated with the aim of providing improved shielding efficiencies against secondary neutrons created through nuclear interactions of primary source particles with matter. It has however been observed that adding boron to polyethylene overall works **counter effectively** for both the absorbed dose (rates) and the dose equivalent (rates). This effect is most likely related to the fact that boron increases the (effective) atomic number of the PE (hence decreasing the shielding effectiveness), but it could also follow from the fact that the secondary neutrons were not sufficiently thermalized by the PE, thereby reducing the effectiveness (i.e. effective range) of the boron.

In general, it can be concluded that light materials provide effective radiation shielding against the moderately intensive but constant GCR, as well as against the stochastic but brutally intensive SPEs. These **observations** are **in line with** studies performed by the **NASA** as they have shown that the higher the hydrogen content of the shield, the better the shielding effectiveness against GCR and SPE.

In terms of **GCR**, it has been observed that the (absorbed) dose (equivalent) rates were the highest during solar minimum, an observation which is in line with solar cycle expectations. During solar minimum, it has been observed that the absorbed dose rates remained nearly constant while the dose equivalent rates decreased with increasing thickness for all materials. During solar maximum, it has overall been observed that the absorbed dose rates increased with increasing thickness for all materials while the dose equivalent rates generally decreased (though less than during solar minimum) up to a certain thickness and then slightly increased for all materials. This “Solar activity – Dose rate” behaviour likely follows from the fact that during solar maximum periods the fluxes of the primary GCR particles are lower but shifted to higher energies opposed to during solar minimum periods, making them harder to shield and produce secondaries which contribute to the dose. These GCR observations are well in line with studies performed in literature.

In terms of **SPE**, it has been observed that the absolute absorbed doses and dose equivalents were the highest for the Sum of October 1989 Tylka Band fits SPE, which is in line with expectations as the latter SPE has the highest fluences over virtually the entire energy range. Moreover, it has been observed that the overall SPE dose reductions are the strongest during less intensive solar outbursts. The latter observations are however only supported by results for shielding thicknesses up to 1 g/cm², since above the latter unreliable results were produced for the Sum of October 1989 Tylka Band fits SPE. For the August 1972 (LaRC) SPE, it has overall been observed that the absorbed doses and dose equivalents dramatically decreased with increasing shielding thickness and this for all materials, pointing out the effectiveness of the shields and the low importance of secondary particles. These SPE observations are well in line with studies performed in literature.

Consequently, by analysing the effect of shielding to GCR and SPE, it has clearly been observed that **SPEs** are much **easier to shield** against **compared to GCR**. This can be explained by the fact that, on one hand, the SPE particle spectrum mainly consists of energic protons compared to the GCR particle spectrum which ranges from protons up to Ni ions, and on the other hand, that, compared to GCR, the SPE particle spectrum is pushed to higher intensities but shifted to significantly lower energies. Indeed, fragmentation of GCR heavy ions can produce important dose-contributing secondary particles, an effect which is not observed for SPEs.

Besides passive shielding, it has been observed that the dose (rate) reduction is also dependent on the solar activity. More particularly, it has been observed that the **shielding effect** against GCR and SPE is the **strongest** during **lower solar activities**. Nevertheless, one could opt to travel during solar maximum periods as this would decrease the permanent GCR exposure. The disadvantage of the latter approach would however be the increased probability on severe SPEs[119].

As overall **bounding case** for passive shielding design in deep space, one ideally considers the **most intensive solar minimum** as during the latter the GCR dose rates are the highest. Once the passive shield has been optimized for GCR (solar minimum), effective shielding against SPEs should inherently be included as the latter's are fairly easy to shield against independent of the solar activity.

Lastly, in the framework of space radiation protection, it has been evaluated which thickness of a material would be required in deep space (1 AU) to reach the Earthly cosmic background radiation (~1 μSv/d). The results estimated that ~1300 g/cm² (~482 cm) of Al and ~1000 g/cm² (~1075 cm) of PE would be required.

[119] In reality the simultaneous occurrence of worst-case scenarios for GCR and SPEs is very unlikely. Nevertheless, even though SPEs are more likely to occur around solar maximum, such events are at present unpredictable. Following this, it cannot be assumed that SPEs will not occur under solar minimum conditions.

9. FUTURE WORK

It must be stated that not all scenarios which could potentially have improved the outcome of this work have effectively been implemented (time restrictions, etc.). Because of this, effort has been made to provide an overview of the aspects which might be considered for future optimizations.

Source terms

- As stated in §5.3, in this work only the DLR model was considered for generating the GCR spectral data (source term for the PHITS transport calculations). For comparison reasons, radiation transport calculations could also be performed using others GCR models, such as the BON2014 and SINP models.
- As stated in §6.4.3.3, historical spectral data of the August 1972 (LaRC) SPE and the Sum October 1989 Tylka Band fits SPE were considered in the SPE transport calculations, neglecting the probabilistic nature of the phenomena. As stated in §2.1.3, the most extreme (worst-case) SPE ever recorded took place on 04/11/2003. The spectral data of this SPE was however not available in OLTARIS. Shielding analysis against this SPE should ideally be performed.

Geometries and materials

- Instead of using a simplified spherical geometry of H_2O for the astronaut's body (§6.4.3.1), simulations could be performed using mathematical models of the human body (anthropomorphic voxel phantoms). In the same vain, instead of using a simplified spherical geometry for the shielding setup (§6.4.3.1), more realistic spacecraft geometries could be considered. For example, the actual or average distance between the shield and the astronaut could be considered. Furthermore, the dose impact on the astronaut by moving inside the spacecraft (closer/farther from the shield) could be studied.
- The shielding materials considered in this work are described in §6.4.3.2. Other materials could be investigated with a focus on practical use. Novel shielding materials which are currently being studied are carbon nanotube (CNT), highly crystalline boron nitride nanotubes (BNNT), melanin and ectoine (Ref. [49]).
- In order to potentially decrease the simulation time, one could study the effect of using a 1D/2D geometry instead of 3D. However, in case of a 1D/2D setup the angular distribution of the source particles would not fully represent the real situation in space. Hence, this approach was not studied further in this work.

Simulations

- Due to time and computer power restrictions, the simulations were performed with an amount of source particles which provided results deemed acceptable for this work. More source particles could be used in PHITS, thereby reducing the statistical error and increasing the confidence in the results produced. This statement is especially true when using thick shields and/or effective materials.
- VRT were not implemented in the simulations as overall satisfying results were obtained within reasonable time frames. VRT could be optimized for all setups with the objective of speeding up the computational time (especially for GCR).

- Only the total dose and total flux per source were tallied. The contribution of each (primary/secondary) particle to the latter's has not been analyzed. This contribution could be investigated to better understand which particles have a dominant contribution to the total dose. For example, if secondary neutrons would dominate the total dose, shielding could be optimizing by using materials which more effectively slow down and capture the neutrons (e.g. PE and Cd).
- As stated in §6.4.3.6, the dose depth distributions in the target were tallied for each configuration as it provides information on the dose deposition pattern. These tally outputs were however not analysed in this work (time restrictions). The analysis could be part of future work.

Dose calculations

- The methodologies applied in this work to obtain doses (SPE) and dose rates (GCR) for the shielded configurations were based on (developed relative to) the unshielded configuration (§7.1). Following this, the source was fixed at a distance of 1 cm from the thickest shield of a material. This approach simplified the simulation/calculation efforts since less simulations were required and less tally outputs needed to be post-processed compared to the approach in which the source would have been repositioned at a certain distance from each shielding configuration. However, the approach in which the source would be repositioned in each configuration would likely yield smaller statistical errors (less particles would escape from the system) and a better angular distribution (more angles would be 'seen' by the water target).

10. REFERENCES

[1] ICRP, 2013. Assessment of Radiation Exposure of Astronauts in Space. ICRP Publication 123. Ann. ICRP 42(4).

[2] Galactic Cosmic Ray Exposure of Humans in Space, Influence of galactic cosmic ray models and shielding on dose calculations for low-Earth orbit and near-Earth interplanetary space, Alankrita Isha Mrigakshi, PhD thesis performed and submitted at the Faculty of Mathematics and Natural Sciences at Kiel University, 2013.

[3] Human exposure to space radiation: role of primary and secondary particles, Trovati et al., Radiation Protection Dosimetry, Vol. 122, No. 1–4, pp. 362-366, 2006.

[4] GCR and SPE organ doses in deep space with different shielding: Monte Carlo simulations based on the FLUKA code coupled to anthropomorphic phantoms, Ballarini et al., Advances in Space Research 37 (2006) 1791-1797, 2006.

[5] Assessment of galactic cosmic ray models, Mrigakshi et al. 2012, Journal of Geophysical Research, Volume 117, Issue A8 , A08109, 2012.

[6] How galactic cosmic ray models affect the estimation of radiation exposure in space, Mrigakshi et al. 2013a, Advances in Space Research, Volume 51, Issue 5, p. 825-834, 2013.

[7] A ready-to-use galactic cosmic ray model, Matthiä et al. 2013, Advances in Space Research, Volume 51, Issue 3, p. 329-338, 2013.

[8] Estimation of galactic cosmic ray exposure inside and outside the Earth's magnetosphere during the recent solar minimum between solar cycles 23 and 24, Mrigakshi et al. 2013b, Advances in Space Research, Volume 52, Issue 5, p. 979-987, 2013.

[9] Belgian public authorities: Federal Agency for Nuclear Control (FANC) https://fanc.fgov.be/nl/professionelen/bescherming-van-de-werknemers/verplichtingen-van-de-exploitanten/officiele consolidated on 12/01/19.

[10] NASA, What Is a Supernova?, https://www.nasa.gov/audience/forstudents/5-8/features/nasa-knows/what-is-a-supernova.html, consolidated on 03/12/18.

[11] NASA, Neutron Stars, https://imagine.gsfc.nasa.gov/science/objects/neutron_stars1.html, consolidated on 03/12/18.

[12] NASA, Space Radiation Environment, Comparison and Validation of GCR Models, Briefing to NAC HEO/SMD Joint Committee, April 2015, https://www.nasa.gov/sites/default/files/files/5_Slaba_NAC_042015_v6_TAGGED.pdf, consolidated on 28/11/18.

[13] NASA, What is a solar flare? https://www.nasa.gov/content/goddard/what-is-a-solar-flare consolidated on 09/01/18.

[14] NASA, Sunspots and Solar Flares, https://spaceplace.nasa.gov/solar-activity/en/, consolidated on 07/02/19.

[15] NASA, What is a coronal mass ejection or CME?, https://www.nasa.gov/content/goddard/what-is-a-coronal-mass-ejection, consolidated on 03/12/18.

[16] NASA, What is a solar prominence? https://www.nasa.gov/content/goddard/what-is-a-solar-prominence, consolidated on 07/02/19.

[17] NASA, Media invited to session on violent solar events of fall 2003, https://www.nasa.gov/centers/goddard/news/topstory/2004/0519solarstorm.html, consolidated on 23/11/18.

[18] NASA, CNEOS is NASA's center for computing asteroid and comet orbits and their odds of Earth impact, https://cneos.jpl.nasa.gov/glossary/au.html, consolidated on 23/11/18.

[19] NASA, Sun Erupts With Significant Flare, https://www.nasa.gov/feature/goddard/2017/active-region-on-sun-continues-to-emit-solar-flares, consolidated on 23/11/18.

[20] NASA, Radiation Belts with Satellites, https://www.nasa.gov/mission_pages/sunearth/news/gallery/20130228-radiationbelts.html, consolidated on 07/02/19.

[21] ICRP, 1991. 1990 Recommendations of the International Commission on Radiological Protection. ICRP Publication 60. Ann. ICRP 21 (1-3).

[22] ICRP, 2007. The 2007 Recommendations of the International Commission on Radiological Protection. ICRP Publication 103. Ann. ICRP 37 (2-4).

[23] ICRU, 2001. Determination of operational dose equivalent quantities for neutrons. ICRU Report 66. J. ICRU 1(3).

[24] IAEA, Safety Glossary, Terminology Used in Nuclear Safety and Radiation Protection, 2007.

[25] IAEA, Safety Standards for protecting people and the environment, Fundamental Safety Principles, Safety Fundamentals, No. SF-1, 2006.

[26] FANC, Officiële dosislimieten, https://fanc.fgov.be/nl/professionelen/bescherming-van-de-werknemers/verplichtingen-van-de-exploitanten/officiele, consolidated on 11/12/18.

[27] PHITS Ver. 2.82, User’s Manual (English version).

[28] ISO15390, Space environment (natural and artificial) – galactic cosmic ray model, 2004.

[29] NASA, Space Radiation Protection, NASA Space Vehicle Design Criteria (Structures), NASA SP-8054, 1970.

[30] Overview of energetic particle hazards during prospective manned missions to Mars, McKenna-Lawlor et al., Planet. Space Sci. 63–64, 123–132.

[31] NASA, Heliophysics and Space Weather, https://svs.gsfc.nasa.gov/30481, consolidated on 07/02/19.

[32] The radiation environment on the surface of Mars - Summary of model calculations and comparison to RAD data, Matthiä et al., Life Sciences in Space Research, Volume 14, Pages 18-28, August 2017.

[33] Radiation transport simulation of the Martian GCR surface flux and dose estimation using spherical geometry in PHITS compared to MSL-RAD measurements, Flores-McLaughlin, J., Life Sciences in Space Research, Volume 14, Pages 36-42, August 2017.

[34] Improvements and developments of physics models in PHITS for space applications, Sihver et al., 2015 IEEE Aerospace Conference, DOI: 10.1109/AERO.2015.7119202.

[35] PHITS—a particle and heavy ion transport code system, Niita et al., Radiation Measurements 41 (2006) 1080 – 1090.

[36] Overview of particle and heavy ion transport code system PHITS, Sato et al., Annals of Nuclear Energy, Annals of Nuclear Energy 82 (2015) 110–115.

[37] Features of Particle and Heavy Ion Transport code System (PHITS) version 3.02, Sato et al., Journal of Nuclear Science and Technology, DOI: 10.1080/00223131.2017.1419890.

[38] A model of galactic cosmic ray fluxes, Nymmik et al., Nucl. Tracks Radiat. Meas., 20(3), 427–429, doi:10.1016/1359-0189(92)90028-T.

[39] Heliospheric modulation of cosmic rays: Monthly reconstruction for 1951–2004, Usoskin et al., J. Geophys. Res., 110, A12108, doi:10.1029/2005JA011250.

[40] NASA galactic cosmic radiation environment model : Badhwar – O'Neill (2014), Golge et al., The 34th International Cosmic Ray Conference, 30 July- 6 August, 2015.

[41] NASA, Badhwar - O'Neill 2014 Galactic Cosmic Ray Flux Model Description, NASA/TP-2015-218569, 2015.

[42] NASA, Badhwar - O'Neill 2011 Galactic Cosmic Ray Flux Model Description, NASA/TP-2013-217376, 2013.

[43] NASA, OLTARIS: On-Line Tool for the Assessment of Radiation in Space, NASA/TP-2010-216722, 2010.

[44] Exploring Monte Carlo Methods, William L. Dunn, J. Kenneth Shultis, Elsevier, 2012.

[45] Empirical model of long-time variations of galactic cosmic ray particle fluxes, Kuznetsov et al. 2017, J. Geophys. Res. Space Physics, 122, 1463–1472, doi:10.1002/ 2016JA022920.

[46] Comparison of space radiation GCR models to recent AMS data, J.W. Norbury et al. 2018, Life Sciences in Space Research 18 (2018) 64–71.

[47] Recent GCR models compared to AMS data, John W. Norbury, Kathryn Whitman, Kerry Lee, Tony C. Slaba, Francis F. Badavi, Solar Energetic Particles, Solar Modulation and Space Radiation, New Opportunities in the AMS-2 Era, Meeting # 3, Washington D.C., USA, April 23 - 26, 2018.

[48] Space radiation protection: Destination Mars, Marco Durante, Life Sciences in Space Research 1 (2014) 2–9.

[49] On the search of novel materials for radiation protection during manned space missions, E. Botek, BIRA-IASB, workshop on radiobiological effects for studies on Earth and for Space missions planning (Lille), March 2019.

[50] Galactic cosmic ray radiation hazard in the unusual extended solar minimum between solar cycles 23 and 24, Schwadron et al., Space Weather, Vol. 8, S00E04, doi:10.1029/2010SW000567, 2010.

[51] Compendium of Material Composition Data for Radiation Transport Modeling, Pacific Northwest National Laboratory, PIET-43741-TM-963, PNNL-15870 Rev. 1, 2011.

[52] NIST, Thermophysical Properties of Hydrogen, https://webbook.nist.gov/cgi/fluid.cgi?Action=Load&ID=C1333740&Type=SatT&Digits=5&PLow=.5&PHigh=1.5&PInc=.1&RefState=DEF&TUnit=K&PUnit=atm&DUnit=kg/m3&HUnit=kJ/mol&WUnit=m/s&VisUnit=uPa*s&STUnit=N/m, consolidated on 15/04/19.

[53] Measuring space radiation shielding effectiveness, Bahadori et al., The European Physical Journal Conferences 153:04001, September 2017.

[54] Radiation Hazard in Space, Leonty I. Miroshnichenko, DOI 10.1007/978-94-017-0301-7, 2003.

[55] Radiation Hazards and the Colonization of Mars, Tore Straume, Steve Blattnig, and Cary Zeitlin (2010), The Human Mission to Mars: Colonizing the Red Planet (J. S. Levine & R. E. Schild, Eds.), Cosmology Science Publishers, Cambridge, MA (pp. 803-849), 2010.

[56] NASA, Solar Cycle Primer, https://www.nasa.gov/mission_pages/sunearth/news/solarcycle-primer.html, consolidated on 18/07/19.

[57] NASA, SpaceMath@NASA, https://spacemath.gsfc.nasa.gov/ consolidated on 18/07/19.

[58] Health Physics in the 21st Century, Joseph John Bevelacqua, ISBN: 978-3-527-40822-1, 2008.

[59] Influence of cosmic radiation spectrum and its variation on the relative efficiency of LiF thermoluminescent detectors – Calculations and measurements, Bilski et al. (2016), Radiation Measurements 88 (2016) 33–40, 2016.

[60] NASA, Space Faring: The Radiation Challenge, An Interdisciplinary Guide on Radiation and Human Space Flight, NASA Human Research Program Engagement and Communications, Radiation iBook, https://www.nasa.gov/sites/default/files/atoms/files/space_radiation_ebook.pdf consolidated on 20/07/19.

[61] NCRP Report No. 132, Radiation Protection Guidance for Activities in Low-Earth Orbit, ISBN 0-929600-65-7, 2000.

[62] CREME96: A Revision of the Cosmic Ray Effects on Micro-Electronics Code, Allen J. Tylka et al. (1997), IEEE TRANSACTIONS ON NUCLEAR SCIENCE, VOL.44, NO.6, DECEMBER 1997.

[63] Time lag of galactic cosmic ray modulation: conformity to general regularities and influence on particle energy spectra, R.A. Nymmik, Advances in Space Research Volume 26, Issue 11, 2000, Pages 1875-1878.

[64] An analytical model, describing dynamics of GCR heavy particles, Nymmik et al. (1994), Adv Space Res. 1994 Oct;14(10):759-63.

[65] Solar Modulation of Galactic Cosmic Rays, Gleeson and Axford, Astrophysical Journal, vol. 154, p.1011, 1968.

[66] NASA, Near-Earth Space Radiation Models, Michael A. Xapsos, Senior Member, IEEE, Patrick M. O'Neill and T. Paul O'Brien, 2012.

[67] NASA, Radiation Shielding Materials Containing Hydrogen, Boron, and Nitrogen: Systematic Computational and Experimental Study - Phase I, NIAC Final Report, 2012.

[68] UNSCEAR, Sources and Effects of Ionizing Radiation, Volume I: sources, Report to the General Assembly Scientific Annexes A and B, UNSCEAR 2008 Report.

APPENDIX 1 – OVERVIEW OF THE GCR MODELS OUTSIDE THE EARTH'S MAGNETOSPHERE AT A DISTANCE OF 1 AU FROM THE SUN

Overview of the models describing GCR spectra outside the Earth's magnetosphere (interplanetary space)

Model	Model type	Modulation function based on	Location of GCR particle estimation	Energy range (MeV/nuc)	Particle (Z)	Validity period	Means of GCR spectra generation[1]	User-friendliness[2] (spectra generation)
CREME96	Semi-empirical based on Nymmik et al. 1992	Monthly-averaged Wolf numbers	Interplanetary space, heliocentric distance of ~1 AU	$10 – 10^5$	1 – 28	1950-1997	Web interface CREME website[3]	*No feedback (Not used in this work)*
CREME2009	Semi-empirical based on ISO15390	Smoothed Wolf numbers	Interplanetary space, heliocentric distance of ~1 AU	$10 – 10^5$	1 – 28	1760 onwards	Web interface CREME website[3]	*No feedback (Not used in this work)*
BON2010 BON2011	Force-Field approximation	Monthly-averaged Sunspot numbers	Interplanetary space, heliocentric distance of ~1 AU	$10 – 10^6$	1 – 94	1955 onwards	Web interface OLTARIS website[4] (only for BON2010)	High due to the intuitive user-interface (only for BON2010)
BON2014	Force-Field approximation	Monthly-averaged Sunspot numbers	Interplanetary space, heliocentric distance of ~1 AU	$10 – 10^6$	1 – 94	1955 onwards	Web interface OLTARIS website[4]	High due to the intuitive user-interface
Burger-Usoskin	Force-Field approximation	NM count rates	Interplanetary space, heliocentric distance of ~1 AU	$10 – 10^6$	1 – 2	1951 onwards	Source code upon request	*No feedback (Not used in this work)*
Matthïa/ACE	Semi-empirical based on ISO15390	ACE/CRIS carbon data	Interplanetary space, heliocentric distance of ~1 AU	$10 – 10^6$	1 – 28	1997 onwards	Web interface OLTARIS website[4]	High due to the intuitive user-interface[5]
Matthïa/Oulu	Semi-empirical based on ISO15390	NM count rates	Interplanetary space, heliocentric distance of ~1 AU	$10 – 10^6$	1 – 28	1964 onwards	Web interface OLTARIS website[4]	High due to the intuitive user-interface[5]
SPENVIS/ ISO15390	Based on ISO15390	Smoothed Wolf numbers	Interplanetary space, heliocentric distance of ~1 AU	$10^3 – 20 \times 10^3$	1 – 92	1950 onwards	Web interface SPENVIS website[6]	*No feedback (Not used in this work)*
SINP 2016	Empirical model based on balloon and spacecraft experimental data	Relation between fluxes and smoothed monthly mean sunspot number	Interplanetary space, heliocentric distance of ~1 AU to ~70 AU	$80 - 10^5$	1 – 28	1973 onwards	Web interface OLTARIS website[4]	High due to the intuitive user-interface

Overview of the models describing GCR spectra outside the Earth's magnetosphere (interplanetary space)

1 If all equations describing the models and required input parameters are available, one could opt performing manual calculation. However, in this work no manual calculations were performed.
2 User-friendliness refers to the ease of obtaining GCR particle spectra.
3 https://creme.isde.vanderbilt.edu/
4 https://oltaris.nasa.gov/
5 OLTARIS does not specify if the Matthïa/ACE or Matthïa/Oulu model is implemented.
6 https://www.spenvis.oma.be/

APPENDIX 2 – GRAPHICAL REPRESENTATION OF CHI-SQUARE RESULTS CALCULATED BETWEEN THE CONSIDERED MODELS AND THE AVAILABLE MEASUREMENTS FOR GCR H, HE, O AND FE NUCLEI (REF. [2])

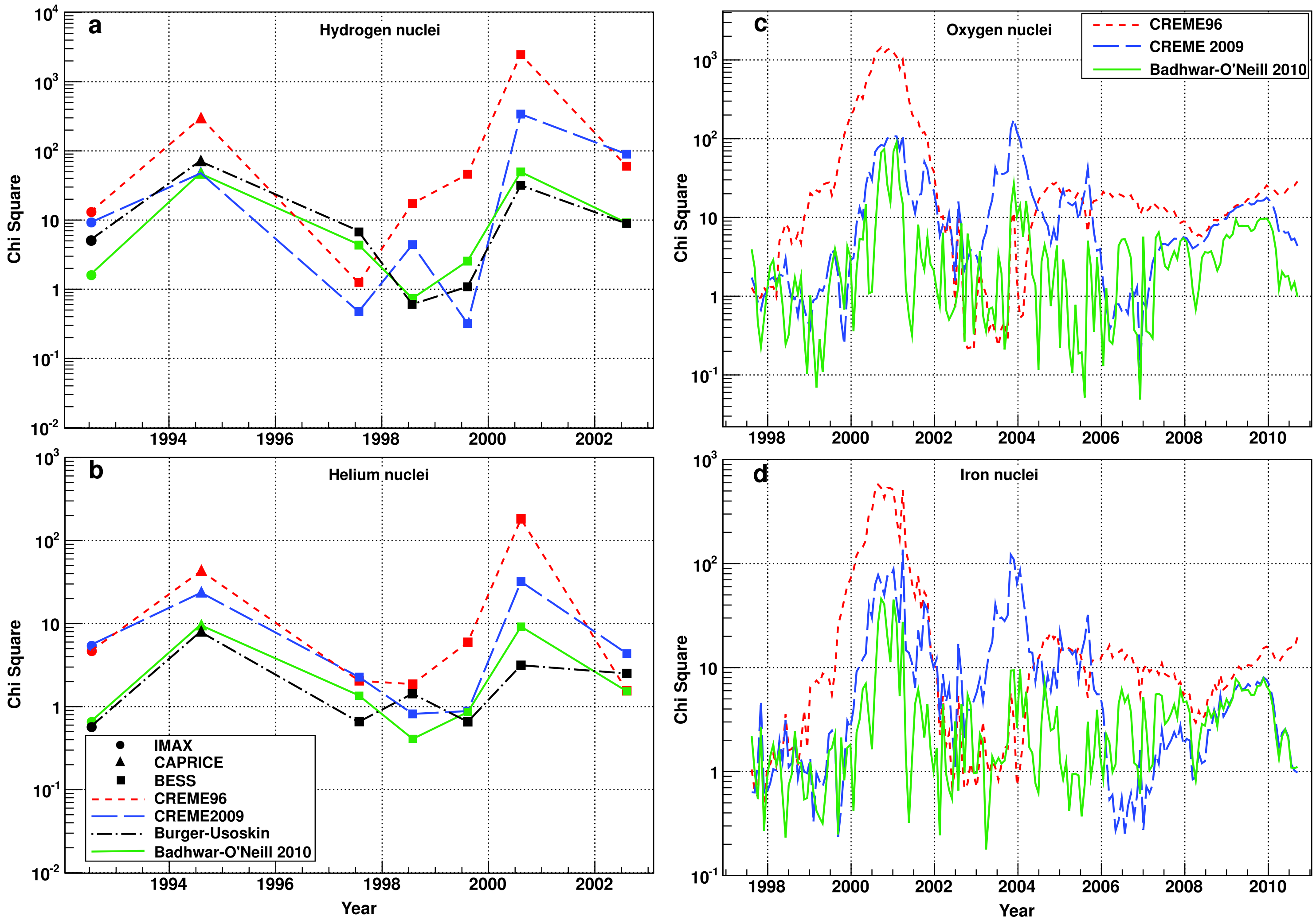

Chi-square to test the capability of Burger-Usoskin (black dashed-dotted lines), CREME96 (red dotted line), CREME2009 (blue dashed line) and BON2010 (green continuous line) models to describe the GCR H, He, O and Fe spectra. It was calculated with respect to the measurements from IMAX (solid circles), CAPRICE-1 (solid triangles) and BESS (solid squares) experiments for GCR H and He particles over an energy range of (a) 210 MeV/nuc to 24 GeV/nuc and (b) 230 MeV/nuc to 24 GeV/nuc. Whereas measurements from ACE/CRIS instrument were used to calculate the chi-square for GCR O and Fe particles over an energy range of (c) 80 MeV/nuc to 231 MeV/nuc and (d) 150 MeV/nuc–500 MeV/nuc.

APPENDIX 3 – SPECTRAL DATA IN FUNCTION OF ALL SOLAR ACTIVITIES FOR ^{1}H, ^{4}HE AND ^{56}FE (BON2014, MATTHIÄ, SINP 2016)

BON2014 – ^{1}H

Plot 1 – Energy vs Flux - Solar Activities

Plot 2 – Energy (log) vs Flux (log) - Solar Activities

Plot 3 – Energy (log) vs Flux (norm) - Solar Activities

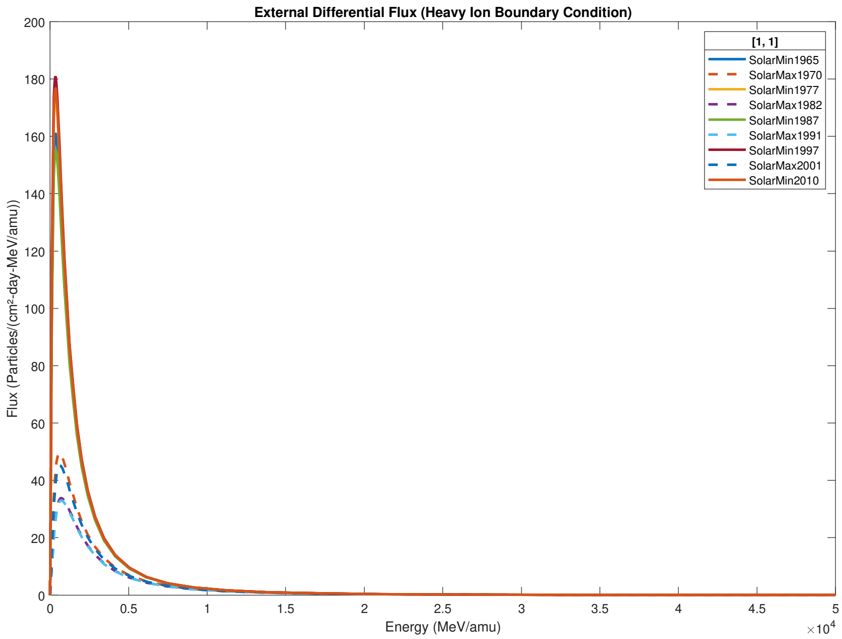

External Differential Flux (Heavy Ion Boundary Condition)
Flux (Particles/(cm²-day-MeV/amu))
Energy (MeV/amu)
×10^4
[1, 1]
SolarMin1965
SolarMax1970
SolarMin1977
SolarMax1982
SolarMin1987
SolarMax1991
SolarMin1997
SolarMax2001
SolarMin2010

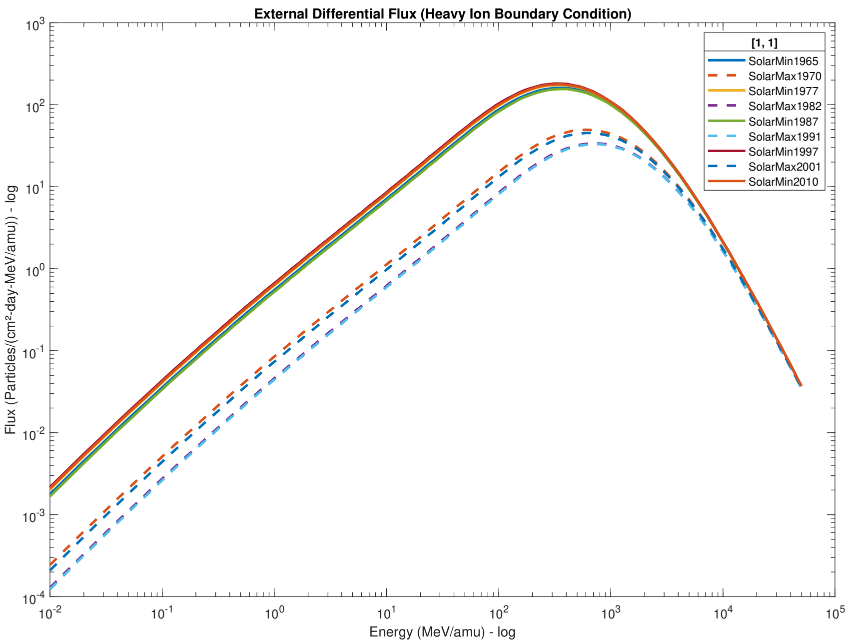

External Differential Flux (Heavy Ion Boundary Condition)
Flux (Particles/(cm²-day-MeV/amu)) - log
Energy (MeV/amu) - log
[1, 1]
SolarMin1965
SolarMax1970
SolarMin1977
SolarMax1982
SolarMin1987
SolarMax1991
SolarMin1997
SolarMax2001
SolarMin2010

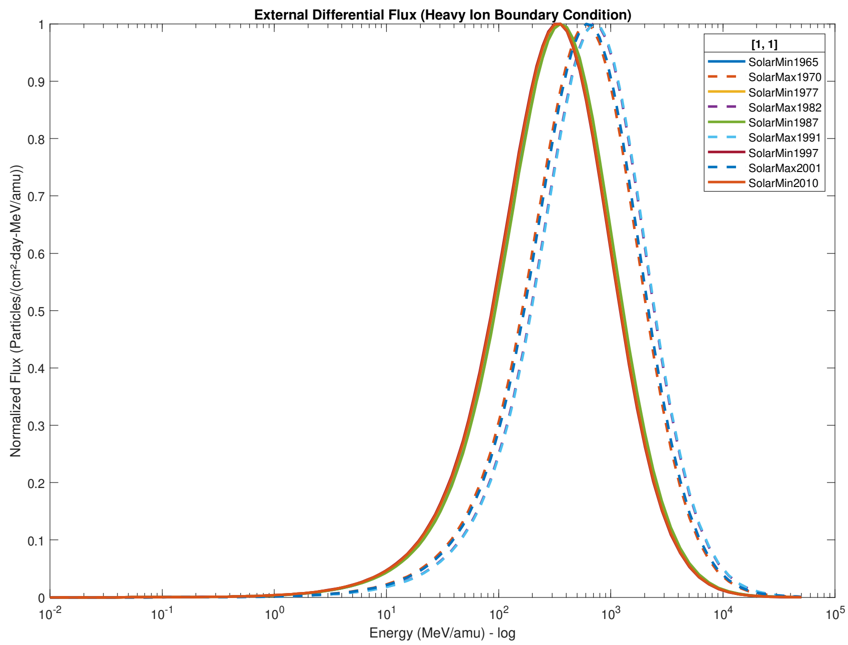

External Differential Flux (Heavy Ion Boundary Condition)
Normalized Flux (Particles/(cm²-day-MeV/amu))
Energy (MeV/amu) - log
[1, 1]
SolarMin1965
SolarMax1970
SolarMin1977
SolarMax1982
SolarMin1987
SolarMax1991
SolarMin1997
SolarMax2001
SolarMin2010

Matthiä2013 – ^{1}H

Plot 1 – Energy vs Flux - Solar Activities

Plot 2 – Energy (log) vs Flux (log) - Solar Activities

Plot 3 – Energy (log) vs Flux (norm) - Solar Activities

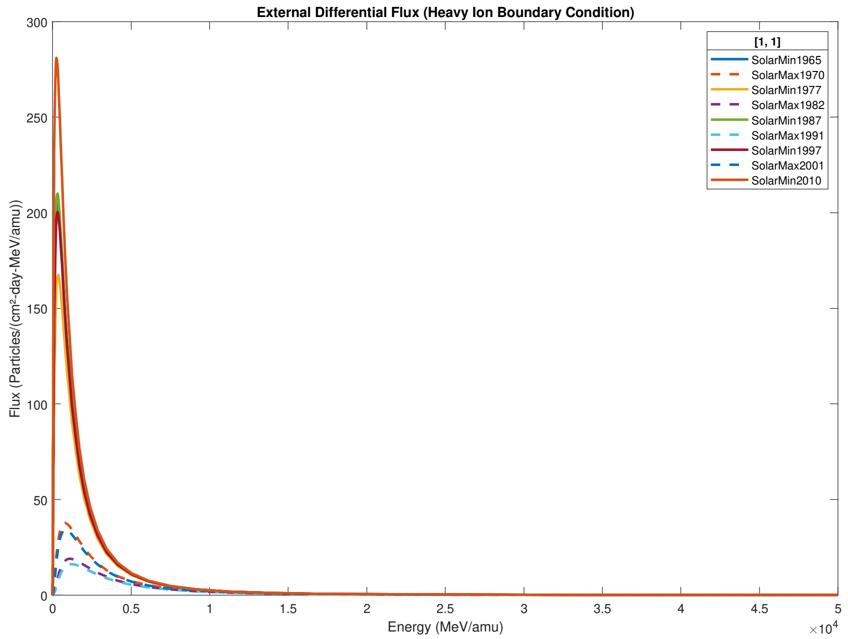
External Differential Flux (Heavy Ion Boundary Condition)
Flux (Particles/(cm²-day-MeV/amu))
Energy (MeV/amu)
×10^4
0
0.5
1
1.5
2
2.5
3
3.5
4
4.5
5
50
100
150
200
250
300
[1, 1]
SolarMin1965
SolarMax1970
SolarMin1977
SolarMax1982
SolarMin1987
SolarMax1991
SolarMin1997
SolarMax2001
SolarMin2010

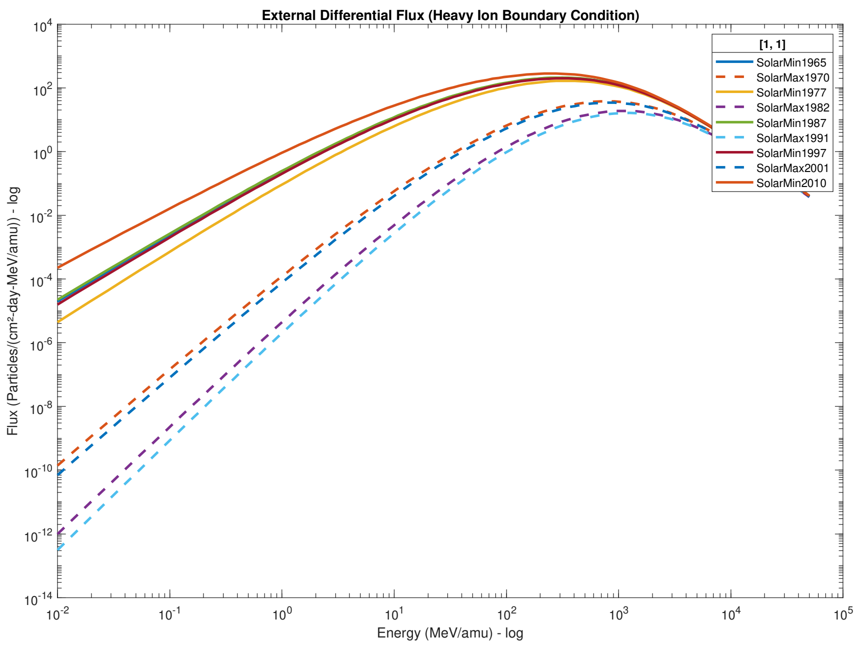
External Differential Flux (Heavy Ion Boundary Condition)
Flux (Particles/(cm²-day-MeV/amu)) - log
Energy (MeV/amu) - log
10^-2
10^-1
10^0
10^1
10^2
10^3
10^4
10^5
10^-14
10^-12
10^-10
10^-8
10^-6
10^-4
10^-2
10^0
10^2
10^4
[1, 1]
SolarMin1965
SolarMax1970
SolarMin1977
SolarMax1982
SolarMin1987
SolarMax1991
SolarMin1997
SolarMax2001
SolarMin2010

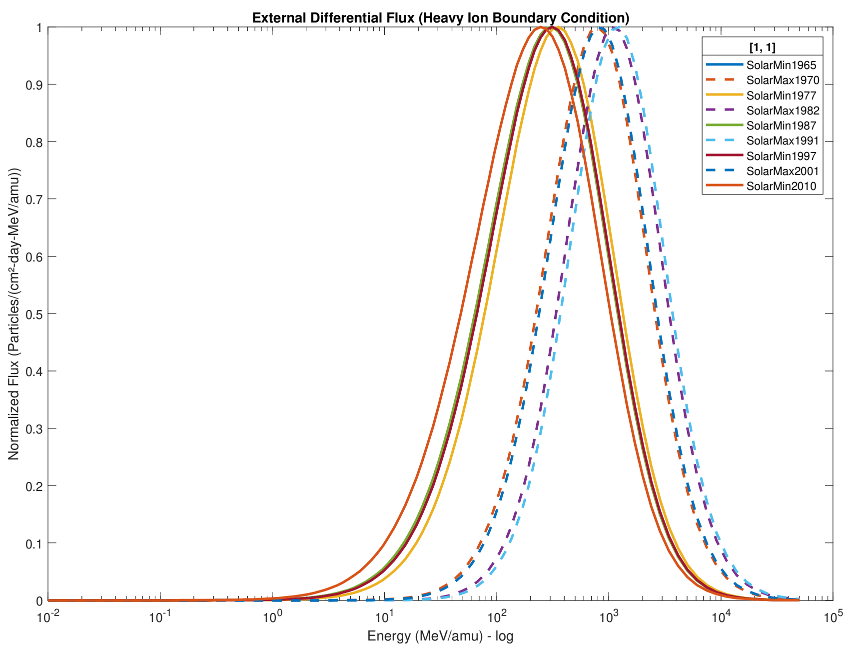
External Differential Flux (Heavy Ion Boundary Condition)
Normalized Flux (Particles/(cm²-day-MeV/amu))
Energy (MeV/amu) - log
10^-2
10^-1
10^0
10^1
10^2
10^3
10^4
10^5
0
0.1
0.2
0.3
0.4
0.5
0.6
0.7
0.8
0.9
1
[1, 1]
SolarMin1965
SolarMax1970
SolarMin1977
SolarMax1982
SolarMin1987
SolarMax1991
SolarMin1997
SolarMax2001
SolarMin2010

SINP2016 – ^{1}H

Plot 1 – Energy vs Flux - Solar Activities

Plot 2 – Energy (log) vs Flux (log) - Solar Activities

Plot 3 – Energy (log) vs Flux (norm) - Solar Activities

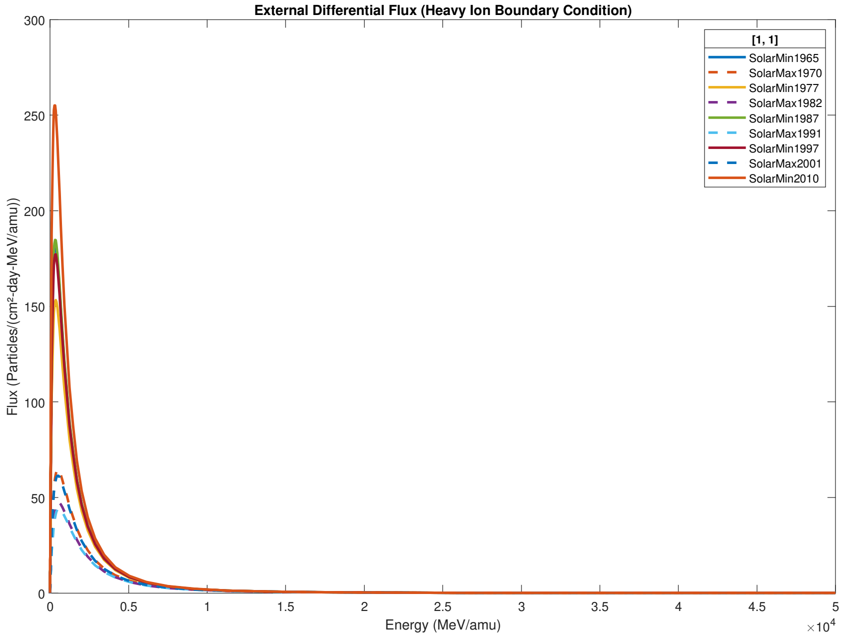

External Differential Flux (Heavy Ion Boundary Condition)
Flux (Particles/(cm²-day-MeV/amu))
Energy (MeV/amu)
×10^4
[1, 1]
SolarMin1965
SolarMax1970
SolarMin1977
SolarMax1982
SolarMin1987
SolarMax1991
SolarMin1997
SolarMax2001
SolarMin2010

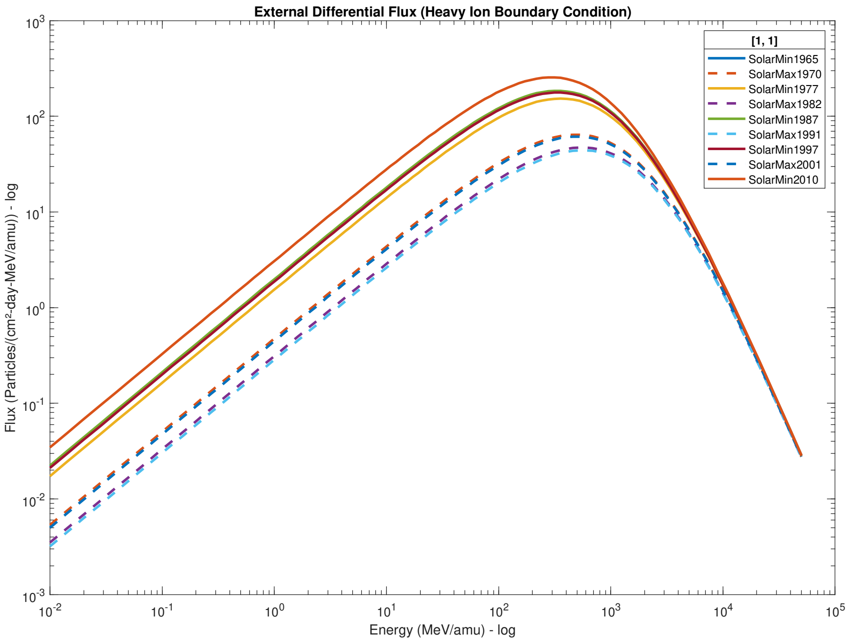

External Differential Flux (Heavy Ion Boundary Condition)
Flux (Particles/(cm²-day-MeV/amu)) - log
Energy (MeV/amu) - log
[1, 1]
SolarMin1965
SolarMax1970
SolarMin1977
SolarMax1982
SolarMin1987
SolarMax1991
SolarMin1997
SolarMax2001
SolarMin2010

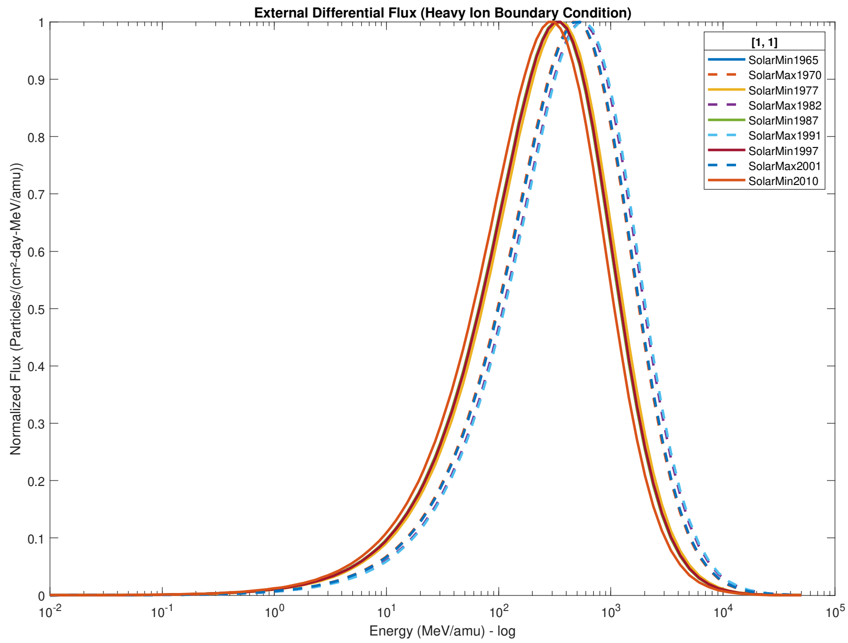

External Differential Flux (Heavy Ion Boundary Condition)
Normalized Flux (Particles/(cm²-day-MeV/amu))
Energy (MeV/amu) - log
[1, 1]
SolarMin1965
SolarMax1970
SolarMin1977
SolarMax1982
SolarMin1987
SolarMax1991
SolarMin1997
SolarMax2001
SolarMin2010

BON2014 – ^{4}He

Plot 1 – Energy vs Flux - Solar Activities

Plot 2 – Energy (log) vs Flux (log) - Solar Activities

Plot 3 – Energy (log) vs Flux (norm) - Solar Activities

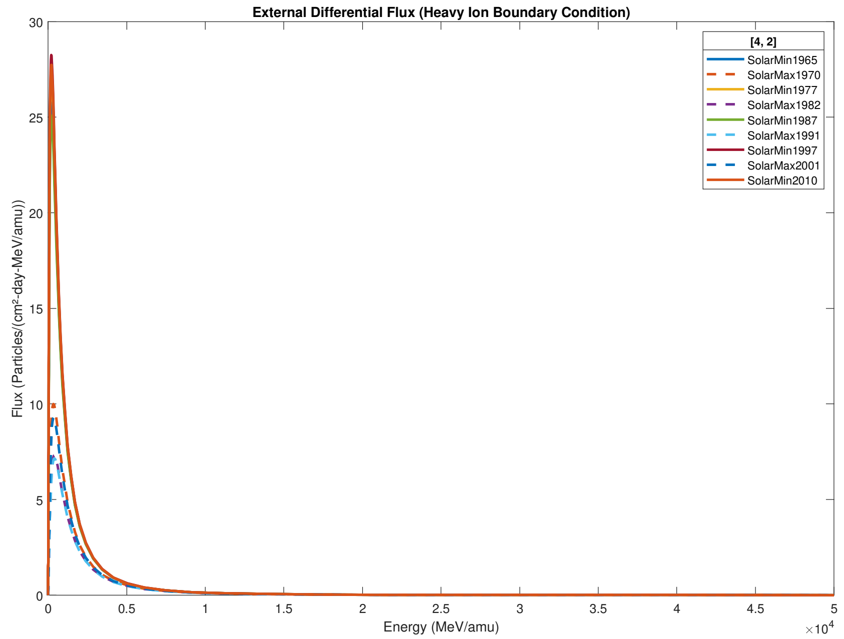
External Differential Flux (Heavy Ion Boundary Condition)
[4, 2]
SolarMin1965
SolarMax1970
SolarMin1977
SolarMax1982
SolarMin1987
SolarMax1991
SolarMin1997
SolarMax2001
SolarMin2010
Flux (Particles/(cm²-day-MeV/amu))
Energy (MeV/amu)
×10^4

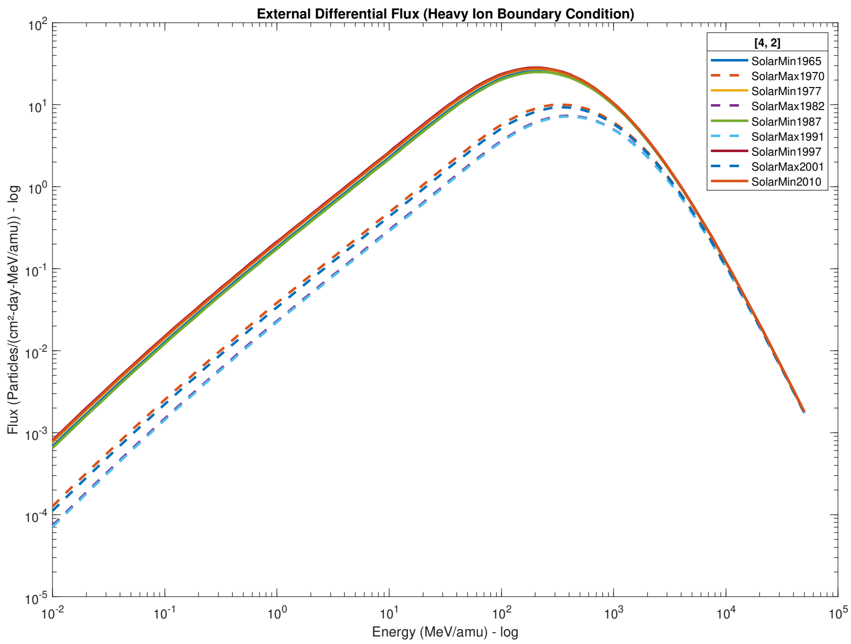
External Differential Flux (Heavy Ion Boundary Condition)
[4, 2]
SolarMin1965
SolarMax1970
SolarMin1977
SolarMax1982
SolarMin1987
SolarMax1991
SolarMin1997
SolarMax2001
SolarMin2010
Flux (Particles/(cm²-day-MeV/amu)) - log
Energy (MeV/amu) - log

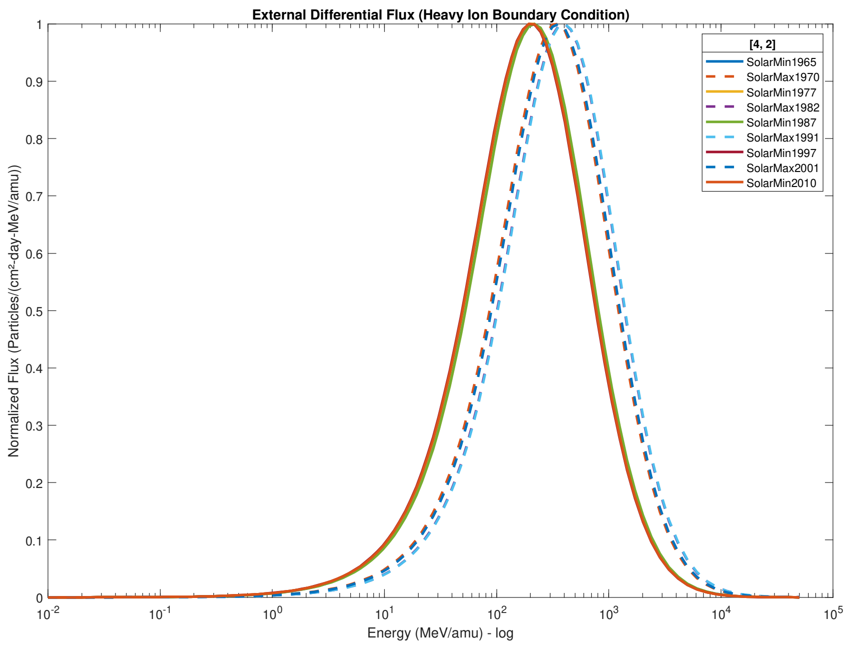
External Differential Flux (Heavy Ion Boundary Condition)
[4, 2]
SolarMin1965
SolarMax1970
SolarMin1977
SolarMax1982
SolarMin1987
SolarMax1991
SolarMin1997
SolarMax2001
SolarMin2010
Normalized Flux (Particles/(cm²-day-MeV/amu))
Energy (MeV/amu) - log

Matthiä2013 – ^{4}He

Plot 1 – Energy vs Flux - Solar Activities

Plot 2 – Energy (log) vs Flux (log) - Solar Activities

Plot 3 – Energy (log) vs Flux (norm) - Solar Activities

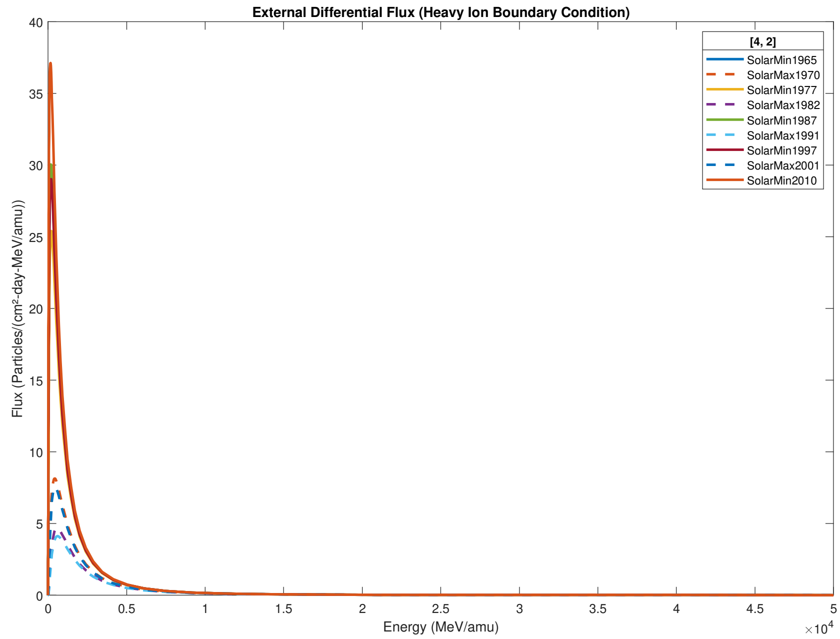
External Differential Flux (Heavy Ion Boundary Condition)
[4, 2]
SolarMin1965
SolarMax1970
SolarMin1977
SolarMax1982
SolarMin1987
SolarMax1991
SolarMin1997
SolarMax2001
SolarMin2010
Flux (Particles/(cm²-day-MeV/amu))
Energy (MeV/amu)
$\times 10^4$

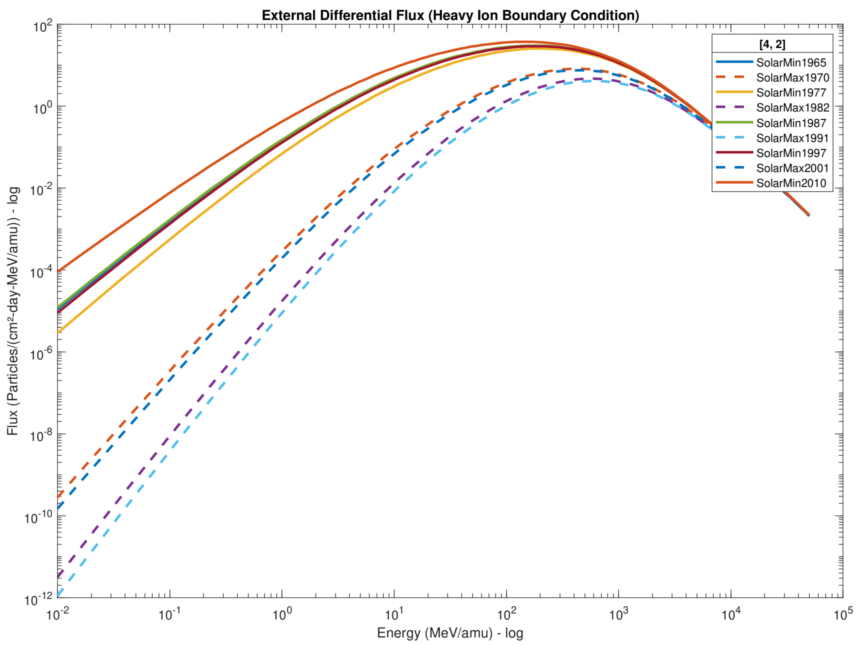
External Differential Flux (Heavy Ion Boundary Condition)
[4, 2]
SolarMin1965
SolarMax1970
SolarMin1977
SolarMax1982
SolarMin1987
SolarMax1991
SolarMin1997
SolarMax2001
SolarMin2010
Flux (Particles/(cm²-day-MeV/amu)) - log
Energy (MeV/amu) - log

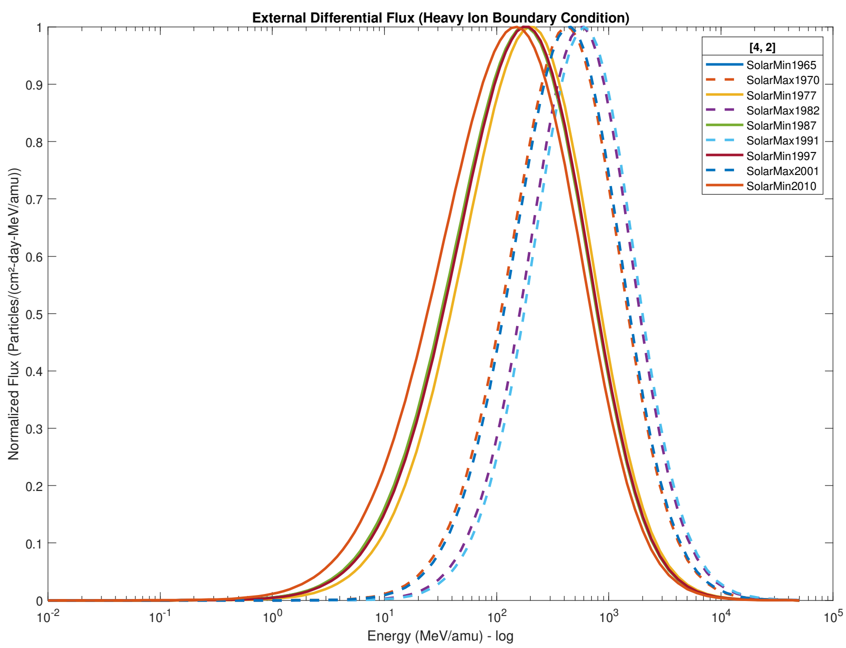
External Differential Flux (Heavy Ion Boundary Condition)
[4, 2]
SolarMin1965
SolarMax1970
SolarMin1977
SolarMax1982
SolarMin1987
SolarMax1991
SolarMin1997
SolarMax2001
SolarMin2010
Normalized Flux (Particles/(cm²-day-MeV/amu))
Energy (MeV/amu) - log

SINP2016 – ^{4}He

Plot 1 – Energy vs Flux - Solar Activities

Plot 2 – Energy (log) vs Flux (log) - Solar Activities

Plot 3 – Energy (log) vs Flux (norm) - Solar Activities

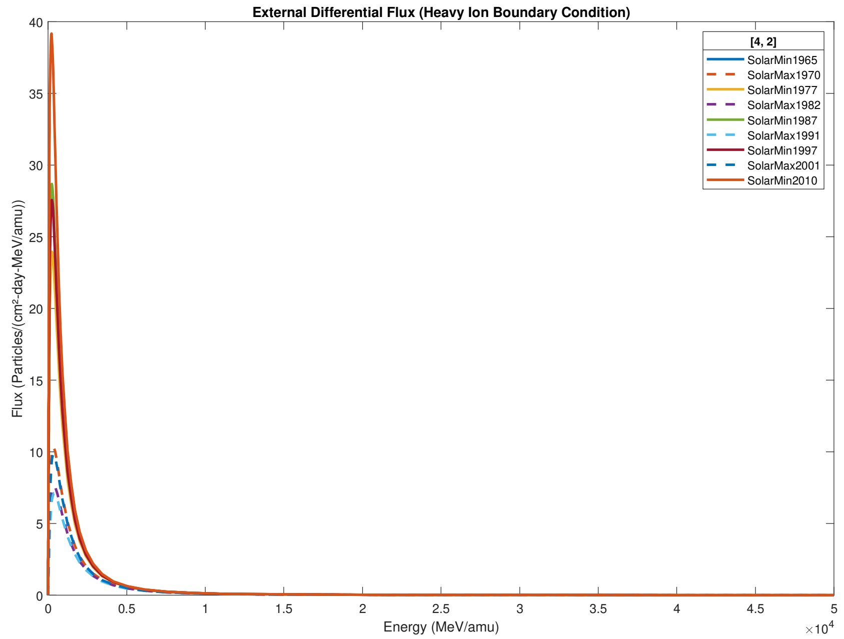

External Differential Flux (Heavy Ion Boundary Condition)
Flux (Particles/(cm²-day-MeV/amu))
Energy (MeV/amu)
×10^4
[4, 2]
SolarMin1965
SolarMax1970
SolarMin1977
SolarMax1982
SolarMin1987
SolarMax1991
SolarMin1997
SolarMax2001
SolarMin2010

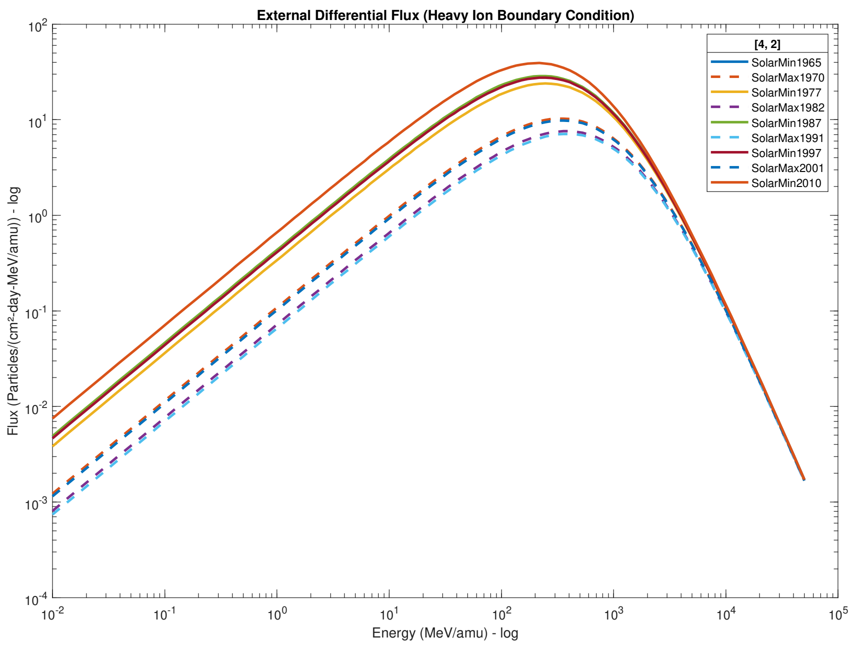

External Differential Flux (Heavy Ion Boundary Condition)
Flux (Particles/(cm²-day-MeV/amu)) - log
Energy (MeV/amu) - log
[4, 2]
SolarMin1965
SolarMax1970
SolarMin1977
SolarMax1982
SolarMin1987
SolarMax1991
SolarMin1997
SolarMax2001
SolarMin2010

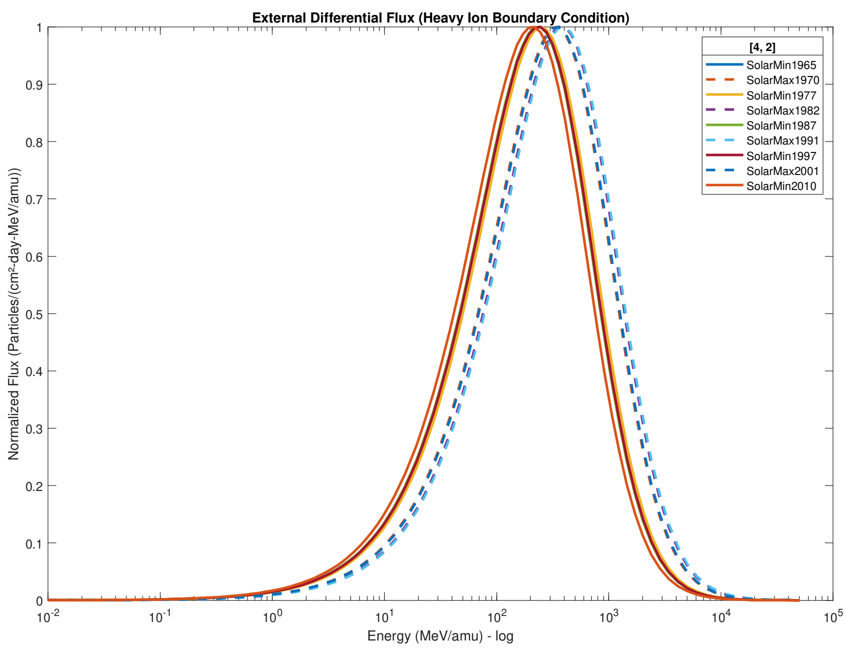

External Differential Flux (Heavy Ion Boundary Condition)
Normalized Flux (Particles/(cm²-day-MeV/amu))
Energy (MeV/amu) - log
[4, 2]
SolarMin1965
SolarMax1970
SolarMin1977
SolarMax1982
SolarMin1987
SolarMax1991
SolarMin1997
SolarMax2001
SolarMin2010

BON2014 – ^{56}Fe

Plot 1 – Energy vs Flux - Solar Activities

Plot 2 – Energy (log) vs Flux (log) - Solar Activities

Plot 3 – Energy (log) vs Flux (norm) - Solar Activities

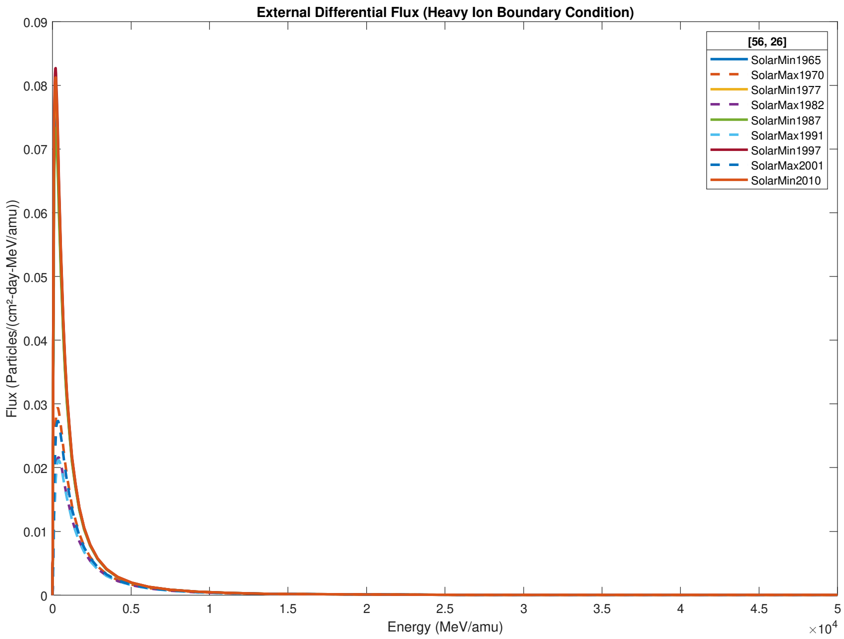
External Differential Flux (Heavy Ion Boundary Condition)
[56, 26]
SolarMin1965
SolarMax1970
SolarMin1977
SolarMax1982
SolarMin1987
SolarMax1991
SolarMin1997
SolarMax2001
SolarMin2010
Flux (Particles/(cm²-day-MeV/amu))
Energy (MeV/amu)
×10^4

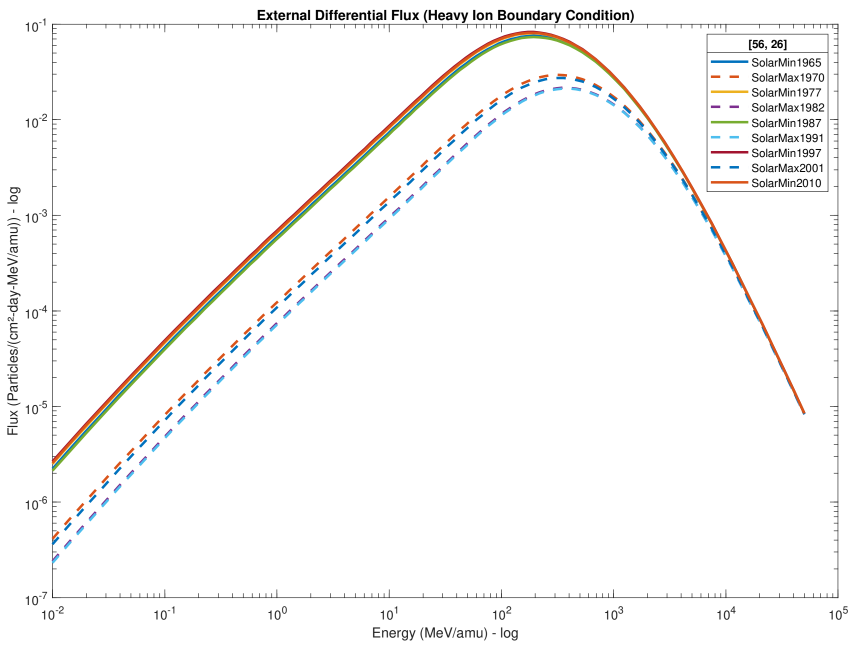
External Differential Flux (Heavy Ion Boundary Condition)
[56, 26]
SolarMin1965
SolarMax1970
SolarMin1977
SolarMax1982
SolarMin1987
SolarMax1991
SolarMin1997
SolarMax2001
SolarMin2010
Flux (Particles/(cm²-day-MeV/amu)) - log
Energy (MeV/amu) - log

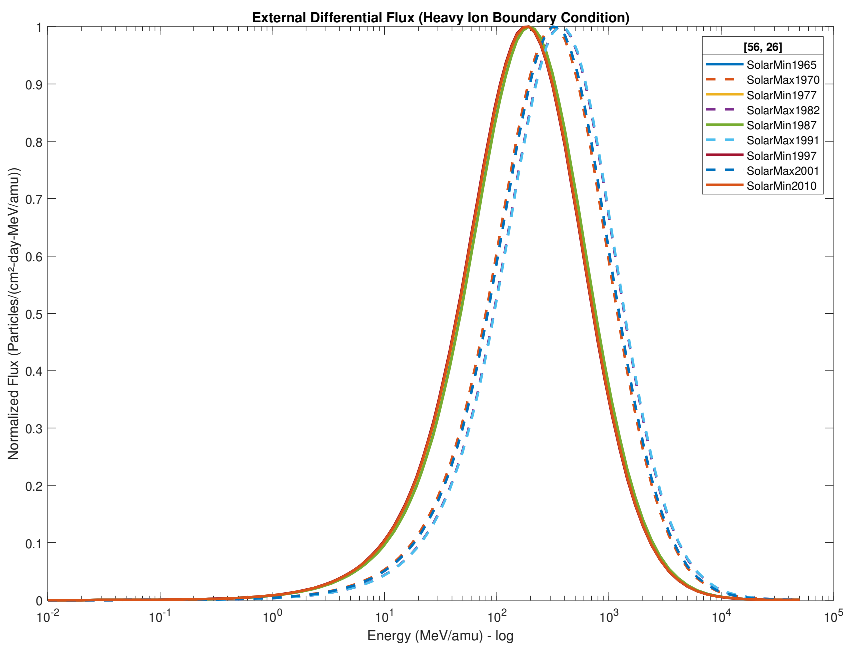
External Differential Flux (Heavy Ion Boundary Condition)
[56, 26]
SolarMin1965
SolarMax1970
SolarMin1977
SolarMax1982
SolarMin1987
SolarMax1991
SolarMin1997
SolarMax2001
SolarMin2010
Normalized Flux (Particles/(cm²-day-MeV/amu))
Energy (MeV/amu) - log

Matthiä2013 – ^{56}Fe

Plot 1 – Energy vs Flux - Solar Activities

Plot 2 – Energy (log) vs Flux (log) - Solar Activities

Plot 3 – Energy (log) vs Flux (norm) - Solar Activities

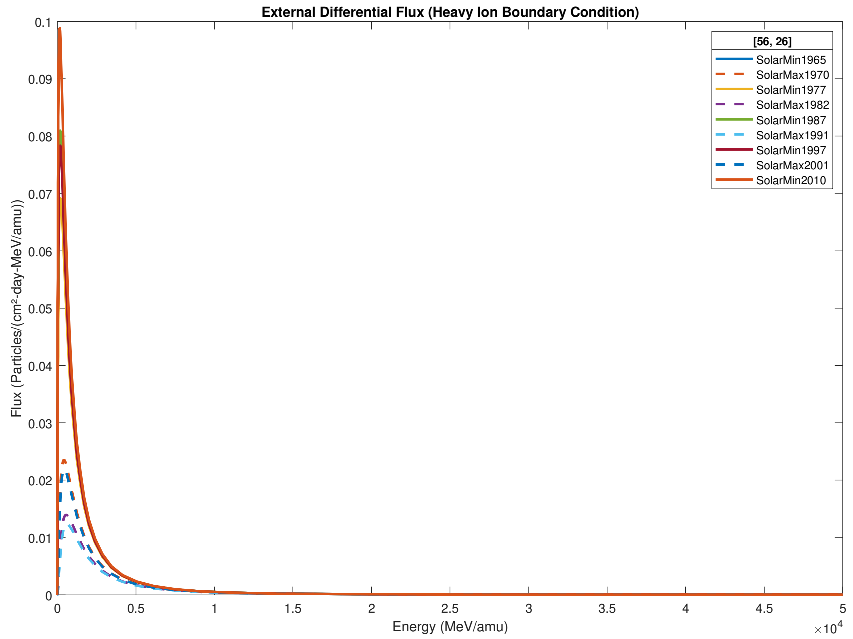

External Differential Flux (Heavy Ion Boundary Condition)
[56, 26]
SolarMin1965
SolarMax1970
SolarMin1977
SolarMax1982
SolarMin1987
SolarMax1991
SolarMin1997
SolarMax2001
SolarMin2010
Flux (Particles/(cm²-day-MeV/amu))
Energy (MeV/amu)
×10⁴

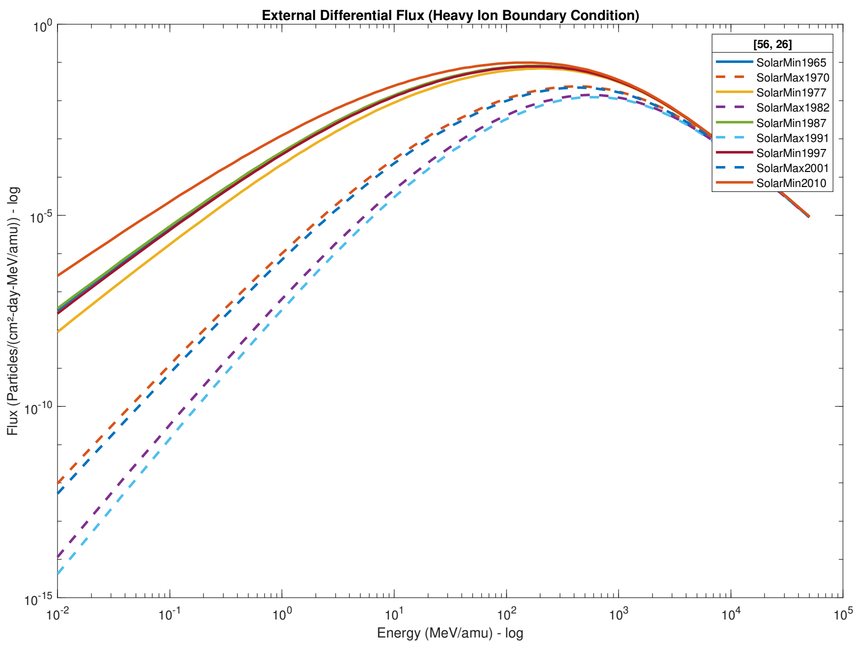

External Differential Flux (Heavy Ion Boundary Condition)
[56, 26]
SolarMin1965
SolarMax1970
SolarMin1977
SolarMax1982
SolarMin1987
SolarMax1991
SolarMin1997
SolarMax2001
SolarMin2010
Flux (Particles/(cm²-day-MeV/amu)) - log
Energy (MeV/amu) - log

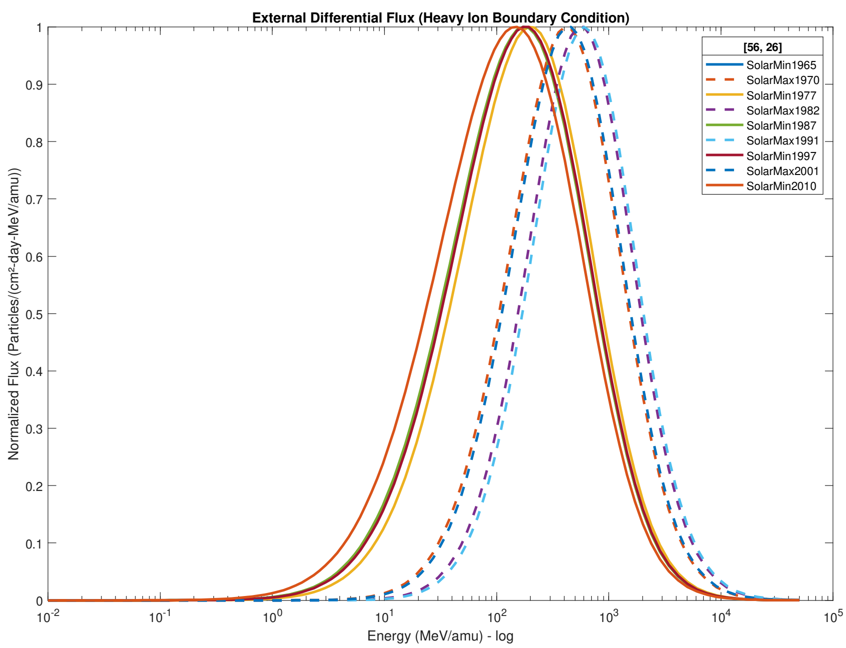

External Differential Flux (Heavy Ion Boundary Condition)
[56, 26]
SolarMin1965
SolarMax1970
SolarMin1977
SolarMax1982
SolarMin1987
SolarMax1991
SolarMin1997
SolarMax2001
SolarMin2010
Normalized Flux (Particles/(cm²-day-MeV/amu))
Energy (MeV/amu) - log

SINP2016 – ^{56}Fe

Plot 1 – Energy vs Flux - Solar Activities

Plot 2 – Energy (log) vs Flux (log) - Solar Activities

Plot 3 – Energy (log) vs Flux (norm) - Solar Activities

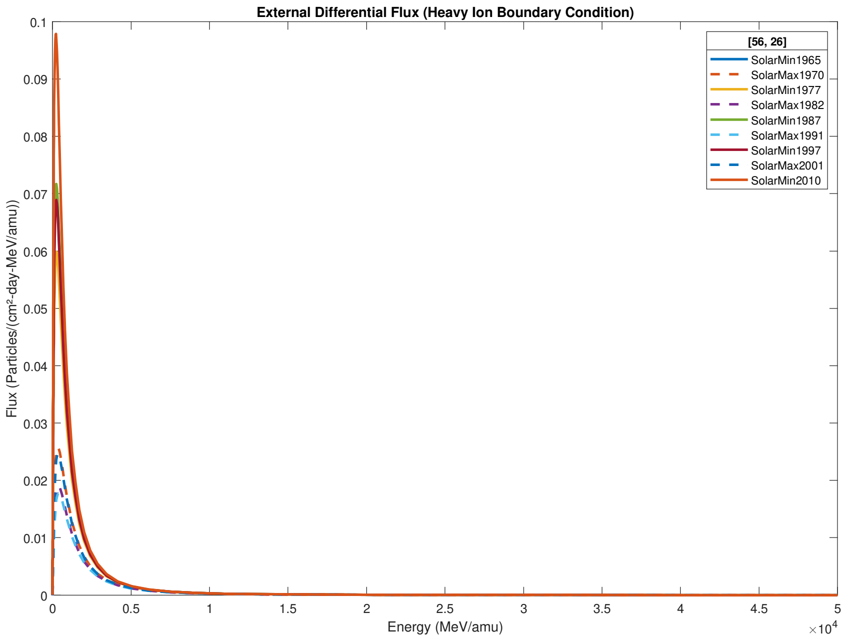
External Differential Flux (Heavy Ion Boundary Condition)
[56, 26]
SolarMin1965
SolarMax1970
SolarMin1977
SolarMax1982
SolarMin1987
SolarMax1991
SolarMin1997
SolarMax2001
SolarMin2010
Flux (Particles/(cm²-day-MeV/amu))
Energy (MeV/amu)
×10⁴

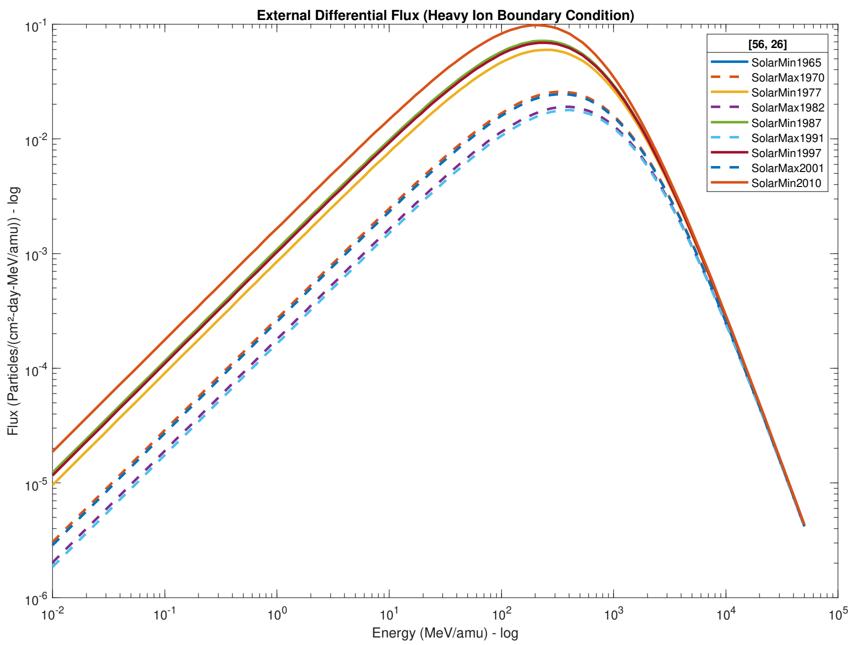
External Differential Flux (Heavy Ion Boundary Condition)
[56, 26]
SolarMin1965
SolarMax1970
SolarMin1977
SolarMax1982
SolarMin1987
SolarMax1991
SolarMin1997
SolarMax2001
SolarMin2010
Flux (Particles/(cm²-day-MeV/amu)) - log
Energy (MeV/amu) - log

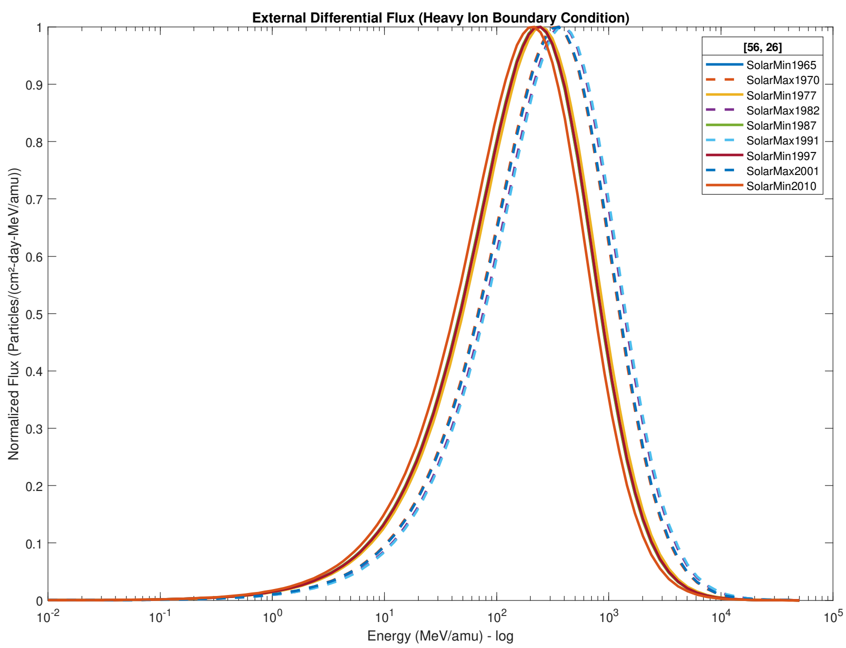
External Differential Flux (Heavy Ion Boundary Condition)
[56, 26]
SolarMin1965
SolarMax1970
SolarMin1977
SolarMax1982
SolarMin1987
SolarMax1991
SolarMin1997
SolarMax2001
SolarMin2010
Normalized Flux (Particles/(cm²-day-MeV/amu))
Energy (MeV/amu) - log

APPENDIX 4 – EXAMPLE OF OLTARIS OUTPUT FILE (GCR – MATTHIA MODEL – 2010 SOLAR MIN)

```
C   Free-Space Boundary Flux (particles/(AMeV-day-cm2)) vs. Energy (AMeV) vs. Isotope
C   Created on Fri Mar  1 07:45:02 2019
C   Job Name: job_9
C   TARIS FORTRAN code version 4.01

C    Energy array dimensions and data
        1     100
    1.000000E-02   1.408122E-02   1.982806E-02   2.780981E-02   3.875467E-02
    5.332453E-02   7.201205E-02   9.504214E-02   1.222573E-01   1.535488E-01
    1.887641E-01   2.276714E-01   2.714374E-01   3.199159E-01   3.737161E-01
    4.336543E-01   5.006712E-01   5.754554E-01   6.594890E-01   7.538421E-01
    8.598675E-01   9.791078E-01   1.111958E+00   1.262183E+00   1.430260E+00
    1.619384E+00   1.831895E+00   2.070313E+00   2.337882E+00   2.638686E+00
    2.976327E+00   3.354537E+00   3.779000E+00   4.255003E+00   4.788643E+00
    5.386816E+00   6.057149E+00   6.808107E+00   7.649509E+00   8.591997E+00
    9.647560E+00   1.082961E+01   1.215322E+01   1.363491E+01   1.529532E+01
    1.715376E+01   1.923466E+01   2.156430E+01   2.417442E+01   2.709740E+01
    3.037216E+01   3.404070E+01   3.815234E+01   4.276254E+01   4.793135E+01
    5.373154E+01   6.023854E+01   6.755091E+01   7.576738E+01   8.500710E+01
    9.540710E+01   1.071423E+02   1.203541E+02   1.352905E+02   1.521613E+02
    1.713748E+02   1.930143E+02   2.178676E+02   2.461532E+02   2.781110E+02
    3.147252E+02   3.571010E+02   4.053476E+02   4.617689E+02   5.268134E+02
    6.024618E+02   6.913280E+02   7.956862E+02   9.191872E+02   1.067888E+03
    1.245753E+03   1.453242E+03   1.709641E+03   2.016451E+03   2.396919E+03
    2.863224E+03   3.444241E+03   4.156085E+03   5.040332E+03   6.133931E+03
    7.488086E+03   9.166967E+03   1.126486E+04   1.386132E+04   1.709441E+04
    2.112206E+04   2.615197E+04   3.243614E+04   4.023251E+04   5.000000E+04


C    Atomic Number Array dimensions and data (atomic-weight and atomic-charge in
brackets)
        1      59
      [  1,   0]     [  1,   1]     [  2,   1]     [  3,   1]     [  3,   2]
      [  4,   2]     [  6,   3]     [  7,   3]     [  8,   4]     [  9,   4]
      [ 10,   5]     [ 11,   5]     [ 12,   6]     [ 13,   6]     [ 14,   7]
      [ 15,   7]     [ 16,   8]     [ 17,   8]     [ 18,   9]     [ 19,   9]
      [ 20,  10]     [ 21,  10]     [ 22,  10]     [ 23,  11]     [ 24,  12]
      [ 25,  12]     [ 26,  12]     [ 27,  13]     [ 28,  14]     [ 29,  15]
      [ 30,  16]     [ 31,  16]     [ 32,  16]     [ 33,  17]     [ 34,  18]
      [ 35,  17]     [ 36,  18]     [ 37,  19]     [ 38,  18]     [ 39,  19]
      [ 40,  20]     [ 41,  20]     [ 42,  20]     [ 43,  21]     [ 44,  22]
      [ 45,  22]     [ 46,  22]     [ 47,  22]     [ 48,  23]     [ 49,  23]
      [ 50,  24]     [ 51,  24]     [ 52,  24]     [ 53,  25]     [ 54,  25]
      [ 55,  26]     [ 56,  26]     [ 57,  27]     [ 58,  28]

C    array dimensions and data
        1     100       1      59
      0.0000e+00     0.0000e+00     0.0000e+00     0.0000e+00     0.0000e+00
      0.0000e+00     0.0000e+00     0.0000e+00     0.0000e+00     0.0000e+00
      0.0000e+00     0.0000e+00     0.0000e+00     0.0000e+00     0.0000e+00
      0.0000e+00     0.0000e+00     0.0000e+00     0.0000e+00     0.0000e+00
      0.0000e+00     0.0000e+00     0.0000e+00     0.0000e+00     0.0000e+00
      0.0000e+00     0.0000e+00     0.0000e+00     0.0000e+00     0.0000e+00
      0.0000e+00     0.0000e+00     0.0000e+00     0.0000e+00     0.0000e+00
      0.0000e+00     0.0000e+00     0.0000e+00     0.0000e+00     0.0000e+00
      0.0000e+00     0.0000e+00     0.0000e+00     0.0000e+00     0.0000e+00
      0.0000e+00     0.0000e+00     0.0000e+00     0.0000e+00     0.0000e+00
      0.0000e+00     0.0000e+00     0.0000e+00     0.0000e+00     0.0000e+00
      0.0000e+00     0.0000e+00     0.0000e+00     0.0000e+00     0.0000e+00
      0.0000e+00     0.0000e+00     0.0000e+00     0.0000e+00     0.0000e+00
      0.0000e+00     0.0000e+00     0.0000e+00     0.0000e+00     0.0000e+00
      0.0000e+00     0.0000e+00     0.0000e+00     0.0000e+00     0.0000e+00
      0.0000e+00     0.0000e+00     0.0000e+00     0.0000e+00     0.0000e+00
      0.0000e+00     0.0000e+00     0.0000e+00     0.0000e+00     0.0000e+00
      0.0000e+00     0.0000e+00     0.0000e+00     0.0000e+00     0.0000e+00
      0.0000e+00     0.0000e+00     0.0000e+00     0.0000e+00     0.0000e+00
      0.0000e+00     0.0000e+00     0.0000e+00     0.0000e+00     0.0000e+00
      2.2674e-04     4.3080e-04     8.1699e-04     1.5346e-03     2.8413e-03
      5.1240e-03     8.9017e-03     1.4784e-02     2.3367e-02     3.5275e-02
```

69	5.1117e-02	7.1435e-02	9.7602e-02	1.3043e-01	1.7129e-01
70	2.2195e-01	2.8462e-01	3.6156e-01	4.5625e-01	5.7222e-01
71	7.1387e-01	8.8641e-01	1.0939e+00	1.3462e+00	1.6489e+00
72	2.0131e+00	2.4491e+00	2.9687e+00	3.5862e+00	4.3188e+00
73	5.1840e+00	6.2000e+00	7.3915e+00	8.7826e+00	1.0400e+01
74	1.2275e+01	1.4437e+01	1.6922e+01	1.9766e+01	2.3006e+01
75	2.6680e+01	3.0830e+01	3.5492e+01	4.0706e+01	4.6513e+01
76	5.2939e+01	6.0016e+01	6.7765e+01	7.6206e+01	8.5341e+01
77	9.5167e+01	1.0566e+02	1.1680e+02	1.2853e+02	1.4078e+02
78	1.5347e+02	1.6647e+02	1.7969e+02	1.9295e+02	2.0608e+02
79	2.1889e+02	2.3118e+02	2.4266e+02	2.5314e+02	2.6232e+02
80	2.6999e+02	2.7580e+02	2.7959e+02	2.8105e+02	2.8003e+02
81	2.7638e+02	2.6995e+02	2.6086e+02	2.4895e+02	2.3458e+02
82	2.1794e+02	1.9932e+02	1.7924e+02	1.5820e+02	1.3659e+02
83	1.1532e+02	9.5588e+01	7.6895e+01	6.0412e+01	4.5947e+01
84	3.3937e+01	2.4238e+01	1.6853e+01	1.1371e+01	7.4747e+00
85	4.7955e+00	3.0090e+00	1.8450e+00	1.1135e+00	6.6118e-01
86	3.8706e-01	2.2363e-01	1.2776e-01	7.2571e-02	4.0822e-02
87	0.0000e+00	0.0000e+00	0.0000e+00	0.0000e+00	0.0000e+00
88	0.0000e+00	0.0000e+00	0.0000e+00	0.0000e+00	0.0000e+00
89	0.0000e+00	0.0000e+00	0.0000e+00	0.0000e+00	0.0000e+00
90	0.0000e+00	0.0000e+00	0.0000e+00	0.0000e+00	0.0000e+00
91	0.0000e+00	0.0000e+00	0.0000e+00	0.0000e+00	0.0000e+00
92	0.0000e+00	0.0000e+00	0.0000e+00	0.0000e+00	0.0000e+00
93	0.0000e+00	0.0000e+00	0.0000e+00	0.0000e+00	0.0000e+00
94	0.0000e+00	0.0000e+00	0.0000e+00	0.0000e+00	0.0000e+00
95	0.0000e+00	0.0000e+00	0.0000e+00	0.0000e+00	0.0000e+00
96	0.0000e+00	0.0000e+00	0.0000e+00	0.0000e+00	0.0000e+00
97	0.0000e+00	0.0000e+00	0.0000e+00	0.0000e+00	0.0000e+00
98	0.0000e+00	0.0000e+00	0.0000e+00	0.0000e+00	0.0000e+00
99	0.0000e+00	0.0000e+00	0.0000e+00	0.0000e+00	0.0000e+00
100	0.0000e+00	0.0000e+00	0.0000e+00	0.0000e+00	0.0000e+00
101	0.0000e+00	0.0000e+00	0.0000e+00	0.0000e+00	0.0000e+00
102	0.0000e+00	0.0000e+00	0.0000e+00	0.0000e+00	0.0000e+00
103	0.0000e+00	0.0000e+00	0.0000e+00	0.0000e+00	0.0000e+00
104	0.0000e+00	0.0000e+00	0.0000e+00	0.0000e+00	0.0000e+00
105	0.0000e+00	0.0000e+00	0.0000e+00	0.0000e+00	0.0000e+00
106	0.0000e+00	0.0000e+00	0.0000e+00	0.0000e+00	0.0000e+00
107	0.0000e+00	0.0000e+00	0.0000e+00	0.0000e+00	0.0000e+00
108	0.0000e+00	0.0000e+00	0.0000e+00	0.0000e+00	0.0000e+00
109	0.0000e+00	0.0000e+00	0.0000e+00	0.0000e+00	0.0000e+00
110	0.0000e+00	0.0000e+00	0.0000e+00	0.0000e+00	0.0000e+00
111	0.0000e+00	0.0000e+00	0.0000e+00	0.0000e+00	0.0000e+00
112	0.0000e+00	0.0000e+00	0.0000e+00	0.0000e+00	0.0000e+00
113	0.0000e+00	0.0000e+00	0.0000e+00	0.0000e+00	0.0000e+00
114	0.0000e+00	0.0000e+00	0.0000e+00	0.0000e+00	0.0000e+00
115	0.0000e+00	0.0000e+00	0.0000e+00	0.0000e+00	0.0000e+00
116	0.0000e+00	0.0000e+00	0.0000e+00	0.0000e+00	0.0000e+00
117	0.0000e+00	0.0000e+00	0.0000e+00	0.0000e+00	0.0000e+00
118	0.0000e+00	0.0000e+00	0.0000e+00	0.0000e+00	0.0000e+00
119	0.0000e+00	0.0000e+00	0.0000e+00	0.0000e+00	0.0000e+00
120	0.0000e+00	0.0000e+00	0.0000e+00	0.0000e+00	0.0000e+00
121	0.0000e+00	0.0000e+00	0.0000e+00	0.0000e+00	0.0000e+00
122	0.0000e+00	0.0000e+00	0.0000e+00	0.0000e+00	0.0000e+00
123	0.0000e+00	0.0000e+00	0.0000e+00	0.0000e+00	0.0000e+00
124	0.0000e+00	0.0000e+00	0.0000e+00	0.0000e+00	0.0000e+00
125	0.0000e+00	0.0000e+00	0.0000e+00	0.0000e+00	0.0000e+00
126	0.0000e+00	0.0000e+00	0.0000e+00	0.0000e+00	0.0000e+00
127	0.0000e+00	0.0000e+00	0.0000e+00	0.0000e+00	0.0000e+00
128	0.0000e+00	0.0000e+00	0.0000e+00	0.0000e+00	0.0000e+00
129	0.0000e+00	0.0000e+00	0.0000e+00	0.0000e+00	0.0000e+00
130	0.0000e+00	0.0000e+00	0.0000e+00	0.0000e+00	0.0000e+00
131	0.0000e+00	0.0000e+00	0.0000e+00	0.0000e+00	0.0000e+00
132	0.0000e+00	0.0000e+00	0.0000e+00	0.0000e+00	0.0000e+00
133	0.0000e+00	0.0000e+00	0.0000e+00	0.0000e+00	0.0000e+00
134	0.0000e+00	0.0000e+00	0.0000e+00	0.0000e+00	0.0000e+00
135	0.0000e+00	0.0000e+00	0.0000e+00	0.0000e+00	0.0000e+00
136	0.0000e+00	0.0000e+00	0.0000e+00	0.0000e+00	0.0000e+00
137	0.0000e+00	0.0000e+00	0.0000e+00	0.0000e+00	0.0000e+00

138	0.0000e+00	0.0000e+00	0.0000e+00	0.0000e+00	0.0000e+00
139	0.0000e+00	0.0000e+00	0.0000e+00	0.0000e+00	0.0000e+00
140	0.0000e+00	0.0000e+00	0.0000e+00	0.0000e+00	0.0000e+00
141	0.0000e+00	0.0000e+00	0.0000e+00	0.0000e+00	0.0000e+00
142	0.0000e+00	0.0000e+00	0.0000e+00	0.0000e+00	0.0000e+00
143	0.0000e+00	0.0000e+00	0.0000e+00	0.0000e+00	0.0000e+00
144	0.0000e+00	0.0000e+00	0.0000e+00	0.0000e+00	0.0000e+00
145	0.0000e+00	0.0000e+00	0.0000e+00	0.0000e+00	0.0000e+00
146	0.0000e+00	0.0000e+00	0.0000e+00	0.0000e+00	0.0000e+00
147	8.9992e-05	1.7640e-04	3.4453e-04	6.6490e-04	1.2613e-03
148	2.3226e-03	4.1047e-03	6.9091e-03	1.1028e-02	1.6763e-02
149	2.4397e-02	3.4175e-02	4.6725e-02	6.2391e-02	8.1768e-02
150	1.0562e-01	1.3485e-01	1.7039e-01	2.1363e-01	2.6593e-01
151	3.2894e-01	4.0454e-01	4.9398e-01	6.0088e-01	7.2674e-01
152	8.7511e-01	1.0490e+00	1.2516e+00	1.4866e+00	1.7584e+00
153	2.0709e+00	2.4278e+00	2.8342e+00	3.2943e+00	3.8125e+00
154	4.3932e+00	5.0404e+00	5.7577e+00	6.5487e+00	7.4158e+00
155	8.3612e+00	9.3857e+00	1.0489e+01	1.1671e+01	1.2930e+01
156	1.4260e+01	1.5657e+01	1.7114e+01	1.8623e+01	2.0173e+01
157	2.1753e+01	2.3349e+01	2.4946e+01	2.6528e+01	2.8076e+01
158	2.9570e+01	3.0991e+01	3.2318e+01	3.3527e+01	3.4598e+01
159	3.5508e+01	3.6236e+01	3.6760e+01	3.7062e+01	3.7124e+01
160	3.6932e+01	3.6477e+01	3.5743e+01	3.4735e+01	3.3469e+01
161	3.1944e+01	3.0164e+01	2.8188e+01	2.6002e+01	2.3684e+01
162	2.1270e+01	1.8796e+01	1.6332e+01	1.3925e+01	1.1609e+01
163	9.4643e+00	7.5838e+00	5.8945e+00	4.4790e+00	3.2954e+00
164	2.3571e+00	1.6319e+00	1.1020e+00	7.2334e-01	4.6349e-01
165	2.9047e-01	1.7840e-01	1.0727e-01	6.3609e-02	3.7169e-02
166	2.1445e-02	1.2227e-02	6.9009e-03	3.8765e-03	2.1581e-03
167	0.0000e+00	0.0000e+00	0.0000e+00	0.0000e+00	0.0000e+00
168	0.0000e+00	0.0000e+00	0.0000e+00	0.0000e+00	0.0000e+00
169	0.0000e+00	0.0000e+00	0.0000e+00	0.0000e+00	0.0000e+00
170	0.0000e+00	0.0000e+00	0.0000e+00	0.0000e+00	0.0000e+00
171	0.0000e+00	0.0000e+00	0.0000e+00	0.0000e+00	0.0000e+00
172	0.0000e+00	0.0000e+00	0.0000e+00	0.0000e+00	0.0000e+00
173	0.0000e+00	0.0000e+00	0.0000e+00	0.0000e+00	0.0000e+00
174	0.0000e+00	0.0000e+00	0.0000e+00	0.0000e+00	0.0000e+00
175	0.0000e+00	0.0000e+00	0.0000e+00	0.0000e+00	0.0000e+00
176	0.0000e+00	0.0000e+00	0.0000e+00	0.0000e+00	0.0000e+00
177	0.0000e+00	0.0000e+00	0.0000e+00	0.0000e+00	0.0000e+00
178	0.0000e+00	0.0000e+00	0.0000e+00	0.0000e+00	0.0000e+00
179	0.0000e+00	0.0000e+00	0.0000e+00	0.0000e+00	0.0000e+00
180	0.0000e+00	0.0000e+00	0.0000e+00	0.0000e+00	0.0000e+00
181	0.0000e+00	0.0000e+00	0.0000e+00	0.0000e+00	0.0000e+00
182	0.0000e+00	0.0000e+00	0.0000e+00	0.0000e+00	0.0000e+00
183	0.0000e+00	0.0000e+00	0.0000e+00	0.0000e+00	0.0000e+00
184	0.0000e+00	0.0000e+00	0.0000e+00	0.0000e+00	0.0000e+00
185	0.0000e+00	0.0000e+00	0.0000e+00	0.0000e+00	0.0000e+00
186	0.0000e+00	0.0000e+00	0.0000e+00	0.0000e+00	0.0000e+00
187	1.9411e-07	3.9516e-07	8.0108e-07	1.6030e-06	3.1483e-06
188	5.9901e-06	1.0908e-05	1.8862e-05	3.0831e-05	4.7852e-05
189	7.0937e-05	1.0099e-04	1.4012e-04	1.8963e-04	2.5160e-04
190	3.2870e-04	4.2420e-04	5.4138e-04	6.8526e-04	8.6077e-04
191	1.0739e-03	1.3315e-03	1.6385e-03	2.0079e-03	2.4455e-03
192	2.9646e-03	3.5764e-03	4.2930e-03	5.1286e-03	6.1000e-03
193	7.2219e-03	8.5086e-03	9.9799e-03	1.1652e-02	1.3544e-02
194	1.5670e-02	1.8049e-02	2.0695e-02	2.3622e-02	2.6842e-02
195	3.0364e-02	3.4193e-02	3.8332e-02	4.2778e-02	4.7529e-02
196	5.2568e-02	5.7880e-02	6.3439e-02	6.9221e-02	7.5186e-02
197	8.1293e-02	8.7491e-02	9.3725e-02	9.9934e-02	1.0605e-01
198	1.1199e-01	1.1768e-01	1.2304e-01	1.2799e-01	1.3242e-01
199	1.3625e-01	1.3939e-01	1.4175e-01	1.4325e-01	1.4382e-01
200	1.4337e-01	1.4188e-01	1.3927e-01	1.3554e-01	1.3075e-01
201	1.2490e-01	1.1800e-01	1.1029e-01	1.0170e-01	9.2551e-02
202	8.2996e-02	7.3193e-02	6.3423e-02	5.3893e-02	4.4736e-02
203	3.6289e-02	2.8914e-02	2.2326e-02	1.6841e-02	1.2290e-02
204	8.7141e-03	5.9757e-03	3.9952e-03	2.5954e-03	1.6454e-03
205	1.0200e-03	6.1959e-04	3.6840e-04	2.1603e-04	1.2483e-04
206	7.1219e-05	4.0152e-05	2.2409e-05	1.2448e-05	6.8528e-06

207	0.0000e+00	0.0000e+00	0.0000e+00	0.0000e+00	0.0000e+00
208	0.0000e+00	0.0000e+00	0.0000e+00	0.0000e+00	0.0000e+00
209	0.0000e+00	0.0000e+00	0.0000e+00	0.0000e+00	0.0000e+00
210	0.0000e+00	0.0000e+00	0.0000e+00	0.0000e+00	0.0000e+00
211	0.0000e+00	0.0000e+00	0.0000e+00	0.0000e+00	0.0000e+00
212	0.0000e+00	0.0000e+00	0.0000e+00	0.0000e+00	0.0000e+00
213	0.0000e+00	0.0000e+00	0.0000e+00	0.0000e+00	0.0000e+00
214	0.0000e+00	0.0000e+00	0.0000e+00	0.0000e+00	0.0000e+00
215	0.0000e+00	0.0000e+00	0.0000e+00	0.0000e+00	0.0000e+00
216	0.0000e+00	0.0000e+00	0.0000e+00	0.0000e+00	0.0000e+00
217	0.0000e+00	0.0000e+00	0.0000e+00	0.0000e+00	0.0000e+00
218	0.0000e+00	0.0000e+00	0.0000e+00	0.0000e+00	0.0000e+00
219	0.0000e+00	0.0000e+00	0.0000e+00	0.0000e+00	0.0000e+00
220	0.0000e+00	0.0000e+00	0.0000e+00	0.0000e+00	0.0000e+00
221	0.0000e+00	0.0000e+00	0.0000e+00	0.0000e+00	0.0000e+00
222	0.0000e+00	0.0000e+00	0.0000e+00	0.0000e+00	0.0000e+00
223	0.0000e+00	0.0000e+00	0.0000e+00	0.0000e+00	0.0000e+00
224	0.0000e+00	0.0000e+00	0.0000e+00	0.0000e+00	0.0000e+00
225	0.0000e+00	0.0000e+00	0.0000e+00	0.0000e+00	0.0000e+00
226	0.0000e+00	0.0000e+00	0.0000e+00	0.0000e+00	0.0000e+00
227	3.8578e-09	8.7996e-09	1.9991e-08	4.4775e-08	9.8241e-08
228	2.0796e-07	4.1881e-07	7.9488e-07	1.4141e-06	2.3699e-06
229	3.7668e-06	5.7132e-06	8.4138e-06	1.2039e-05	1.6840e-05
230	2.3143e-05	3.1366e-05	4.1978e-05	5.5668e-05	7.3201e-05
231	9.5538e-05	1.2386e-04	1.5922e-04	2.0381e-04	2.5916e-04
232	3.2791e-04	4.1279e-04	5.1689e-04	6.4400e-04	7.9872e-04
233	9.8587e-04	1.2106e-03	1.4798e-03	1.8003e-03	2.1799e-03
234	2.6271e-03	3.1513e-03	3.7622e-03	4.4707e-03	5.2878e-03
235	6.2250e-03	7.2939e-03	8.5064e-03	9.8736e-03	1.1408e-02
236	1.3118e-02	1.5013e-02	1.7099e-02	1.9384e-02	2.1867e-02
237	2.4549e-02	2.7424e-02	3.0483e-02	3.3712e-02	3.7091e-02
238	4.0594e-02	4.4187e-02	4.7834e-02	5.1485e-02	5.5085e-02
239	5.8575e-02	6.1889e-02	6.4942e-02	6.7665e-02	6.9970e-02
240	7.1783e-02	7.3004e-02	7.3575e-02	7.3415e-02	7.2487e-02
241	7.0761e-02	6.8206e-02	6.4897e-02	6.0811e-02	5.6103e-02
242	5.0877e-02	4.5255e-02	3.9439e-02	3.3603e-02	2.7877e-02
243	2.2521e-02	1.7811e-02	1.3598e-02	1.0106e-02	7.2370e-03
244	5.0165e-03	3.3501e-03	2.1744e-03	1.3669e-03	8.3625e-04
245	4.9910e-04	2.9129e-04	1.6607e-04	9.3254e-05	5.1530e-05
246	2.8083e-05	1.5109e-05	8.0397e-06	4.2566e-06	2.2318e-06
247	0.0000e+00	0.0000e+00	0.0000e+00	0.0000e+00	0.0000e+00
248	0.0000e+00	0.0000e+00	0.0000e+00	0.0000e+00	0.0000e+00
249	0.0000e+00	0.0000e+00	0.0000e+00	0.0000e+00	0.0000e+00
250	0.0000e+00	0.0000e+00	0.0000e+00	0.0000e+00	0.0000e+00
251	0.0000e+00	0.0000e+00	0.0000e+00	0.0000e+00	0.0000e+00
252	0.0000e+00	0.0000e+00	0.0000e+00	0.0000e+00	0.0000e+00
253	0.0000e+00	0.0000e+00	0.0000e+00	0.0000e+00	0.0000e+00
254	0.0000e+00	0.0000e+00	0.0000e+00	0.0000e+00	0.0000e+00
255	0.0000e+00	0.0000e+00	0.0000e+00	0.0000e+00	0.0000e+00
256	0.0000e+00	0.0000e+00	0.0000e+00	0.0000e+00	0.0000e+00
257	0.0000e+00	0.0000e+00	0.0000e+00	0.0000e+00	0.0000e+00
258	0.0000e+00	0.0000e+00	0.0000e+00	0.0000e+00	0.0000e+00
259	0.0000e+00	0.0000e+00	0.0000e+00	0.0000e+00	0.0000e+00
260	0.0000e+00	0.0000e+00	0.0000e+00	0.0000e+00	0.0000e+00
261	0.0000e+00	0.0000e+00	0.0000e+00	0.0000e+00	0.0000e+00
262	0.0000e+00	0.0000e+00	0.0000e+00	0.0000e+00	0.0000e+00
263	0.0000e+00	0.0000e+00	0.0000e+00	0.0000e+00	0.0000e+00
264	0.0000e+00	0.0000e+00	0.0000e+00	0.0000e+00	0.0000e+00
265	0.0000e+00	0.0000e+00	0.0000e+00	0.0000e+00	0.0000e+00
266	0.0000e+00	0.0000e+00	0.0000e+00	0.0000e+00	0.0000e+00
267	4.8743e-08	1.0603e-07	2.2974e-07	4.9110e-07	1.0294e-06
268	2.0856e-06	4.0309e-06	7.3659e-06	1.2662e-05	2.0575e-05
269	3.1801e-05	4.7029e-05	6.7640e-05	9.4673e-05	1.2970e-04
270	1.7474e-04	2.3235e-04	3.0527e-04	3.9758e-04	5.1366e-04
271	6.5888e-04	8.3976e-04	1.0617e-03	1.3367e-03	1.6723e-03
272	2.0821e-03	2.5795e-03	3.1795e-03	3.8999e-03	4.7623e-03
273	5.7883e-03	7.0005e-03	8.4282e-03	1.0100e-02	1.2049e-02
274	1.4307e-02	1.6910e-02	1.9895e-02	2.3300e-02	2.7163e-02
275	3.1521e-02	3.6410e-02	4.1864e-02	4.7912e-02	5.4586e-02

276	6.1898e-02	6.9865e-02	7.8487e-02	8.7764e-02	9.7673e-02
277	1.0818e-01	1.1925e-01	1.3081e-01	1.4278e-01	1.5506e-01
278	1.6754e-01	1.8007e-01	1.9251e-01	2.0467e-01	2.1635e-01
279	2.2734e-01	2.3743e-01	2.4634e-01	2.5386e-01	2.5972e-01
280	2.6372e-01	2.6558e-01	2.6514e-01	2.6222e-01	2.5678e-01
281	2.4875e-01	2.3810e-01	2.2515e-01	2.0982e-01	1.9271e-01
282	1.7414e-01	1.5451e-01	1.3447e-01	1.1455e-01	9.5136e-02
283	7.7050e-02	6.1166e-02	4.6947e-02	3.5126e-02	2.5363e-02
284	1.7752e-02	1.1988e-02	7.8779e-03	5.0199e-03	3.1162e-03
285	1.8888e-03	1.1203e-03	6.4958e-04	3.7114e-04	2.0877e-04
286	1.1587e-04	6.3503e-05	3.4434e-05	1.8580e-05	9.9305e-06
287	1.7348e-06	3.4416e-06	6.8026e-06	1.3285e-05	2.5495e-05
288	4.7475e-05	8.4789e-05	1.4411e-04	2.3206e-04	3.5556e-04
289	5.2125e-04	7.3495e-04	1.0110e-03	1.3578e-03	1.7892e-03
290	2.3231e-03	2.9811e-03	3.7851e-03	4.7683e-03	5.9636e-03
291	7.4106e-03	9.1553e-03	1.1229e-02	1.3720e-02	1.6666e-02
292	2.0156e-02	2.4266e-02	2.9076e-02	3.4682e-02	4.1197e-02
293	4.8724e-02	5.7359e-02	6.7237e-02	7.8476e-02	9.1195e-02
294	1.0552e-01	1.2156e-01	1.3942e-01	1.5921e-01	1.8102e-01
295	2.0492e-01	2.3095e-01	2.5914e-01	2.8948e-01	3.2196e-01
296	3.5648e-01	3.9294e-01	4.3118e-01	4.7102e-01	5.1221e-01
297	5.5446e-01	5.9743e-01	6.4073e-01	6.8395e-01	7.2659e-01
298	7.6815e-01	8.0806e-01	8.4577e-01	8.8066e-01	9.1211e-01
299	9.3949e-01	9.6220e-01	9.7958e-01	9.9111e-01	9.9623e-01
300	9.9449e-01	9.8555e-01	9.6897e-01	9.4473e-01	9.1321e-01
301	8.7435e-01	8.2818e-01	7.7625e-01	7.1817e-01	6.5602e-01
302	5.9077e-01	5.2347e-01	4.5601e-01	3.8980e-01	3.2575e-01
303	2.6620e-01	2.1377e-01	1.6652e-01	1.2679e-01	9.3476e-02
304	6.6996e-02	4.6474e-02	3.1444e-02	2.0680e-02	1.3277e-02
305	8.3365e-03	5.1302e-03	3.0907e-03	1.8365e-03	1.0753e-03
306	6.2167e-04	3.5518e-04	2.0089e-04	1.1308e-04	6.3089e-05
307	0.0000e+00	0.0000e+00	0.0000e+00	0.0000e+00	0.0000e+00
308	0.0000e+00	0.0000e+00	0.0000e+00	0.0000e+00	0.0000e+00
309	0.0000e+00	0.0000e+00	0.0000e+00	0.0000e+00	0.0000e+00
310	0.0000e+00	0.0000e+00	0.0000e+00	0.0000e+00	0.0000e+00
311	0.0000e+00	0.0000e+00	0.0000e+00	0.0000e+00	0.0000e+00
312	0.0000e+00	0.0000e+00	0.0000e+00	0.0000e+00	0.0000e+00
313	0.0000e+00	0.0000e+00	0.0000e+00	0.0000e+00	0.0000e+00
314	0.0000e+00	0.0000e+00	0.0000e+00	0.0000e+00	0.0000e+00
315	0.0000e+00	0.0000e+00	0.0000e+00	0.0000e+00	0.0000e+00
316	0.0000e+00	0.0000e+00	0.0000e+00	0.0000e+00	0.0000e+00
317	0.0000e+00	0.0000e+00	0.0000e+00	0.0000e+00	0.0000e+00
318	0.0000e+00	0.0000e+00	0.0000e+00	0.0000e+00	0.0000e+00
319	0.0000e+00	0.0000e+00	0.0000e+00	0.0000e+00	0.0000e+00
320	0.0000e+00	0.0000e+00	0.0000e+00	0.0000e+00	0.0000e+00
321	0.0000e+00	0.0000e+00	0.0000e+00	0.0000e+00	0.0000e+00
322	0.0000e+00	0.0000e+00	0.0000e+00	0.0000e+00	0.0000e+00
323	0.0000e+00	0.0000e+00	0.0000e+00	0.0000e+00	0.0000e+00
324	0.0000e+00	0.0000e+00	0.0000e+00	0.0000e+00	0.0000e+00
325	0.0000e+00	0.0000e+00	0.0000e+00	0.0000e+00	0.0000e+00
326	0.0000e+00	0.0000e+00	0.0000e+00	0.0000e+00	0.0000e+00
327	4.7995e-08	1.0301e-07	2.2029e-07	4.6500e-07	9.6315e-07
328	1.9301e-06	3.6937e-06	6.6917e-06	1.1418e-05	1.8435e-05
329	2.8340e-05	4.1718e-05	5.9758e-05	8.3343e-05	1.1382e-04
330	1.5292e-04	2.0282e-04	2.6588e-04	3.4560e-04	4.4572e-04
331	5.7085e-04	7.2659e-04	9.1758e-04	1.1542e-03	1.4428e-03
332	1.7953e-03	2.2233e-03	2.7397e-03	3.3601e-03	4.1034e-03
333	4.9885e-03	6.0353e-03	7.2697e-03	8.7175e-03	1.0407e-02
334	1.2368e-02	1.4632e-02	1.7233e-02	2.0206e-02	2.3585e-02
335	2.7405e-02	3.1699e-02	3.6500e-02	4.1836e-02	4.7737e-02
336	5.4218e-02	6.1295e-02	6.8972e-02	7.7253e-02	8.6119e-02
337	9.5548e-02	1.0550e-01	1.1592e-01	1.2675e-01	1.3789e-01
338	1.4924e-01	1.6068e-01	1.7208e-01	1.8327e-01	1.9407e-01
339	2.0430e-01	2.1376e-01	2.2221e-01	2.2945e-01	2.3523e-01
340	2.3938e-01	2.4162e-01	2.4182e-01	2.3979e-01	2.3548e-01
341	2.2883e-01	2.1976e-01	2.0857e-01	1.9516e-01	1.8003e-01
342	1.6347e-01	1.4582e-01	1.2765e-01	1.0944e-01	9.1543e-02
343	7.4719e-02	5.9805e-02	4.6322e-02	3.4995e-02	2.5537e-02
344	1.8075e-02	1.2354e-02	8.2198e-03	5.3064e-03	3.3386e-03

345	2.0517e-03	1.2342e-03	7.2597e-04	4.2086e-04	2.4025e-04
346	1.3533e-04	7.5293e-05	4.1450e-05	2.2706e-05	1.2323e-05
347	0.0000e+00	0.0000e+00	0.0000e+00	0.0000e+00	0.0000e+00
348	0.0000e+00	0.0000e+00	0.0000e+00	0.0000e+00	0.0000e+00
349	0.0000e+00	0.0000e+00	0.0000e+00	0.0000e+00	0.0000e+00
350	0.0000e+00	0.0000e+00	0.0000e+00	0.0000e+00	0.0000e+00
351	0.0000e+00	0.0000e+00	0.0000e+00	0.0000e+00	0.0000e+00
352	0.0000e+00	0.0000e+00	0.0000e+00	0.0000e+00	0.0000e+00
353	0.0000e+00	0.0000e+00	0.0000e+00	0.0000e+00	0.0000e+00
354	0.0000e+00	0.0000e+00	0.0000e+00	0.0000e+00	0.0000e+00
355	0.0000e+00	0.0000e+00	0.0000e+00	0.0000e+00	0.0000e+00
356	0.0000e+00	0.0000e+00	0.0000e+00	0.0000e+00	0.0000e+00
357	0.0000e+00	0.0000e+00	0.0000e+00	0.0000e+00	0.0000e+00
358	0.0000e+00	0.0000e+00	0.0000e+00	0.0000e+00	0.0000e+00
359	0.0000e+00	0.0000e+00	0.0000e+00	0.0000e+00	0.0000e+00
360	0.0000e+00	0.0000e+00	0.0000e+00	0.0000e+00	0.0000e+00
361	0.0000e+00	0.0000e+00	0.0000e+00	0.0000e+00	0.0000e+00
362	0.0000e+00	0.0000e+00	0.0000e+00	0.0000e+00	0.0000e+00
363	0.0000e+00	0.0000e+00	0.0000e+00	0.0000e+00	0.0000e+00
364	0.0000e+00	0.0000e+00	0.0000e+00	0.0000e+00	0.0000e+00
365	0.0000e+00	0.0000e+00	0.0000e+00	0.0000e+00	0.0000e+00
366	0.0000e+00	0.0000e+00	0.0000e+00	0.0000e+00	0.0000e+00
367	1.6132e-06	3.1947e-06	6.3040e-06	1.2290e-05	2.3547e-05
368	4.3778e-05	7.8069e-05	1.3251e-04	2.1311e-04	3.2615e-04
369	4.7764e-04	6.7282e-04	9.2478e-04	1.2409e-03	1.6340e-03
370	2.1199e-03	2.7185e-03	3.4492e-03	4.3422e-03	5.4271e-03
371	6.7396e-03	8.3210e-03	1.0200e-02	1.2454e-02	1.5119e-02
372	1.8274e-02	2.1987e-02	2.6329e-02	3.1387e-02	3.7262e-02
373	4.4044e-02	5.1820e-02	6.0711e-02	7.0819e-02	8.2252e-02
374	9.5117e-02	1.0952e-01	1.2554e-01	1.4329e-01	1.6284e-01
375	1.8424e-01	2.0754e-01	2.3276e-01	2.5989e-01	2.8892e-01
376	3.1976e-01	3.5231e-01	3.8644e-01	4.2198e-01	4.5872e-01
377	4.9639e-01	5.3468e-01	5.7327e-01	6.1179e-01	6.4978e-01
378	6.8683e-01	7.2242e-01	7.5608e-01	7.8725e-01	8.1539e-01
379	8.3995e-01	8.6042e-01	8.7619e-01	8.8682e-01	8.9181e-01
380	8.9077e-01	8.8339e-01	8.6927e-01	8.4839e-01	8.2105e-01
381	7.8719e-01	7.4682e-01	7.0126e-01	6.5016e-01	5.9532e-01
382	5.3755e-01	4.7778e-01	4.1764e-01	3.5839e-01	3.0081e-01
383	2.4702e-01	1.9942e-01	1.5626e-01	1.1975e-01	8.8920e-02
384	6.4227e-02	4.4931e-02	3.0674e-02	2.0367e-02	1.3208e-02
385	8.3808e-03	5.2138e-03	3.1768e-03	1.9096e-03	1.1314e-03
386	6.6209e-04	3.8296e-04	2.1933e-04	1.2503e-04	7.0650e-05
387	0.0000e+00	0.0000e+00	0.0000e+00	0.0000e+00	0.0000e+00
388	0.0000e+00	0.0000e+00	0.0000e+00	0.0000e+00	0.0000e+00
389	0.0000e+00	0.0000e+00	0.0000e+00	0.0000e+00	0.0000e+00
390	0.0000e+00	0.0000e+00	0.0000e+00	0.0000e+00	0.0000e+00
391	0.0000e+00	0.0000e+00	0.0000e+00	0.0000e+00	0.0000e+00
392	0.0000e+00	0.0000e+00	0.0000e+00	0.0000e+00	0.0000e+00
393	0.0000e+00	0.0000e+00	0.0000e+00	0.0000e+00	0.0000e+00
394	0.0000e+00	0.0000e+00	0.0000e+00	0.0000e+00	0.0000e+00
395	0.0000e+00	0.0000e+00	0.0000e+00	0.0000e+00	0.0000e+00
396	0.0000e+00	0.0000e+00	0.0000e+00	0.0000e+00	0.0000e+00
397	0.0000e+00	0.0000e+00	0.0000e+00	0.0000e+00	0.0000e+00
398	0.0000e+00	0.0000e+00	0.0000e+00	0.0000e+00	0.0000e+00
399	0.0000e+00	0.0000e+00	0.0000e+00	0.0000e+00	0.0000e+00
400	0.0000e+00	0.0000e+00	0.0000e+00	0.0000e+00	0.0000e+00
401	0.0000e+00	0.0000e+00	0.0000e+00	0.0000e+00	0.0000e+00
402	0.0000e+00	0.0000e+00	0.0000e+00	0.0000e+00	0.0000e+00
403	0.0000e+00	0.0000e+00	0.0000e+00	0.0000e+00	0.0000e+00
404	0.0000e+00	0.0000e+00	0.0000e+00	0.0000e+00	0.0000e+00
405	0.0000e+00	0.0000e+00	0.0000e+00	0.0000e+00	0.0000e+00
406	0.0000e+00	0.0000e+00	0.0000e+00	0.0000e+00	0.0000e+00
407	0.0000e+00	0.0000e+00	0.0000e+00	0.0000e+00	0.0000e+00
408	0.0000e+00	0.0000e+00	0.0000e+00	0.0000e+00	0.0000e+00
409	0.0000e+00	0.0000e+00	0.0000e+00	0.0000e+00	0.0000e+00
410	0.0000e+00	0.0000e+00	0.0000e+00	0.0000e+00	0.0000e+00
411	0.0000e+00	0.0000e+00	0.0000e+00	0.0000e+00	0.0000e+00
412	0.0000e+00	0.0000e+00	0.0000e+00	0.0000e+00	0.0000e+00
413	0.0000e+00	0.0000e+00	0.0000e+00	0.0000e+00	0.0000e+00

0.0000e+00	0.0000e+00	0.0000e+00	0.0000e+00	0.0000e+00
0.0000e+00	0.0000e+00	0.0000e+00	0.0000e+00	0.0000e+00
0.0000e+00	0.0000e+00	0.0000e+00	0.0000e+00	0.0000e+00
0.0000e+00	0.0000e+00	0.0000e+00	0.0000e+00	0.0000e+00
0.0000e+00	0.0000e+00	0.0000e+00	0.0000e+00	0.0000e+00
0.0000e+00	0.0000e+00	0.0000e+00	0.0000e+00	0.0000e+00
0.0000e+00	0.0000e+00	0.0000e+00	0.0000e+00	0.0000e+00
0.0000e+00	0.0000e+00	0.0000e+00	0.0000e+00	0.0000e+00
0.0000e+00	0.0000e+00	0.0000e+00	0.0000e+00	0.0000e+00
0.0000e+00	0.0000e+00	0.0000e+00	0.0000e+00	0.0000e+00
0.0000e+00	0.0000e+00	0.0000e+00	0.0000e+00	0.0000e+00
0.0000e+00	0.0000e+00	0.0000e+00	0.0000e+00	0.0000e+00
0.0000e+00	0.0000e+00	0.0000e+00	0.0000e+00	0.0000e+00
7.7094e-10	1.7549e-09	3.9794e-09	8.8991e-09	1.9502e-08
4.1248e-08	8.3029e-08	1.5757e-07	2.8036e-07	4.7005e-07
7.4757e-07	1.1347e-06	1.6726e-06	2.3956e-06	3.3546e-06
4.6158e-06	6.2640e-06	8.3951e-06	1.1150e-05	1.4685e-05
1.9198e-05	2.4934e-05	3.2114e-05	4.1190e-05	5.2486e-05
6.6555e-05	8.3974e-05	1.0540e-04	1.3165e-04	1.6370e-04
2.0260e-04	2.4948e-04	3.0581e-04	3.7313e-04	4.5316e-04
5.4782e-04	6.5919e-04	7.8951e-04	9.4127e-04	1.1170e-03
1.3195e-03	1.5514e-03	1.8157e-03	2.1150e-03	2.4525e-03
2.8305e-03	3.2514e-03	3.7172e-03	4.2299e-03	4.7902e-03
5.3988e-03	6.0550e-03	6.7577e-03	7.5045e-03	8.2914e-03
9.1136e-03	9.9640e-03	1.0835e-02	1.1717e-02	1.2597e-02
1.3462e-02	1.4299e-02	1.5087e-02	1.5810e-02	1.6448e-02
1.6984e-02	1.7392e-02	1.7657e-02	1.7758e-02	1.7681e-02
1.7417e-02	1.6955e-02	1.6303e-02	1.5455e-02	1.4439e-02
1.3274e-02	1.1985e-02	1.0617e-02	9.2091e-03	7.7924e-03
6.4323e-03	5.2042e-03	4.0751e-03	3.1117e-03	2.2954e-03
1.6425e-03	1.1352e-03	7.6388e-04	4.9888e-04	3.1762e-04
1.9758e-04	1.2035e-04	7.1712e-05	4.2125e-05	2.4374e-05
1.3921e-05	7.8551e-06	4.3869e-06	2.4382e-06	1.3428e-06
4.0249e-07	7.8895e-07	1.5409e-06	2.9738e-06	5.6410e-06
1.0388e-05	1.8358e-05	3.0901e-05	4.9323e-05	7.4971e-05
1.0912e-04	1.5285e-04	2.0898e-04	2.7904e-04	3.6571e-04
4.7237e-04	6.0312e-04	7.6205e-04	9.5545e-04	1.1894e-03
1.4712e-03	1.8093e-03	2.2093e-03	2.6874e-03	3.2504e-03
3.9140e-03	4.6917e-03	5.5978e-03	6.6488e-03	7.8647e-03
9.2625e-03	1.0859e-02	1.2676e-02	1.4734e-02	1.7052e-02
1.9650e-02	2.2544e-02	2.5753e-02	2.9291e-02	3.3170e-02
3.7399e-02	4.1982e-02	4.6920e-02	5.2207e-02	5.7837e-02
6.3789e-02	7.0039e-02	7.6558e-02	8.3311e-02	9.0249e-02
9.7322e-02	1.0447e-01	1.1162e-01	1.1870e-01	1.2563e-01
1.3233e-01	1.3869e-01	1.4464e-01	1.5007e-01	1.5487e-01
1.5896e-01	1.6224e-01	1.6461e-01	1.6598e-01	1.6629e-01
1.6546e-01	1.6345e-01	1.6020e-01	1.5571e-01	1.5008e-01
1.4328e-01	1.3534e-01	1.2652e-01	1.1676e-01	1.0640e-01
9.5602e-02	8.4532e-02	7.3493e-02	6.2709e-02	5.2316e-02
4.2688e-02	3.4237e-02	2.6638e-02	2.0263e-02	1.4927e-02
1.0691e-02	7.4119e-03	5.0126e-03	3.2956e-03	2.1152e-03
1.3280e-03	8.1709e-04	4.9221e-04	2.9245e-04	1.7122e-04
9.8991e-05	5.6555e-05	3.1986e-05	1.8006e-05	1.0045e-05
0.0000e+00	0.0000e+00	0.0000e+00	0.0000e+00	0.0000e+00
0.0000e+00	0.0000e+00	0.0000e+00	0.0000e+00	0.0000e+00
0.0000e+00	0.0000e+00	0.0000e+00	0.0000e+00	0.0000e+00
0.0000e+00	0.0000e+00	0.0000e+00	0.0000e+00	0.0000e+00
0.0000e+00	0.0000e+00	0.0000e+00	0.0000e+00	0.0000e+00
0.0000e+00	0.0000e+00	0.0000e+00	0.0000e+00	0.0000e+00
0.0000e+00	0.0000e+00	0.0000e+00	0.0000e+00	0.0000e+00
0.0000e+00	0.0000e+00	0.0000e+00	0.0000e+00	0.0000e+00
0.0000e+00	0.0000e+00	0.0000e+00	0.0000e+00	0.0000e+00
0.0000e+00	0.0000e+00	0.0000e+00	0.0000e+00	0.0000e+00
0.0000e+00	0.0000e+00	0.0000e+00	0.0000e+00	0.0000e+00
0.0000e+00	0.0000e+00	0.0000e+00	0.0000e+00	0.0000e+00
0.0000e+00	0.0000e+00	0.0000e+00	0.0000e+00	0.0000e+00
0.0000e+00	0.0000e+00	0.0000e+00	0.0000e+00	0.0000e+00
0.0000e+00	0.0000e+00	0.0000e+00	0.0000e+00	0.0000e+00
0.0000e+00	0.0000e+00	0.0000e+00	0.0000e+00	0.0000e+00

483	0.0000e+00	0.0000e+00	0.0000e+00	0.0000e+00	0.0000e+00
484	0.0000e+00	0.0000e+00	0.0000e+00	0.0000e+00	0.0000e+00
485	0.0000e+00	0.0000e+00	0.0000e+00	0.0000e+00	0.0000e+00
486	0.0000e+00	0.0000e+00	0.0000e+00	0.0000e+00	0.0000e+00
487	0.0000e+00	0.0000e+00	0.0000e+00	0.0000e+00	0.0000e+00
488	0.0000e+00	0.0000e+00	0.0000e+00	0.0000e+00	0.0000e+00
489	0.0000e+00	0.0000e+00	0.0000e+00	0.0000e+00	0.0000e+00
490	0.0000e+00	0.0000e+00	0.0000e+00	0.0000e+00	0.0000e+00
491	0.0000e+00	0.0000e+00	0.0000e+00	0.0000e+00	0.0000e+00
492	0.0000e+00	0.0000e+00	0.0000e+00	0.0000e+00	0.0000e+00
493	0.0000e+00	0.0000e+00	0.0000e+00	0.0000e+00	0.0000e+00
494	0.0000e+00	0.0000e+00	0.0000e+00	0.0000e+00	0.0000e+00
495	0.0000e+00	0.0000e+00	0.0000e+00	0.0000e+00	0.0000e+00
496	0.0000e+00	0.0000e+00	0.0000e+00	0.0000e+00	0.0000e+00
497	0.0000e+00	0.0000e+00	0.0000e+00	0.0000e+00	0.0000e+00
498	0.0000e+00	0.0000e+00	0.0000e+00	0.0000e+00	0.0000e+00
499	0.0000e+00	0.0000e+00	0.0000e+00	0.0000e+00	0.0000e+00
500	0.0000e+00	0.0000e+00	0.0000e+00	0.0000e+00	0.0000e+00
501	0.0000e+00	0.0000e+00	0.0000e+00	0.0000e+00	0.0000e+00
502	0.0000e+00	0.0000e+00	0.0000e+00	0.0000e+00	0.0000e+00
503	0.0000e+00	0.0000e+00	0.0000e+00	0.0000e+00	0.0000e+00
504	0.0000e+00	0.0000e+00	0.0000e+00	0.0000e+00	0.0000e+00
505	0.0000e+00	0.0000e+00	0.0000e+00	0.0000e+00	0.0000e+00
506	0.0000e+00	0.0000e+00	0.0000e+00	0.0000e+00	0.0000e+00
507	1.5287e-07	2.9684e-07	5.7421e-07	1.0975e-06	2.0619e-06
508	3.7608e-06	6.5858e-06	1.0990e-05	1.7400e-05	2.6251e-05
509	3.7943e-05	5.2809e-05	7.1760e-05	9.5260e-05	1.2414e-04
510	1.5947e-04	2.0251e-04	2.5452e-04	3.1742e-04	3.9305e-04
511	4.8361e-04	5.9161e-04	7.1860e-04	8.6945e-04	1.0460e-03
512	1.2527e-03	1.4935e-03	1.7722e-03	2.0934e-03	2.4625e-03
513	2.8839e-03	3.3620e-03	3.9025e-03	4.5102e-03	5.1899e-03
514	5.9459e-03	6.7824e-03	7.7027e-03	8.7097e-03	9.8052e-03
515	1.0990e-02	1.2264e-02	1.3625e-02	1.5071e-02	1.6597e-02
516	1.8196e-02	1.9860e-02	2.1579e-02	2.3342e-02	2.5136e-02
517	2.6944e-02	2.8750e-02	3.0535e-02	3.2280e-02	3.3962e-02
518	3.5560e-02	3.7050e-02	3.8410e-02	3.9614e-02	4.0640e-02
519	4.1464e-02	4.2066e-02	4.2424e-02	4.2520e-02	4.2340e-02
520	4.1868e-02	4.1105e-02	4.0033e-02	3.8663e-02	3.7023e-02
521	3.5114e-02	3.2943e-02	3.0584e-02	2.8022e-02	2.5348e-02
522	2.2602e-02	1.9826e-02	1.7095e-02	1.4460e-02	1.1953e-02
523	9.6598e-03	7.6714e-03	5.9057e-03	4.4431e-03	3.2346e-03
524	2.2883e-03	1.5658e-03	1.0447e-03	6.7723e-04	4.2838e-04
525	2.6494e-04	1.6053e-04	9.5189e-05	5.5658e-05	3.2060e-05
526	1.8231e-05	1.0243e-05	5.6957e-06	3.1522e-06	1.7286e-06
527	1.9521e-08	4.2403e-08	9.1771e-08	1.9603e-07	4.1077e-07
528	8.3242e-07	1.6099e-06	2.9450e-06	5.0695e-06	8.2508e-06
529	1.2776e-05	1.8930e-05	2.7284e-05	3.8272e-05	5.2552e-05
530	7.0974e-05	9.4610e-05	1.2464e-04	1.6278e-04	2.1092e-04
531	2.7139e-04	3.4701e-04	4.4019e-04	5.5617e-04	6.9832e-04
532	8.7274e-04	1.0855e-03	1.3434e-03	1.6547e-03	2.0294e-03
533	2.4777e-03	3.0104e-03	3.6415e-03	4.3852e-03	5.2570e-03
534	6.2739e-03	7.4539e-03	8.8160e-03	1.0380e-02	1.2167e-02
535	1.4197e-02	1.6492e-02	1.9070e-02	2.1950e-02	2.5153e-02
536	2.8691e-02	3.2576e-02	3.6815e-02	4.1416e-02	4.6373e-02
537	5.1680e-02	5.7321e-02	6.3272e-02	6.9503e-02	7.5969e-02
538	8.2621e-02	8.9391e-02	9.6214e-02	1.0300e-01	1.0965e-01
539	1.1606e-01	1.2212e-01	1.2768e-01	1.3264e-01	1.3684e-01
540	1.4017e-01	1.4246e-01	1.4362e-01	1.4350e-01	1.4205e-01
541	1.3921e-01	1.3492e-01	1.2928e-01	1.2223e-01	1.1400e-01
542	1.0475e-01	9.4637e-02	8.3992e-02	7.3091e-02	6.2144e-02
543	5.1626e-02	4.2094e-02	3.3280e-02	2.5696e-02	1.9204e-02
544	1.3944e-02	9.7971e-03	6.7107e-03	4.4674e-03	2.9027e-03
545	1.8445e-03	1.1487e-03	7.0040e-04	4.2122e-04	2.4966e-04
546	1.4613e-04	8.4539e-05	4.8422e-05	2.7606e-05	1.5600e-05
547	0.0000e+00	0.0000e+00	0.0000e+00	0.0000e+00	0.0000e+00
548	0.0000e+00	0.0000e+00	0.0000e+00	0.0000e+00	0.0000e+00
549	0.0000e+00	0.0000e+00	0.0000e+00	0.0000e+00	0.0000e+00
550	0.0000e+00	0.0000e+00	0.0000e+00	0.0000e+00	0.0000e+00
551	0.0000e+00	0.0000e+00	0.0000e+00	0.0000e+00	0.0000e+00

552	0.0000e+00	0.0000e+00	0.0000e+00	0.0000e+00	0.0000e+00
553	0.0000e+00	0.0000e+00	0.0000e+00	0.0000e+00	0.0000e+00
554	0.0000e+00	0.0000e+00	0.0000e+00	0.0000e+00	0.0000e+00
555	0.0000e+00	0.0000e+00	0.0000e+00	0.0000e+00	0.0000e+00
556	0.0000e+00	0.0000e+00	0.0000e+00	0.0000e+00	0.0000e+00
557	0.0000e+00	0.0000e+00	0.0000e+00	0.0000e+00	0.0000e+00
558	0.0000e+00	0.0000e+00	0.0000e+00	0.0000e+00	0.0000e+00
559	0.0000e+00	0.0000e+00	0.0000e+00	0.0000e+00	0.0000e+00
560	0.0000e+00	0.0000e+00	0.0000e+00	0.0000e+00	0.0000e+00
561	0.0000e+00	0.0000e+00	0.0000e+00	0.0000e+00	0.0000e+00
562	0.0000e+00	0.0000e+00	0.0000e+00	0.0000e+00	0.0000e+00
563	0.0000e+00	0.0000e+00	0.0000e+00	0.0000e+00	0.0000e+00
564	0.0000e+00	0.0000e+00	0.0000e+00	0.0000e+00	0.0000e+00
565	0.0000e+00	0.0000e+00	0.0000e+00	0.0000e+00	0.0000e+00
566	0.0000e+00	0.0000e+00	0.0000e+00	0.0000e+00	0.0000e+00
567	0.0000e+00	0.0000e+00	0.0000e+00	0.0000e+00	0.0000e+00
568	0.0000e+00	0.0000e+00	0.0000e+00	0.0000e+00	0.0000e+00
569	0.0000e+00	0.0000e+00	0.0000e+00	0.0000e+00	0.0000e+00
570	0.0000e+00	0.0000e+00	0.0000e+00	0.0000e+00	0.0000e+00
571	0.0000e+00	0.0000e+00	0.0000e+00	0.0000e+00	0.0000e+00
572	0.0000e+00	0.0000e+00	0.0000e+00	0.0000e+00	0.0000e+00
573	0.0000e+00	0.0000e+00	0.0000e+00	0.0000e+00	0.0000e+00
574	0.0000e+00	0.0000e+00	0.0000e+00	0.0000e+00	0.0000e+00
575	0.0000e+00	0.0000e+00	0.0000e+00	0.0000e+00	0.0000e+00
576	0.0000e+00	0.0000e+00	0.0000e+00	0.0000e+00	0.0000e+00
577	0.0000e+00	0.0000e+00	0.0000e+00	0.0000e+00	0.0000e+00
578	0.0000e+00	0.0000e+00	0.0000e+00	0.0000e+00	0.0000e+00
579	0.0000e+00	0.0000e+00	0.0000e+00	0.0000e+00	0.0000e+00
580	0.0000e+00	0.0000e+00	0.0000e+00	0.0000e+00	0.0000e+00
581	0.0000e+00	0.0000e+00	0.0000e+00	0.0000e+00	0.0000e+00
582	0.0000e+00	0.0000e+00	0.0000e+00	0.0000e+00	0.0000e+00
583	0.0000e+00	0.0000e+00	0.0000e+00	0.0000e+00	0.0000e+00
584	0.0000e+00	0.0000e+00	0.0000e+00	0.0000e+00	0.0000e+00
585	0.0000e+00	0.0000e+00	0.0000e+00	0.0000e+00	0.0000e+00
586	0.0000e+00	0.0000e+00	0.0000e+00	0.0000e+00	0.0000e+00
587	1.8174e-08	3.7729e-08	7.8034e-08	1.5935e-07	3.1944e-07
588	6.2023e-07	1.1519e-06	2.0296e-06	3.3762e-06	5.3264e-06
589	8.0172e-06	1.1577e-05	1.6284e-05	2.2326e-05	2.9999e-05
590	3.9679e-05	5.1835e-05	6.6957e-05	8.5777e-05	1.0905e-04
591	1.3770e-04	1.7282e-04	2.1526e-04	2.6704e-04	3.2927e-04
592	4.0415e-04	4.9371e-04	6.0017e-04	7.2618e-04	8.7488e-04
593	1.0493e-03	1.2525e-03	1.4885e-03	1.7611e-03	2.0743e-03
594	2.4323e-03	2.8395e-03	3.2999e-03	3.8181e-03	4.3978e-03
595	5.0429e-03	5.7567e-03	6.5421e-03	7.4010e-03	8.3358e-03
596	9.3457e-03	1.0430e-02	1.1588e-02	1.2815e-02	1.4107e-02
597	1.5458e-02	1.6858e-02	1.8299e-02	1.9767e-02	2.1250e-02
598	2.2732e-02	2.4193e-02	2.5617e-02	2.6982e-02	2.8264e-02
599	2.9440e-02	3.0488e-02	3.1379e-02	3.2090e-02	3.2598e-02
600	3.2879e-02	3.2912e-02	3.2680e-02	3.2168e-02	3.1380e-02
601	3.0310e-02	2.8954e-02	2.7355e-02	2.5501e-02	2.3459e-02
602	2.1263e-02	1.8953e-02	1.6599e-02	1.4256e-02	1.1962e-02
603	9.8090e-03	7.8981e-03	6.1647e-03	4.7003e-03	3.4678e-03
604	2.4858e-03	1.7237e-03	1.1652e-03	7.6542e-04	4.9065e-04
605	3.0755e-04	1.8890e-04	1.1357e-04	6.7337e-05	3.9341e-05
606	2.2695e-05	1.2937e-05	7.3007e-06	4.1005e-06	2.2825e-06
607	3.6957e-07	7.2318e-07	1.4100e-06	2.7166e-06	5.1447e-06
608	9.4586e-06	1.6691e-05	2.8056e-05	4.4726e-05	6.7907e-05
609	9.8733e-05	1.3817e-04	1.8875e-04	2.5183e-04	3.2979e-04
610	4.2565e-04	5.4309e-04	6.8573e-04	8.5918e-04	1.0688e-03
611	1.3212e-03	1.6239e-03	1.9817e-03	2.4090e-03	2.9118e-03
612	3.5042e-03	4.1981e-03	5.0059e-03	5.9423e-03	7.0250e-03
613	8.2689e-03	9.6885e-03	1.1304e-02	1.3132e-02	1.5190e-02
614	1.7495e-02	2.0062e-02	2.2906e-02	2.6040e-02	2.9474e-02
615	3.3217e-02	3.7271e-02	4.1637e-02	4.6309e-02	5.1284e-02
616	5.6540e-02	6.2060e-02	6.7815e-02	7.3776e-02	7.9900e-02
617	8.6144e-02	9.2452e-02	9.8769e-02	1.0503e-01	1.1116e-01
618	1.1710e-01	1.2274e-01	1.2804e-01	1.3288e-01	1.3719e-01
619	1.4088e-01	1.4388e-01	1.4609e-01	1.4745e-01	1.4788e-01
620	1.4733e-01	1.4575e-01	1.4310e-01	1.3937e-01	1.3463e-01

621	1.2886e-01	1.2208e-01	1.1450e-01	1.0606e-01	9.7059e-02
622	8.7620e-02	7.7886e-02	6.8118e-02	5.8508e-02	4.9177e-02
623	4.0461e-02	3.2741e-02	2.5730e-02	1.9786e-02	1.4751e-02
624	1.0703e-02	7.5260e-03	5.1666e-03	3.4515e-03	2.2528e-03
625	1.4392e-03	9.0179e-04	5.5358e-04	3.3531e-04	2.0024e-04
626	1.1812e-04	6.8884e-05	3.9781e-05	2.2869e-05	1.3033e-05
627	3.8466e-10	8.6406e-10	1.9337e-09	4.2687e-09	9.2376e-09
628	1.9305e-08	3.8426e-08	7.2179e-08	1.2725e-07	2.1160e-07
629	3.3405e-07	5.0368e-07	7.3785e-07	1.0508e-06	1.4635e-06
630	2.0036e-06	2.7058e-06	3.6094e-06	4.7721e-06	6.2574e-06
631	8.1456e-06	1.0535e-05	1.3514e-05	1.7263e-05	2.1911e-05
632	2.7678e-05	3.4789e-05	4.3504e-05	5.4138e-05	6.7074e-05
633	8.2715e-05	1.0150e-04	1.2398e-04	1.5076e-04	1.8247e-04
634	2.1984e-04	2.6366e-04	3.1475e-04	3.7402e-04	4.4242e-04
635	5.2093e-04	6.1053e-04	7.1225e-04	8.2704e-04	9.5600e-04
636	1.0998e-03	1.2594e-03	1.4353e-03	1.6281e-03	1.8379e-03
637	2.0649e-03	2.3085e-03	2.5681e-03	2.8427e-03	3.1306e-03
638	3.4298e-03	3.7374e-03	4.0507e-03	4.3655e-03	4.6774e-03
639	4.9814e-03	5.2723e-03	5.5430e-03	5.7877e-03	5.9990e-03
640	6.1710e-03	6.2946e-03	6.3653e-03	6.3756e-03	6.3217e-03
641	6.2006e-03	6.0091e-03	5.7520e-03	5.4267e-03	5.0448e-03
642	4.6140e-03	4.1435e-03	3.6496e-03	3.1466e-03	2.6455e-03
643	2.1689e-03	1.7425e-03	1.3540e-03	1.0256e-03	7.4998e-04
644	5.3170e-04	3.6383e-04	2.4227e-04	1.5648e-04	9.8477e-05
645	6.0522e-05	3.6406e-05	2.1413e-05	1.2412e-05	7.0841e-06
646	3.9899e-06	2.2195e-06	1.2217e-06	6.6916e-07	3.6311e-07
647	0.0000e+00	0.0000e+00	0.0000e+00	0.0000e+00	0.0000e+00
648	0.0000e+00	0.0000e+00	0.0000e+00	0.0000e+00	0.0000e+00
649	0.0000e+00	0.0000e+00	0.0000e+00	0.0000e+00	0.0000e+00
650	0.0000e+00	0.0000e+00	0.0000e+00	0.0000e+00	0.0000e+00
651	0.0000e+00	0.0000e+00	0.0000e+00	0.0000e+00	0.0000e+00
652	0.0000e+00	0.0000e+00	0.0000e+00	0.0000e+00	0.0000e+00
653	0.0000e+00	0.0000e+00	0.0000e+00	0.0000e+00	0.0000e+00
654	0.0000e+00	0.0000e+00	0.0000e+00	0.0000e+00	0.0000e+00
655	0.0000e+00	0.0000e+00	0.0000e+00	0.0000e+00	0.0000e+00
656	0.0000e+00	0.0000e+00	0.0000e+00	0.0000e+00	0.0000e+00
657	0.0000e+00	0.0000e+00	0.0000e+00	0.0000e+00	0.0000e+00
658	0.0000e+00	0.0000e+00	0.0000e+00	0.0000e+00	0.0000e+00
659	0.0000e+00	0.0000e+00	0.0000e+00	0.0000e+00	0.0000e+00
660	0.0000e+00	0.0000e+00	0.0000e+00	0.0000e+00	0.0000e+00
661	0.0000e+00	0.0000e+00	0.0000e+00	0.0000e+00	0.0000e+00
662	0.0000e+00	0.0000e+00	0.0000e+00	0.0000e+00	0.0000e+00
663	0.0000e+00	0.0000e+00	0.0000e+00	0.0000e+00	0.0000e+00
664	0.0000e+00	0.0000e+00	0.0000e+00	0.0000e+00	0.0000e+00
665	0.0000e+00	0.0000e+00	0.0000e+00	0.0000e+00	0.0000e+00
666	0.0000e+00	0.0000e+00	0.0000e+00	0.0000e+00	0.0000e+00
667	0.0000e+00	0.0000e+00	0.0000e+00	0.0000e+00	0.0000e+00
668	0.0000e+00	0.0000e+00	0.0000e+00	0.0000e+00	0.0000e+00
669	0.0000e+00	0.0000e+00	0.0000e+00	0.0000e+00	0.0000e+00
670	0.0000e+00	0.0000e+00	0.0000e+00	0.0000e+00	0.0000e+00
671	0.0000e+00	0.0000e+00	0.0000e+00	0.0000e+00	0.0000e+00
672	0.0000e+00	0.0000e+00	0.0000e+00	0.0000e+00	0.0000e+00
673	0.0000e+00	0.0000e+00	0.0000e+00	0.0000e+00	0.0000e+00
674	0.0000e+00	0.0000e+00	0.0000e+00	0.0000e+00	0.0000e+00
675	0.0000e+00	0.0000e+00	0.0000e+00	0.0000e+00	0.0000e+00
676	0.0000e+00	0.0000e+00	0.0000e+00	0.0000e+00	0.0000e+00
677	0.0000e+00	0.0000e+00	0.0000e+00	0.0000e+00	0.0000e+00
678	0.0000e+00	0.0000e+00	0.0000e+00	0.0000e+00	0.0000e+00
679	0.0000e+00	0.0000e+00	0.0000e+00	0.0000e+00	0.0000e+00
680	0.0000e+00	0.0000e+00	0.0000e+00	0.0000e+00	0.0000e+00
681	0.0000e+00	0.0000e+00	0.0000e+00	0.0000e+00	0.0000e+00
682	0.0000e+00	0.0000e+00	0.0000e+00	0.0000e+00	0.0000e+00
683	0.0000e+00	0.0000e+00	0.0000e+00	0.0000e+00	0.0000e+00
684	0.0000e+00	0.0000e+00	0.0000e+00	0.0000e+00	0.0000e+00
685	0.0000e+00	0.0000e+00	0.0000e+00	0.0000e+00	0.0000e+00
686	0.0000e+00	0.0000e+00	0.0000e+00	0.0000e+00	0.0000e+00
687	2.1318e-08	4.3540e-08	8.8602e-08	1.7808e-07	3.5152e-07
688	6.7258e-07	1.2323e-06	2.1444e-06	3.5279e-06	5.5111e-06
689	8.2223e-06	1.1779e-05	1.6448e-05	2.2400e-05	2.9910e-05

690	3.9329e-05	5.1088e-05	6.5637e-05	8.3651e-05	1.0582e-04
691	1.3297e-04	1.6609e-04	2.0593e-04	2.5433e-04	3.1225e-04
692	3.8163e-04	4.6427e-04	5.6210e-04	6.7743e-04	8.1300e-04
693	9.7138e-04	1.1552e-03	1.3679e-03	1.6126e-03	1.8928e-03
694	2.2120e-03	2.5736e-03	2.9811e-03	3.4381e-03	3.9475e-03
695	4.5124e-03	5.1353e-03	5.8183e-03	6.5625e-03	7.3696e-03
696	8.2384e-03	9.1683e-03	1.0157e-02	1.1201e-02	1.2297e-02
697	1.3437e-02	1.4615e-02	1.5822e-02	1.7048e-02	1.8280e-02
698	1.9505e-02	2.0709e-02	2.1875e-02	2.2987e-02	2.4025e-02
699	2.4971e-02	2.5806e-02	2.6508e-02	2.7060e-02	2.7441e-02
700	2.7635e-02	2.7626e-02	2.7398e-02	2.6944e-02	2.6266e-02
701	2.5360e-02	2.4223e-02	2.2891e-02	2.1353e-02	1.9664e-02
702	1.7850e-02	1.5943e-02	1.3998e-02	1.2060e-02	1.0158e-02
703	8.3670e-03	6.7710e-03	5.3160e-03	4.0797e-03	3.0321e-03
704	2.1911e-03	1.5329e-03	1.0460e-03	6.9406e-04	4.4962e-04
705	2.8493e-04	1.7700e-04	1.0767e-04	6.4607e-05	3.8208e-05
706	2.2316e-05	1.2882e-05	7.3625e-06	4.1884e-06	2.3617e-06
707	0.0000e+00	0.0000e+00	0.0000e+00	0.0000e+00	0.0000e+00
708	0.0000e+00	0.0000e+00	0.0000e+00	0.0000e+00	0.0000e+00
709	0.0000e+00	0.0000e+00	0.0000e+00	0.0000e+00	0.0000e+00
710	0.0000e+00	0.0000e+00	0.0000e+00	0.0000e+00	0.0000e+00
711	0.0000e+00	0.0000e+00	0.0000e+00	0.0000e+00	0.0000e+00
712	0.0000e+00	0.0000e+00	0.0000e+00	0.0000e+00	0.0000e+00
713	0.0000e+00	0.0000e+00	0.0000e+00	0.0000e+00	0.0000e+00
714	0.0000e+00	0.0000e+00	0.0000e+00	0.0000e+00	0.0000e+00
715	0.0000e+00	0.0000e+00	0.0000e+00	0.0000e+00	0.0000e+00
716	0.0000e+00	0.0000e+00	0.0000e+00	0.0000e+00	0.0000e+00
717	0.0000e+00	0.0000e+00	0.0000e+00	0.0000e+00	0.0000e+00
718	0.0000e+00	0.0000e+00	0.0000e+00	0.0000e+00	0.0000e+00
719	0.0000e+00	0.0000e+00	0.0000e+00	0.0000e+00	0.0000e+00
720	0.0000e+00	0.0000e+00	0.0000e+00	0.0000e+00	0.0000e+00
721	0.0000e+00	0.0000e+00	0.0000e+00	0.0000e+00	0.0000e+00
722	0.0000e+00	0.0000e+00	0.0000e+00	0.0000e+00	0.0000e+00
723	0.0000e+00	0.0000e+00	0.0000e+00	0.0000e+00	0.0000e+00
724	0.0000e+00	0.0000e+00	0.0000e+00	0.0000e+00	0.0000e+00
725	0.0000e+00	0.0000e+00	0.0000e+00	0.0000e+00	0.0000e+00
726	0.0000e+00	0.0000e+00	0.0000e+00	0.0000e+00	0.0000e+00
727	0.0000e+00	0.0000e+00	0.0000e+00	0.0000e+00	0.0000e+00
728	0.0000e+00	0.0000e+00	0.0000e+00	0.0000e+00	0.0000e+00
729	0.0000e+00	0.0000e+00	0.0000e+00	0.0000e+00	0.0000e+00
730	0.0000e+00	0.0000e+00	0.0000e+00	0.0000e+00	0.0000e+00
731	0.0000e+00	0.0000e+00	0.0000e+00	0.0000e+00	0.0000e+00
732	0.0000e+00	0.0000e+00	0.0000e+00	0.0000e+00	0.0000e+00
733	0.0000e+00	0.0000e+00	0.0000e+00	0.0000e+00	0.0000e+00
734	0.0000e+00	0.0000e+00	0.0000e+00	0.0000e+00	0.0000e+00
735	0.0000e+00	0.0000e+00	0.0000e+00	0.0000e+00	0.0000e+00
736	0.0000e+00	0.0000e+00	0.0000e+00	0.0000e+00	0.0000e+00
737	0.0000e+00	0.0000e+00	0.0000e+00	0.0000e+00	0.0000e+00
738	0.0000e+00	0.0000e+00	0.0000e+00	0.0000e+00	0.0000e+00
739	0.0000e+00	0.0000e+00	0.0000e+00	0.0000e+00	0.0000e+00
740	0.0000e+00	0.0000e+00	0.0000e+00	0.0000e+00	0.0000e+00
741	0.0000e+00	0.0000e+00	0.0000e+00	0.0000e+00	0.0000e+00
742	0.0000e+00	0.0000e+00	0.0000e+00	0.0000e+00	0.0000e+00
743	0.0000e+00	0.0000e+00	0.0000e+00	0.0000e+00	0.0000e+00
744	0.0000e+00	0.0000e+00	0.0000e+00	0.0000e+00	0.0000e+00
745	0.0000e+00	0.0000e+00	0.0000e+00	0.0000e+00	0.0000e+00
746	0.0000e+00	0.0000e+00	0.0000e+00	0.0000e+00	0.0000e+00
747	1.0436e-10	2.4468e-10	5.7157e-10	1.3164e-09	2.9697e-09
748	6.4596e-09	1.3352e-08	2.5968e-08	4.7252e-08	8.0856e-08
749	1.3100e-07	2.0224e-07	3.0288e-07	4.4035e-07	6.2544e-07
750	8.7241e-07	1.1997e-06	1.6287e-06	2.1906e-06	2.9212e-06
751	3.8663e-06	5.0830e-06	6.6256e-06	8.6002e-06	1.1089e-05
752	1.4229e-05	1.8165e-05	2.3069e-05	2.9150e-05	3.6671e-05
753	4.5913e-05	5.7193e-05	7.0919e-05	8.7530e-05	1.0753e-04
754	1.3148e-04	1.6001e-04	1.9383e-04	2.3371e-04	2.8049e-04
755	3.3505e-04	3.9835e-04	4.7139e-04	5.5518e-04	6.5085e-04
756	7.5935e-04	8.8171e-04	1.0188e-03	1.1717e-03	1.3408e-03
757	1.5269e-03	1.7300e-03	1.9503e-03	2.1873e-03	2.4402e-03
758	2.7078e-03	2.9881e-03	3.2790e-03	3.5771e-03	3.8787e-03

4.1794e-03	4.4741e-03	4.7562e-03	5.0197e-03	5.2569e-03
5.4617e-03	5.6239e-03	5.7386e-03	5.7965e-03	5.7921e-03
5.7215e-03	5.5804e-03	5.3712e-03	5.0914e-03	4.7507e-03
4.3568e-03	3.9187e-03	3.4529e-03	2.9742e-03	2.4947e-03
2.0374e-03	1.6283e-03	1.2565e-03	9.4376e-04	6.8311e-04
4.7860e-04	3.2309e-04	2.1196e-04	1.3469e-04	8.3291e-05
5.0249e-05	2.9644e-05	1.7084e-05	9.6977e-06	5.4170e-06
2.9845e-06	1.6233e-06	8.7330e-07	4.6745e-07	2.4779e-07
0.0000e+00	0.0000e+00	0.0000e+00	0.0000e+00	0.0000e+00
0.0000e+00	0.0000e+00	0.0000e+00	0.0000e+00	0.0000e+00
0.0000e+00	0.0000e+00	0.0000e+00	0.0000e+00	0.0000e+00
0.0000e+00	0.0000e+00	0.0000e+00	0.0000e+00	0.0000e+00
0.0000e+00	0.0000e+00	0.0000e+00	0.0000e+00	0.0000e+00
0.0000e+00	0.0000e+00	0.0000e+00	0.0000e+00	0.0000e+00
0.0000e+00	0.0000e+00	0.0000e+00	0.0000e+00	0.0000e+00
0.0000e+00	0.0000e+00	0.0000e+00	0.0000e+00	0.0000e+00
0.0000e+00	0.0000e+00	0.0000e+00	0.0000e+00	0.0000e+00
0.0000e+00	0.0000e+00	0.0000e+00	0.0000e+00	0.0000e+00
0.0000e+00	0.0000e+00	0.0000e+00	0.0000e+00	0.0000e+00
0.0000e+00	0.0000e+00	0.0000e+00	0.0000e+00	0.0000e+00
0.0000e+00	0.0000e+00	0.0000e+00	0.0000e+00	0.0000e+00
0.0000e+00	0.0000e+00	0.0000e+00	0.0000e+00	0.0000e+00
0.0000e+00	0.0000e+00	0.0000e+00	0.0000e+00	0.0000e+00
0.0000e+00	0.0000e+00	0.0000e+00	0.0000e+00	0.0000e+00
0.0000e+00	0.0000e+00	0.0000e+00	0.0000e+00	0.0000e+00
0.0000e+00	0.0000e+00	0.0000e+00	0.0000e+00	0.0000e+00
0.0000e+00	0.0000e+00	0.0000e+00	0.0000e+00	0.0000e+00
0.0000e+00	0.0000e+00	0.0000e+00	0.0000e+00	0.0000e+00
0.0000e+00	0.0000e+00	0.0000e+00	0.0000e+00	0.0000e+00
0.0000e+00	0.0000e+00	0.0000e+00	0.0000e+00	0.0000e+00
0.0000e+00	0.0000e+00	0.0000e+00	0.0000e+00	0.0000e+00
0.0000e+00	0.0000e+00	0.0000e+00	0.0000e+00	0.0000e+00
0.0000e+00	0.0000e+00	0.0000e+00	0.0000e+00	0.0000e+00
0.0000e+00	0.0000e+00	0.0000e+00	0.0000e+00	0.0000e+00
0.0000e+00	0.0000e+00	0.0000e+00	0.0000e+00	0.0000e+00
0.0000e+00	0.0000e+00	0.0000e+00	0.0000e+00	0.0000e+00
0.0000e+00	0.0000e+00	0.0000e+00	0.0000e+00	0.0000e+00
0.0000e+00	0.0000e+00	0.0000e+00	0.0000e+00	0.0000e+00
0.0000e+00	0.0000e+00	0.0000e+00	0.0000e+00	0.0000e+00
0.0000e+00	0.0000e+00	0.0000e+00	0.0000e+00	0.0000e+00
0.0000e+00	0.0000e+00	0.0000e+00	0.0000e+00	0.0000e+00
0.0000e+00	0.0000e+00	0.0000e+00	0.0000e+00	0.0000e+00
0.0000e+00	0.0000e+00	0.0000e+00	0.0000e+00	0.0000e+00
0.0000e+00	0.0000e+00	0.0000e+00	0.0000e+00	0.0000e+00
0.0000e+00	0.0000e+00	0.0000e+00	0.0000e+00	0.0000e+00
0.0000e+00	0.0000e+00	0.0000e+00	0.0000e+00	0.0000e+00
0.0000e+00	0.0000e+00	0.0000e+00	0.0000e+00	0.0000e+00
0.0000e+00	0.0000e+00	0.0000e+00	0.0000e+00	0.0000e+00
2.3989e-10	5.6157e-10	1.3093e-09	3.0091e-09	6.7715e-09
1.4689e-08	3.0270e-08	5.8691e-08	1.0646e-07	1.8159e-07
2.9328e-07	4.5136e-07	6.7389e-07	9.7671e-07	1.3829e-06
1.9229e-06	2.6358e-06	3.5666e-06	4.7811e-06	6.3539e-06
8.3799e-06	1.0977e-05	1.4255e-05	1.8434e-05	2.3676e-05
3.0257e-05	3.8469e-05	4.8649e-05	6.1212e-05	7.6666e-05
9.5560e-05	1.1850e-04	1.4625e-04	1.7966e-04	2.1965e-04
2.6728e-04	3.2370e-04	3.9019e-04	4.6812e-04	5.5900e-04
6.6438e-04	7.8591e-04	9.2531e-04	1.0843e-03	1.2647e-03
1.4681e-03	1.6961e-03	1.9501e-03	2.2316e-03	2.5413e-03
2.8799e-03	3.2475e-03	3.6438e-03	4.0679e-03	4.5178e-03
4.9912e-03	5.4842e-03	5.9929e-03	6.5113e-03	7.0328e-03
7.5494e-03	8.0527e-03	8.5310e-03	8.9743e-03	9.3697e-03
9.7068e-03	9.9687e-03	1.0147e-02	1.0227e-02	1.0200e-02
1.0060e-02	9.7988e-03	9.4225e-03	8.9261e-03	8.3271e-03
7.6381e-03	6.8746e-03	6.0645e-03	5.2328e-03	4.3993e-03
3.6037e-03	2.8904e-03	2.2403e-03	1.6913e-03	1.2316e-03
8.6878e-04	5.9108e-04	3.9112e-04	2.5088e-04	1.5674e-04
9.5593e-05	5.7048e-05	3.3280e-05	1.9131e-05	1.0827e-05
6.0463e-06	3.3345e-06	1.8195e-06	9.8800e-07	5.3144e-07
1.1625e-10	2.7445e-10	6.4555e-10	1.4970e-09	3.4000e-09

7.4436e-09	1.5480e-08	3.0279e-08	5.5381e-08	9.5209e-08
1.5491e-07	2.4007e-07	3.6086e-07	5.2643e-07	7.5012e-07
1.0496e-06	1.4476e-06	1.9710e-06	2.6585e-06	3.5552e-06
4.7184e-06	6.2202e-06	8.1295e-06	1.0581e-05	1.3679e-05
1.7598e-05	2.2524e-05	2.8679e-05	3.6333e-05	4.5825e-05
5.7521e-05	7.1834e-05	8.9300e-05	1.1049e-04	1.3608e-04
1.6680e-04	2.0351e-04	2.4713e-04	2.9871e-04	3.5937e-04
4.3032e-04	5.1286e-04	6.0835e-04	7.1819e-04	8.4395e-04
9.8695e-04	1.1486e-03	1.3303e-03	1.5334e-03	1.7587e-03
2.0072e-03	2.2792e-03	2.5749e-03	2.8939e-03	3.2351e-03
3.5971e-03	3.9773e-03	4.3727e-03	4.7790e-03	5.1911e-03
5.6028e-03	6.0076e-03	6.3959e-03	6.7597e-03	7.0883e-03
7.3730e-03	7.5996e-03	7.7612e-03	7.8449e-03	7.8429e-03
7.7495e-03	7.5589e-03	7.2742e-03	6.8920e-03	6.4260e-03
5.8866e-03	5.2870e-03	4.6499e-03	3.9962e-03	3.3426e-03
2.7210e-03	2.1666e-03	1.6647e-03	1.2444e-03	8.9577e-04
6.2380e-04	4.1829e-04	2.7245e-04	1.7179e-04	1.0537e-04
6.3024e-05	3.6849e-05	2.1039e-05	1.1829e-05	6.5430e-06
3.5689e-06	1.9213e-06	1.0229e-06	5.4184e-07	2.8419e-07
1.4703e-07	2.7898e-07	5.2744e-07	9.8572e-07	1.8118e-06
3.2368e-06	5.5594e-06	9.1142e-06	1.4204e-05	2.1128e-05
3.0153e-05	4.1492e-05	5.5791e-05	7.3343e-05	9.4714e-05
1.2062e-04	1.5192e-04	1.8944e-04	2.3446e-04	2.8818e-04
3.5204e-04	4.2765e-04	5.1594e-04	6.2009e-04	7.4114e-04
8.8201e-04	1.0450e-03	1.2324e-03	1.4471e-03	1.6922e-03
1.9704e-03	2.2840e-03	2.6364e-03	3.0303e-03	3.4681e-03
3.9523e-03	4.4848e-03	5.0670e-03	5.7004e-03	6.3853e-03
7.1215e-03	7.9083e-03	8.7437e-03	9.6251e-03	1.0550e-02
1.1512e-02	1.2507e-02	1.3528e-02	1.4568e-02	1.5617e-02
1.6667e-02	1.7706e-02	1.8725e-02	1.9710e-02	2.0651e-02
2.1533e-02	2.2345e-02	2.3073e-02	2.3704e-02	2.4226e-02
2.4627e-02	2.4896e-02	2.5022e-02	2.4997e-02	2.4815e-02
2.4469e-02	2.3960e-02	2.3279e-02	2.2436e-02	2.1446e-02
2.0312e-02	1.9037e-02	1.7664e-02	1.6182e-02	1.4644e-02
1.3071e-02	1.1485e-02	9.9255e-03	8.4216e-03	6.9887e-03
5.6746e-03	4.5312e-03	3.5109e-03	2.6607e-03	1.9532e-03
1.3945e-03	9.6395e-04	6.5016e-04	4.2639e-04	2.7303e-04
1.7102e-04	1.0500e-04	6.3116e-05	3.7421e-05	2.1864e-05
1.2614e-05	7.1912e-06	4.0585e-06	2.2798e-06	1.2692e-06
0.0000e+00	0.0000e+00	0.0000e+00	0.0000e+00	0.0000e+00
0.0000e+00	0.0000e+00	0.0000e+00	0.0000e+00	0.0000e+00
0.0000e+00	0.0000e+00	0.0000e+00	0.0000e+00	0.0000e+00
0.0000e+00	0.0000e+00	0.0000e+00	0.0000e+00	0.0000e+00
0.0000e+00	0.0000e+00	0.0000e+00	0.0000e+00	0.0000e+00
0.0000e+00	0.0000e+00	0.0000e+00	0.0000e+00	0.0000e+00
0.0000e+00	0.0000e+00	0.0000e+00	0.0000e+00	0.0000e+00
0.0000e+00	0.0000e+00	0.0000e+00	0.0000e+00	0.0000e+00
0.0000e+00	0.0000e+00	0.0000e+00	0.0000e+00	0.0000e+00
0.0000e+00	0.0000e+00	0.0000e+00	0.0000e+00	0.0000e+00
0.0000e+00	0.0000e+00	0.0000e+00	0.0000e+00	0.0000e+00
0.0000e+00	0.0000e+00	0.0000e+00	0.0000e+00	0.0000e+00
0.0000e+00	0.0000e+00	0.0000e+00	0.0000e+00	0.0000e+00
0.0000e+00	0.0000e+00	0.0000e+00	0.0000e+00	0.0000e+00
0.0000e+00	0.0000e+00	0.0000e+00	0.0000e+00	0.0000e+00
0.0000e+00	0.0000e+00	0.0000e+00	0.0000e+00	0.0000e+00
0.0000e+00	0.0000e+00	0.0000e+00	0.0000e+00	0.0000e+00
0.0000e+00	0.0000e+00	0.0000e+00	0.0000e+00	0.0000e+00
0.0000e+00	0.0000e+00	0.0000e+00	0.0000e+00	0.0000e+00
0.0000e+00	0.0000e+00	0.0000e+00	0.0000e+00	0.0000e+00
0.0000e+00	0.0000e+00	0.0000e+00	0.0000e+00	0.0000e+00
0.0000e+00	0.0000e+00	0.0000e+00	0.0000e+00	0.0000e+00
0.0000e+00	0.0000e+00	0.0000e+00	0.0000e+00	0.0000e+00
0.0000e+00	0.0000e+00	0.0000e+00	0.0000e+00	0.0000e+00
0.0000e+00	0.0000e+00	0.0000e+00	0.0000e+00	0.0000e+00
0.0000e+00	0.0000e+00	0.0000e+00	0.0000e+00	0.0000e+00
0.0000e+00	0.0000e+00	0.0000e+00	0.0000e+00	0.0000e+00
0.0000e+00	0.0000e+00	0.0000e+00	0.0000e+00	0.0000e+00
0.0000e+00	0.0000e+00	0.0000e+00	0.0000e+00	0.0000e+00

897	0.0000e+00	0.0000e+00	0.0000e+00	0.0000e+00	0.0000e+00
898	0.0000e+00	0.0000e+00	0.0000e+00	0.0000e+00	0.0000e+00
899	0.0000e+00	0.0000e+00	0.0000e+00	0.0000e+00	0.0000e+00
900	0.0000e+00	0.0000e+00	0.0000e+00	0.0000e+00	0.0000e+00
901	0.0000e+00	0.0000e+00	0.0000e+00	0.0000e+00	0.0000e+00
902	0.0000e+00	0.0000e+00	0.0000e+00	0.0000e+00	0.0000e+00
903	0.0000e+00	0.0000e+00	0.0000e+00	0.0000e+00	0.0000e+00
904	0.0000e+00	0.0000e+00	0.0000e+00	0.0000e+00	0.0000e+00
905	0.0000e+00	0.0000e+00	0.0000e+00	0.0000e+00	0.0000e+00
906	0.0000e+00	0.0000e+00	0.0000e+00	0.0000e+00	0.0000e+00
907	1.6064e-09	3.4020e-09	7.1768e-09	1.4943e-08	3.0527e-08
908	6.0349e-08	1.1399e-07	2.0395e-07	3.4398e-07	5.4944e-07
909	8.3623e-07	1.2196e-06	1.7315e-06	2.3944e-06	3.2433e-06
910	4.3228e-06	5.6885e-06	7.3995e-06	9.5440e-06	1.2214e-05
911	1.5522e-05	1.9604e-05	2.4566e-05	3.0660e-05	3.8027e-05
912	4.6945e-05	5.7673e-05	7.0499e-05	8.5767e-05	1.0389e-04
913	1.2526e-04	1.5029e-04	1.7953e-04	2.1348e-04	2.5269e-04
914	2.9777e-04	3.4929e-04	4.0786e-04	4.7410e-04	5.4861e-04
915	6.3195e-04	7.2463e-04	8.2712e-04	9.3978e-04	1.0630e-03
916	1.1968e-03	1.3412e-03	1.4961e-03	1.6611e-03	1.8357e-03
917	2.0190e-03	2.2101e-03	2.4075e-03	2.6097e-03	2.8148e-03
918	3.0206e-03	3.2245e-03	3.4240e-03	3.6159e-03	3.7969e-03
919	3.9635e-03	4.1123e-03	4.2392e-03	4.3407e-03	4.4130e-03
920	4.4530e-03	4.4572e-03	4.4230e-03	4.3486e-03	4.2342e-03
921	4.0792e-03	3.8834e-03	3.6533e-03	3.3876e-03	3.0965e-03
922	2.7855e-03	2.4609e-03	2.1330e-03	1.8102e-03	1.4981e-03
923	1.2094e-03	9.5725e-04	7.3272e-04	5.4688e-04	3.9398e-04
924	2.7518e-04	1.8547e-04	1.2166e-04	7.7383e-05	4.7955e-05
925	2.9016e-05	1.7181e-05	9.9446e-06	5.6718e-06	3.1846e-06
926	1.7641e-06	9.6501e-07	5.2223e-07	2.8123e-07	1.5000e-07
927	0.0000e+00	0.0000e+00	0.0000e+00	0.0000e+00	0.0000e+00
928	0.0000e+00	0.0000e+00	0.0000e+00	0.0000e+00	0.0000e+00
929	0.0000e+00	0.0000e+00	0.0000e+00	0.0000e+00	0.0000e+00
930	0.0000e+00	0.0000e+00	0.0000e+00	0.0000e+00	0.0000e+00
931	0.0000e+00	0.0000e+00	0.0000e+00	0.0000e+00	0.0000e+00
932	0.0000e+00	0.0000e+00	0.0000e+00	0.0000e+00	0.0000e+00
933	0.0000e+00	0.0000e+00	0.0000e+00	0.0000e+00	0.0000e+00
934	0.0000e+00	0.0000e+00	0.0000e+00	0.0000e+00	0.0000e+00
935	0.0000e+00	0.0000e+00	0.0000e+00	0.0000e+00	0.0000e+00
936	0.0000e+00	0.0000e+00	0.0000e+00	0.0000e+00	0.0000e+00
937	0.0000e+00	0.0000e+00	0.0000e+00	0.0000e+00	0.0000e+00
938	0.0000e+00	0.0000e+00	0.0000e+00	0.0000e+00	0.0000e+00
939	0.0000e+00	0.0000e+00	0.0000e+00	0.0000e+00	0.0000e+00
940	0.0000e+00	0.0000e+00	0.0000e+00	0.0000e+00	0.0000e+00
941	0.0000e+00	0.0000e+00	0.0000e+00	0.0000e+00	0.0000e+00
942	0.0000e+00	0.0000e+00	0.0000e+00	0.0000e+00	0.0000e+00
943	0.0000e+00	0.0000e+00	0.0000e+00	0.0000e+00	0.0000e+00
944	0.0000e+00	0.0000e+00	0.0000e+00	0.0000e+00	0.0000e+00
945	0.0000e+00	0.0000e+00	0.0000e+00	0.0000e+00	0.0000e+00
946	0.0000e+00	0.0000e+00	0.0000e+00	0.0000e+00	0.0000e+00
947	0.0000e+00	0.0000e+00	0.0000e+00	0.0000e+00	0.0000e+00
948	0.0000e+00	0.0000e+00	0.0000e+00	0.0000e+00	0.0000e+00
949	0.0000e+00	0.0000e+00	0.0000e+00	0.0000e+00	0.0000e+00
950	0.0000e+00	0.0000e+00	0.0000e+00	0.0000e+00	0.0000e+00
951	0.0000e+00	0.0000e+00	0.0000e+00	0.0000e+00	0.0000e+00
952	0.0000e+00	0.0000e+00	0.0000e+00	0.0000e+00	0.0000e+00
953	0.0000e+00	0.0000e+00	0.0000e+00	0.0000e+00	0.0000e+00
954	0.0000e+00	0.0000e+00	0.0000e+00	0.0000e+00	0.0000e+00
955	0.0000e+00	0.0000e+00	0.0000e+00	0.0000e+00	0.0000e+00
956	0.0000e+00	0.0000e+00	0.0000e+00	0.0000e+00	0.0000e+00
957	0.0000e+00	0.0000e+00	0.0000e+00	0.0000e+00	0.0000e+00
958	0.0000e+00	0.0000e+00	0.0000e+00	0.0000e+00	0.0000e+00
959	0.0000e+00	0.0000e+00	0.0000e+00	0.0000e+00	0.0000e+00
960	0.0000e+00	0.0000e+00	0.0000e+00	0.0000e+00	0.0000e+00
961	0.0000e+00	0.0000e+00	0.0000e+00	0.0000e+00	0.0000e+00
962	0.0000e+00	0.0000e+00	0.0000e+00	0.0000e+00	0.0000e+00
963	0.0000e+00	0.0000e+00	0.0000e+00	0.0000e+00	0.0000e+00
964	0.0000e+00	0.0000e+00	0.0000e+00	0.0000e+00	0.0000e+00
965	0.0000e+00	0.0000e+00	0.0000e+00	0.0000e+00	0.0000e+00

966	0.0000e+00	0.0000e+00	0.0000e+00	0.0000e+00	0.0000e+00
967	0.0000e+00	0.0000e+00	0.0000e+00	0.0000e+00	0.0000e+00
968	0.0000e+00	0.0000e+00	0.0000e+00	0.0000e+00	0.0000e+00
969	0.0000e+00	0.0000e+00	0.0000e+00	0.0000e+00	0.0000e+00
970	0.0000e+00	0.0000e+00	0.0000e+00	0.0000e+00	0.0000e+00
971	0.0000e+00	0.0000e+00	0.0000e+00	0.0000e+00	0.0000e+00
972	0.0000e+00	0.0000e+00	0.0000e+00	0.0000e+00	0.0000e+00
973	0.0000e+00	0.0000e+00	0.0000e+00	0.0000e+00	0.0000e+00
974	0.0000e+00	0.0000e+00	0.0000e+00	0.0000e+00	0.0000e+00
975	0.0000e+00	0.0000e+00	0.0000e+00	0.0000e+00	0.0000e+00
976	0.0000e+00	0.0000e+00	0.0000e+00	0.0000e+00	0.0000e+00
977	0.0000e+00	0.0000e+00	0.0000e+00	0.0000e+00	0.0000e+00
978	0.0000e+00	0.0000e+00	0.0000e+00	0.0000e+00	0.0000e+00
979	0.0000e+00	0.0000e+00	0.0000e+00	0.0000e+00	0.0000e+00
980	0.0000e+00	0.0000e+00	0.0000e+00	0.0000e+00	0.0000e+00
981	0.0000e+00	0.0000e+00	0.0000e+00	0.0000e+00	0.0000e+00
982	0.0000e+00	0.0000e+00	0.0000e+00	0.0000e+00	0.0000e+00
983	0.0000e+00	0.0000e+00	0.0000e+00	0.0000e+00	0.0000e+00
984	0.0000e+00	0.0000e+00	0.0000e+00	0.0000e+00	0.0000e+00
985	0.0000e+00	0.0000e+00	0.0000e+00	0.0000e+00	0.0000e+00
986	0.0000e+00	0.0000e+00	0.0000e+00	0.0000e+00	0.0000e+00
987	6.2255e-09	1.3157e-08	2.7695e-08	5.7536e-08	1.1728e-07
988	2.3133e-07	4.3596e-07	7.7837e-07	1.3102e-06	2.0888e-06
989	3.1734e-06	4.6205e-06	6.5492e-06	9.0426e-06	1.2230e-05
990	1.6276e-05	2.1386e-05	2.7778e-05	3.5775e-05	4.5715e-05
991	5.8011e-05	7.3155e-05	9.1533e-05	1.1406e-04	1.4125e-04
992	1.7410e-04	2.1354e-04	2.6061e-04	3.1653e-04	3.8277e-04
993	4.6074e-04	5.5189e-04	6.5812e-04	7.8123e-04	9.2314e-04
994	1.0859e-03	1.2715e-03	1.4821e-03	1.7198e-03	1.9865e-03
995	2.2841e-03	2.6144e-03	2.9787e-03	3.3783e-03	3.8142e-03
996	4.2865e-03	4.7950e-03	5.3389e-03	5.9172e-03	6.5272e-03
997	7.1662e-03	7.8300e-03	8.5141e-03	9.2128e-03	9.9191e-03
998	1.0625e-02	1.1323e-02	1.2002e-02	1.2652e-02	1.3262e-02
999	1.3820e-02	1.4314e-02	1.4729e-02	1.5055e-02	1.5279e-02
1000	1.5390e-02	1.5378e-02	1.5232e-02	1.4948e-02	1.4529e-02
1001	1.3971e-02	1.3275e-02	1.2464e-02	1.1535e-02	1.0522e-02
1002	9.4451e-03	8.3261e-03	7.2005e-03	6.0963e-03	5.0327e-03
1003	4.0521e-03	3.1989e-03	2.4416e-03	1.8170e-03	1.3049e-03
1004	9.0848e-04	6.1023e-04	3.9885e-04	2.5278e-04	1.5606e-04
1005	9.4065e-05	5.5479e-05	3.1983e-05	1.8167e-05	1.0158e-05
1006	5.6038e-06	3.0524e-06	1.6448e-06	8.8196e-07	4.6839e-07
1007	0.0000e+00	0.0000e+00	0.0000e+00	0.0000e+00	0.0000e+00
1008	0.0000e+00	0.0000e+00	0.0000e+00	0.0000e+00	0.0000e+00
1009	0.0000e+00	0.0000e+00	0.0000e+00	0.0000e+00	0.0000e+00
1010	0.0000e+00	0.0000e+00	0.0000e+00	0.0000e+00	0.0000e+00
1011	0.0000e+00	0.0000e+00	0.0000e+00	0.0000e+00	0.0000e+00
1012	0.0000e+00	0.0000e+00	0.0000e+00	0.0000e+00	0.0000e+00
1013	0.0000e+00	0.0000e+00	0.0000e+00	0.0000e+00	0.0000e+00
1014	0.0000e+00	0.0000e+00	0.0000e+00	0.0000e+00	0.0000e+00
1015	0.0000e+00	0.0000e+00	0.0000e+00	0.0000e+00	0.0000e+00
1016	0.0000e+00	0.0000e+00	0.0000e+00	0.0000e+00	0.0000e+00
1017	0.0000e+00	0.0000e+00	0.0000e+00	0.0000e+00	0.0000e+00
1018	0.0000e+00	0.0000e+00	0.0000e+00	0.0000e+00	0.0000e+00
1019	0.0000e+00	0.0000e+00	0.0000e+00	0.0000e+00	0.0000e+00
1020	0.0000e+00	0.0000e+00	0.0000e+00	0.0000e+00	0.0000e+00
1021	0.0000e+00	0.0000e+00	0.0000e+00	0.0000e+00	0.0000e+00
1022	0.0000e+00	0.0000e+00	0.0000e+00	0.0000e+00	0.0000e+00
1023	0.0000e+00	0.0000e+00	0.0000e+00	0.0000e+00	0.0000e+00
1024	0.0000e+00	0.0000e+00	0.0000e+00	0.0000e+00	0.0000e+00
1025	0.0000e+00	0.0000e+00	0.0000e+00	0.0000e+00	0.0000e+00
1026	0.0000e+00	0.0000e+00	0.0000e+00	0.0000e+00	0.0000e+00
1027	1.1449e-08	2.3214e-08	4.6882e-08	9.3478e-08	1.8300e-07
1028	3.4720e-07	6.3075e-07	1.0885e-06	1.7765e-06	2.7540e-06
1029	4.0789e-06	5.8030e-06	8.0482e-06	1.0888e-05	1.4444e-05
1030	1.8870e-05	2.4354e-05	3.1088e-05	3.9361e-05	4.9460e-05
1031	6.1735e-05	7.6589e-05	9.4307e-05	1.1565e-04	1.4097e-04
1032	1.7105e-04	2.0655e-04	2.4819e-04	2.9683e-04	3.5346e-04
1033	4.1899e-04	4.9428e-04	5.8053e-04	6.7878e-04	7.9008e-04
1034	9.1551e-04	1.0561e-03	1.2128e-03	1.3865e-03	1.5780e-03

1.7879e-03	2.0166e-03	2.2643e-03	2.5309e-03	2.8165e-03
3.1199e-03	3.4404e-03	3.7764e-03	4.1265e-03	4.4883e-03
4.8592e-03	5.2362e-03	5.6158e-03	5.9942e-03	6.3671e-03
6.7298e-03	7.0773e-03	7.4045e-03	7.7056e-03	7.9752e-03
8.2075e-03	8.3970e-03	8.5376e-03	8.6247e-03	8.6533e-03
8.6193e-03	8.5200e-03	8.3513e-03	8.1137e-03	7.8113e-03
7.4440e-03	7.0128e-03	6.5327e-03	6.0012e-03	5.4380e-03
4.8528e-03	4.2559e-03	3.6647e-03	3.0921e-03	2.5463e-03
2.0471e-03	1.6153e-03	1.2336e-03	9.1951e-04	6.6214e-04
4.6269e-04	3.1227e-04	2.0526e-04	1.3093e-04	8.1419e-05
4.9462e-05	2.9418e-05	1.7110e-05	9.8093e-06	5.5377e-06
3.0851e-06	1.6975e-06	9.2419e-07	5.0073e-07	2.6875e-07
0.0000e+00	0.0000e+00	0.0000e+00	0.0000e+00	0.0000e+00
0.0000e+00	0.0000e+00	0.0000e+00	0.0000e+00	0.0000e+00
0.0000e+00	0.0000e+00	0.0000e+00	0.0000e+00	0.0000e+00
0.0000e+00	0.0000e+00	0.0000e+00	0.0000e+00	0.0000e+00
0.0000e+00	0.0000e+00	0.0000e+00	0.0000e+00	0.0000e+00
0.0000e+00	0.0000e+00	0.0000e+00	0.0000e+00	0.0000e+00
0.0000e+00	0.0000e+00	0.0000e+00	0.0000e+00	0.0000e+00
0.0000e+00	0.0000e+00	0.0000e+00	0.0000e+00	0.0000e+00
0.0000e+00	0.0000e+00	0.0000e+00	0.0000e+00	0.0000e+00
0.0000e+00	0.0000e+00	0.0000e+00	0.0000e+00	0.0000e+00
0.0000e+00	0.0000e+00	0.0000e+00	0.0000e+00	0.0000e+00
0.0000e+00	0.0000e+00	0.0000e+00	0.0000e+00	0.0000e+00
0.0000e+00	0.0000e+00	0.0000e+00	0.0000e+00	0.0000e+00
0.0000e+00	0.0000e+00	0.0000e+00	0.0000e+00	0.0000e+00
0.0000e+00	0.0000e+00	0.0000e+00	0.0000e+00	0.0000e+00
0.0000e+00	0.0000e+00	0.0000e+00	0.0000e+00	0.0000e+00
0.0000e+00	0.0000e+00	0.0000e+00	0.0000e+00	0.0000e+00
0.0000e+00	0.0000e+00	0.0000e+00	0.0000e+00	0.0000e+00
0.0000e+00	0.0000e+00	0.0000e+00	0.0000e+00	0.0000e+00
0.0000e+00	0.0000e+00	0.0000e+00	0.0000e+00	0.0000e+00
0.0000e+00	0.0000e+00	0.0000e+00	0.0000e+00	0.0000e+00
0.0000e+00	0.0000e+00	0.0000e+00	0.0000e+00	0.0000e+00
0.0000e+00	0.0000e+00	0.0000e+00	0.0000e+00	0.0000e+00
0.0000e+00	0.0000e+00	0.0000e+00	0.0000e+00	0.0000e+00
0.0000e+00	0.0000e+00	0.0000e+00	0.0000e+00	0.0000e+00
0.0000e+00	0.0000e+00	0.0000e+00	0.0000e+00	0.0000e+00
0.0000e+00	0.0000e+00	0.0000e+00	0.0000e+00	0.0000e+00
0.0000e+00	0.0000e+00	0.0000e+00	0.0000e+00	0.0000e+00
0.0000e+00	0.0000e+00	0.0000e+00	0.0000e+00	0.0000e+00
0.0000e+00	0.0000e+00	0.0000e+00	0.0000e+00	0.0000e+00
0.0000e+00	0.0000e+00	0.0000e+00	0.0000e+00	0.0000e+00
0.0000e+00	0.0000e+00	0.0000e+00	0.0000e+00	0.0000e+00
0.0000e+00	0.0000e+00	0.0000e+00	0.0000e+00	0.0000e+00
0.0000e+00	0.0000e+00	0.0000e+00	0.0000e+00	0.0000e+00
0.0000e+00	0.0000e+00	0.0000e+00	0.0000e+00	0.0000e+00
0.0000e+00	0.0000e+00	0.0000e+00	0.0000e+00	0.0000e+00
0.0000e+00	0.0000e+00	0.0000e+00	0.0000e+00	0.0000e+00
0.0000e+00	0.0000e+00	0.0000e+00	0.0000e+00	0.0000e+00
0.0000e+00	0.0000e+00	0.0000e+00	0.0000e+00	0.0000e+00
0.0000e+00	0.0000e+00	0.0000e+00	0.0000e+00	0.0000e+00
4.7984e-08	9.4549e-08	1.8558e-07	3.5978e-07	6.8528e-07
1.2664e-06	2.2448e-06	3.7873e-06	6.0560e-06	9.2171e-06
1.3427e-05	1.8819e-05	2.5738e-05	3.4370e-05	4.5040e-05
5.8160e-05	7.4226e-05	9.3729e-05	1.1743e-04	1.4605e-04
1.8047e-04	2.2169e-04	2.7035e-04	3.2837e-04	3.9654e-04
4.7668e-04	5.7035e-04	6.7917e-04	8.0502e-04	9.5013e-04
1.1164e-03	1.3056e-03	1.5203e-03	1.7625e-03	2.0342e-03
2.3374e-03	2.6739e-03	3.0454e-03	3.4531e-03	3.8982e-03
4.3810e-03	4.9019e-03	5.4602e-03	6.0550e-03	6.6852e-03
7.3476e-03	8.0395e-03	8.7569e-03	9.4955e-03	1.0250e-02
1.1013e-02	1.1779e-02	1.2539e-02	1.3286e-02	1.4009e-02
1.4701e-02	1.5350e-02	1.5947e-02	1.6481e-02	1.6942e-02
1.7319e-02	1.7603e-02	1.7783e-02	1.7853e-02	1.7805e-02
1.7632e-02	1.7332e-02	1.6898e-02	1.6335e-02	1.5653e-02
1.4852e-02	1.3937e-02	1.2937e-02	1.1848e-02	1.0709e-02
9.5380e-03	8.3532e-03	7.1877e-03	6.0644e-03	4.9973e-03
4.0236e-03	3.1820e-03	2.4377e-03	1.8240e-03	1.3198e-03

9.2738e-04	6.2991e-04	4.1697e-04	2.6804e-04	1.6806e-04
1.0299e-04	6.1816e-05	3.6297e-05	2.1013e-05	1.1981e-05
6.7433e-06	3.7490e-06	2.0627e-06	1.1295e-06	6.1274e-07
0.0000e+00	0.0000e+00	0.0000e+00	0.0000e+00	0.0000e+00
0.0000e+00	0.0000e+00	0.0000e+00	0.0000e+00	0.0000e+00
0.0000e+00	0.0000e+00	0.0000e+00	0.0000e+00	0.0000e+00
0.0000e+00	0.0000e+00	0.0000e+00	0.0000e+00	0.0000e+00
0.0000e+00	0.0000e+00	0.0000e+00	0.0000e+00	0.0000e+00
0.0000e+00	0.0000e+00	0.0000e+00	0.0000e+00	0.0000e+00
0.0000e+00	0.0000e+00	0.0000e+00	0.0000e+00	0.0000e+00
0.0000e+00	0.0000e+00	0.0000e+00	0.0000e+00	0.0000e+00
0.0000e+00	0.0000e+00	0.0000e+00	0.0000e+00	0.0000e+00
0.0000e+00	0.0000e+00	0.0000e+00	0.0000e+00	0.0000e+00
0.0000e+00	0.0000e+00	0.0000e+00	0.0000e+00	0.0000e+00
0.0000e+00	0.0000e+00	0.0000e+00	0.0000e+00	0.0000e+00
0.0000e+00	0.0000e+00	0.0000e+00	0.0000e+00	0.0000e+00
0.0000e+00	0.0000e+00	0.0000e+00	0.0000e+00	0.0000e+00
0.0000e+00	0.0000e+00	0.0000e+00	0.0000e+00	0.0000e+00
0.0000e+00	0.0000e+00	0.0000e+00	0.0000e+00	0.0000e+00
0.0000e+00	0.0000e+00	0.0000e+00	0.0000e+00	0.0000e+00
0.0000e+00	0.0000e+00	0.0000e+00	0.0000e+00	0.0000e+00
0.0000e+00	0.0000e+00	0.0000e+00	0.0000e+00	0.0000e+00
0.0000e+00	0.0000e+00	0.0000e+00	0.0000e+00	0.0000e+00
0.0000e+00	0.0000e+00	0.0000e+00	0.0000e+00	0.0000e+00
0.0000e+00	0.0000e+00	0.0000e+00	0.0000e+00	0.0000e+00
1.2677e-08	2.5665e-08	5.1752e-08	1.0304e-07	2.0144e-07
3.8168e-07	6.9257e-07	1.1940e-06	1.9468e-06	3.0155e-06
4.4632e-06	6.3459e-06	8.7964e-06	1.1895e-05	1.5772e-05
2.0597e-05	2.6574e-05	3.3910e-05	4.2920e-05	5.3918e-05
6.7281e-05	8.3450e-05	1.0273e-04	1.2596e-04	1.5351e-04
1.8623e-04	2.2485e-04	2.7015e-04	3.2306e-04	3.8467e-04
4.5595e-04	5.3787e-04	6.3172e-04	7.3863e-04	8.5977e-04
9.9632e-04	1.1494e-03	1.3201e-03	1.5093e-03	1.7181e-03
1.9469e-03	2.1965e-03	2.4669e-03	2.7581e-03	3.0703e-03
3.4023e-03	3.7533e-03	4.1218e-03	4.5063e-03	4.9042e-03
5.3130e-03	5.7294e-03	6.1498e-03	6.5702e-03	6.9860e-03
7.3924e-03	7.7839e-03	8.1554e-03	8.5006e-03	8.8135e-03
9.0881e-03	9.3185e-03	9.4980e-03	9.6213e-03	9.6829e-03
9.6780e-03	9.6031e-03	9.4535e-03	9.2287e-03	8.9318e-03
8.5621e-03	8.1198e-03	7.6193e-03	7.0571e-03	6.4532e-03
5.8171e-03	5.1592e-03	4.4983e-03	3.8483e-03	3.2183e-03
2.6319e-03	2.1150e-03	1.6487e-03	1.2563e-03	9.2697e-04
6.6502e-04	4.6184e-04	3.1289e-04	2.0611e-04	1.3256e-04
8.3412e-05	5.1451e-05	3.1079e-05	1.8520e-05	1.0877e-05
6.3094e-06	3.6174e-06	2.0534e-06	1.1603e-06	6.4986e-07
0.0000e+00	0.0000e+00	0.0000e+00	0.0000e+00	0.0000e+00
0.0000e+00	0.0000e+00	0.0000e+00	0.0000e+00	0.0000e+00
0.0000e+00	0.0000e+00	0.0000e+00	0.0000e+00	0.0000e+00
0.0000e+00	0.0000e+00	0.0000e+00	0.0000e+00	0.0000e+00
0.0000e+00	0.0000e+00	0.0000e+00	0.0000e+00	0.0000e+00
0.0000e+00	0.0000e+00	0.0000e+00	0.0000e+00	0.0000e+00
0.0000e+00	0.0000e+00	0.0000e+00	0.0000e+00	0.0000e+00
0.0000e+00	0.0000e+00	0.0000e+00	0.0000e+00	0.0000e+00
0.0000e+00	0.0000e+00	0.0000e+00	0.0000e+00	0.0000e+00
0.0000e+00	0.0000e+00	0.0000e+00	0.0000e+00	0.0000e+00
0.0000e+00	0.0000e+00	0.0000e+00	0.0000e+00	0.0000e+00
0.0000e+00	0.0000e+00	0.0000e+00	0.0000e+00	0.0000e+00
0.0000e+00	0.0000e+00	0.0000e+00	0.0000e+00	0.0000e+00
0.0000e+00	0.0000e+00	0.0000e+00	0.0000e+00	0.0000e+00
0.0000e+00	0.0000e+00	0.0000e+00	0.0000e+00	0.0000e+00
0.0000e+00	0.0000e+00	0.0000e+00	0.0000e+00	0.0000e+00
0.0000e+00	0.0000e+00	0.0000e+00	0.0000e+00	0.0000e+00
0.0000e+00	0.0000e+00	0.0000e+00	0.0000e+00	0.0000e+00
0.0000e+00	0.0000e+00	0.0000e+00	0.0000e+00	0.0000e+00
2.6302e-07	5.1745e-07	1.0140e-06	1.9629e-06	3.7334e-06
6.8900e-06	1.2197e-05	2.0556e-05	3.2836e-05	4.9932e-05
7.2682e-05	1.0180e-04	1.3914e-04	1.8570e-04	2.4323e-04
3.1392e-04	4.0046e-04	5.0547e-04	6.3303e-04	7.8703e-04
9.7215e-04	1.1938e-03	1.4554e-03	1.7673e-03	2.1335e-03
2.5641e-03	3.0672e-03	3.6516e-03	4.3274e-03	5.1066e-03

5.9994e-03	7.0153e-03	8.1679e-03	9.4681e-03	1.0927e-02
1.2555e-02	1.4363e-02	1.6358e-02	1.8549e-02	2.0942e-02
2.3539e-02	2.6341e-02	2.9347e-02	3.2552e-02	3.5951e-02
3.9527e-02	4.3267e-02	4.7150e-02	5.1156e-02	5.5253e-02
5.9412e-02	6.3595e-02	6.7765e-02	7.1877e-02	7.5884e-02
7.9740e-02	8.3389e-02	8.6783e-02	8.9865e-02	9.2580e-02
9.4875e-02	9.6699e-02	9.7997e-02	9.8726e-02	9.8844e-02
9.8312e-02	9.7113e-02	9.5207e-02	9.2600e-02	8.9339e-02
8.5416e-02	8.0837e-02	7.5750e-02	7.0113e-02	6.4121e-02
5.7856e-02	5.1411e-02	4.4956e-02	3.8614e-02	3.2463e-02
2.6722e-02	2.1638e-02	1.7022e-02	1.3106e-02	9.7871e-03
7.1158e-03	5.0158e-03	3.4530e-03	2.3142e-03	1.5159e-03
9.7237e-04	6.1190e-04	3.7739e-04	2.2972e-04	1.3790e-04
8.1792e-05	4.7969e-05	2.7865e-05	1.6114e-05	9.2396e-06
3.7409e-12	9.0966e-12	2.2032e-11	5.2580e-11	1.2279e-10
2.7604e-10	5.8838e-10	1.1770e-09	2.1965e-09	3.8444e-09
6.3563e-09	9.9931e-09	1.5222e-08	2.2481e-08	3.2402e-08
4.5831e-08	6.3869e-08	8.7824e-08	1.1960e-07	1.6142e-07
2.1618e-07	2.8749e-07	3.7893e-07	4.9731e-07	6.4816e-07
8.4051e-07	1.0843e-06	1.3911e-06	1.7757e-06	2.2561e-06
2.8526e-06	3.5880e-06	4.4919e-06	5.5966e-06	6.9398e-06
8.5647e-06	1.0520e-05	1.2860e-05	1.5647e-05	1.8949e-05
2.2840e-05	2.7399e-05	3.2714e-05	3.8874e-05	4.5984e-05
5.4132e-05	6.3423e-05	7.3953e-05	8.5825e-05	9.9123e-05
1.1393e-04	1.3030e-04	1.4830e-04	1.6794e-04	1.8920e-04
2.1206e-04	2.3641e-04	2.6215e-04	2.8906e-04	3.1689e-04
3.4533e-04	3.7403e-04	4.0241e-04	4.3004e-04	4.5622e-04
4.8045e-04	5.0170e-04	5.1956e-04	5.3300e-04	5.4125e-04
5.4383e-04	5.4012e-04	5.2986e-04	5.1263e-04	4.8881e-04
4.5876e-04	4.2302e-04	3.8280e-04	3.3935e-04	2.9370e-04
2.4812e-04	2.0545e-04	1.6488e-04	1.2910e-04	9.7794e-05
7.1940e-05	5.1192e-05	3.5501e-05	2.3927e-05	1.5738e-05
1.0126e-05	6.3856e-06	3.9442e-06	2.4033e-06	1.4437e-06
8.5666e-07	5.0256e-07	2.9198e-07	1.6887e-07	9.6832e-08
8.1758e-10	1.7559e-09	3.7569e-09	7.9325e-09	1.6431e-08
3.2920e-08	6.2971e-08	1.1401e-07	1.9437e-07	3.1353e-07
4.8148e-07	7.0798e-07	1.0129e-06	1.4110e-06	1.9245e-06
2.5821e-06	3.4199e-06	4.4768e-06	5.8102e-06	7.4813e-06
9.5657e-06	1.2154e-05	1.5322e-05	1.9236e-05	2.4000e-05
2.9803e-05	3.6831e-05	4.5288e-05	5.5421e-05	6.7527e-05
8.1901e-05	9.8850e-05	1.1878e-04	1.4208e-04	1.6919e-04
2.0055e-04	2.3667e-04	2.7801e-04	3.2512e-04	3.7850e-04
4.3865e-04	5.0606e-04	5.8120e-04	6.6445e-04	7.5626e-04
8.5681e-04	9.6630e-04	1.0848e-03	1.2123e-03	1.3485e-03
1.4930e-03	1.6453e-03	1.8046e-03	1.9699e-03	2.1398e-03
2.3131e-03	2.4877e-03	2.6620e-03	2.8334e-03	2.9996e-03
3.1578e-03	3.3053e-03	3.4385e-03	3.5546e-03	3.6502e-03
3.7224e-03	3.7675e-03	3.7832e-03	3.7665e-03	3.7163e-03
3.6313e-03	3.5102e-03	3.3562e-03	3.1675e-03	2.9506e-03
2.7091e-03	2.4471e-03	2.1728e-03	1.8928e-03	1.6122e-03
1.3428e-03	1.0985e-03	8.7210e-04	6.7677e-04	5.0882e-04
3.7204e-04	2.6348e-04	1.8206e-04	1.2238e-04	8.0349e-05
5.1628e-05	3.2532e-05	2.0084e-05	1.2234e-05	7.3482e-06
4.3602e-06	2.5579e-06	1.4862e-06	8.5962e-07	4.9295e-07

APPENDIX 5 – EXAMPLE OF SOURCE TERM DATASET (GENERATED BY MATLAB SCRIPT) TO BE IMPORTED IN PHITS

```
[ S o u r c e ]
totfact = 3.22697e+06        # global normalization factor - if positive, the source particle is generated according to this ratio
iscorr  = 0                  # multi-source correlation option - if 0, normal multi-source

<source> = 0.904146      # defines a multi-source, the relative weight is defined by this number
s-type   = 10            # spherical shell with energy distribution
proj     = 1H
x0 =  0.0000       # (D=0.0) center position of x-axis [cm]
y0 =  0.0000       # (D=0.0) center position of y-axis [cm]
z0 =  0.0000       # (D=0.0) center position of z-axis [cm]
r1 =    1000       # inner radius [cm]
r2 =    1000       # outer radius [cm]
dir =   -all       # direction of beam [isotropic]
e-type =   21      # energy distribution by data set of energy bins e(i) and differential probabilities of the particle generation dflux/dE(i)
  ne =     100
   0.0000000e+00   2.2674000e-04
   1.0000000e-02   4.3080000e-04
   1.4081220e-02   8.1699000e-04
   1.9828060e-02   1.5346000e-03
   2.7809810e-02   2.8413000e-03
   3.8754670e-02   5.1240000e-03
   5.3324530e-02   8.9017000e-03
   7.2012050e-02   1.4784000e-02
   9.5042140e-02   2.3367000e-02
   1.2225730e-01   3.5275000e-02
   1.5354880e-01   5.1117000e-02
   1.8876410e-01   7.1435000e-02
   2.2767140e-01   9.7602000e-02
   2.7143740e-01   1.3043000e-01
   3.1991590e-01   1.7129000e-01
   3.7371610e-01   2.2195000e-01
   4.3365430e-01   2.8462000e-01
   5.0067120e-01   3.6156000e-01
   5.7545540e-01   4.5625000e-01
   6.5948900e-01   5.7222000e-01
   7.5384210e-01   7.1387000e-01
   8.5986750e-01   8.8641000e-01
   9.7910780e-01   1.0939000e+00
   1.1119580e+00   1.3462000e+00
   1.2621830e+00   1.6489000e+00
   1.4302600e+00   2.0131000e+00
   1.6193840e+00   2.4491000e+00
   1.8318950e+00   2.9687000e+00
   2.0703130e+00   3.5862000e+00
   2.3378820e+00   4.3188000e+00
   2.6386860e+00   5.1840000e+00
   2.9763270e+00   6.2000000e+00
   3.3545370e+00   7.3915000e+00
   3.7790000e+00   8.7826000e+00
   4.2550030e+00   1.0400000e+01
   4.7886430e+00   1.2275000e+01
   5.3868160e+00   1.4437000e+01
   6.0571490e+00   1.6922000e+01
   6.8081070e+00   1.9766000e+01
   7.6495090e+00   2.3006000e+01
   8.5919970e+00   2.6680000e+01
   9.6475600e+00   3.0830000e+01
   1.0829610e+01   3.5492000e+01
   1.2153220e+01   4.0706000e+01
   1.3634910e+01   4.6513000e+01
   1.5295320e+01   5.2939000e+01
   1.7153760e+01   6.0016000e+01
   1.9234660e+01   6.7765000e+01
   2.1564300e+01   7.6206000e+01
   2.4174420e+01   8.5341000e+01
```

```
   2.7097400e+01   9.5167000e+01
   3.0372160e+01   1.0566000e+02
   3.4040700e+01   1.1680000e+02
   3.8152340e+01   1.2853000e+02
   4.2762540e+01   1.4078000e+02
   4.7931350e+01   1.5347000e+02
   5.3731540e+01   1.6647000e+02
   6.0238540e+01   1.7969000e+02
   6.7550910e+01   1.9295000e+02
   7.5767380e+01   2.0608000e+02
   8.5007100e+01   2.1889000e+02
   9.5407100e+01   2.3118000e+02
   1.0714230e+02   2.4266000e+02
   1.2035410e+02   2.5314000e+02
   1.3529050e+02   2.6232000e+02
   1.5216130e+02   2.6999000e+02
   1.7137480e+02   2.7580000e+02
   1.9301430e+02   2.7959000e+02
   2.1786760e+02   2.8105000e+02
   2.4615320e+02   2.8003000e+02
   2.7811100e+02   2.7638000e+02
   3.1472520e+02   2.6995000e+02
   3.5710100e+02   2.6086000e+02
   4.0534760e+02   2.4895000e+02
   4.6176890e+02   2.3458000e+02
   5.2681340e+02   2.1794000e+02
   6.0246180e+02   1.9932000e+02
   6.9132800e+02   1.7924000e+02
   7.9568620e+02   1.5820000e+02
   9.1918720e+02   1.3659000e+02
   1.0678880e+03   1.1532000e+02
   1.2457530e+03   9.5588000e+01
   1.4532420e+03   7.6895000e+01
   1.7096410e+03   6.0412000e+01
   2.0164510e+03   4.5947000e+01
   2.3969190e+03   3.3937000e+01
   2.8632240e+03   2.4238000e+01
   3.4442410e+03   1.6853000e+01
   4.1560850e+03   1.1371000e+01
   5.0403320e+03   7.4747000e+00
   6.1339310e+03   4.7955000e+00
   7.4880860e+03   3.0090000e+00
   9.1669670e+03   1.8450000e+00
   1.1264860e+04   1.1135000e+00
   1.3861320e+04   6.6118000e-01
   1.7094410e+04   3.8706000e-01
   2.1122060e+04   2.2363000e-01
   2.6151970e+04   1.2776000e-01
   3.2436140e+04   7.2571000e-02
   4.0232510e+04   4.0822000e-02
   5.0000000e+04

<source> = 0.087398      # defines a multi-source, the relative weight is defined by this number
s-type   = 10      # spherical shell with energy distribution
proj     = 4He
x0 =  0.0000       # (D=0.0) center position of x-axis [cm]
y0 =  0.0000       # (D=0.0) center position of y-axis [cm]
z0 =  0.0000       # (D=0.0) center position of z-axis [cm]
r1 =    1000       # inner radius [cm]
r2 =    1000       # outer radius [cm]
dir =   -all       # direction of beam [isotropic]
e-type =   21      # energy distribution by data set of energy bins e(i) and differential probabilities of the particle generation dflux/dE(i)
  ne =     100
   0.0000000e+00   8.9992000e-05
   1.0000000e-02   1.7640000e-04
   1.4081220e-02   3.4453000e-04
   1.9828060e-02   6.6490000e-04
```

APPENDIX 6 – EXAMPLE OF PHITS OUTPUT FILE (TALLY RESULTS)

```
[ T - T r a c k ]
    title = Track Detection in reg mesh
     mesh =  reg             # mesh type is region-wise
      reg = 101
   volume                    # combined, lattice or level structure
   non     reg      vol      # reg definition
    1      101   6.5450E+04 # 101
   e-type =    2             # e-mesh is linear given by emin, emax and ne
     emin =  1.0000000E-20  # minimum value of e-mesh points
     emax =  1.0000000E+35  # maximum value of e-mesh points
#    edel =  1.0000000E+35  # mesh width of e-mesh points
       ne =    1             # number of e-mesh points
#    data = ( e(i), i = 1, ne + 1 )
#              1.00000E-20  1.00000E+35
     unit =    1             # unit is [1/cm^2/source]
 material =  all             # (D=all) number of specific material
     axis =  reg             # axis of output
     file = track_reg.out   # file name of output for the above axis
     part =  all
# kf/name :  0
    gshow =    1             # 0: no 1:bnd, 2:bnd+mat, 3:bnd+reg 4:bnd+lat
    resol =    1             # (D=1) resolution of gshow or rshow
    width = 0.5000000       # (D=0.5) width of lines for gshow or rshow
#    used :        main (  %)        temp (  %)       total (  %)
#  memory :          10 (  0)           0 (  0)          10 (  0)

#-------------------------------------------------------------------------------
#newpage:
#   no. =  1
#  ie =  1
#   e = (   1.0000E-20  -   1.0000E+35  )

x: Serial Num. of Region
y: Flux [1/cm^2/source]
p: xlin ylog afac(0.8) form(0.9)
h:   x      n     n          y(all     ),l3   n
#  num    reg    volume     all          r.err
    1     101   6.5450E+04   2.2041E+01  0.0023

#   sum over    6.5450E+04   2.2041E+01

'no. =  1,  ie =  1'
msuc: {\huge Track Detection in reg mesh}
msdl: {\it plotted by \ANGEL \version}
msdr: {\it calculated by \PHITS  2.88}
wt: s(0.7)
\vspace{-3}
  emin  &=&   1.0000E-20 [MeV]
  emax  &=&   1.0000E+35 [MeV]
e:

# Information for Restart Calculation
# This calculation was newly started
# istdev =  2 # 1:Batch variance, 2:History variance
# resc2  = 3.09856521770753757E+00 # Total source weight or Total source weight / maxcas
# resc3  = 1.00000000000000000E+07 # Total history number or Total batch number
# maxcas =    10000000 # History / Batch, only used for istdev=1
# rijklst= 173130845167769.0 # Next initial random number
```

```
[ T - Deposit ]
    title = Absorbed dose in reg mesh
     mesh =  reg            # mesh type is region-wise
      reg = 101
   volume                   # combined, lattice or level structure
   non     reg      vol     # reg definition
    1      101   6.5450E+04 # 101
     unit =    0            # unit is [Gy/source]
   letmat =    0            # (D=0) mat ID for LET, 0:real mat, <0: electron for H2O
  dedxfnc =    0            # (D=0) user defined multiplier, 0(no), 1, 2
 material =  all            # (D=all) number of specific material
   output =  dose           # total deposit energy
  deposit =    0            # (D=0) 0-> total deposit dist, 1-> each process
     axis =   reg           # axis of output
     file = D_all_reg.out   # file name of output for the above axis
     part =  all
# kf/name :  0
    gshow =    1            # 0: no 1:bnd, 2:bnd+mat, 3:bnd+reg 4:bnd+lat
    resol =    1            # (D=1) resolution of gshow or rshow
    width = 0.5000000       # (D=0.5) width of lines for gshow or rshow
#    used :        main (  %)        temp (  %)       total (  %)
#  memory :           7 (  0)           0 (  0)           7 (  0)

#-----------------------------------------------------------------------------------------
#newpage:
#   no. =  1

x: Serial Num. of Region
y: Dose [Gy/source]
p: xlin ylog afac(0.8) form(0.9)
h:   x      n      n          y(all     ),l3   n
#  num    reg     volume     all         r.err
    1     101   6.5450E+04   2.1869E-08  0.0071

'no. =  1'
msuc: {\huge Absorbed dose in reg mesh}
msdl: {\it plotted by \ANGEL \version}
msdr: {\it calculated by \PHITS  2.88}

# Information for Restart Calculation
# This calculation was newly started
# istdev =  2 # 1:Batch variance, 2:History variance
# resc2  = 3.09856521770753757E+00 # Total source weight or Total source weight / maxcas
# resc3  = 1.00000000000000000E+07 # Total history number or Total batch number
# maxcas =    10000000 # History / Batch, only used for istdev=1
# rijklst= 173130845167769.0 # Next initial random number
```

```
[ T - Deposit ]
    title = Dose equivalent in reg mesh
     mesh =  reg            # mesh type is region-wise
      reg = 101
   volume                   # combined, lattice or level structure
   non     reg      vol     # reg definition
    1      101   6.5450E+04 # 101
     unit =    0            # unit is [Gy/source]
   letmat =    0            # (D=0) mat ID for LET, 0:real mat, <0: electron for H2O
  dedxfnc =    1            # (D=0) user defined multiplier, 0(no), 1, 2
 material =  all            # (D=all) number of specific material
   output =  dose           # total deposit energy
  deposit =    0            # (D=0) 0-> total deposit dist, 1-> each process
     axis =   reg           # axis of output
     file = HQ_all_reg.out  # file name of output for the above axis
     part =  all
# kf/name :  0
    gshow =    1            # 0: no 1:bnd, 2:bnd+mat, 3:bnd+reg 4:bnd+lat
    resol =    1            # (D=1) resolution of gshow or rshow
    width = 0.5000000       # (D=0.5) width of lines for gshow or rshow
#    used :        main (  %)        temp (  %)       total (  %)
#  memory :           7 (  0)           0 (  0)           7 (  0)

#-----------------------------------------------------------------------------
#newpage:
#   no. =  1

x: Serial Num. of Region
y: Dose [Gy/source]
p: xlin ylog afac(0.8) form(0.9)
h:   x      n     n          y(all     ),l3   n
#  num    reg     volume     all          r.err
    1     101   6.5450E+04   6.7899E-08   0.0359

'no. =  1'
msuc: {\huge Dose equivalent in reg mesh}
msdl: {\it plotted by \ANGEL \version}
msdr: {\it calculated by \PHITS  2.88}

# Information for Restart Calculation
# This calculation was newly started
# istdev =  2 # 1:Batch variance, 2:History variance
# resc2  = 3.09856521770753757E+00 # Total source weight or Total source weight / maxcas
# resc3  = 1.00000000000000000E+07 # Total history number or Total batch number
# maxcas =    10000000 # History / Batch, only used for istdev=1
# rijklst= 173130845167769.0 # Next initial random number
```